Resolving Dopamine Secretion at Individual Varicosities using Carbon Nanotube-Based Optical Dopamine Nanosensors

Dissertation

for the award of the degree
“Doctor rerum naturalium” (Dr. rer. nat.)
of the Georg-August-Universität Göttingen

within the doctoral program
Cellular and Molecular Physiology of the Brain
of the Göttingen Graduate Center for Neurosciences, Biophysics
and Molecular Biosciences (GGNB)

submitted by

Sofia Elizarova

born in
Leningrad (St. Petersburg), Russian Federation
Göttingen, 2021

Members of the Thesis Advisory Committee

Prof. Dr. Nils Brose
Department of Molecular Neurobiology, Max Planck Institute for Experimental Medicine, Göttingen

Prof. Dr. Tiago Fleming Outeiro
Experimental Neurodegeneration, University Medical Center, Göttingen

Prof. Dr. Sebastian Kruss
Institute of Physical Chemistry, University of Göttingen, Göttingen

Members of the Examination Board

Prof. Dr. Nils Brose (1st reviewer)
Department of Molecular Neurobiology, Max Planck Institute for Experimental Medicine, Göttingen

Prof. Dr. Tiago Fleming Outeiro (2nd reviewer)
Experimental Neurodegeneration, University Medical Center, Göttingen

Further members of the Examination Board

Prof. Dr. Sebastian Kruss
Institute of Physical Chemistry, University of Göttingen, Göttingen

Prof. Dr. Thomas Dresbach
Department of Anatomy and Embryology, University Medical Center, Göttingen

Prof. Dr. Silvio O. Rizzoli
Department of Neuro- and Sensory Physiology, University Medical Center Göttingen, Göttingen

Prof. Dr. Dr. Oliver Schlüter
Psychiatry and Psychotherapy, University Medical Center Göttingen, Göttingen

Date of oral examination: July 5th, 2021

Declaration

I hereby declare that this thesis was written independently and with no other sources and aids than quoted. The work presented here has been, in part, made public in the manuscript “A fluorescent nanosensor paint reveals the heterogeneity of dopamine release from neurons at individual release sites” (Elizarova et al., 2021) through the preprint server for biology BioRxiv.

Sofia Elizarova

Göttingen, May 12th, 2021

Table of Contents

Abstract

Dopamine (DA) is a neurotransmitter that controls vital brain functions such as motor control and motivation, but little is known about the molecular mechanisms that control DA release. Neurotransmission through DA differs substantially from well characterized neurotransmitters, such as glutamate. Dopaminergic secretion sites (varicosities) are functionally and structurally highly diverse, but the molecular basis for this diversity could not be examined to date due to the inability of existing methods to resolve DA secretion at individual release sites, especially across large varicosity populations. I circumvent this critical limitation using a layer comprised of individual small (0.7 nm x 200 nm) carbon nanotube-based nanosensors, that report local, nanomolar DA concentrations through reversible fluorescence increase (> 900 nm). I present an experimental strategy for the use of these sensors for the detection of DA secretion from long-term differentiated, primary dopaminergic cultures with high spatiotemporal resolution: “Adsorbed Nanosensors Detecting Release of Dopamine” (AndromeDA). AndromeDA combines a novel low-density, glia-free ventral midbrain neuron co-culture with a high-density nanosensor layer. At the same time, AndromeDA allows the identification of EGFP-labeled dopaminergic axons during live-cell imaging through a custom-built dual camera set up. Through imaging of millions of nanosensors in parallel, AndromeDA detects local DA secretion events from up to 100 varicosities simultaneously (hotspots), as well as DA diffusion through the extracellular space. AndromeDA facilitates, for the first time, the correlation of subcellular structures with local DA secretion events using a direct DA detection method, and allows the comparison of single release events across large varicosity populations with a temporal resolution similar to existing methods (15 data points/s). I validate that AndromeDA hotspots are representative of *bona fide* DA secretion events through spatio-temporal analysis and pharmacological tools. Using this new methodology, I confirm the previous proposition that action potential-evoked DA release is highly heterogeneous across individual release sites and occurs only at a subpopulation (~17%) of all varicosities. In addition, I show that AndromeDA can detect DA release mediated by spontaneous DAergic neuron activity, as well as rapid electrically evoked action potentials. Finally, I investigate the expression and functional role of Mammalian uncoordinated 13 (Munc13) priming proteins in dopaminergic neurons. I find, that only Munc13-1 is detectable by immunocytochemistry in dopaminergic active zones, and that deletion of Munc13-1 and -2 abolishes electrically evoked (but not KCl evoked) DA release, demonstrating that vesicle priming by Munc13 proteins is required for action potential mediated DA secretion. Imaging with AndromeDA is versatile and readily applicable to other *in vitro* systems, with an unprecedented ability to spatially correlate DA secretion events to presynaptic structures, which will enable a detailed dissection of the molecular mechanisms that give rise to the heterogeneity of the DA system.

Zusammenfassung

Dopamin (DA) ist ein essentieller Botenstoff im Zentralen Nervensystem, der wichtige Funktionen des Gehirns reguliert und bei neurologischen Krankheiten eine zentrale Rolle spielt. Dennoch sind die molekularen Mechanismen der DA Sekretion kaum untersucht. Dopaminerge Transmission unterscheidet sich wesentlich von anderen, gründlich erforschten Neurotransmittern wie Glutamat. Die Strukturen, aus denen DA freigesetzt wird (Varikositäten), sind strukturell und funktionell sehr divers, jedoch konnte die molekulare Basis dieser Diversität bis heute nicht ausreichend untersucht werden. Der Grund hierfür sind hauptsächlich fehlende Methoden, welche die Freisetzung von DA auf Ebene einzelner Varikositäten räumlich auflösen können. Ich überwinde diese kritische Limitation durch Anwendung von kleinen (0,7 nm x 200 nm) Nanosensoren, die aus Kohlenstoff-Nanoröhren hergestellt werden und schon nanomolare DA Konzentrationen spezifisch und reversibel durch einen Anstieg ihrer Nahinfrarot Emission detektieren (> 900 nm). In dieser Arbeit präsentiere ich eine neue experimentelle Strategie zur Anwendung dieser Nanosensoren auf ausdifferenzierten, primären dopaminergen Neuronen, die DA Freisetzung mit hoher raumzeitlicher Auflösung (15 Bilder/s) abbilden kann: *„Adsorbed Nanosensors Detecting Release of Dopamine*“ (AndromeDA). AndromeDA kombiniert eine neurartige, Glia-freie dopaminerge Zellkultur mit einer homogenen Schicht aus Nanosensoren. Der maßgeschneiderte optische Weg des Mikroskopie-Aufbaus erlaubte es, nicht nur das Nahinfrarot Signal der Sensoren, sondern auch parallel dazu dopaminerge EGFP exprimierende Axone abzubilden. AndromeDA erlaubt die zeitgleiche Aufzeichnung von exozytotischen Ereignissen aus bis zu 100 Varikositäten und identifiziert lokale „Hotspots“ der DA Freisetzung. Somit ermöglicht AndromeDA die räumliche Korrelation von DA Freisetzung mit sub-zellulären Strukturen. Nach ausführlicher Validierung dieser neuen Methodik zeige ich, dass die Freisetzung von DA an diskreten Varikositäten stark variiert und dass DA von nur ~17% aller Varikositäten abgesondert wird. Darüberhinaus beobachte ich DA Exozytose, die nicht extern induziert ist und demonstriere, dass diese Eregnisse ebenfalls aus neuronaler Aktivität resultieren. Schließlich undersuche ich die Rolle und Expression von Mammalian uncoordinated 13 (Munc13) *priming* Proteinen in dopaminergen Neuronen und lege dar, dass nur die Munc13-1 Isoform in dopaminergen aktiven Zonen durch cytochemische Analysen vorgefunden werden kann, und dass die genetische Entfernung von Munc13-1 und Munc13-2 die elektisch-induzierte (jedoch nicht über Kalium induzierte) Ausschüttung von DA unterbindet. Somit demonstriere ich, dass Munc13 Proteine für Aktions Potential-vermittelte DA Sekretion benötigt werden. AndromeDA ist eine funktionale hochauflösende bildgebende Methode, die neue Einblicke in den DA Sekretions-Apparat ermöglicht.

List of Figures

List of Abbreviations

A. u.	Arbitrary unit
AFM	Atomic force microscopy
AI	Artificial intelligence
AndromeDA	Adsorbed nanosensors detecting release of dopamine
AP5	(2R)-Amino-5-phosphonopentanoate
APTES	(3-Aminopropyl)-triethoxysilane
BCA	Bicinchoninic acid
BF	Bright field
Bp	Basepairs
BSA	Bovine serum albumin
$CaCl_2$	Calcium chloride
CAMP	Cyclic adenosine monophosphate
CAPS	Ca^{2+} dependent activator protein for secretion
CO_2	Carbon dioxide
CNiFERs	Cell-based neurotransmitter fluorescent engineered reporters
CPLX	Complexin
DA	Dopamine
DART	Dopamine recognition tool
DAT	Dopamine transporter
DIV	Days in vitro
DKO	Double knock-out
DMEM	Dulbecco's modified eagle medium
DMSO	Dimethyl sulfoxide
DNA	Deoxyribonucleic acid
DNTP	Deoxynucleoside triphosphate
DPBS	Dulbecco's phosphate-buffered saline
DTT	Dithiothreitol
E. g.	Exempli gratia
E12.5	Embryonic day 12.5
E18	Embryonic day 18
EC_{50}	Half maximal effective concentration
ECL	Enhanced chemiluminescence
ECS	Extracellular space
EDTA	Ethylendiaminetetraacetic acid
EGFP	Enhanced green fluorescent protein
ELKS	High content in the amino acids E, L, K, and S
En passant	in passing
EYFP	Enhanced yellow fluorescent protein
F	Fluorescence
FACS	Fluorescence-activated cell sorting
FELASA	Federation of European Laboratory Animal Science Associations
FBS	Fetal bovine serum
FFNs	False fluorescence neurotransmitters
FIJI	Fiji Is Just ImageJ
FRET	Fluorescence resonance energy transfer
FSCV	Fast scan cyclic voltammetry

FUDR	5-Fluorodeoxyuridine + uridine
GABA	γ-aminobutyric acid
GDNF	Human glial-derived neurotrophic factor
GPCR	G-protein coupled receptor
GRABDA	GPCR-activation-based dopamine sensor
GT	Guanine (G) and thymine (T)
GA	Guanine (G) and Adenine (A)
HBSS	Hanks' balanced salt solution
HCl	Hydrogen chloride
HEK	Human embryonic kidney cells
HEPES	4-(2-hydroxyethyl)-1-piperazineethanesulfonic acid
HRP	Horseradish peroxidase
Hz	Hertz
ICC	Immunocytochemistry
KCl	Potassium chloride
Kd	Equilibrium dissociation constant
kDa	Kilodalton
KI	Knock-in
KO	Knock-out
L-DOPA	L-3,4-dihydroxyphenylalanine
LGC-53	Ligand-gated channel 53
LOD	Limit of detection
MAP2	Microtubule-associated protein 2
MICA	Transparent mineral silicates
MgCl2	Magnesium chloride
MOPS	3-Morpholinopropane-1-sulfonic acid
MTS	3-(4,5-dimethylthiazol-2-yl)-5-(3-carboxymethoxyphenyl)-2-(4-sulfophenyl)-2H-tetrazolium
Munc13	Mammalian uncoordinated-13 protein
NaCl	Sodium chloride
NAN	Not a number
NaOH	Sodium hydroxide
NBA	Neurobasal A
NBQX	2,3-dihydroxy-6-nitro-7-sulfamoyl-benzo(f)quinoxaline
NIR	Near-infrared
NMRI	Naval Medical Research Institute
NS	Not significant
NSF	N -ethyl maleimide-sensitive factor
O/N	Overnight
O_2	Dioxide
P0	Postnatal day 0
PBS	Phosphate-buffered saline
PC12	pheochromocytoma of rat adrenal medulla
PCR	Polymerase chain reaction
PDL	Poly-D-lysine
PFA	Paraformaldehyde
PH	Potential of hydrogen
PLL	Poly-L-lysine
PLO	Poly-L-ornithine
PMSF	Phenyl methyl sulphonyl fluoride

PMT	Photo multiplier tubes
PNG	Portable network graphics
PSD	Post synaptic density
RIM	Rab3-interacting molecule
ROI	Region of interest
Rpm	Rounds per minute
RRP	Readily-releasable pool
RT	Room temperature
SDS-PAGE	Sodium dodecyl sulphate polyacrylamide gel electrophoresis
SEM	Standard error of the mean
SNAPs	NSF-adaptor proteins
SNAP-25	Synaptosomal associated protein of 25 kDa
SNAREs	N-ethylmaleimide-factor attachment protein receptors
SNc	Substantia nigra pars compacta
SsDNA	Single-stranded deoxyribonucleic acid
STX	STX1
SV	Synaptic vesicle
SWCNT	Single-walled Carbon Nanotube
SYB	Synaptobrevin
SYP	Synapsin
SYT	Synaptotagmin
TH	Tyrosine hydroxylase
TIFF	Tag image file format
TTX	Tetrodotoxin
UV	Ultraviolet
VGLUT	Vesicular glutamate transporter
VM	Ventral midbrain
VMAT2	Vesicular monoamine transporter 2
VTA	Ventral tegmental area
W	Watt
WB	Western blot
WT	Wild-type

1 Introduction

The brain consists of billions of interconnected neurons that communicate with each other through the release of chemical messengers, the neurotransmitters, at highly specialized structures called synapses. This intercellular communication is required for all brain functions, from motor control to perception and cognition. A typical chemical synapse consists of a pre-synaptic terminal, that contains neurotransmitter filled synaptic vesicles (SVs), and a postsynaptic structure located immediately opposite the presynaptic terminal, which contains concentrated receptors that are activated by the neurotransmitter. These structures are separated by a narrow gap called the synaptic cleft. Together, the pre- and postsynaptic structure form the synapse, the basic unit that organizes information transfer in the brain. Molecular biology techniques have allowed the thorough dissection of the composition of the “typical synapse” over the last three decades, paving the way for a deep understanding of how synaptic transmission is regulated on a molecular level and the creation of a detailed model of the underlying molecular machinery. However, most of these efforts have focused on synapses that operate on a sub-millisecond timescale with high fidelity and precision through ionotropic receptors. Within the context of synapses of the brain, typical model synapses use the neurotransmitters glutamate or, to a lesser extent, γ-aminobutyric acid (GABA). Other neurotransmitters, including dopamine (DA), have been investigated mainly with respect to their function, such as in behavior, or their involvement in disease, but the molecular regulation of these synapses has been far less studied.

Intercellular signal transmission via DA, referred to as DAergic neurotransmission, differs fundamentally from neurotransmission at fast synapses in important ways. Many DAergic presynaptic boutons, called varicosities, lack a postsynaptic element, sometimes referred to as non-synaptic varicosities (Descarries et al., 1996). Receptors for DA are also located outside of synaptic clefts (Pickel et al., 1996; Sesack et al., 1994), meaning that when DA is released either from a non-synaptic varicosity or a varicosity that forms a synapse, DA must diffuse through the extracellular space (ECS) to act on receptors on the target cell. DA receptors are also metabotropic, which function much more slowly than the ionotropic receptors that mediate glutamatergic and GABAergic transmission. DAergic varicosities are structurally and functionally diverse (Daniel et al., 2009; Descarries et al., 1996; Liu et al., 2018), which is presumably underpinned by molecular differences between varicosities. Studying functional differences between varicosities, and their molecular bases, requires examining DA secretion at discrete

varicosities. Such an examination has been hindered by methodological limitations in DA detection. Recent advances in optical methods allowed a first insight into the regulation of DA release on a subcellular level, but many aspects of DAergic transmission, such as functional and structural heterogeneity of individual release sites remain poorly understood. My doctoral work therefore focuses on the employment of a newly developed class of optical DA sensors, that is based on fluorescent nanomaterials rather than classical fluorophores, for the detection of single DA secretion events from primary neuronal cultures. These materials, single-walled carbon nanotubes (SWCNTs), have unique properties and represent promising candidates for overcoming the long-standing methodological challenges that have prevented a detailed examination of the DA release machinery in the past.

1.1 DA in brain function and disease

DA was the first neurotransmitter to be discovered in the central nervous system (Carlsson, 1959). While there are DAergic neurons located in peripheral tissues, such as the gut, I will focus on DAergic neurons in the brain. DA is synthesized in neurons via a well-characterized pathway in which tyrosine is converted to L-3,4-dihydroxy-phenylalanine (L-DOPA) by tyrosine hydroxylase (TH), which is the rate-limiting step in DA synthesis. L-DOPA is then converted to DA by aromatic L-amino acid decarboxylase.

Most of the neurons that synthesize and release DA have their somata located in the ventral tegmental area (VTA) and the substantia nigra pars compacta (SNc) of the ventral midbrain (VM). This VM neuronal population is small, comprising only ~10.000 - ~20.000 neurons in rodents, and ~450.000 neurons in humans (German et al., 1983; Oorschot, 1996). These neurons form extensive and dense innervation throughout the brain. A single neuronal axon from the VM can reach up to half a meter in length and form as many as 300,000 presynaptic boutons (Matsuda et al., 2009). In a simplified view, VM DAergic neurons form three major DAergic pathways (Björklund 2007). The nigrostriatal pathway consists of DAergic projections from the SNc to the dorsal striatum (caudate putamen), which primarily regulates motor function. The mesolimbic pathway consists of projections from the VTA to the ventral striatum (nucleus accumbens) and is critical for motivation to work for rewards (Mohebi et al., 2019). The mesocortical pathway consists of projections from the VTA to the prefrontal cortex and supports cognitive functions like reinforcement learning (Berke, 2018; Gershman and Uchida, 2019).

There are five types of DA receptors (D1-D5), all of which are G-protein coupled metabotropic receptors that act through modulation of adenylate cyclase activity. Activation of DA receptors on target cells has various effects, depending in part on the receptor types expressed, with activation of D2-type (D2, D3 and D4) receptors generally leading to inhibition, and activation of D1-type (D1, D5) receptors to activation of the target cells, respectively (Beaulieu et al., 2015; Gonon, 1997; Missale et al., 1998). DA receptor activation can result in effects in the target cell such as the regulation of neurotransmitter release, cell membrane excitability, and receptor trafficking (Madadi Asl et al., 2019; Tritsch and Sabatini, 2012). DA can also act on D2 receptors expressed by DAergic neurons, inhibiting DAergic neuronal excitability and DA secretion through cyclic adenosine monophosphate (cAMP)-dependent mechanisms (Ford, 2014).

The importance of DAergic neurons of the VM in the is further highlighted by their role in pathophysiology, such as in Parkinson's disease and schizophrenia. With ~1% prevalence in humans above the age of 60, Parkinson's disease is the second most common neurodegenerative disorder (Tysnes and Storstein, 2017) and is characterized by clinical motor symptoms such as resting tremor and muscle rigidity. These symptoms are attributed to the progressive loss of DAergic neurons in the SNc, specifically, resulting in a loss of DA secretion in the dorsal striatum. Parkinson's disease can be partially treated, but not cured, by oral administration of the DA precursor L-DOPA (Cools, 2006; Mosharov et al., 2015). In addition, approximately ~0.3% of the worldwide population develop schizophrenia in early adulthood (Charlson et al., 2018). While the etiology of this complex disease remains somewhat mysterious, the symptoms of schizophrenia are linked to elevated DA levels in the striatum and prefrontal cortex (Grace, 2016; Kesby et al., 2018; Klein et al., 2019; Lyon et al., 2011). Classic antipsychotic drugs used in the treatment of schizophrenia, such as phenothiazine-based antipsychotic drugs, are potent DA D2 receptor antagonists. Consistent with the involvement of DA in psychosis, the massive DA release evoked in the striatum by the abuse of amphetamine-type stimulants or cocaine can induce psychosis (Hsieh et al., 2014). The pharmacological effects of these highly addictive drugs, which are consumed by ~0.3-1.3% of the world's population, are directly attributed to aberrant DA homeostasis (Carboni et al., 1989; Sulzer, 2011; Sulzer et al., 2005). DA is therefore implicated in neurological disorders arising in the modern, aging society more than any other neurotransmitter, and understanding its molecular regulation is of crucial importance for the effective prevention and treatment of these neurological and neuropsychiatric disorders.

1.2 The molecular machinery of neurotransmitter release

For the most part, the molecular machinery of neurotransmitter release has been described in glutamatergic systems such as hippocampal pyramidal neurons. Fast synapses perform synaptic transmission that allows intercellular signal propagation on a millisecond timescale. At rest, the electrical potential across the neuronal plasma membrane is maintained in the negative range (~-70 mV) by electrochemical gradients. An electrical signal (action potential) is initiated by sufficient local depolarization of the membrane at the axon hillock (~+55 mV) through the opening of ion channels, and from there it propagates along the axon away from the soma. When the action potential reaches a presynaptic bouton, the highly specialized molecular machinery present at the release site facilitates the coupling of neurotransmitter secretion to the incoming action potential with high precision and fidelity. The bouton depolarizes, triggering neurotransmitter release through a complex cascade of molecular events.

This machinery facilitating neurotransmitter secretion involves scaffold proteins, priming proteins, Ca^{2+} sensors and Ca^{2+} channels, among others, which are spatially arranged in a highly structured manner in a region called the active zone (Figure 1a) (Südhof, 2012). Proteins such as bassoon, Rab3-interacting molecule (RIM), ELKS and piccolo organize the active zone by providing a presynaptic molecular scaffold and are commonly used as molecular markers for active zones. Neurotransmitter-filled SV are arranged along the active zone and can fuse with the plasma membrane on a sub-millisecond timescale in response to arriving stimuli, resulting in the exocytic release of the neurotransmitter content of the SVs (Wojcik and Brose, 2007). The fundamental molecular machines required for the fusion of SVs with the plasma membranes are N-ethylmaleimide-factor attachment protein receptors (SNAREs), which consist of proteins present in the plasma membrane (syntaxin1 [STX1] and synaptosomal associated protein of 25 kDa [SNAP25]) and the SV membrane (synaptobrevin2 [SYB2]). The assembly of these proteins into a helical SNARE complex tethers the SV to the plasma membrane and provides the force for membrane fusion (Figure 1b) (Südhof, 2013).

Before a SV can fuse, it must undergo a maturation process (“priming”), which in morphological terms describes their direct contact, or “docking”, with the active zone. In functional terms, priming renders a SV capable of undergoing fusion with the plasma membrane, either spontaneously or due to an action potential (Imig et al., 2014). Primed SVs constitute a subpopulation of the total SVs in a presynaptic bouton, and are referred to as the readily-releasable pool (RRP). The priming process involves sequential steps

of assembly and activation of the SNARE complex and is strictly dependent on the assistance of priming proteins such as mammalian uncoordinated proteins 13 and 18 (Munc13 and Munc18) and complexin (CPLX). Munc13 and Munc18, for example, are required to stabilize the open conformation of STX1 and mediate its interaction with the other SNARE proteins (Ma et al., 2011). The importance of the priming process for SV fusion competency is highlighted by the total arrest of synaptic transmission when Munc13 or Munc18 expression are genetically abolished (Augustin et al., 1999b; Varoqueaux et al., 2002; Verhage et al., 2000).

Upon the arrival of an action potential, voltage-gated Ca^{2+} channels in the active zone open, allowing the influx of Ca^{2+} into the synaptic terminal. The Ca^{2+} sensor protein, synaptotagmin1 (SYT1), which is anchored in the membrane of the primed SV, binds to the SNARE complex with assistance of CPLX when Ca^{2+} levels are elevated, triggering SV fusion. The neurotransmitter content of the SV is then secreted into the synaptic cleft, which is ~30 nm wide (Imig et al., 2014; Zuber et al., 2005), through a fusion pore that forms between the SV and plasma membrane (Südhof, 2013). After fusion, the SNARE complex is disassembled by conserved specialized ATPases, the N-ethyl maleimide-sensitive factors (NSF), and their adaptors (SNAPs) (Söllner et al., 1993). Importantly, the arrival of an action potential does not always result in the fusion of a SV. There is only a probability that SV fusion will occur with each action potential. This probability varies between different types of presynaptic boutons, and even between terminals formed by a single neuron (Murthy et al., 1997). The probability of SV exocytosis in glutamatergic hippocampal terminals, for example, is between ~0.1 and ~0.2, meaning that each action potential has a 10% - 20% chance of triggering exocytosis. The probability of SV exocytosis can be modulated, which is a phenomenon known as presynaptic plasticity.

The fusion of a SV results in the collapse the SV into the plasma membrane. Therefore, SVs have to be regenerated, occurring through a process called synaptic vesicle endocytosis. There are multiple ways SVs can be recycled by SV endocytosis, which are controlled by distinct molecular machineries. SV endocytosis compensates for the loss of SVs through SV fusion and ensures that SVs remain available for further neurotransmitter release, maintaining the fidelity of neurotransmission (Chanaday et al., 2019; Sudhof, 2004).

Once secreted, neurotransmitters diffuse across the narrow synaptic cleft and activate postsynaptic receptors on the target cell, which can lead, for example, to the

depolarization of the target cell membrane in the case of ionotropic glutamate receptors. In fast synapses, the abundance of the neurotransmitter, e.g. glutamate, is spatially limited by the architecture of the synaptic cleft and temporally controlled by glutamate uptake of surrounding glia, which limit glutamate diffusion from the synapse (Zoli et al., 1998). The half-life of glutamate in the synaptic cleft has been estimated to be 0.8 ms (Clements et al., 1992). Through the precise, rapidly acting presynaptic machinery, rapid action of ionotropic receptors and limited diffusion of neurotransmitter, glutamate and GABA act with a high degree of temporal and spatial precision.

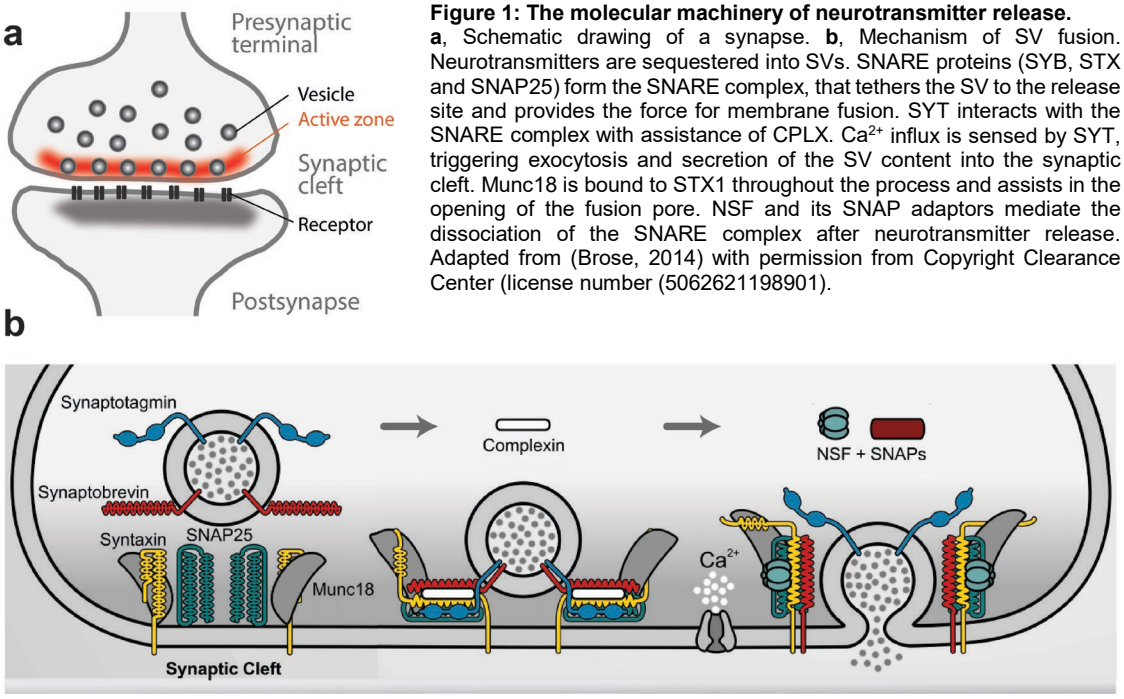

Figure 1: The molecular machinery of neurotransmitter release. **a**, Schematic drawing of a synapse. **b**, Mechanism of SV fusion. Neurotransmitters are sequestered into SVs. SNARE proteins (SYB, STX and SNAP25) form the SNARE complex, that tethers the SV to the release site and provides the force for membrane fusion. SYT interacts with the SNARE complex with assistance of CPLX. Ca^{2+} influx is sensed by SYT, triggering exocytosis and secretion of the SV content into the synaptic cleft. Munc18 is bound to STX1 throughout the process and assists in the opening of the fusion pore. NSF and its SNAP adaptors mediate the dissociation of the SNARE complex after neurotransmitter release. Adapted from (Brose, 2014) with permission from Copyright Clearance Center (license number (5062621198901).

1.3 DAergic neurotransmission

1.3.1 Volume transmission

Contrasting with the fast, spatially precise mode of transmission mediated by GABA and glutamate, DAergic transmission functions on a much slower time scale and with less spatial precision.

For the purpose of DA secretion, DA is synthesized in the cytosol and sequestered in SVs by the vesicular monoamine transporter 2 (VMAT2). SVs are concentrated in local swellings along the axon (varicosities) from which DA can then be released (Figure 2a). DA secretion sites are often not aligned with corresponding postsynaptic structures (non-synaptic varicosities), and DA receptors are mainly located extra-synaptically (Descarries et al., 1996; Nirenberg et al., 1996a; Pickel et al., 1996; Sesack et al., 1994). As a consequence, DA has to diffuse from its site of release to reach its target receptors, a mechanism that is common to all catecholamines called “volume transmission” (Figure 2b) (Cragg et al., 2001; Taber and Hurley, 2014). The effective range of released DA is thought to be controlled by the balance of DA release and DA clearance from the ECS through uptake activity of the DA transporter (DAT) (Cragg and Rice, 2004; Sulzer et al., 2016). DA volume transmission is also influenced by the geometry of the surrounding tissue in the brain (Cragg et al., 2001). DAT is exclusively expressed by DAergic neurons and located mainly on the axonal plasma membrane (Nirenberg et al., 1996b) (Figure 2a). It was estimated, that DA diffuses up to 7 µm from its release site and has a half-life of 30 ms (Sulzer et al., 2016), thus affecting large areas of the target region, which is in strong contrast to the brief half-life and the small effective range of secreted glutamate.

The relatively slow speed of DAergic transmission is also a result of mammalian DA receptors being exclusively metabotropic, thus signaling is more than two orders of magnitude slower than ionotropic signaling (Missale et al., 1998). Overall, DAergic transmission occurs over a greater area and slower time scale than fast neurotransmission.

1.3.2 Electrical activity of DAergic neurons

There are two defined modes of DAergic neuronal activity, based on their pattern of action potential firing: tonic and burst firing (Floresco et al., 2003; Hyland et al., 2002). Tonic, or spontaneous pacemaker firing, is characterized by neuronal firing regularly at 2 – 5 Hz, which maintains a homogenously distributed extracellular DA concentration in

the range of 10 – 30 nM in the striatum (Grace and Bunney, 1984a; Venton et al., 2003). Burst, or phasic firing, in contrast, describes brief bursts of 2 – 6 action potentials at 15 – 30 Hz frequency and leads to increased DA release (Grace and Bunney, 1984b). As a consequence, DA is secreted faster than it is taken up by DAT activity during burst firing and accumulates locally, resulting in a transient, steep rise in the extracellular DA concentration. In awake animals, these steep DA transients encode reward prediction errors and occur when the received reward is better than expected (Schultz, 2019). Accordingly, activity of midbrain DAergic neurons is briefly decreased when the received reward is lower than expected. In this fashion, patterns of tonic and phasic firing regulate reinforcement learning behaviors.

1.3.3 Heterogeneity of DAergic secretion sites

While DA transients are essential for brain function, it is not known how DA release patterns are regulated across populations of individual DAergic varicosities. In glutamatergic neurons, even the individual presynaptic boutons formed by a single neuron exhibit a large degree of functional diversity (Murthy et al., 1997). Studies in DAergic neurons also point towards a high level of heterogeneity between individual DA secretion sites (illustrated in Figure 2). Early electron microscopy studies of the striatum found that DAergic boutons are morphologically diverse and differ from fast-acting release sites (Descarries et al., 1996). Fast-acting synapses almost exclusively consist of a terminal presynaptic bouton with an active zone, which is tightly associated with a postsynapse. The majority (~65%) of DAergic varicosities, in contrast, occur *en passant* (meaning that the presynaptic bouton is formed not at a terminal, but along the axon) and without a post-synaptic structure (non-synaptic). Only ~35% of DAergic boutons formed synapses with dendritic structures or cell bodies (synaptic) (Descarries et al. 1996). Similar proportions of synaptic and non-synaptic varicosities were observed later using fluorescence microscopy in neuronal cultures (Daniel et al., 2009). This observation also demonstrates a surprising similarity of varicosities in culture and in the adult brain, indicating that the formation of synaptic and non-synaptic varicosities is an intrinsic property of DAergic neurons.

In addition to this structural heterogeneity, DAergic varicosities exhibit considerable functional heterogeneity. When exocytosis was monitored in synaptic and non-synaptic varicosities separately in neuronal culture, it was found that only ~64% of synaptic varicosities underwent SV recycling upon stimulation (Daniel et al., 2009). A subsequent study using striatal slices found that only ~17% of all DAergic varicosities exhibited exocytosis upon neuronal stimulation (Pereira et al., 2016). A large proportion of DAergic

varicosities therefore does not exhibit DA release, despite containing SV clusters and exhibiting Ca^{2+} influx (Pereira et al. 2016). While the function of non-releasing, or “silent” varicosities is not clear, it is speculated that they could be involved in the spatial modulation of DA release, represent immature release sites, or serve as DA storage sites, sequestering DA from the cytosol to prevent DA-induced cytotoxicity (Jiang et al., 2008; Pereira et al., 2016). The DAergic varicosities that do exhibit exocytosis, on the other hand, show high functional variation with respect to the number of SVs that undergo exocytosis upon action potential firing, and the likelihood that an action potential will trigger SV fusion (Daniel et al., 2009; Gubernator et al., 2009; Pan and Ryan, 2012).

Another aspect of the functional heterogeneity of varicosities formed by DAergic neurons lies in the capacity of some neurons to release either glutamate or GABA in addition to DA. While it is now well recognized that DAergic neurons can synthesize and package glutamate into SVs by expressing the vesicular glutamate transporter (VGLUT2) (Dal Bo et al., 2004), it is still unclear whether glutamate and DA are secreted from the same SVs, distinct SVs within the same varicosity, or whether these two neurotransmitters are segregated completely into distinct varicosities. It is possible, for example, that glutamate is released from DAergic neurons at synaptic varicosities forming true synapses in apposition to postsynaptic densities, while DA is released from non-synaptic varicosities and signals via volume transmission (Descarries et al., 2008; Fortin et al., 2019; Sulzer and Rayport, 2000; Trudeau et al., 2014; Zhang et al., 2015). The mechanisms underlying the capacity of some neurons to release GABA in addition to DA are much less clear, since the proteins required for GABA synthesis and SV packaging are absent from DAergic neurons (Tritsch et al., 2016, 2012).

Finally, contributing to DA release heterogeneity, in addition to DA release from SVs clustered at axonal varicosities, DA secretion has also been observed from somatodendritic regions of neurons. This mode of DA release likely uses distinct mechanisms for secretion than those operating in axonal release, as SV clusters are absent in the dendrites and soma of DAergic neurons (Nirenberg et al., 1996a). However, VMAT2 is localized to other organelles aside from SVs, such as the Golgi apparatus in the soma, and tubulovesicular membrane structures in soma and dendrites that could be involved in somatodendritic DA storage and secretion (Figure 2a) (Bergquist and Ludwig, 2008; Bergquist et al., 2002; Nirenberg et al., 1996a; Witkovsky et al., 2009). Functionally, dendritically released DA contributes to the regulation of motor control by stimulating GABAergic transmission in the VM through D1-type DA receptors. In addition,

dendritically released DA regulates the activity of DAergic neurons through D2 DA receptor mediated auto-inhibition (Ford, 2014; Ludwig et al., 2016).

In summary, these studies demonstrate that DA acts through several distinct modes of transmission, differing from the classical model of fast neurotransmission. Individual DAergic release sites are highly heterogenous with respect to their structure and function, and need to be investigated individually in order to fully understand how DA release is regulated on a cellular and molecular level. In the scope of this work, I focused solely on axonal DA release, although somatodendritic release could also be investigated with the methodology established in this study.

1.3.4 Molecular regulation of axonal DA release

While the molecular SV fusion machinery that governs the release of fast neurotransmitters is well characterized (Figure 1) the molecular regulation of DA release and especially with respect to the differences across varicosity populations, is poorly understood. That axonal DA release is vesicular was confirmed by the observation of quantal DA release events and the dependence of DA release on VMAT2 activity (Fon et al., 1997; Pothos et al., 1998). Functional differences between individual varicosities, such as their probability of DA exocytosis upon the arrival of an action potential, are presumably determined by the protein machinery present at each varicosity. Only about ~30% of VMAT2-positive SV clusters contain the active zone scaffolds bassoon, RIM and ELKS (Daniel et al., 2009; Liu et al., 2018). In neuronal cultures, stimulus-evoked exocytosis was observed only in varicosities that co-labeled for bassoon (Daniel et al., 2009). Deletion of RIM, but not ELKs, abolished DA release in striatal slices as measured by amperometry (Liu et al., 2018). It is therefore believed that DA release sites are sparse and require active zones that are somewhat differently organized than in fast synapses (Figure 2b), which require both RIM and ELKs to function (Held et al., 2016).

At synapses utilizing fast-acting neurotransmitters, the tight association of primed SVs to Ca^{2+} channels facilitates the rapid, synchronous coupling of action potentials to SV fusion though Ca^{2+} sensors on the SV membrane. Like fast synapses, DAergic varicosities utilize Ca^{2+} as secretory trigger. Axonal DA release is effectively abolished with extracellular Ca^{2+} concentration below 0.5 mM (Fortin et al., 2006) and depends on Ca^{2+} channels (Brimblecombe et al., 2015). In addition, several studies have confirmed that the vesicular Ca^{2+} sensor SYT1 is expressed in DAergic neurons, is present at DAergic varicosities and synaptosomes, and is required for axonal DA release (Banerjee et al., 2020b; Liu et al., 2018; Mendez et al., 2011; Thuret et al., 2004). Interestingly,

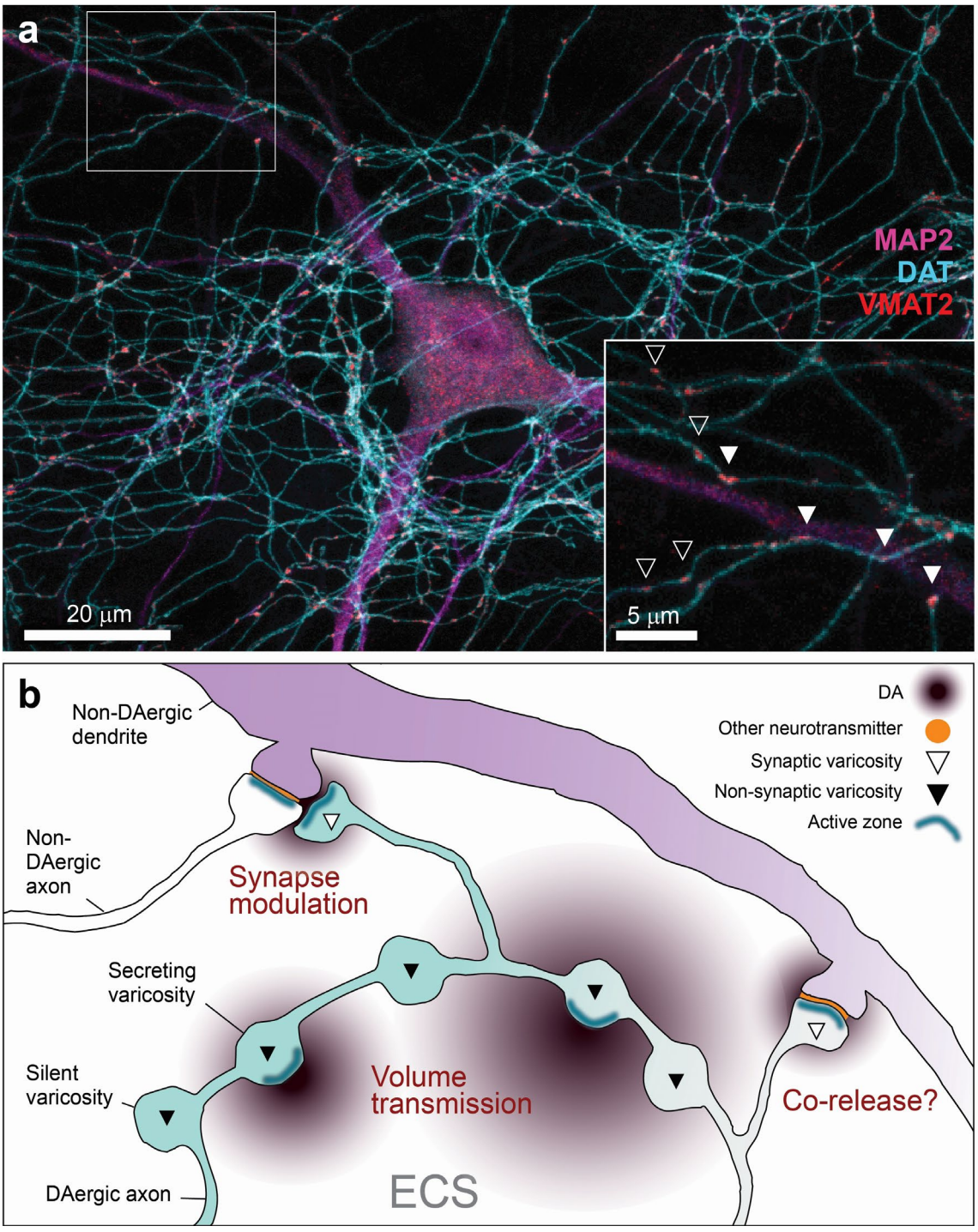

Figure 2: DAergic neurons form structurally and functionally distinct varicosities.
a, Confocal image of a dissociated DAergic neuron in culture at DIV14, demonstrating synaptic (white arrows) and non-synaptic (black arrows) varicosities formed along the axon. Somata and dendrites were immunolabeled with microtubule-associated protein 2 (MAP2, magenta), DAergic axons with DAT (cyan) and DAergic SVs with VMAT2 (red). The white box is shown as magnified inset. Scale bar for left image = 20 µm, scale bar for inset = 5 µm. **b**, DA is released from varicosities into the ECS by volume transmission. A DAergic axon (cyan) can form distinct release sites, including synaptic and non-synaptic varicosities. Some varicosities do not secrete DA, presumably due to the lack of active zones (silent varicosities). Synaptic varicosities might serve the release of other neurotransmitters (co-release).

silent DAergic varicosities exhibit stimulus-dependent Ca^{2+} influx, indistinguishable from varicosities that exhibit exocytosis (Pereira et al., 2016). Exocytosis in DAergic neurons is also controlled by the presence of calbindin, which is a fast, Ca^{2+} buffering protein expressed at high concentrations in VTA DAergic neurons, but not SNc DAergic neurons (Pan and Ryan, 2012). Therefore, the control of SV fusion by Ca^{2+} in DAergic varicosities likely involves other mechanisms, such as local Ca^{2+} buffering.

In terms of other synaptic proteins involved in neurotransmitter release, VM neurons have been shown to express CPLX1 (Thuret et al., 2004), and DAergic varicosities mostly exhibit immunolabeling for the SV membrane proteins synaptophysin (an abundant protein in the SV membrane) and SYB2 (Bergquist et al., 2002; Daniel et al., 2009; Pereira et al., 2016). In addition, axonal DA release is, at least partially, dependent on SNAP25 and SYB2 function (Bergquist et al., 2002). Therefore, it is likely that some molecular components are common to both DAergic release and the release of fast neurotransmitters. How these molecules function in DAergic neurons and how they contribute to the functional heterogeneity of DAergic release sites, however, can only be fully understood by dissecting DA release of individual varicosities, rather than studying patterns of DA bulk release from large neuronal populations.

1.4 Methods for studying DA secretion

Unlike fast-acting neurotransmitters, the secretion of which can be indirectly detected by measuring changes in the membrane potential of the postsynapse with electrophysiological techniques, most DA transmission does not mediate a postsynaptic change in membrane potential that can be detected with electrophysiology. Therefore, DA secretion has to be studied with alternative methods. In the following section, I will briefly review methods that are used to investigate DA release.

1.4.1 Classical methods

DA is a highly oxidizable neurotransmitter. If not stabilized, for example by the low pH of the SV lumen, DA rapidly oxidizes to *ortho*-quinone products (Guillot and Miller 2009). Almost 50 years ago, it was discovered that this property can be exploited to detect DA through oxidation or reduction at a solid electrode, yielding extremely sensitive measurements of DA release through faradaic currents (Gonon et al., 1978; Kissinger et al., 1973) – the basic principle of today's electrochemical techniques, such as fast scan

cyclic voltammetry (FSCV) and amperometry (Figure 3a). To date, these two methods have been the gold standard for investigating DA secretion.

A key drawback of these electrochemical techniques is poor specificity for DA versus other catecholamines. While amperometry provides the best method for DA detection in terms of temporal resolution, with DA transients on a sub-millisecond time scale (Bucher and Wightman, 2015), the electrode is unable to discriminate between DA, epinephrine, norepinephrine, and their metabolites due to their similar redox potential. FSCV provides improved chemical selectivity by cycling the potential of the electrode between a positive and negative voltage, resulting in cyclic voltammograms with characteristic shapes for individual compounds (Kile et al., 2012). However, the improved chemical selectivity comes at the cost of temporal resolution, since these voltammograms typically require 100 ms to complete the cycle between measurements.

Another common technique to measure DA in the brain is microdialysis. To do this, extracellular fluid is sampled through a semi-permeable membrane (Figure 3b), which is then subjected to quantitative chemical analysis. The chemical composition of the sampled fluid can be quantified by liquid chromatography or mass spectrometry with high specificity and sensitivity. However, the duration of the sampling procedure (in the order of minutes) and the large size of the probe (in the order of micrometers) result in a low spatial and temporal resolution of the DA abundance. In addition, tissue damage caused by the probe can interfere with normal cell function (Borland et al., 2005).

1.4.2 Genetically expressed DA sensors

In recent years, several DA sensing strategies have been developed as alternative DA detection methods to electrochemistry. Several approaches utilize the genetic expression of protein-based DA sensors. These sensors typically consist of a DA receptor that has been altered to provide a measurable readout upon DA binding. Examples for such DA sensors are the ligand gated channel 53 (LGC-53) (Figure 3c), cell-based neurotransmitter fluorescent engineered reporters (CNiFERs), dLight and G-protein coupled receptor-activation-based DA sensors ($GRAB_{DA}$) (Figure 3d).

LGC-53 is a chloride channel discovered in *Caenorhabditis elegans*, and the only known ionotropic DA receptor. Transfection of this channel into cultured neurons and striatal brain slices allowed the detection of phasic DA release though measurements of the DA-mediated Cl^- current by whole-cell electrophysiology (Kress et al. 2014, Ringstad et al. 2009). CNiFERs consist of genetically altered human embryonic kidney cells (HEK293)

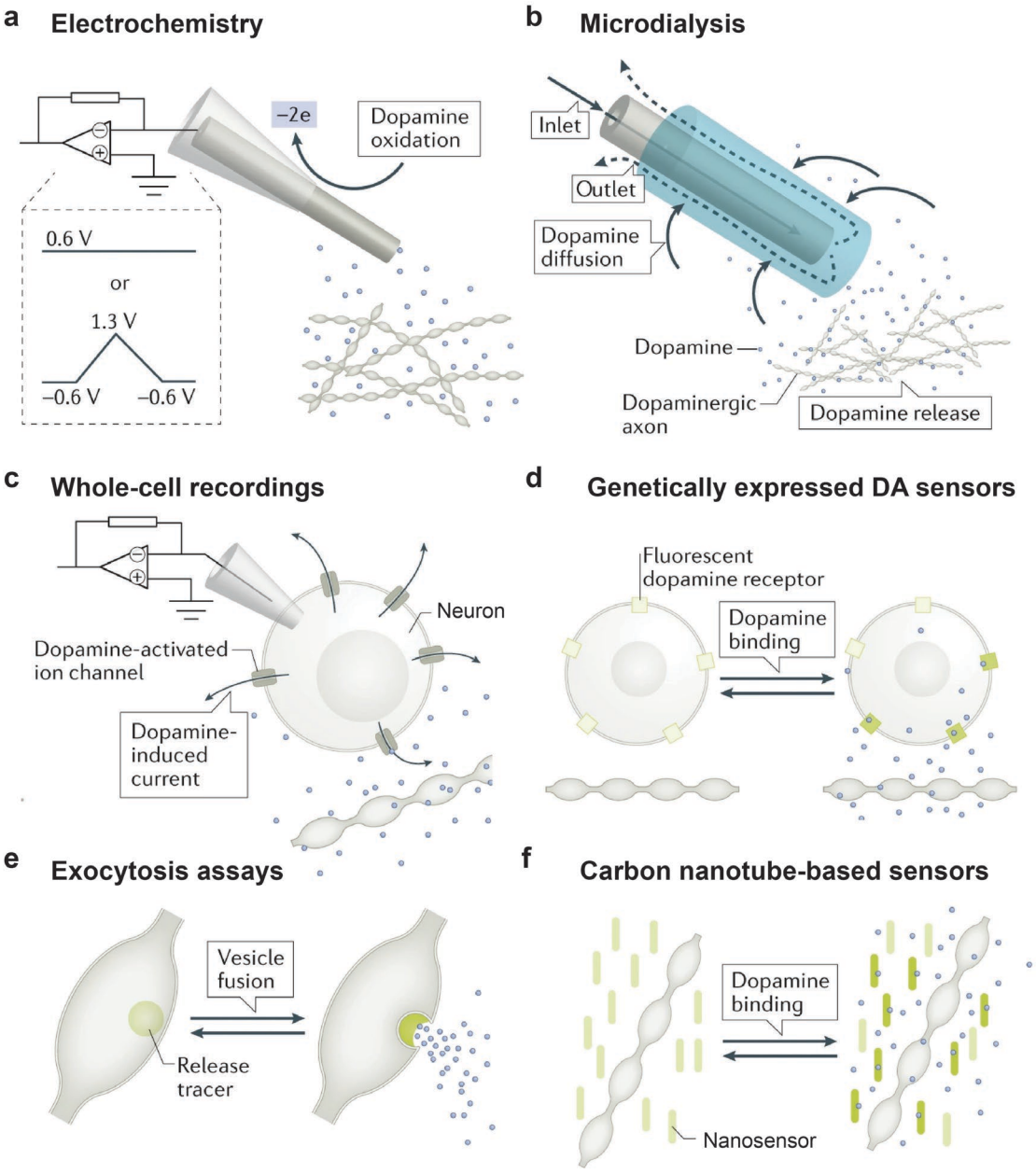

Figure 3: Methods of DA detection.
a, Amperometry provides the best temporal resolution of current techniques (sub-millisecond) but suffers from a low chemical selectivity. FSCV improves the chemical selectivity at the cost of temporal resolution (~100 ms). **b**, Microdialysis enables sampling of the chemical environment in the brain through a semi-permeable membrane, allowing analysis of the fluid with high chemical specificity and sensitivity, but low temporal resolution due to the long sampling procedure (order of minutes). **c**, Whole-cell electrophysiology can be used to measure currents mediated by ion channels that are activated by DA, such as LGC-53 from *C. elegans*. **d**, Genetic fluorescent DA sensors, such as $GRAB_{DA}$, dLight and CNiFERs, are based on cell expression and report DA either through direct activation of a permutated GFP that is conjugated to a DA receptor, or by detection of DA-induced Ca^{2+} influx through FRET and yield a temporal resolution comparable to FSCV. **e**, Fluorescent dyes that allow the monitoring of exocytosis from single release sites include FFNs, styryl dyes (FM) and pH-sensitive fluorophores that are conjugated on the intraluminal side to VMAT2 (VMAT-pHluorin). They are capable of measuring dynamics of neurotransmitter release at single synapses, but do not reflect DA release specifically. **f**, SWCNT-based sensors detect DA though corona phase molecular recognition, and are made by conjugating oligonucleotides to their surface. Their key advantages are the resistance to photobleaching and ability to report DA release with very high spatiotemporal resolution. Adapted from (Liu et al., 2021) with permission from Copyright Clearance Center (license number 5057220997443).

cells that constitutively express a D2 DA receptor that triggers Ca^{2+} influx when activated by DA, combined with a fluorescent Ca^{2+} sensor that reports elevated Ca^{2+} levels by fluorescence resonance energy transfer (FRET) in the cells (Muller et al., 2014). Similar ideas led to the parallel invention of dLight and $GRAB_{DA}$ sensors (Patriarchi et al., 2018; Sun et al., 2018) (Figure 3d). These are genetically modified DA receptors are coupled to circularly permuted green fluorescence protein (GFP). DA binding to these receptors causes a conformational change of the GFP, increasing its fluorescence emission. While CNiFERs are 30x more sensitive for DA than other catecholamines, with a dynamic range of ~1 to ~10 nM, they require monitoring on a timescale of seconds. In addition, their ability to resolve DA diffusion in space is limited by the relatively large size of the cells, which act as sensor. $GRAB_{DA}$ and dLight on the other hand, exhibit an even larger selectivity for DA (up to 70x), and a larger dynamic range (0.1 µM to 10 µM) and can be measured at a speed comparable to FSCV. Therefore, dLight and $GRAB_{DA}$ are currently popular optical DA sensors used to study DA secretion in the brain by fiber photometry (reviewed in Dinarvand et al., 2020).

1.4.3 Exocytosis assays

Methods for detecting and quantifying exocytosis at varicosities have also been used to study neurotransmitter release from DAergic neurons (Figure 3e). Styryl (FM) dyes, for example, fluorescently label the plasma membrane and are internalized at presynaptic structures during stimulus-dependent SV endocytosis. The membranes of these newly formed SVs are fluorescently labeled as a result. Subsequent neuronal stimulation then results in exocytosis, and release of the styryl dye into the ECS, allowing analysis of endo- and exocytosis (Hoopmann et al., 2012). Using FM-143 in neuronal cultures, exocytosis at single varicosities in DAergic neurons was monitored, revealing a striking functional heterogeneity across discrete release sites (Daniel et al., 2009). Similar results were achieved with false fluorescence neurotransmitters (FFNs), which mimic the chemical structure of DA, act as substrates for VMAT2 and DAT, and are thereby loaded into SVs in DAergic varicosities. Thus, FFNs detect exocytosis at varicosities and allowed the fluorescent tracking of DA release in neuron cultures and striatal brain slices (Gubernator et al., 2009; Pereira et al., 2016; Zhang et al., 2009). Another strategy to assess single varicosity release are VMAT2-tagged pHluorins, whose fluorescence is quenched in acidic SVs but is restored when the SV lumen is exposed to the ECS during exocytosis (Pan and Ryan, 2012).

1.4.4 Optical DA sensors based on carbon nanotubes

In recent years, SWCNTs have gained popularity in various biomedical applications due to their unique properties (Figure 3f and Figure 4) (Cha et al., 2013). They are ~0.7 nm in diameter (Iijima and Ichihashi, 1993), several hundred nanometers in length (Figure 4a) and emit fluorescence in the near infrared (NIR) fluorescence spectrum (O'Connell et al., 2002). SWCNTs are nanoscale graphene cylinders, and the exact wavelength of their emission is dependent on the angle at which the graphene sheet is "rolled up", which is described as chirality index (m, n) (Bachilo et al., 2002). The SWCNTs used in this study have a chirality index of (6,5), resulting in an emission peak at 990 nm (Figure 4b). SWCNTs are extremely stable materials that do not bleach or blink, and their emission wavelength lies in the tissue transparency window (Heller et al., 2005). These features allow low autofluorescence and the potential for deep tissue imaging (Welsher et al., 2011) and multiplexing with other fluorophores in the visible fluorescence spectrum, such as GFP. SWCNTs have a large surface area-to-volume ratio, since every carbon atom is a surface atom. Importantly, this surface can be modified by the attachment of biomolecules, such as proteins, nanobodies, and single-stranded deoxyribonucleic acid (ssDNA), introducing new functions to these molecules. By functionalizing SWCNTs with different biomolecules and screening the fluorescence response to different analytes, SWCNTs have been widely used as building blocks for biosensors (Bisker et al., 2016; Giraldo et al., 2019; Harvey et al., 2019; Hendler-Neumark and Bisker, 2019). In this manner, it was discovered that ssDNA-functionalized SWCNTs act as fluorescent DA sensors that increase in NIR fluorescence in a concentration-dependent manner upon reversible DA binding (Figure 4b) (Dinarvand et al., 2020; Kruss et al., 2014; E Polo and Kruss, 2016). The detection of DA by the nanosensor depends on the three-dimensional structure formed by the SWCNT with the ssDNA molecule attached to its surface, a sensing mechanism that was termed corona phase molecular recognition (Zhang et al., 2013). The first SWCNT-based nanosensors used for DA detection in biological systems were used to detect evoked DA release from cultured pheochromocytoma of rat adrenal medulla (PC12) cells (Kruss et al., 2017, 2014) and acute striatal brain slices (Beyene et al., 2019). For PC12 cells, a chirality purified SWCNT-$(GA)_{15}$ nanosensor (functionalized with guanine and adenine nucleotides) was used, while experiments with brain sliced employed a mixture of SWCNT-$(GT)_6$ (nanosensors functionalized with thymine and adenine nucleotides) with different chiralities. However, both nanosensors could not discriminate between DA and other catecholamines. An extremely useful quality of SWCNT-based sensors is the ability to adjust the corona phase recognition to fit the experimental sensing

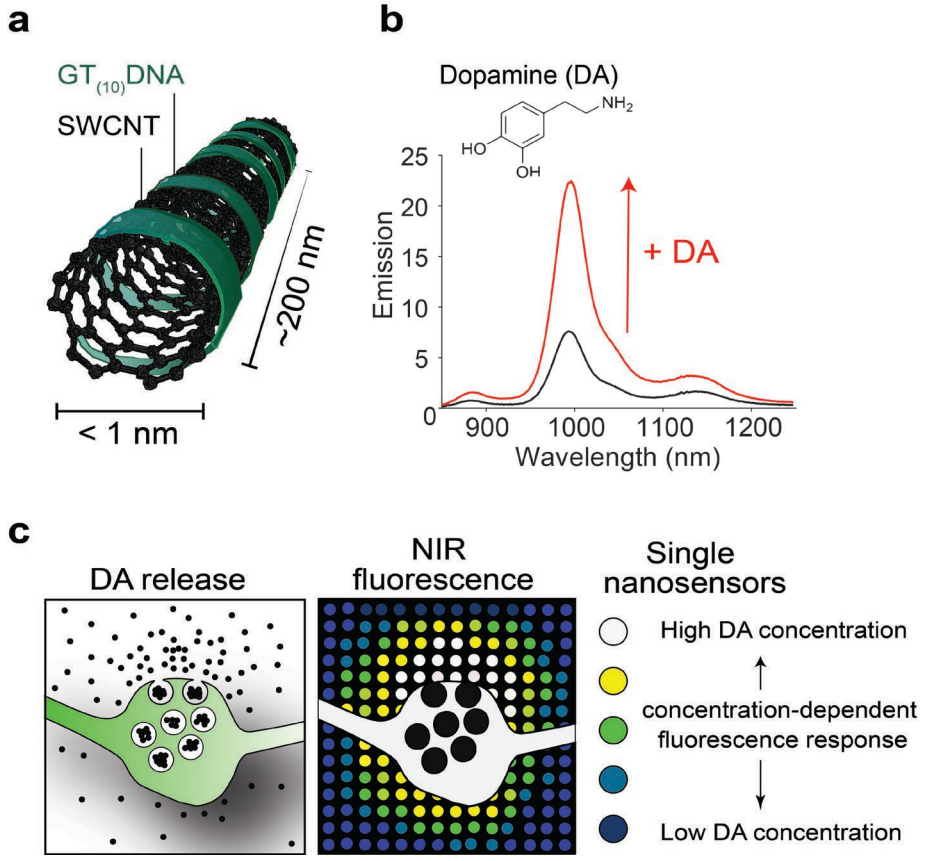

Figure 4: Functionalized SWCNT-$(GT)_{10}$ nanotubes as DA sensors.
a, Schematic of the nanosensors used in this study, each consisting of a (6,5)-SWCNT-$(GT)_{10}$ complex. **b**, Nanosensors report DA through fluorescence increase in the NIR (peak at 990 nm). The emission spectra of nanosensors are shown before (black trace) and after the addition of 100 µM DA (red trace). Spectra were obtained with nanosensors dispersed in phosphate-buffered saline (PBS). **c**, Schematic of a DAergic varicosity (in green) that secretes DA (black dots, left panel) and the underlying surface containing immobilized nanosensors (right panel). Each circle in the right panel represents a single nanosensor that reports the local DA concentration in a dose-dependent manner.

requirements by manipulating the biomolecule on the SWCNT surface (Mann et al., 2017; Meyer et al., 2017). After screening multiple different ssDNA sequences, it was found that using $(GT)_{10}$ ssDNA to functionalize the SWCNTs, a new nanosensor was created that selectively responds to DA over other catecholamines (Mann et al., 2017). A single SWCNT-based sensor, imaged after immobilization on a glass surface, can report DA binding in a concentration-dependent and reversable fashion (Kruss et al., 2014). When many nanosensors are immobilized on a glass coverslip, a single microscopy image can capture thousands of individual sensors, each representing a separate point of measurement in space (Kruss et al., 2017). This experimental approach therefore has the advantage of being able to detect DA with high spatial resolution over time, as demonstrated by the application of SWCNT nanosensors to PC12 cells, where a nanosensor-coated glass surface was used to detect evoked DA release (Kruss et al., 2017). Through this method, it was possible to identify discrete “hotspots” of DA release at the PC12 cell membranes, which represented putative DA release sites. In summary,

SWCNT are versatile tools for analyte detection and present the most promising candidates to approach DA detection on a subcellular level.

1.4.5 Current methodological limitations

In order to understand how discrete varicosities contribute to the generation of DA transients in the brain, and how the functional diversity of these varicosities is regulated on a molecular level, it is essential to monitor DA release events at a level of resolution that allows the correlation of DA release with specific varicosities. This requires both the ability to observe and discriminate single varicosities, as well as discriminate DA release events in time and space. While electrochemical methods were instrumental in understanding the implication of DA for normal brain function, behavior and disease, they generally measure the summed DA secretion from many varicosities in the local area. Amperometric recordings from single varicosities have been reported, however they are extremely challenging to perform and only yield data from a single varicosity at a time (Staal et al., 2007). Moreover, the spatial resolution of electrochemical methods is limited to the number and position of electrodes, hence, these methods are unsuited for the resolution of single DA release events across large varicosity populations.

This limitation regarding spatial resolution can potentially be overcome using new optical methods such as genetically expressed DA sensors. However, despite their improvement in the discrimination of DA from other catecholamines, and the spatial resolution for DA detection compared to electrochemical techniques, they have not been shown to detect DA release events from individual varicosities. In addition, their capability of detecting secreted DA is limited by expression levels of the DA sensor and its localization to cell membranes. Thus, while these sensors are a useful and popular alternative to FSCV, with similar temporal resolution, there is no evidence thus far that they are capable of investigating the release of DA from single varicosities.

Optical exocytosis assays, in contrast, allow monitoring of neurotransmitter secretion from a high number of varicosities in parallel. Applied in DAergic neuron cultures, they provided valuable insights into the release properties of single DAergic varicosities. These assays, however, are difficult to interpret due to the capacity of DAergic neurons to release multiple transmitters. The observation of exocytotic events does not directly reflect the release of DA itself and does not inform us about the dynamics and diffusion of secreted DA.

In summary, classical methods for studying DA signaling cannot resolve DA secretion at the level of large numbers of individual varicosities. Thus, their ability to investigate questions about how synaptic molecules control DA secretion is limited. Most studies that have adopted new optical methods, such as genetically encoded DA sensors, have focused on the detection of bulk DA release and have not attempted to resolve individual DA release events. This also includes SWCNT-based catecholamine nanosensors, which have been applied to striatal brain slices to demonstrate their suitability for imaging DA release and diffusion in biologically relevant systems, but have not correlated the release of DA to subcellular structures or addressed questions related to the molecular regulation of DA secretion (Beyene et al., 2019). As such, there was no clear advance in spatial resolution compared to genetically-encoded DA sensors. The only study to exploit the gain in spatial resolution of optical DA nanosensors and assign DA release to subcellular structures was the study of Kruss and colleagues (2017) in PC12 cell cultures using a SWCNT-$(GA)_{15}$ catecholamine sensor. This study highlights immobilized SWCNT-based sensors deployed in cell culture as an ideal system to optically monitor DA release dynamics from single release sites. SWCNT-based DA sensors can potentially detect discrete DA release events from DAergic subcellular structures (Figure 4c) with a spatial resolution that was not achievable before, but is crucial for the detection of local transient DA secretion events. SWCNT-based DA sensors, however, have not been used previously for this purpose.

1.5 Aims of the study

DAergic neurons are an intriguing neuronal subtype due to their unconventional characteristics such as neurotransmitter co-release, somatodendritic release, and functional as well as structural heterogeneity of axonal varicosities. In addition, DA is vitally important in human behavior and disease. Understanding how DA secretion is regulated on a molecular level is best achieved by resolving DA secretion at single release sites. DAergic neurons form up to hundreds of thousands of varicosities per neuron. To study the function of large, functionally diverse populations of varicosities requires a method capable of examining many varicosities simultaneously. This requirement can be achieved with immobilized SWCNT-based DA sensors deployed in a neuronal culture system. However, to date, such a strategy for using DA nanosensors does not exist.

The aim of my doctoral work is therefore to utilize the improved DA-specific nanosensor, SWCNT-$(GT)_{10}$ (Mann et al., 2017), for the examination of DA secretion, with a focus on individual varicosities. To accomplish this, I will first establish an experimental strategy for the application of SWCNT-based nanosensors to mature primary DAergic cultures, which allow the growth of DAergic axonal presynaptic boutons at a low density, thus facilitating their clear distinction, as opposed to the dense varicosities of striatal slices. Secondly, I will validate this methodological approach in cultured neurons using pharmacological tools. Third, I will use the nanosensors to detect and characterize brief, transient DA secretion events (“hotspots”) from single varicosities across large varicosity populations in neuronal cultures. Finally, I will investigate the role of Munc13 priming proteins, which are an absolute requirement for fast neurotransmission, but are of unknown importance in the regulation of DA secretion. Through these investigations I will gain insight into DA release at a more fundamental level than had previously been achievable.

2 Material and Methods

2.1 Animals

2.1.1 Mouse lines

Wild-type C57BL/6N P0	
Munc13-2-EYFP	(Cooper et al., 2012)
Munc13-3-EGFP	(Cooper et al., 2012)
Munc13-1 KO	(Augustin et al., 1999b)
Munc13-2 KO	(Varoqueaux et al., 2002)
TH-EGFP	(Matsushita et al., 2002; Sawamoto et al., 2001)

All mouse breedings and experiments were performed with the permission of the Niedersächsisches Landesamt für Verbraucherschutz und Lebensmittelsicherheit (LAVES, permit numbers 33.19-42502-04-19/3254, 33.19.42502-04-15/1817 and 33.19-42502-04-18/2756). Animals were kept in groups according to the European Union Directive 63/2010/EU and ETS 123. Mice were housed in cages that were individually ventilated (type II 8 superlong, 435 cm^2 floor area; TECHNIPLAST), at 21 ± 1°C, 55% relative humidity, under a 12 h/12 h light/dark cycle, in specific pathogen-free conditions, with tap water and food *ad libitum*. Cages were changed once a week and provided with nesting material. Animal health was daily inspected by a veterinarian and by animal caretakers. Health monitoring (serological analyses, microbiological, parasitological and pathological examinations) was done quarterly according to the Federation of European Laboratory Animal Science Associations (FELASA) recommendations with either Naval Medical Research Institute (NMRI) sentinel mice or animals from the colony. The mouse colony used for experiments did not show signs of pathogens. The sex of neonatal mice used for generating cultures was not checked.

Munc13-1 knock-out (KO), Munc13-2 KO, Munc13-2 Enhanced yellow fluorescent protein (EYFP) and Munc13-3 enhanced green fluorescent protein (EGFP) mouse lines were originally generated in the host laboratory of Prof. Nils Brose. TH-EGFP mice (B6.B6D2-Tg (TH-EGFP)21-31Koba [RBRC02095]) were kindly provided by the RIKEN BRC through the National Bio-Resource Project of the MEXT/AMED, Japan. To investigate the role of Munc13-1 and -2 in DA secretion, TH-EGFP mice were bred with mice lacking Munc13-1 (Unc13A) and Munc13-2 (Unc13B) genes. For final experiments,

TH-EGFP(+/-) Munc13-1(-/-) Munc13-2(-/-) embryonic mice were generated by breeding the genotypes EGFP(+/-) Munc13-1(+/-) Munc13-2(-/-) with Munc13-1(+/-) Munc13-2(-/-).

2.1.2 Genotyping

Genotyping was performed by the AGCT laboratory[1] with genomic DNA extracted from tail biopsies. Primers for detecting the TH-EGFP transgene were: 5'-TGTGGCTTTCTGAA CTTGACA-3', 5'-ACCAGAGGCATACAGGGACA-3', 5'-CTACACCCTGGTCATCATCCT GC-3', and 5'-TCCAGCTCGACCAGGATG-3'. These primers generate a 119 basepair (bp) product as an internal polymerase chain reaction (PCR) control (beta actin amplification), plus a 268 bp product from mice expressing the THEGFP transgene. Primers for detecting Munc13-1 KO: 5'-CTTACCCA TCTGAGAGCCGGAATTCCA-3', 5'-CTCCGAGGGGAA TGCGCTTCCG TTTCCTG-3', and 5'-GAGCGCGCGCGGCGGAGTTGTTGAC-3'. Presence of the WT Munc13-1 allele resulted in a 250 bp band, while presence of the Munc13-1 KO allele resulted in a 230 bp band. Primers for detecting Munc13-1 KO: 5'-CTCCACTGCCCCCTTTTACTGT-3', 5'-TCAAGGGACTGT TCTAGCAATGTT-3', and 5'-GAGCGCGCGCGGCGGAGTTGTT GAC-3'. Presence of the WT Munc13-2 allele resulted in a 322 bp band, while presence of the Munc13-2 KO allele resulted in a 349 bp band. Primers for detecting the Munc13-2 EYFP KI gene were: 5'-GATGAGACAGGCATGACCAT -3', 5'-ACAGCTAACTCTCCCTG ACTGA-3' and 5'-CATGGTCCTGCTGGAGTTCGTG -3'. Presence of the Munc13-2-EYFP KI gene resulted in a 220 bp band, while absence of the Munc13-2-EYFP KI gene resulted in a 190 bp band. Primers for detecting the Munc13-3 EGFP KI gene were: 5'-TCTCTCAGAGGACCAGCGA-3', 5'-TGGCACTTCATGGA ACATTTAT-3' and 5'-CATGG TCCTGCTGGAGTTCGTG -3'. Presence of the Munc13-3-EGFP KI gene resulted in a 340 bp band, while absence of the Munc13-3-EGFP KI gene resulted in a 283 bp band.

PCR (20 µL) were performed using 1 U of MyTaq HS DNA polymerase in MyTaq reaction buffer, 1 pmol/µL of each primer, and 0.25 mM of each deoxynucleoside triphosphate (dNTP), supplemented with 2.5 mM $MgCl_2$. PCR reactions were performed using the following cycling conditions: 96°C for 3 min, 33 cycles of 94°C for 30s – 62°C for 1 min -72°C for 1min, 72°C for 7 min.

[1] Max Planck Institute of Experimental Medicine, Göttingen

2.2 Materials

2.2.1 Chemicals and reagents

Reagent	Company	Cat. No.
(6,5)-Single-walled carbon nanotubes (SWCNTs)	Sigma-Aldrich	773735
10 mm-path cuvette	Hellma	105.200-QS
12 mm round coverslips # 1.5	Thermo Scientific	1188
20 G needle	BD Microlance	301300
24 -well cell culture plate	Greiner	662160
25 G needle	BD microlance	300400
25 mm round glass coverslips # 1	Menzel Gläser	CBAD00250RA133
2-Propanol	Emsure	1.09634.1000
D-AP5	Tocris Bioscience	106
5 mL syringe	BD	202202
50 mL reaction tube	Falcon Cornig	352070
500 mL 0.22 filter systems	Cornig	431097
5-Fluorodeoxyuridine	Sigma-Aldrich	F0503
6-well plate	Greiner	657160
96-well plate	TPP	92096
Acetic acid	Emsure	1.00063.2511
Aprotinin	Roth	A162.3
Aqua-Poly-mount	Polysciences	18606
B27 serum-free supplement (50x)	Gibco life technologies	17504-044
BCA protein assay	Pierce	1859078
Bovine serum albumin (BSA)	Sigma-Aldrich	A4503
Bromphenol Blue	BioRad	161-0404
Calcium chloride ($CaCl_2$)	Biomol	2450
CellTiter 96	Promega	G3580
Collagen 1	Becton Dickinson GmbH	354236
Cysteine	Sigma	C7477
Deuterium hydroxide (D_2O)	Sigma-Aldrich	151882
D-Glucose monohydrate	Sigma-Aldrich	49159
Dimethyl sulfoxide (DMSO)	Sigma-Aldrich	D2650
Disodium hydrogen phosphate (Na_2HPO_4*$2H_2O$)	Emsure	K46347280506
Dithiothreitol (DTT)	Biomol	04010.5
Dopamine hydrochlorid (DA * HCl)	Sigma-Aldrich	H8502
Dulbecco's modified eagle medium (DMEM)	Gibco life technologies	41966-029
Dulbecco's phosphate-buffered saline (DPBS)	Gibco life technologies	14190-094
Ethanol	Honeywell	K115032205
Ethylendiaminetetraacetic acid (EDTA)	Merck	1.0818.0250
Fetal bovine serum (FBS), heat-inactivated	Gibco life technologies	A15-104
Glass slides Superfrost Plus	Menzel Gläser	J1800AMNZ
GlutaMAX	Gibco life technologies	35050038
Glycerol	Emsure	1.04094.1000
Glycine	Sigma	33226
Hank's Balanced Salt Solution (HBSS)	Gibco life technologies	14170-088
HEPES	Roth	91005.3
Human glial-derived neurotrophic factor (GDNF)	Alomone labs	G-240
Hydrochloric acid 37%	Merck	1.003.172.500

Isoflurane	Baxter	19D01A31
L-DOPA	Tocris Bioscience	3788
Leupeptin	Peptide Institute	4041
Magnesium chloride hexahydrate ($MgCl_2$*$6H_20$)	Merck	1.05833.1000
MemCode reversible protein stain kit	Pierce	24580
Methanol	J. T. Baker	8404.25
Milk powder	Ferma	0203V04
Millex syringe filter units, 0.22 µm	Gibco life technologies	SLGP033RS
MITO serum extender	BD	355006
MyTaq HS DNA polymerase	Bioline	BIO-21113
NBQX	Hello Bio	BH0443
Neurobasal-A Medium (1x)	Gibco life technologies	10888-022
Nitrocellulose membranes	GE Healthcare	10600001
NuPAGE 4-12% Bis-Tris gradient gels	Novex life technologies	NP0336BOX
PageRuler Prestained Protein Ladder Plus	Thermo Scientific	26619
Papain	Worthington Biochemical	LS003126
Parafilm	Benis	PM 996
Paraformaldehyde (PFA)	Serva	UN2213
Penicillin/Streptomycin (100x)	Gibco life technologies	15140-122
PMSF	Sigma	P7626
Poly - L - lysine (PLL)	Sigma-Aldrich	P4707
Poly - D - lysine (PDL)	Sigma-Aldrich	P6407
Poly - L - ornithine (PLO)	Sigma-Aldrich	P4957
Potassium chloride (KCl)	Merck	1.049.361.000
Potassium dihydrogen phosphate (KH_2PO_4)	Merck	1.04.873.1000
Razor blade	GEM	E71962
Reserpine	Tocris Bioscience	2742
Sodium chloride (NaCl)	Merck	1.06404.1000
Sodium dodecyl sulfate (SDS)	GERBU GmBH	288.38
Sodium hydroxide (NaOH)	Merck	1.064.980.1000
Sucrose	Merck	1.07651.1000
Sulpiride	Sigma-Aldrich	S8010
T75 cell culture flasks	Sarstedt	83.39.11.002
Tail biopsy tubes	Cornig	MTS-11-8-C
Tedrodotoxin (TTX)	Tocris Bioscience	
Triton X-100	Roche	10 789 704 001
Trizma base (Tris)	Sigma	T1503
Trypsin inhibitor	Sigma-Aldrich	T9253
Trypsin-EDTA (0.05%)	Gibco life technologies	25300-056
Tryptophan blue	Thermo Scientific	15250061
Tween-20	Sigma Aldrich	P7949
Uridine	Sigma-Aldrich	U3750

2.2.2 Equipment

Equipment	Company
100x oil-immersion objective lens	UPLSAPO100XS, Olympus
561 nm laser	Cobolt Jive, Cobolt AB, Solna
Apotome	Zeiss
Cell culture hood	Heraeus Hera Safe
Cell culture incubator	Heraeus Hera Cell 240
CMOS camera, Andor Zyla 5.5	Andor Technology Ltd.
Dissection hood	Heraeus Hera Guard
ECL Chemostar	Intas
External light sources	KL 1500 LCD, Schott
Foreceps set	Aesculap
Heating block	Eppendorf
Hemocytometer	Marienfeld/ Neubauer
Imaging chamber (RC21-BRFS)	Warner Instruments
InGaAs camera, Cheetah-640-TE1	Xenics
IX53 microscope	Olympus
Laboratory fume food	Infralab
LSE341 light source	LOT-Quantum Design GmbH
MFP-3D Origin	Asylum Research
Mini-PROTEAN Cell	Biorad
Monochromator	
Multifuge	Heraeus
Perfusion flow regulator (64-0220, FR-50)	Warner Instruments
Peristaltic pump	Perimax-12/1 Spetec
PH meter	W. Krannich
Microplate reader	MWG-Biotech
Potter homogenizor	B. Braun
Scanner	Epson
Shaker	Vortex Genie
Shamrock 193i spectrometer	Andor Technology Ltd
Sonic Dismembrator, Model 120	Fisher Scientific
Sonication tip, probe 12921181	Fisher Scientific
Stereomicrope, Stemi 2000	Zeiss
Stimulus Generator 4000	Multichannel systems
Table centrifuges	Eppendorf
Thermomixer comfort	Eppendorf
Ultracentrifuge (TLA-100.3 rotor)	Beckmann
Ultrospec3100pro spectrophotometer	BioScience
UV–vis–nIR spectrometer	JASCO V-670
Valve control system (VC 6)	Warner Instruments
Water filter system	Sartorius
X-Cell Sure Lock Apparatus	Novex
xCite 120Q	Excelitas Technologies

2.2.3 Antibodies

Antigen	Species	Company	Cat. Number	Dilution	Use
Bassoon	Guinea Pig	Synaptic Systems	141 004	1:2000	ICC
Bassoon	Mouse	Stress Gene/Enzo	ADIVAM-PS003-F	1:1000	ICC
Complexin1	Rabbit	Proteintech	10246-2-AP	1:400	ICC
DAT	Rat	Merck Millipore	MAB369	1:1000	ICC
GFP	Mouse	Merck Millipore	MAB3580	1:1000	ICC
MAP2	Chicken	Novus Biologicals	NB300-213	1:2000	ICC
Munc13-1	Rabbit	Synaptic Systems	126 103	1:1000	ICC
Piccolo	Rabbit	Synaptic Systems	142 002	1:1000	ICC
Rab3A 42.2	Mouse	Synaptic Systems	107 111	1:2000	ICC
RIM1/2	Rabbit	Synaptic Systems	140 203	1:1000	ICC
SNAP25	Rabbit	Synaptic Systems	111002	1:2000	ICC
Synapsin1	Mouse	Synaptic Systems	106 011	1:4000	ICC
Synaptobrevin1	Rabbit	Synaptic Systems	104002	1:2000	ICC
Synaptotagmin1	Mouse	Synaptic Systems	105 011	1:2000	ICC
Synaptotagmin2	Rabbit	Synaptic Systems	105 223	1:1000	ICC
TH	Rabbit	Synaptic Systems	213 102	1:1000	ICC
TH	Mouse	Synaptic Systems	213 111	1:2000	ICC
VMAT2	Rabbit	Frontier Institute	AB2571857	1:2000	ICC
Munc13-1 C. 40	Rabbit	Brose laboratory		1:1000	WB
ubMunc13-2 C. 52	Rabbit	Brose laboratory		1:1000	WB
Actin AC-40	Mouse	Sigma	A4700	1:2000	WB

For immunocytochemistry (ICC), secondary antibodies were coupled to Alexa 405, 488, 555, 568 or 633 fluorophores (Thermo Fischer) and were used in a concentration of 1:1000. For western blotting (WB), secondary antibodies were coupled to horseradish peroxidase (HRP) (Jackson Immunoresearch) and were used in a concentration of 1:5000.

2.2.4 Media and solutions

All aliquots were freshly thawed before use and not frozen and reused again unless stated otherwise.

2.2.4.1 Solutions for neuron culture

Papain Solution: 0.2 mg/mL cysteine, 1 mM $CaCl_2$ and 0.5 mM ethylendiaminetetraacetic acid (EDTA) in Dulbecco's modified eagle medium (DMEM). Before each brain dissection, Papain solution (25 units per mL final concentration) was added to the buffer and the solution infused with carbogen (95% O_2, 5% CO_2) for 15 min until the solution becomes clear. The cleared solution was sterile-filtered using 0.22 µm filter units,

distributed into 1.5 mL Eppendorf tubes and kept on ice until use. Papain Solution was prepared by technical staff and stored at -20°C until use.

Stop Solution: 2.5 mg/mL Bovine serum albumin (BSA), 2.5 mg/mL trypsin inhibitor and 10% fetal bovine serum (FBS) in DMEM. Chemicals were dissolved and solution was sterile-filtered through a 0.22 µm vacuum filter unit. Stop Solution was prepared by technical staff and stored at -20°C until use.

Trituration Medium: 10% FBS in Neurobasal A (NBA). Solution was stored for maximum 3 weeks at 4°C.

Astrocyte Medium: 10% FBS, 2 mM GlutaMAX, Penicillin (200 U/mL)/Streptomycin (200 µg/mL), 0.01% MITO serum extender in DMEM. Chemicals were dissolved and solution was sterile-filtered through a 0.22 µm vacuum filter unit. Solution was prepared by technical staff.

FUDR 1000x stock: 16.5 mg/mL uridine, 6.7 mg/mL 5-fluorodeoxyuridine in ddH_2O. 100 mg 5-fluorodeoxyuridine and 247 mg uridine were dissolved in 15 mL sterile ddH_2O. The solution was filtered, distributed into 50 µL aliquots and stored at -20°C. Before application to the neuron cultures, the stock was diluted 1:100 in Culture Medium and 30 µL of the 1:100 solution added to a cell culture well containing 3 mL Culture Medium to a final concentration of 67 µg/mL 5-fluorodeoxyuridine and 165 µg/mL uridine.

GDNF 1000x stock: 10 µg/mL human glial-derived neurotrophic factor (GDNF) in ddH_2O. 10 mg of GDNF were dissolved in 1 mL sterile ddH_2O, divided in 50 µL aliquots and stored at -20°C. Before application to the neuron cultures, the stock was diluted 1:100 in Culture Medium and 30 µL of the 1:100 solution added to a cell culture well containing 3 mL Culture Medium to a final concentration of 10 ng/mL.

Culture Medium: 8% FBS, 2% B-27, Penicillin (200 U/mL)/Streptomycin (200 µg/mL), 2 mM GlutaMAX in NBA. Chemicals were stored as aliquots at -20°C. Medium was stored for a maximum of 2 weeks at 4°C.

1M HCl: 1 M HCl in ddH_2O. 37% fuming HCl was diluted in ddH_2O in a fume hood and stored in a closed bottle until use for coverslip washing.

2.2.4.2 Solutions for immunocytochemistry

4% PFA solution: 4% Paraformaldehyde (PFA) in PBS. 60 mL of ddH_2O were poured into a 100 mL glass bottle and mixed with two drops of 1 M NaOH. The solution was heated to approximately 60° C by microwaving for 33 s at 900 W. In a fume hood, 4 g PFA were added to the hot water and the solution mixed for 15 min on a magnetic stirrer until the PFA completely dissolved. 10 mL of 10x PBS was added to 90 mL ddH_2O. Using a waterbath, the PFA solution was cooled to room temperature (RT) and pH was adjusted to 7.4 with HCl titration. The solution was divided into 5 mL aliquots and stored at -20°C. To ensure reproducible fixation conditions, the PFA aliquots were stored for maximum six months.

Blocking solution: 10% BSA in PBS. 4 g BSA was dissolved in 40 mL PBS, by mixing it in a 50 mL Falcon tube using a magnetic stirrer for approximately 15 min. The solution was stored at 4°C for maximum seven days.

3% BSA: 3% BSA in PBS. 9 mL of Blocking Solution were diluted in 30 mL with PBS for ICC and stored at 4°C for maximum seven days.

10x PBS: 1.37 M NaCl, 27 mM KCl, 100 mM Na_2HPO_4 and 18 mM KH_2PO_4 were dissolved in ddH_2O. The pH was adjusted to 7.4 with NaOH tablets and the solution was stored at RT.

0.2% Triton-X-100: 0.2% Triton-X-100 in PBS. To ease pipetting for further dilutions, a 10% stock was created through mixing of 1 mL 100% Triton-X-100 with 9 mL PBS using a cut 1000 mL tip. This solution was stored up to a year at 4°C and further diluted to 0.2% Triton-X-100 with PBS for permeabilization of PFA-fixed neuron samples.

2.2.4.3 Solutions for AndromeDA imaging

Imaging Buffer: 136 mM NaCl, 2.5 mM KCl, 2 mM $CaCl_2$, 1.3 mM $MgCl_2$, 10 mM 4-(2-hydroxyethyl)-1-piperazineethanesulfonic acid (HEPES) and 10 mM D-glucose were dissolved in ddH_2O and the pH was adjusted by titration with HCl. The solution was filtered using a 500 mL vacuum filter system (0.22 µm pore size) and stored at RT.

Reserpine 5000x stock: 5 mM reserpine in dimethyl sulfoxide (DMSO). Pulverized reserpine was dissolved, separated into 200 µL aliquots and stored at -20°C until use.

For each imaging session, a fresh aliquot was taken from the -20°C storage. First, the 5000x stock was diluted 1:100 in Culture Medium in a separate reaction tube to prevent precipitation of DMSO. The resulting 50x solution was then added directly to the medium, in which neurons were cultured, to a final concentration of 1 µM reserpine.

L-DOPA 50x stock: 5 mM L-DOPA was dissolved in ddH_2O. Aliquots of 200 µL were stored at -20°C until use. L-DOPA aliquots were freshly thawed and added directly to the cell medium, resulting in a final concentration of 100 µM before live-cell experiments.

Sulpiride 1000x stock: 10 mM sulpiride in 0.1 M HCL in ddH2O. Pulverized sulpiride was dissolved, separated into 200 µL aliquots and stored at -20°C until use. Sulpiride was added to the Imaging Buffer to a final concentration of 10 µM before each live-cell experiment.

NBQX 1000x stock: 10 mM 2,3-dihydroxy-6-nitro-7-sulfamoyl-benzo(f)quinoxaline (NBQX) was dissolved in DMSO and stored at -20°C in 100 µL aliquots until use. NBQX was added to the Imaging Buffer to a final concentration of 10 µM before each live-cell experiment. This stock was prepared by technical staff.

D-AP5 2000x stock: 100 mM (2R)-Amino-5-phosphonopentanoate (D-AP-5) in ddH_2O. Pulverized D-AP5 was dissolved, separated into 100 µL aliquots and stored at -20°C until use. D-AP5 was added to the Imaging Buffer to a final concentration of 50 µM before each live-cell experiment. This stock was prepared by technical staff.

TTX 10000x stock: 3 mM Tetrodotoxin (TTX) in ddH_2O. TTX was dissolved, separated into 50 µL aliquots and stored at -20°C until use. TTX was added to the Imaging Buffer to a final concentration of 300 nM. Aliquots were frozen after experiments and reused up to 3 times. This stock was prepared by technical staff.

2.2.4.4 Synthesis of $GT_{(10)}$ functionalized SWCNTs

Deuterated PBS: 137 mM NaCl, 2.7 mM KCl, 10 mM Na_2HPO_4 and 1.8 mM KH_2PO_4 in D_2O. Chemicals were dissolved in deuterium dioxide, the pH adjusted to 7.4 through NaOH titration, the solution was autoclaved for 15 min at 121°C and stored at 4°C until use.

Nanosensor stock**:** 300 nM SWCNT-$(GT)_{10}$ in deuterated PBS. Prepared as described in section 2.3.4.

$(GT)_{10}$ stock: 200 pmol/µL $(GT)_{10}$ in deuterated PBS. Oligonucleotides were synthesized, purified and provided by the local DNA facility[2]. The dry DNA pellet was dissolved in deuterated PBS, distributed into 500 µL aliquots and stored at – 20°C.

SWCNT stock: 9 mg/ mL SWCNT in ddH_2O. Chirality enriched (6,5)-SWCNTs were added to ddH_2O under a laboratory fume hood and stored at 4°C until further use. SWCNTs do not dissolve in PBS and hence aggregate at the bottom of the tube. This mixing step was performed primarily to abolish the electrostatic charge of the naïve SWCNTs and to ease further pipetting steps.

2.2.4.5 Solutions for Western Blotting

2 x Laemmli Buffer: 100 mM Tris Base, 4% sodium dodecyl sulphate (SDS), 0.2% Bromphenol Blue, 20% glycerol, 200 mM dithiothreitol (DTT), pH 6.8 in ddH_2O.

MOPS Buffer: 50 mM 3-Morpholinopropane-1-sulfonic acid (MOPS), 50 mM Tris Base, 0.1% SDS, 1 mM EDTA, pH 7.7 in ddH_2O.

Transfer Buffer: 3 g Tris Base, 14.4 g Glycine, 200 mL methanol in 1 L H_2O.

PBST: 0.1% Tween-20 in PBS.

Homogenization Buffer: 320 mM sucrose, 5 mM HEPES, 1 mM EDTA. Chemicals were dissolved and pH adjusted to 7.4.

Protease Inhibitors: Leupeptin 1000x: 0.5 mg/mL in ddH2O, used in 0.5 µg/mL final concentration. Aprotinin 1000x: 1 mg/mL in ddH_2O, used in 1 µg/mL final concentration. Phenyl methyl sulphonyl fluoride (PMSF) 1000x: 17.4 mg/mL in 2-Propanol, used in 17.4 µg/mL final concentration. Aliquots were prepared by technical assistants and stored at -20°C.

[2] AGCT laboratory, Max Planck Institute of Experimental Medicine, Göttingen

2.3 Experimental procedures

2.3.1 SDS PAGE and Western Blotting

Following tissue dissection for dissociated neuron cultures (section 2.3.2), remaining brains were transferred to 1.5 mL Eppendorf tubes, snap-frozen in liquid nitrogen and stored at -80°C until use. For homogenization, brains were thawed on ice and 500 µL ice-cold Homogenization Buffer supplemented with protease inhibitors. Samples were then transferred to glass vials and homogenized with 10 pulses at 900 rounds per minute (rpm) using a glas/Teflon homogenizor at 4°C. Protein concentration of the brain homogenate was determined using a bicinchoninic acid (BCA) assay, measuring the absorbance at a wavelength of 575 nm in a microplate reader. Proteins samples were mixed with 2x Laemmli Buffer, boiled for 5 min and separated by SDS-PAGE (SDS-polyacrylamide gel electrophoresis) on commercially pursued NuPAGE 4-12% Bis-Tris gradient gels along with 5 µL of protein ladder. Per lane, 20 µg of protein were loaded. Gels were run in MOPS Buffer in a X-Cell Sure Lock Apparatus at constant 120 V. Afterwards, proteins were transferred to nitrocellulose membranes for 16 h at a constant current of 45 mA in Transfer Buffer at 4°C. Before immunoblotting, membranes were treated with MemCode reversible protein stain. Images of stained membranes were obtained using a scanner, and the protein stain removed using the companies' Stain Eraser solution. Membranes were subsequently blocked for 1 h with 5% milk powder in PBST. Primary antibodies were applied in 5% milk powder in PBST for 2 h and removed by three 5 min washes in 5% milk in PBST. HRP-conjugated secondary antibodies were applied for 1 h in 5% milk powder in PBST. HRP-reactive protein-bands were detected via the enhanced chemiluminescence (ECL) WB detection system and visualized using an ECL fluorescence imager.

2.3.2 Dissociated primary murine neuron culture

2.3.2.1 Coverslip preparation

Round glass coverslips (25 mm, # 1) were incubated in 1 M HCl overnight (O/N), gently shaken at RT, rinsed repeatedly with ddH_2O afterwards and kept in 70% ethanol until use. Clean coverslips were placed in 6-well cell culture dishes and ultraviolet (UV)-sterilized for 30 min until dry. After sterilization, coverslips were coated in 0.0008% PLL in Dulbecco's phosphate-buffered saline (DPBS) for 2 h at 37°C, washed three times for 5 min with DPBS afterwards and kept at 37°C until use.

2.3.2.2 Cortical astrocyte culture

Confluent primary cortical cultures were prepared in T75 cell cultures flasks as described previously (Burgalossi et al., 2012) with assistance from Anja Günther[3] and Dr. Chung Ku Lee[3]. In brief, the cortex of a C57BL/6N mouse at postnatal day 0 (P0) was dissected under a stereomicroscope in ice-cold Hanks' balanced salt solution (HBSS), divided into smaller chunks with forceps and transferred to 500 µL 0.05% Trypsin-EDTA solution, prewarmed to 37°C. The brain tissue was enzymatically digested at 37°C for 15 min, 450 rpm and washed twice with 500 µL Astrocyte Medium. Afterwards, the tissue was triturated 30 times using a 1000 µL pipette tip, and the supernatant containing single cells seeded into a single T75 Cell culture flask. Cells were grown at 37°C, 5% CO_2 for 5 – 9 days. Afterwards, the flask was shaken vigorously for 1 min on a vortex mixer and washed with 5 mL warm Astrocyte Medium to remove all but type I astrocytes. 3 mL of warm 0.05% Trypsin-EDTA solution was added to the cells and incubated at 37°C, 5% CO_2 for 5 min for enzymatic digestion of the remaining astrocyte layer. The flask was tapped, suspended cells collected in 5 mL Astrocyte Medium and centrifuged for 5 min, 1500 rpm in a 15 mL Falcon tube. The supernatant was removed, cells resuspended in 5 mL Astrocyte Medium and counted in a hemocytometer. Cells were seeded in a 24-well cell culture plate on PLL coated, sterile round 12 mm coverslips (# 1.5) at a density of 5 x 10^4 cells/ well and grown for 3-5 days to confluency at 37°C, 5% CO_2, followed by addition of FUDR in order to stop further cell division. Astrocytes on coverslips were used as feeder layers to a maximum 14 days after the dissection and discarded afterwards.

2.3.2.3 P0 hippocampal culture

Hippocampal neurons were prepared based on a previously described protocol (Burgalossi et al., 2012). In brief, neonatal C57BL/6 P0 mice were decapitated and the hippocampi dissected in a dish containing cold HBSS. Dissections were performed with a stereomicroscope in a sterile biohazard hood. Hippocampi from each brain were transferred to a 1.5 mL Eppendorf tube containing 500 µL of ice-cold Papain Solution and incubated for 45 min at 37°C, 400 rpm for digestion of the tissue. After 45 min, the supernatant was removed, Stop Solution (37°C) was added and the samples were incubated for another 15 min at 37°C, 400 rpm in order to terminate the enzymatic tissue digestion. The supernatant was replaced with 200 µL of Trituration Medium and tissue chunks gently triturated for 10 times using a 200 µL pipette tip to bring single cells in suspension. Samples were left for 2 min at RT in order to let non-dissociated tissue settle

[3] Max Planck Institute of Experimental Medicine, Göttingen

at the bottom of the tube. Supernatants containing single cells were collected in pre-warmed Culture Medium (37°C). This trituration procedure was repeated, hippocampal cells were seeded at a density of 3 x 10^4 in 24-well plates containing 12 mm round glass coverslips with astrocyte feeder layers (section 2.3.2.2) and grown at 37°C with 5% CO_2 for 14 days before use in ICC.

2.3.2.4 P0 ventral midbrain culture

Ventral midbrain (VM) neurons were prepared based on two methods described previously (Daniel et al., 2009; Rayport et al., 1992). In brief, pups were decapitated, the heads sprayed with ethanol, and placed in a sterile biohazard hood. The brain was placed on a polystyrene block with the ventral side of the brain facing up. Using a stereomicroscope, a brain slice containing the midbrain was rapidly dissected using a razor blade and the ventral part of the midbrain then separated using forceps. This tissue was transferred to 500 µL Papain Solution, enzymatically digested at 34°C, shaking at 400 rpm for 45 min and incubated afterwards for 15 min in Trituration Medium. The supernatant was replaced with 200 µL Trituration Medium and tissue chunks gently triturated for 10 times using a 200 µL pipette tip. Samples were left for 2 min at RT in order to let non-dissociated tissue settle to the bottom of the tube. Supernatants containing single cells were collected in warm Culture Medium (37°C). This trituration procedure was performed twice and collected cells centrifuged in a 15 mL falcon tube for 5 min at 1500 rpm. Afterwards, the supernatant was discarded, the cell pellet resuspended in Culture Medium supplemented with GDNF and cells seeded into 24-well cell culture plates on astrocyte feeder layers (section 2.3.2.2) at a density of 3 x 10^4 cells per well. One day after plating, FUDR was added to the wells. VM cultures were grown at 37°C, 5% CO_2 for 2 – 6 weeks without media change before use in ICC experiments.

2.3.2.5 P0 cerebellar granule culture

Cerebellar granule neurons were cultured based on a previously published method (Cousin et al., 1995). The cerebella of neonatal P0 mice were dissected in cold HBSS using a stereomicroscope, transferred to cold Papain Solution, divided into small pieces with forceps and digested and triturated as described for hippocampal neurons (section 2.3.2.3). After trituration, cells were plated in a small volume of DMEM containing 10% FBS on sterile PLL coated round 12 mm coverslips. For one 24-well plate, cerebella from two brains were used. The plate was kept for 1 h at 37°C with 5% CO_2 to allow the cells to settle on the coverslip. After 1 h, medium was changed to Culture Medium

supplemented with 20 mM KCl. Cerebellar granule cultures were fixed with 4% PFA after 10 to 14 days of maturation and kept at 4°C after fixation in PBS until use.

2.3.2.6 E12.5 ventral midbrain culture

WT VM neurons were prepared on embryonic day 12.5 (E12.5) based on published protocols (Weinert et al., 2015). In summary, pregnant females were anesthetized by isoflurane, sacrificed by cervical dislocation and decapitated. Mouse pups (E12.5) were taken through cesarean section. Ventral mesencephala were dissected and collected in a 5 mL falcon tube containing 5 mL cold HBSS. Afterwards, HBSS was replaced with 1 mL warm 0.05% Trypsin EDTA solution and incubated for 8 min at 37°C for enzymatic tissue digestion. The supernatant was removed and digestion stopped with 1 mL warm 100% FBS. Tissue was washed three times and triturated in Culture Medium, first by using a 5 ml syringe connected to a 20 gauge needle and two more times using a 25 gauge needle. The cell suspension was centrifuged for 5 min at 200 rpm, RT and cell pellet resuspended in 1 mL Culture Medium. Cells were counted using tryptophan blue in a hemocytometer and seeded at a density of 4 x 10^4 per well, in a 24-well plates containing DIV 7 hippocampal neurons prepared as described in section 2.3.2.8.

2.3.2.7 E18 Munc13-DKO mutant culture

The deletion of both Munc13-1 and Munc13-2 alleles leads to impaired neurotransmission resulting in a lethal phenotype once the offspring is separated from the mother (Augustin et al., 1999b; Varoqueaux et al., 2002). Munc13 double-knock-out (DKO) mutant embryos were therefore prepared from pregnant females on embryonic day 18 (E18) and generated by breeding Munc13-1(-/+) Munc13-2(-/-) mice. The mothers were anesthetized by isoflurane, sacrificed by cervical dislocation and decapitated. E18 pups were taken through cesarean section and VM neurons dissected and triturated without further delay as described in section 2.3.2.4. Single pups were processed separately and neurons from each mouse seeded in separate wells on astrocyte feeder layers as described in section 2.3.2.4 for ICC. For AndromeDA imaging, VM neurons were prepared from E18 Munc13-DKO embryos carrying the TH-EGFP transgene (TH-EGFP(+/-) Munc13-1(-/-) Munc13-2(-/-)). Neurons from one embryo were thereby plated in a single well containing a 25 mm round coverslip with 5-7 days old dissociated hippocampal neurons as described in section 2.3.2.8. The remains of the brain were checked for EGFP-fluorescence under a stereomicroscope and only EGFP positive mutants were further cultured for live cell experiments. The genotypes were

confirmed through genotyping of tail biopsies by the local DNA facility (AGCT laboratory)[4].

2.3.2.8 Hippocampal and ventral midbrain co-cultures for AndromeDA imaging

WT hippocampal neurons were prepared as described in section 2.3.2.3, plated on PLL-coated 25 mm round coverslips in 6 well-plates at a density of 5 x 10^4 cells per well and grown at 37°C, 5% CO_2. One day after plating, cell debris was removed from the cultures by discarding the cell culture medium and applying 10 drops of pre-warmed Culture Medium using a 1000 µL pipette tip directly onto the coverslip from a height of approximately 5 cm. This "washing" procedure was repeated and the medium then replaced with pre-warmed (37°C) Culture Medium supplemented with FUDR to inhibit cell proliferation. After the primary hippocampal cultures matured for 5-7 days, VM neurons were dissected as described in section 2.3.2.4. To identify DAergic neurons in the co-culture during live cell experiments, VM neurons were prepared from neonatal mice expressing EGFP under the TH promoter (TH-EGFP). During dissection and trituration, VMs from individual mice were kept separate and the remaining brain tissue from each mouse examined for the presence of EGFP using a fluorescence stereomicroscope with external light sources. Tissue from brains in which EGFP was detected were then pooled after trituration in a 15 mL falcon tube and centrifuged for 5 min at 1500 rpm. Afterwards, the supernatant was discarded and the cell pellet resuspended in 1 mL Culture Medium. VM neurons (1.5 x 10^5 cells per well) were seeded on top of the hippocampal neurons (7 days old) and human GDNF was added to the wells to a final concentration of 10 ng/mL to promote midbrain neuron survival. Neuron cultures were grown at 37°C with 5% CO_2. The next day, cells were washed by removing the culture media and applying 10 drops of pre-warmed Culture Medium using a 1000 mL pipette tip directly onto the coverslip from a height of approximately 5 cm. After washing, 3 mL of pre-conditioned Culture Medium containing FUDR and GDNF were added per well and neurons grown at 37°C with 5% CO_2 for a period of 3-6 weeks without changing the medium. For conditioning, 25 mL of Culture Medium was applied on primary cultures of cortical glia in a single T75 Cell culture flasks (section 2.3.2.2) and incubated for 24 h at 37°C with 5% CO_2. After this period, conditioned Culture Medium was collected and kept at 37°C until use. A single T75 flask containing confluent cortical glia age DIV 10-28 was used for up to five rounds of conditioning.

[4] Max Planck Institute of Experimental Medicine, Göttingen

2.3.3 Immunocytochemistry

2.3.3.1 Sample fixation

Method 1: Sample fixation with PFA/methanol. Medium was discarded and neuronal cultures washed once in RT PBS. After discarding the PBS, prewarmed 4% PFA (37°C) was added for exactly 2 min per well at RT. After 2 min, the 4% PFA was removed, replaced with -20°C cold methanol and samples quickly transferred in a -20°C freezer for a 15 min incubation. Subsequently, samples were washed 3 times in PBS and stored at maximum 7 days at 4°C.

Method 2: Sample fixation with 10 min PFA. Media was discarded and neuronal cultures washed once in RT PBS. After discarding the PBS, prewarmed 4% PFA (37°C) was applied on the coverslips for exactly 10 min per well at RT. After 10 min, the 4% PFA was removed and samples washed once in PBS. Then, 0.2% Triton-X-100 in PBS were added for cell permeabilization and cells incubated for 10 min at RT with gentle agitation. Subsequently, samples were washed 3 times in PBS and stored for a maximum of 7 days at 4°C.

Method 3: Sample fixation with 2 min PFA. Sample fixation with 2 min PFA. Media was discarded and neuronal cultures washed once in RT PBS. After discarding the PBS, prewarmed 4% PFA (37°C) was added for exactly 2 min per well at RT. After 2 min, the 4% PFA was removed and samples washed once in PBS. Then, 0.2% Triton-X-100 in PBS were added for cell permeabilization and cells incubated for 15 min at RT and gentle shaking. Subsequently, samples were washed 3 times in PBS and stored at maximum 7 days at 4°C.

2.3.3.2 Immunolabeling and mounting procedure

Following fixation, samples were incubated for 1 h in Blocking Solution with gentle shaking in order to block non-specific binding sites. After blocking, the Blocking Solution was discarded. Primary antibodies were diluted in 3% BSA in PBS, applied on the fixed samples and incubated for O/N at 4°C. To reduce evaporation, a wet tissue paper was placed below the lid of the cell culture dish and the dish sealed with parafilm. Afterwards, the coverslips were washed 3 times in RT PBS, gently shaking for 5 min during each washing step. After the last washing step, secondary antibodies were applied in 3% BSA in PBS and incubated for 1 h, with gentle agitation in the dark. The samples were protected from light to prevent fluorophores from bleaching. After 1 h, the secondary

antibody solution was removed and the coverslips washed for another three times with PBS for 5 min, gently shaking. Excess liquid was removed from the coverslips using tissue paper and coverslips mounted in Poly Aqua Mount on glass-slides. For storage, mounted samples were kept at 4°C and protected from ambient light.

Immunolabeling of Munc13 isoforms in DAergic neurons. For quantitative analysis of Munc13-1 protein expression, VM neurons from wild-type (WT) C57BL/6N P0 neonatals were prepared as described in section 2.3.2.4. As negative control and for estimation of the background signal, Munc13-1/2 DKO VM neurons from E18 pups were prepared as described in section 2.3.2.7 with maximum 2 days apart. WT and Munc13 DKO neurons were processed in parallel during all subsequent steps including 10 min fixation with 4% PFA (section 2.3.3.1, method 2), immunolabeling (section 2.3.3.2) and image acquisition section (section 2.4.3.1). Samples were labeled simultaneously with anti-bassoon antibodies for identification of pre-synaptic active zones, anti-TH antibodies for identification of DAergic neurons and anti-Munc13-1 for visualization of Munc13-1.

Antibodies that reliably distinguish between Munc13 isoforms are not commercially available. Therefore, an alternative strategy to visualize individual Munc13 isoforms was utilized, using mice previously described and generated (Cooper et al., 2012) that express fluorescently tagged Munc13 proteins. For quantitative analysis of Munc13-2 proteins expression, VM neurons from mice expressing Munc13-2-EYFP fusion proteins were prepared from P0 neonatals as described in section 2.3.2.4. As a positive control for immunolabeling against Munc13-2-EGFP fusion proteins, primary hippocampal neurons were prepared from the remaining brain tissue after separation of the VM following the procedure described in section 2.3.2.3. For quantitative analysis of Munc13-3 expression, cerebellar granule neurons, which express Munc13-3 (Augustin et al., 2001; Ishiyama et al., 2014) were dissected first from the cerebella of mice expressing Munc13-3-EGFP fusion proteins following the culture protocol described in section 2.3.2.5. VM neurons were then prepared from the remaining brain tissue as described before (section 2.3.2.4). Cerebellar granule neurons served thereby as positive control for immunolabeling against Munc13-3-EGFP fusion proteins. Munc13-2-EYFP and Munc13-3-EGFP KI neurons were processed in parallel to the respective controls during all subsequent steps including 2 min fixation with 4% PFA (section 2.3.3.1, method 3), immunolabeling (section 2.3.3.2) and image acquisition (section 2.4.3.1). Samples were labeled simultaneously with anti-bassoon antibodies for identification of presynaptic active zones, anti-GFP for visualization of Munc13-2 and Munc13-3 fusion proteins, and either anti-TH (for VM neurons) or anti-MAP2 (for control neurons).

Immunolabeling of EGFP in TH-EGFP DAergic neurons. VM neurons from TH-EGFP mice were plated on hippocampal DIV 5 - 7 neurons following the procedure described in section 2.3.2.8. and grown for 2 - 3 weeks at 37°C and 5% CO_2. Neurons were then fixed with 4% PFA for 10 min (section 2.3.3.1, method 2), and immunolabeled against TH for identification of DAergic cells and GFP. Using a ZEISS Apotome microscope, somata of TH+/GFP+, TH+/GFP-, TH-/GFP+ cells were counted though a 40x objective lens by manual scanning of the entire coverslip.

Immunolabeling of DAergic neurons in different culture systems. VM neurons were prepared from WT E12.5 embryos (section 2.3.2.6) or WT P0 neonatals, seeded on 5 - 7 old primary hippocampal neurons on PLL-coated coverslips as described in section 2.3.2.8 and grown for 2 weeks at 37°C and 5% CO_2. DAergic E12.5 neurons were then fixed for 10 min with 4% PFA (section 2.3.3.1, method 2), and immunolabeled using anti-TH, anti-MAP2 and anti-synapsin (SYP) antibodies (section 2.3.3.2). DAergic P0 neurons were fixed with PFA/ methanol (section 2.3.3.1, method 1), and immunolabeled against the dopamine transporter (DAT), VMAT2 and SYP. In this case, primary antibodies against VMAT2 and SYP were first incubated for 48 h at 4°C and samples washed 3 times with PBS. Only then, primary antibodies against DAT were applied O/N at 4°C. The separation of primary antibodies was performed to prevent cross-reactivity between anti-DAT antibodies (derived from rat) with anti-SYP antibodies (derived from mouse). For some samples, coverslips were first coated O/N with the diluted Nanosensor Stock in DPBS (1:1000, 0.3 nM) and neurons subsequently cultured on top of the nanosensor layer. Neurons on nanosensors were fixed with PFA/methanol (section 2.3.3.1, method 1) and immunolabeled against TH and MAP2.

Immunolabeling of presynaptic proteins at DAergic active zones. VM neurons were prepared from WT P0 neonatal mice and grown on astrocyte feeder layers as described in section 2.3.2.4. At DIV14, neurons were fixed with 4% PFA (section 2.3.3.1, method 2), or PFA in combination with methanol (section 2.3.3.1, method 1), and immunolabeled against DAT, bassoon, and the presynaptic protein of interest (either SYT1, SYT2, CPLX1, RIM, piccolo, SYB1, SNAP25 or rab3A).

2.3.4 Synthesis of $(GT)_{10}$ functionalized SWCNTs

SWCNT-$(GT)_{10}$ nanosensors were prepared based on previous protocols (Kruss et al., 2014; Mann et al., 2017). Using a cut 1000 µL pipette tip, a few SWCNTs “flakes” from the SWCNT stock were collected and added to 500 µL of a freshly-thawed $(GT)_{10}$ stock

aliquot, thereby keeping the transferred volume to a minimum. The aggregates were disrupted through tip-sonication using a 2 mm tip in an ice-cold water bath for 1 h at 30% amplitude. During this process, SWCNTs are functionalized by attachment of the $(GT)_{10}$ oligomers to their surface, making them soluble in aqueous solutions, thus retaining single SWCNTs-$(GT)_{10}$ complexes in the supernatant. These complexes were separated from the non-functionalized SWCNTs by centrifugation at 16000 rpm and 4°C for 30 min in a table-top centrifuge. The supernatant was transferred to a new 1.5 mL Eppendorf tube. This step was repeated 2 times. The concentration of nanosensors was determined through collection of absorption spectra (section 2.3.6.1) and adjusted to 300 nM. This Nanosensor stock was stored at 4°C for maximum of 3 weeks.

2.3.5 Cytotoxicity assay

Cell viability assays were performed in collaboration with Tabea Oswald and Angela Ruebeling[5] to determine if exposure to nanosensors is toxic for neuronal cultures. Hippocampal P0 neurons were prepared as described in 2.3.2.3 and seeded in PLL-coated 96-well cell culture plates. Two hippocampi from one brain were thereby distributed in 48 wells and grown for 14 days at 37°C, 5% CO_2. Afterwards, medium was removed and cells washed in Imaging Buffer once. In the first assay (Figure 12b), Imaging Buffer was removed from the cells, 100 µL of the diluted Nanosensor stock (30 nM in Imaging Buffer, section 2.2.4.4) applied on the mature neuron cultures and samples incubated for different time periods (30 min, 60 min or 120 min) at 37°C, 5% CO_2, followed by two washes with Imaging Buffer to remove the nanosensor solution. As positive controls for comparison, some cells were not washed at all and some cells were washed with Imaging Buffer but not exposed to nanosensors. In the second assay (Figure 13c), media was discarded and hippocampal neurons DIV14 washed once in Imaging Buffer. Then, Imaging Buffer was removed from the cells and the undiluted Nanosensor stock (300 nM in PBS) applied on the mature neuron cultures. The nanosensor solution was removed from the cells immediately (resulting in a ~3 s incubation time) by washing twice in Imaging Buffer. After washing, 100 µL Imaging Buffer was added to each well and samples incubated for 30 min, 60 min or 120 min at 37°C, 5% CO_2. For each incubation time, some wells were washed in parallel but not treated with nanosensors as positive controls for comparison. After respective incubation periods, a colorimetric cell viability assay was performed by using the Promega CellTiter 96 tetrazolium compound (3-[4,5-dimethylthiazol-2-yl]-5-[3-carboxymethoxyphenyl]-

[5] Cell Culture Laboratory, Institute of Physical Chemistry, University of Göttingen, Göttingen

2-[4-sulfophenyl]-2H-tetrazolium, MTS) as described in the companies' protocol. The quantity of the colorimetric product was determined by measuring the absorbance at 490 nm wavelength using a microplate reader. For each condition, four wells were analyzed as technical replicates.

2.3.6 Spectroscopy

2.3.6.1 UV-VIS-NIR absorbance spectroscopy

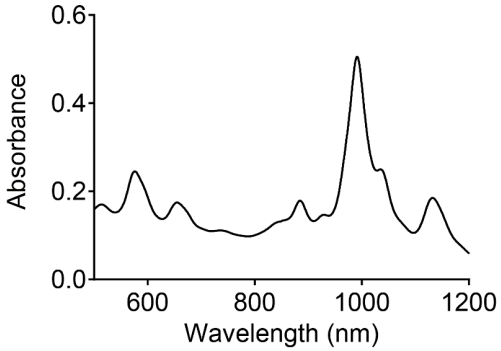

Figure 5: VIS-NIR absorbance spectrum of SWCNT-$(GT)_{10}$ nanosensors.
Representative VIS-NIR absorbance spectrum of a 1:100 diluted solution of SWCNT-$(GT)_{10}$ nanosensors after sonication.

Concentration of the Nanosensor stock was determined by measuring the absorption spectrum on a UV–VIS–NIR spectrometer in a 10 mm-path cuvette. For this calculation, the maximum absorbance peak at 990 nm (Figure 5), the molar extinction coefficient (Schöppler et al., 2011) and an estimated sensor length of 200 nm (Figure 8) were used as parameters.

2.3.6.2 NIR-fluorescence spectroscopy

The NIR-fluorescence spectra of SWCNT-$(GT)_{10}$ nanosensors were acquired with a Shamrock 193i spectrometer on an IX53 microscope. The Nanosensor stock was diluted in PBS (1:1000), 200 µL placed in a 96-well plate and excited through a monochromator at 561 nm, connected to a LSE341 light source. NIR-Fluorescence spectra were taken before and after the addition of 100 µM DA.

2.4 Imaging

2.4.1 Atomic force microscopy

Atomic Force Microscopy (AFM) was carried out in collaboration with Florian Mann[6] and Gabriele Selvaggio[6] and conducted in intermittent-contact mode (scan rate = 0.5 Hz, 512

[6] Kruss Laboratory, Institute for Physical Chemistry, University of Göttingen, Göttingen

lines) using an MFP-3D Origin instrument equipped with rectangular cantilevers (Al-coating, tetrahedral tip, ν_{res} = 300 kHz, k = 26 N·m^{-1}). Freshly cleaved muscovite MICA (flat, transparent mineral silicates) was coated with PLL and treated with the Nanosensor stock for ~3 s. The coated MICA was rinsed with ddH_2O and dried using a N_2-stream before sample measurement. Analysis of the acquired images was performed via the open-source software Gwyddion. Length of nanosensors were measured from AFM images either with Gwyddion or “Fiji ist just ImageJ” (Fiji).

2.4.2 Near-infrared microscopy

2.4.2.1 Microscope configuration and image acquisition

Imaging was carried out using a custom optical setup built by Florian Mann[6] and Claudia Geißler[7]. In brief, the system was based on an Olympus IX53 microscope and incorporated two cameras for simultaneous imaging of NIR (InGaAs camera) and visible light (CMOS camera). EGFP was excited using a xCite 120Q fluorescence lamp in combination with an EGFP excitation filter. EGFP fluorescence emission was filtered by passage through a 650 nm short-pass filter, a 561 nm notch filter and a 525/50 nm bandpass filter while guided to the CMOS camera for detection. SWCNTs were exited using a 561 nm laser and detected by the InGaAs camera after separation from the EGFP emission by dichroic mirrors. Images were captured using a 100x oil-immersion objective lens. NIR Images were acquired and saved in XVI format, exported as 16-bit Portable network graphics (PNG) image sequences (left aligned) through the Xeneth64 Software and transformed into 16-bit Tag image file format (TIFF) stacks in Fiji. EGFP and bright field (BF) images were acquired using the Andor Solis imaging software and exported and stored in TIFF format. Corresponding images from the two cameras were aligned using test samples by cropping and scaling the CMOS camera image to fit the dimensions of the InGaAs camera image.

2.4.2.2 Configuration of the imaging chamber

All NIR and live cell imaging was carried out in a RC21-BRFS imaging chamber at RT (21°C). This chamber had an oval-shaped bath with dimensions of 18.0 x 6.3 x 2.3 mm and two parallel platinum electrodes attached on the bottom. 25 mm round coverslips, containing neuronal cell cultures, immobilized nanosensors, or both, were sealed to the bottom of the imaging chamber using silicon grease, and the chamber mounted on a PH-2 anodized aluminum platform. In the closed bath configuration, the imaging chamber

[7] Laser Laboratorium Göttingen e.V., Göttingen

was sealed water-tight by a second 25 mm round coverslip from the top. To deliver solutions to the coverslip in the closed bath configuration, a perfusion system was used, controlled through a valve control system and a flow regulator. The flow rate was calibrated using Bromphenol Blue and maintained at (0.5 mL/min) to ensure laminar flow. Liquid waste was removed from the chamber with a peristaltic pump. In the open bath configuration, the coverslips were clamped to the PH-2 platform without a second coverslip on the top. For this configuration, the liquid in the chamber was static during imaging with no flow applied. In this case, solutions were delivered and buffers exchanged by manual pipetting. For all live cell experiments, an open bath configuration of the imaging chamber was chosen to allow the fast delivery of DA and KCl to the neurons during imaging. The fast delivery of DA to the nanosensors was important, as DA oxidizes in solution within minutes, an antioxidants (such as ascorbic acid) could not be used in this study because they evoke an nanosensor response as well (Elena Polo and Kruss, 2016).

2.4.2.3 Optimization of AndromeDA for live cell imaging

Nanosensor adsorption on different substrates. To determine a suitable substrate that allowed homogenous surface distribution of nanosensors and supported neuronal growth, nanosensors were adsorbed on three substrates that are typically used for neuron adhesion. 25 mm round coverslips were washed and sterilized as described in section 2.3.2.1 and coated with 0.0008% Poly-L-lysine (PLL), Poly-D-lysine (PDL)/collagen (Burgalossi et al., 2012) or 0.0008% Poly-L-ornithine (PLO) in DPBS for 2 h at 37°C, 5% CO_2. Afterwards, coverslips were repeatedly washed in DPBS. After removal of the last wash, 10 µL Nanosensor stock (section 2.3.4) was applied directly to the glass surface. After ~3 s, nanosensors were removed by repeated washes in Imaging Buffer. The coverslips were mounted on the imaging chamber in an open bath configuration and NIR images of the resulting nanosensor surface taken before and after the application of 100 µM DA. Pixel intensities were analyzed in Fiji and plotted using Graph Pad Prism.

Duration of nanosensor adsorption on cell cultures. To determine the optimal duration for homogenous nanosensors adsorption on coverslips that contain mature neurons, nanosensors (section 2.3.4) were applied on 14 day old dissociated primary hippocampal neuron cultures grown on PLL-coated glass (section 2.3.2.8) and incubated for ~3 s, 5 min, 10 min, 30 min or 1 h. In some experiments, hippocampal-VM co-cultures were prepared as described in section 2.3.2.8 and the nanosensors stock incubated on

the cells for 1 h. Neurons were repeatedly washed in Imaging Buffer to remove residual media and 10 µL Nanosensor stock (section 2.3.4) applied directly on the cells. For the shorter incubation periods (~3 s and 5 min), cells were kept at RT. For the longer incubation times, 1 mL of Imaging Buffer was added to the wells 5 min after nanosensor application and samples kept at 37°C, 5% CO_2. Subsequently, the nanosensors were removed by repeated washes in Imaging Buffer, coverslips mounted on the imaging chamber in an open bath configuration and NIR images of the resulting nanosensor surface taken. Pixel intensities were analyzed in Fiji and Graph Pad Prism.

Functionality of nanosensors under cell culture conditions. To determine the functionality of the nanosensor layer after prolonged incubation under cell culture conditions, coverslips were coated with nanosensors, neurons grown on top until maturation, and images of the nanosensor layer taken before and after the addition of 100 µM DA. Therefore, coverslips were prepared as described in section 2.3.2.1. The Nanosensor stock (section 2.3.4) was diluted 1:1000 in DPBS. 2 mL of this dilution were added to each well, incubated O/N at RT and washed three times with DPBS afterwards. Hippocampal and VM neurons were dissected and co-cultured as described in section 2.3.2.8. Neurons were grown at 37°C, 5% CO_2 for 3 - 6 weeks without media change before experimentation.

To complement this experiment, some nanosensor coated coverslips were incubated in Culture Medium. DA response of nanosensors was assessed after 3 days and 22 days of incubation at 37°C, 5% CO_2. Nanosensor-coated coverslips in PBS processed in parallel served as control. For this purpose, the closed configuration of the imaging chamber was used and samples perfused (0.5 mL/min) with increasing concentrations of DA (10 nM, 1 µM, 100 µM). DA was freshly dissolved in PBS and used for maximum 15 min afterwards to minimize oxidation. Between DA treatments, the imaging region was not changed, while samples were perfused for 10 min with PBS to remove residual DA. NIR images were acquired at 1 frame/s, normalized as described in (section 2.4.2.6.1) and pixel mean intensities calculated in Fiji.

2.4.2.4 DA dose-response experiments

The dose-dependency of the nanosensor surface response to DA was determined by perfusion of solutions with increasing DA concentrations in PBS (0.1 nM, 1 nM, 10 nM, 100 nM, 1 µM, 10 µM, 100 µM) on 25 mm round glass coverslips. Imaging was performed in closed configuration of the imaging chamber during perfusion (0.5 mL/min) controlled

through a valve control system and a flow regulator. Liquid waste was removed from the chamber with a peristaltic pump. DA was freshly dissolved in PBS and the solution used for maximum 15 min afterwards to minimize oxidation. A single coverslip was perfused with each DA concentration from lowest to highest, washing in between DA treatments by perfusing the coverslip with PBS for 10 min. The imaging region was not changed between DA treatments. NIR images were acquired at 1 frame/s, normalized as described in (section 2.4.2.6.1) and pixel mean intensity values collected from the entire image using the measure stack function in Fiji. The EC_{50} dose response curve was calculated by first calculating the peak fluorescence response to each DA concentration, plotting the responses with the *x*-axis in log10 format, and then fitting a sigmoidal curve to the data the using nonlinear regression function in Graph Pad Prism.

2.4.2.5 AndromeDA imaging of secreted DA

2.4.2.5.1 Live cell image acquisition

Live-cell imaging experiments were performed when VM neurons grown on hippocampal cells were 3 to 6 weeks old (section 2.3.2.8). Before imaging, a coverslip containing cultured neurons was washed five times with 1 mL of Imaging Buffer in a well of a 6-well plate. After the last wash, the Imaging Buffer was removed and 10 µL Nanosensor stock applied to the semi-dry coverslip. The coverslip was then immediately washed five times in fresh buffer to remove unbound nanosensors. The coverslip was then mounted on the imaging chamber using an open bath configuration and 500 µL of Imaging Buffer added to the chamber. The glutamate receptor antagonists NBQX and AP5 were included in the Imaging Buffer during all live-cell experiments to ensure that the detected DA signal was not a product of circuit activity from glutamatergic neurons in the culture, and the D2-Receptor antagonist sulpiride was included to prevent DA-induced auto-inhibition of DAergic neurons during the experiments. Two forms of stimulation were used to evoke DA release: electrical field stimulation and chemical depolarization. Field stimulation utilized square wave biphasic pulses delivered by a Stimulus Generator 4000 through two parallel platinum electrodes that were built into either side of the imaging chamber. 200 pulses (biphasic, 2 ms in duration, 16 V/cm field strength) were delivered at 20 Hz. For chemical depolarization, 3 M KCl was added to the chamber and rapidly mixed by pipetting, for a final K^+ concentration of 90 mM in the imaging chamber. Experiments typically followed the following format: Imaging prior to and during 20 Hz stimulation > Wash > Imaging prior to and during KCl stimulation > Wash > Imaging prior to and during 100 µM DA addition. Washing consisted of removing the buffer and replacing with fresh Imaging Buffer five times to remove residual DA from the chamber. For 100 µM DA

treatment, 1 mM DA (freshly dissolved) was added to the chamber to a final chamber concentration of 100 µM after mixing by pipetting. 100 µM DA saturated the nanosensors, and thus gave a readout of the maximum fluorescence response. This 100 µM DA control was performed at the end of each experiment to allow correction for variations in maximum fluorescence between individual nanosensor batches. Negative control experiments were performed by following the described stimulation procedures on coverslips that did not contain cells.

2.4.2.5.2 L-DOPA and reserpine treatment

The vesicular DA content was modulated through treatment of the VM cultures with reserpine (VMAT2 inhibitor) or L-DOPA (DA precursor). For reserpine treatment, reserpine was added to the culture medium to a final concentration of 1 µM and incubated for 90 min at 37°C and 5% CO_2 prior to experimentation (Sulzer et al., 1996). Nanosensors were then applied to the neurons in fresh Imaging Buffer (containing 1 µM reserpine) as described in section 2.4.2.5.1. For L-DOPA treatment, L-DOPA was added to the culture medium to a final concentration of 100 µM and the cells were incubated at 37°C and 5% CO_2 for 45 min (Pothos et al., 1996, 1998). Nanosensors were applied as described before and experiments conducted in fresh Imaging Buffer without L-DOPA, since nanosensors respond to L-DOPA, presumably due to its high chemical similarity to DA (Kruss et al., 2014).

2.4.2.5.3 TTX treatment

To inhibit action potential firing, neurons were treated with 300 nM TTX. This concentration was chosen as it is routinely used in our lab to completely inhibit spontaneous action potential firing but rapidly (within 5 seconds) washes out when the buffer is switched to TTX-free buffer. Imaging was carried out for 5 minutes in the presence of TTX in Imaging Buffer, followed by repeated washing of the coverslip with Imaging Buffer without TTX. After washing, neurons were imaged during stimulation following the standard format described in section 2.4.2.5.1.

2.4.2.6 Image processing and analysis

2.4.2.6.1 Near-infrared image processing

Background subtraction. Prior to analysis, images were first corrected to remove background fluorescence resulting from ambient light around the imaging system. To do this, a “background image”, acquired by capturing a frame of the buffer-filled imaging chamber without any cells, was subtracted from all frames of the image sequence.

$\Delta F/F_0$ normalization. To empathize changes in NIR fluorescence intensity of the nanosensor layer relative to the baseline, images were normalized. To do this, the initial fluorescence, F_0, was calculated for each image sequence as the intensity of the projected mean image of the first 10 frames using the maximum projection function in Fiji. For every frame in the image sequence, the change in fluorescence intensity for every pixel, $\Delta F/F_0$, was calculated using the Image calculator function. Once this operation was performed for all images in the sequence, the resulting normalized image sequence was saved as a TIFF-stack and used for further analysis.

Exclusion of nanosensor-free areas from analysis. Since the nanosensors bind preferably to exposed glass around the cells, parts of the coverslip that were covered by larger cellular structures such as cell bodies, dendrites and sparse glia contained no nanosensors. Thus, these areas of the imaging field appeared as nanosensor-free “shadows” in NIR images (Figure 8a, Figure 14). These regions were excluded from the quantitative analysis of normalized image sequences. For the exclusion, a mask was created from binarized, thresholded NIR images and applied to the raw image sequence. Areas enclosed by the mask then had their intensity values set to “Not a number” (NaN) thus excluding these regions from further analysis.

For all representative NIR AndromeDA images, a Gaussian filter was applied to the images to improve the visualization of the NIR fluorescence. The Gaussian filter was not used for image analysis and data collection.

2.4.2.6.2 Data processing

Accounting for nanosensor batch-to-batch variations. Although all nanosensor batches were prepared using the sample protocol, different batches exhibited variation in the relative fluorescence increase to the application 100 µM DA, which ranged between ~40% - ~200%. Possible causes for this are deviating positions of the sonication tip during sonication or the dramatically different neuronal landscapes in-between imaging fields, leading to distinct coverage of the nanosensors on the coverslip surface. Experiments were carried out over months, using different batches of nanosensors, and thus batch variation in nanosensor responsiveness needed to be accounted for in order to compare experiments performed using different batches of nanosensors. To account for batch variation in nanosensor responsiveness, the maximum fluorescence activation of nanosensors within each imaging field (F_{max}) was first calculated as the mean fluorescence increase of the imaging field in response to 100 µM DA (excluding

nanosensor-free areas). Normalized $\Delta F/F_0$ time traces for each experiment were then divided by the F_{max} of the corresponding experiment, thus accounting for nanosensor batch variation and allowing the comparison of data from experiments conducted using different batches of nanosensors.

Baseline correction. During NIR imaging, a slow gradual decline of nanosensor fluorescence intensity was observed. DA nanosensors are thought not to undergo photobleaching (Heller et al., 2005; O'Connell et al., 2002), and thus the loss of fluorescence may be caused by a gradual detachment of single nanosensors from the coverslip followed by diffusion out of the imaging focal plane. To correct for this gradual loss in signal intensity, a linear curve was fit to the fluorescence trace of the first 150 frames using OriginLab Pro or Microsoft Excel. The projected curve was then used for baseline correction by subtraction. This calculation was not required for the generation of hotspot traces 2.4.2.6.4, as the baseline drift was automatically accounted for by the subtraction of the mean fluorescence in the imaging field from the signal within hotspot ROIs.

2.4.2.6.3 Selection of areas for quantitative analysis of DA release

Average DA release across all varicosities. To account for the variation in axonal density between imaging regions, fluorescence intensity was quantified from regions around EGFP-expressing, DAergic varicosities and not the entire imaging field. Varicosities were manually selected based on their morphology (local increase of axon diameter) and expanded by 10 pixels (2 µm), creating a ROI that encompassed DAergic varicosities and the immediate surrounding area. This mask was applied on the normalized NIR image sequence, average fluorescence intensity within the ROI measured for each image in the sequence, and the measured fluorescence intensity plotted over time.

DA release at discrete "hotspots". Hotspots of DA release were defined as localized, transient increases in AndromeDA fluorescence above the surrounding fluorescence signal. To detect hotspots reliably and in an unbiased fashion, the Fiji Plug In "Dopamine Recognition Tool" (DART) was developed by Dr. Ali Shaib[8] and Abed Chouaib[9]. In brief, DART is a Java object-oriented language algorithm, that used machine learning to identify AndromeDA hotspots from NIR videos by comparing pixel intensities of consecutive NIR images. While comparing consecutive images, DART reduced noise

[8] Max Planck Institute of Experimental Medicine, Göttingen
[9] Center for Integrative Physiology and Molecular Medicine, Homburg

through a series of machine-based decision-making steps that involve thresholding, median filtering and eroding. As a result, a binary image was formed consisting of “true” events as larger white pixel areas over a black background. The white pixel areas thereby indicated regions of fluorescence changes above to the background (hotspots). The algorithm then used the binary image to segment and label the white areas as individual events (hotspots) and created Fiji compatible ROIs from the outline of these regions (hotspot ROIs). The hotspot ROI masks served as a spatial “map” of all hotspots detected by DART in each experiment and for the selection of areas for quantification of hotspot signals. DART was applied on raw, unprocessed NIR image sequences and yielded in Fiji compatible ROIs outlining each hotspot. DART was used only for detection and generation of hotspots ROIs and not for image processing prior to data analysis.

2.4.2.6.4 Generation of hotspot fluorescence traces

To quantify the AndromeDA fluorescence within each hotspot, the ROI mask for a given hotspot was applied to the normalized $\Delta F/F_0$ image stack (section 2.4.2.6.1) corresponding to that experiment. The mean fluorescence intensity within each ROI was then quantified in Fiji using the multi-measure function. The resulting fluorescence traces were manually checked to verify that the ROIs contained *bona fide* hotspots of localized, transient AndromeDA activation. For comparing hotspot characteristics such as onset and fluorescence amplitude it was crucial to obtain the fluorescence change corresponding specifically to each hotspot. In most cases, this was difficult because the slow and steady activation of nanosensors in the ECS (due to diffusing DA) obscured the brief fluorescence peaks of the hotspots. To isolate the fluorescence change of specific hotspots the mean fluorescence intensity was measured in a region containing no axons. For each frame, the hotspot fluorescence was then calculated as follows: $\Delta F/F_0$ (hotspot DART ROI) - $\Delta F/F_0$ (ECS). The resulting fluorescence values for each DART ROI were plotted as a time sequence describing the relative increase in NIR fluorescence above the background AndromeDA activation, thereby correcting for the activation of AndromeDA by diffusing DA from other nearby release sites.

2.4.2.6.5 Analysis of hotspot proximity to DAergic varicosities

The spatial distance between each AndromeDA hotspot and the nearest axonal varicosity was measured in all experiments. To do this, Fiji-compatible ROIs generated by DART (section 2.4.2.6.2) were overlaid on the image of EGFP-positive DAergic axons from the corresponding imaging field. Then, the straight-segment tool was utilized to draw a line from the estimated center of the hotspot to the estimated center of the closest

varicosity. These lines were stored in the ROI-Manager and their length in µm determined through the multi-measure function, thus giving a measurement of the distance between each hotspot and its nearest varicosity. To create randomized distance measurements as negative controls for comparison, hotspot-varicosity distances were measured using non-corresponding NIR and EGFP images. This control was performed to verify that the spatial association of hotspots and DAergic cell structures was not a coincidental effect of the data distribution or an effect of high axon density.

2.4.2.6.6 Analysis of hotspot onset and peak amplitudes

It was important to analyze the time at which hotspots appeared during NIR movies in relation to neuronal stimulation. The time point at which a hotspot appeared was defined at the time at which the hotspot exhibited its maximum fluorescence relative to the surrounding space. To determine this, hotspot ROIs generated by DART (section 2.4.2.6.2) were for used collection of fluorescence intensity traces over time using the multi-measure function on normalized NIR TIFF-stacks in Fiji. The data was exported to Microsoft Excel and corrected for baseline drift as described in section 2.4.2.6.1. To prevent obscuring of local hotspot peak amplitudes by unspecific single-frame noise, the time trace was smoothed across 15 data points using the moving AVERAGE command. The highest peak amplitude in the resulting time traces was returned with the MAX command and the position of the maximum value in time was returned using the Syntax MATCH(maximum value;data range; 0). The time point at which the maximal amplitude was observed was then used at the time at which the hotspot was observed for the purposes of determining the relationship between neuronal stimulation and the occurrence of hotspots.

2.4.2.6.7 Analysis of hotspots evoked by different stimuli

To investigate whether chemically-evoked depolarization induced hotspots from the same locations on DAergic axon as electrical field stimulation, hotspot ROIs generated by DART (section 2.4.2.6.2) were used to create binary images in Fiji, with pixel values within the ROIs = 1 and pixel values outside of the ROIs = 0. Hotspots evoked by 90 mM KCl were assigned the false-color Look-up-table “CYAN” and hotspots evoked by 20 Hz stimulation were assigned the false-color Look-up-table “MAGENTA”. Both color channels were merged into a multi-color TIFF-stack. As a result, regions on the coverslip that contained hotspots evoked by both stimulation paradigms appeared in white in the overlay. White, magenta, and cyan areas were manually selected using the

wand trace tool and used for further analysis of overlapping hotspot areas as well as hotspot counts.

2.4.3 Confocal light microscopy

2.4.3.1 Image acquisition

Confocal images from primary neurons were acquired using a Leica TCS SP5 equipped with hybrid GaAsP detectors. For fluorophore detection, four channels (at 633 nm, 568 nm or 555 nm, 488 nm and 405 nm) were scanned sequentially in line scanning mode (xyz) at 400 Hz using a 100x oil-immersion objective with a numeral aperture of 1.44. Images were acquired in 512x512 format with line averaging = 7, pixel size x,y = 145 nm and pinhole setting = 1 AU. Photo multiplier tubes (PMTs) were set to prevent bleed-through and cross-talk of fluorescent signals. For spectral detectors, the laser power, offset and gain were adjusted for each channel at the beginning of each imaging session. Hybrid GaAsP Detectors (HyD) were used in Photon Counting mode. First, an overview of the entire imaging field was captured, followed by a magnification with zoom factor 4 of the region of interest (ROI). Z-stacks were taken with a step size of 300 nm with up to 15 planes per neuron. For representative images, a maximum projection of the z-stack was performed using stack-functions in Fiji. For quantitative analysis of synaptic proteins expression, only one plane of the z-stack was used. Acquired images were saved and stored as LIF files from the LAS AF Leica Software. Files were exported to TIF files for analysis through the Bio-Formats importer in Fiji.

2.4.3.2 Image analysis

For analysis of Munc13 expression, images were acquired with a Leica TCS SP5 as described. Blind to the genotype and other fluorophores, bassoon-positive puncta were selected with the wand tracing tool in Fiji. ROIs were created based on the outline of bassoon puncta. Each ROI thereby represented one bassoon punctum. Through the ROI manager, these ROIs were applied to the corresponding images of Munc13-1 or EGFP labeling and the mean pixel intensity within each ROI calculated using the measure function. For statistical comparisons, the median values of all ROIs from a single coverslip were calculated. VM neurons were analyzed as described above with one additional preceding step. To exclude Munc13 and bassoon signals from non-DAergic axons, a mask was created first by thresholding the TH or DAT channel. This mask was applied on color channels showing fluorescent signals from Mun13 and bassoon

labeling. Using the “clear outside” function, all regions in the image that did not contain DAergic cell structures were excluded from subsequent quantification.

2.5 Statistical analysis

All statistical analysis was performed using Prism 8 (GraphPad). For ICC, *n* refers either to the number of independent cultures analyzed or the number of independent animals analyzed, as specified in figure legends. For nanosensor experiments, the sample sizes *n* refer to the number of independent coverslips analyzed. In general, each coverslip of neurons was imaged using 3 protocols in succession with washing in between as follows: electrical stimulation, K^+ stimulation and DA application. Protocols were not repeated for a given coverslip. Where appropriate, data was analyzed for normality of distribution using the Shapiro-Wilks normality test. Where all data sets were normally distributed, samples were compared using an unpaired two-way Welch’s t-test for comparing two samples or the Brown-Forsythe and Welch ANOVA test for three or more samples. For non-parametric data, the Mann-Whitney test was used for comparing two data sets, and the Kruskal-Wallis test was used for comparing three or more samples. The significance level for p was set at < 0.05. All data is represented as mean with standard error of the mean (SEM) (for normally distributed data), or median (for non-parametric data). An experimental sample (i.e. a given coverslip) was excluded from analysis if no induced increase in nanosensor fluorescence was observed during KCl stimulation or the final addition of 100 µM DA at the end of the experiment. Experiments were repeated using neurons from at least 3 independent neuron cultures. NIR image sequences that were obscured through *y-x* drift, focal loss, or other obstacles such as air bubbles in the imaging chamber were excluded from analysis.

2.6 Software

Images were acquired using the Andor Solis, Xenics or Leica AF Software. Microscopy images were stores as PNG, TIFF or LIF Bioformat. Images were analyzed in Fiji (2.0.0-rc69/1.52u/Java 1.8.0_172, 64-bit) either manually or using custom-written macros. Data was then collected and stored in Microsoft excel sheets. All statistical analysis was carried out in GraphPad Prism 6 or 8. All figures were composed in Adobe Illustrator CC 2020. Analysis of the acquired AFM images was performed via the open-source software Gwyddion. Baseline corrections of fluorescence time traces were performed in OriginLab Pro or Microsoft Excel.

3 Results

3.1 Adaptation of AndromeDA for live cell imaging

3.1.1 Properties of nanosensors on a glass surface

The (6,5)-SWCNT-$(GT)_{10}$ DA nanosensor used in this study was originally developed and characterized by our collaborators[10] with respect to its sensitivity (K_d = 9.2 nmol/L, limit of detection [LOD = 0.1 nmol/L], specificity to DA, its dynamic range (1 nM – 10 µM) and physical length (500 nm – 800 nm) (Mann et al., 2017; Nißler et al., 2019). In these previous validation experiments, the average fluorescence response to analytes was typically assessed using spectroscopy, with nanosensors suspended in aqueous solution. Therefore, these data cannot be directly translated to a thin nanosensor layer immobilized through adsorption on a glass surface. The adsorption procedure could potentially favor a fraction of the suspended nanosensors, shifting the overall properties of the nanosensor population. In addition, with spectroscopy, it is not possible to detect larger nanosensor aggregates that remain un-disrupted by sonication during the preparation procedure. Nanosensor aggregates differ considerably in brightness from single sensors, making it difficult to calibrate the dynamic range of the camera. Furthermore, nanosensor aggregates exhibit non-homogenous fluorescence response to the analyte, due to possible contamination with non-functionalized SWCNTs, which are fluorescent but not responsive to DA, and the effect of proximity quenching (O'Connell et al., 2002; Powell et al., 2018). Thus, nanosensor aggregates are undesirable when creating a nanosensor-coated surface. In the first part of my doctoral work, I therefore experimented with different conditions to develop a protocol for homogenous, aggregate-free nanosensor surfaces that retain their responsiveness to DA and would also support neuronal growth.

3.1.1.1 Adsorption of nanosensors on different substrates

Previous protocols used (3-Aminopropyl)-triethoxysilane (APTES) functionalization to facilitate the surface adsorption of SWCNTs (Kruss et al., 2017). APTES efficiently introduces primary amines to silica substrates, allowing for further modifications by

[10] Kruss laboratory, Institute for Physical Chemistry, University of Göttingen, Göttingen

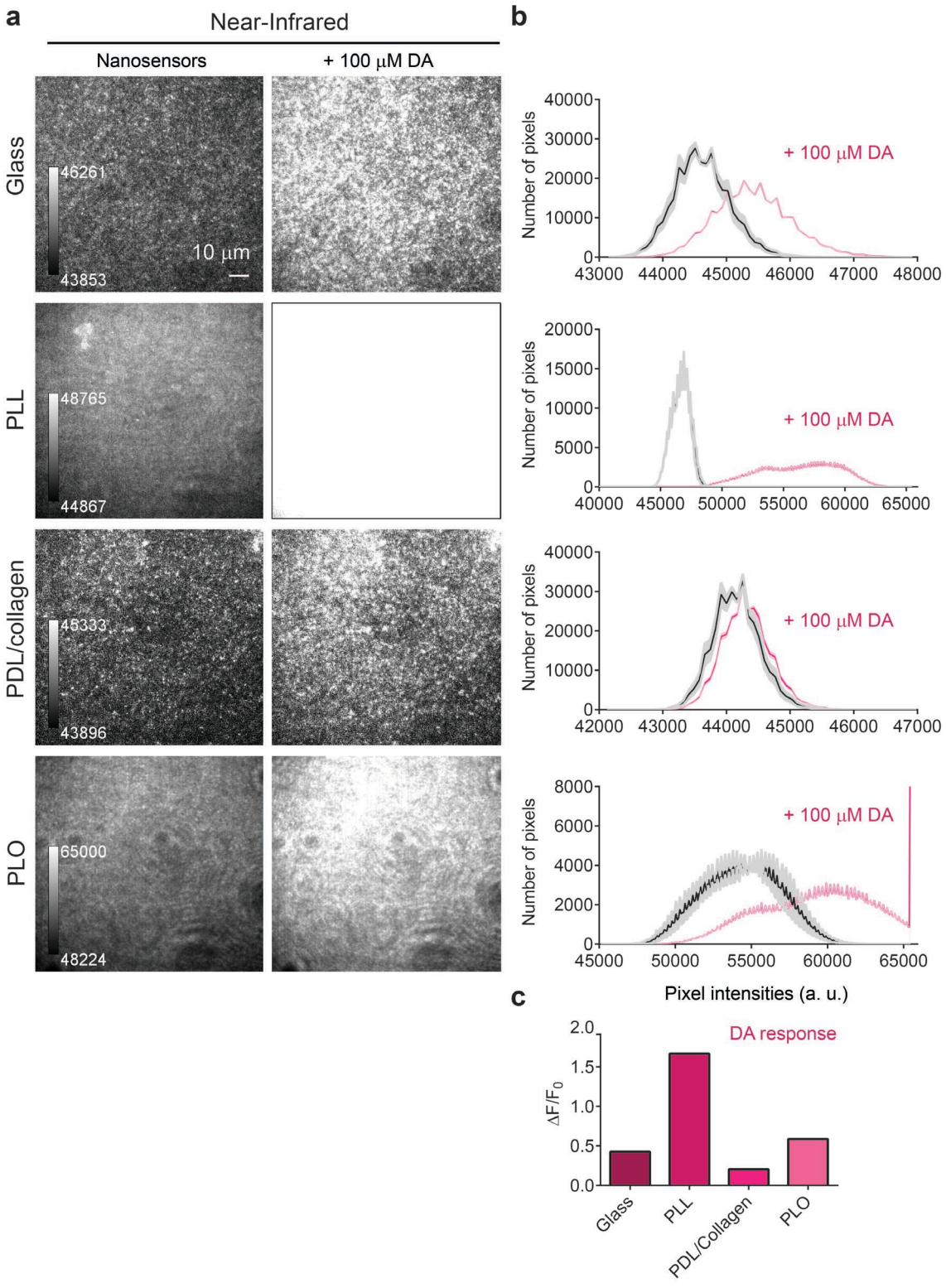

Figure 6: DA response of nanosensors adsorbed on different substrates.
Nanosensor stock solution (300 nM) was applied on glass coverslips coated with either PLL, PLO or a mixture of PDL and collagen (PDL/collagen) and removed after ~3 s by repeated washes in Imaging Buffer. Uncoated glass coverslips (Glass) served as comparison. **a**, NIR images showing the resulting nanosensor surface before (left panels) and after the addition of 100 µM DA (right panels). Scale bar = 10 µm. **b**, Frequency distribution of pixel intensities quantified from NIR images of nanosensor surfaces before (black line) and after the addition of 100 µM DA (magenta line). Graphs represent 3 images from *n* = 1 nanosensor batch (mean ± SEM). **c**, Average peak response of nanosensor surfaces to 100 µM DA.

biomolecules such as SWCNTs. APTES is a toxic compound, although its cytotoxicity in cell culture applications is disputed (Niu et al., 2015). Since the effect on neuronal viability of prolonged APTES exposure was unclear, I tested whether the classical substrates for neuronal cultures PLL, PLO and a mixture of PDL/collagen could substitute for APTES during nanosensor surface adsorption. Glass coverslips were coated O/N with the substrates, followed by a brief incubation with suspended nanosensors. NIR images were taken of the resulting coverslip surface (Figure 6a, left panels) and the distribution of pixel intensities analyzed as an approximation of the uniformity of the nanosensor coating, allowing a quantitative comparison of the different substrates (Figure 6b, gray traces). A high variation of pixel intensities would thereby indicate a less uniform adsorption across the glass surface. While PDL/collagen, PLL and the control surface without any substrate, demonstrated a relatively uniform adsorption of nanosensors in the resulting NIR images, with minimal pixel intensity variation (~3000 arbitrary units [a. u.] for glass only and PDL/collagen, ~5000 a. u. for PLL), PLO surfaces showed a 3x greater range of pixel intensities (~15000 a. u.). To assess the responsiveness of the nanosensor surfaces to DA, coated coverslips were treated with 100 µM DA (Figure 6a, right panels) and the mean change in fluorescence ($\Delta F/F_0$) of the images in response to DA calculated. Upon DA application, nanosensors on glass coverslips (without substrate) demonstrated a relative fluorescence increase of ~42%, nanosensors on PLL of ~167%, nanosensors on PDL/collagen of ~20%, and nanosensors on PLO of ~59%, respectively (Figure 6c). Since nanosensors adsorbed uniformly on PLL and demonstrated the greatest response to 100 µM DA, PLL was chosen as the substrate for nanosensor adsorption in subsequent live cell experiments.

3.1.1.2 DA dose-response of immobilized nanosensors

To evaluate the dynamic range of immobilized nanosensors on PLL-coated coverslips, nanosensor surfaces were perfused (0.5 mL/min) with increasing concentrations of DA dissolved in PBS (0.1 nM, 1 nM, 10 nM, 100 nM, 1 µM, 10 µM, 100 µM) (Figure 7a). The average fluorescence response to DA application increased in a dose-dependent manner, reaching maximal (saturating) fluorescence with the application of 10 µM DA. Washing the surface by perfusion with PBS for 10 min reversed the fluorescence to the initial (baseline) intensity, confirming the reversibility of the DA-nanosensor interaction (Figure 7b). Calculation of the dose-response curve from maximum peak values revealed the dynamic range (10 nM DA – 10 µM DA) and the half maximal effective DA concentration (EC_{50} = 299 nM), as well as a fluorescence increase relative to the baseline of up to 40% (Figure 7c).

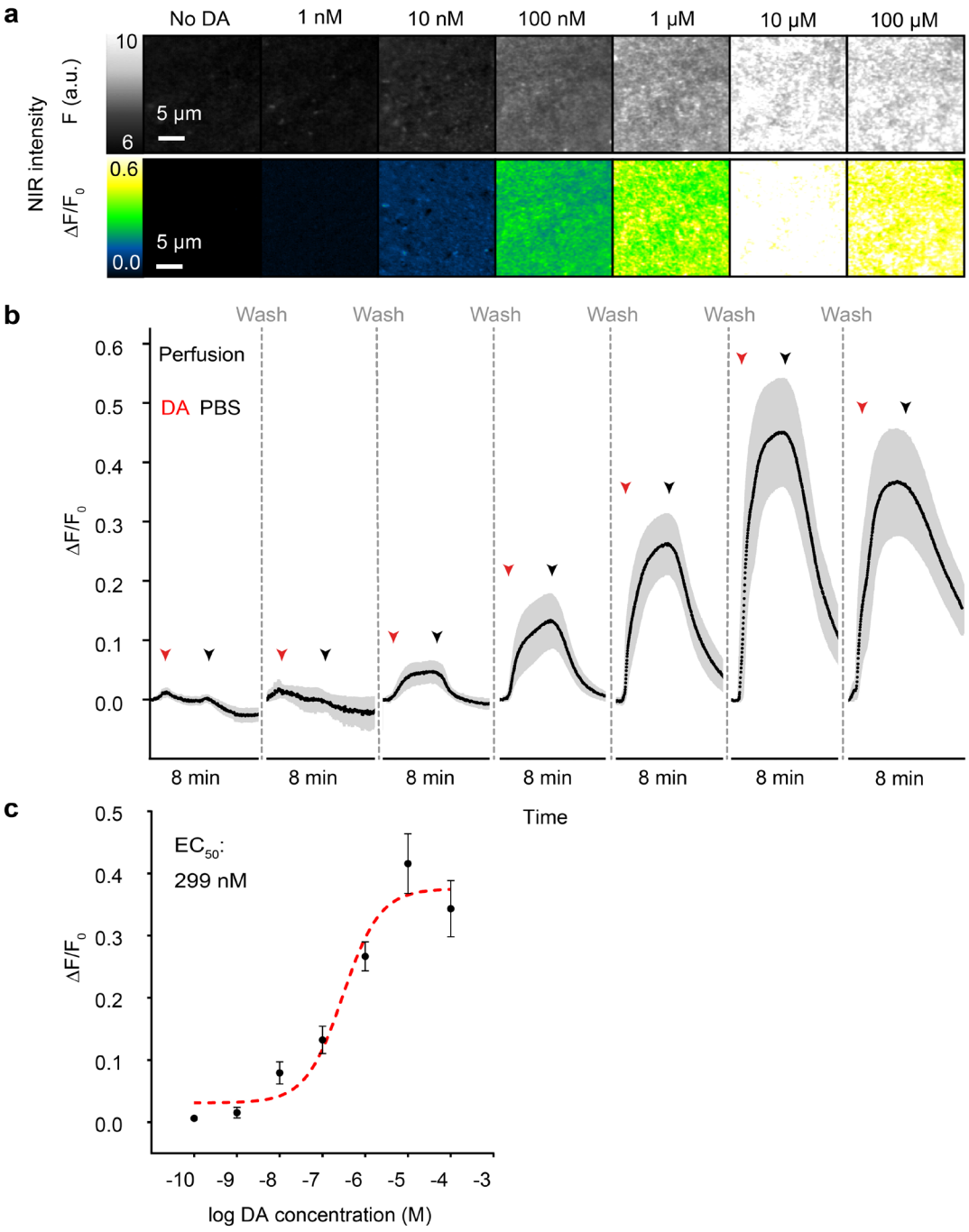

Figure 7: Dose-dependency and reversibility of nanosensor surface activation by DA.
a, Raw (upper) and normalized (lower) images of immobilized nanosensors on a single glass coverslip during perfusion with increasing DA concentrations (0.1 nM, 1 nM, 10 nM, 100 nM, 1 µM, 10 µM, 100 µM). a.u. Scale bar = 5 µm. **b**, Plots showing normalized average nanosensor NIR fluorescence during perfusion. Freshly dissolved DA in PBS was applied at the time point shown (red arrowheads), followed by a PBS wash to remove the DA (black arrowheads). Imaging was temporarily stopped after 8 min (indicated by breaks in the *x*-axis) and washing continued for 10 min. Mean values (black line) and ± SEM (gray area) from $n = 3$ independent nanosensor batches are shown. **c**, Dose-response curve calculated from the mean maximum peak responses during perfusion with DA, demonstrating the dynamic range (10 nM DA – 10 µM DA) and the EC_{50} = 299 nM. Individual values represent mean ± SEM.

3.1.1.3 Surface coverage and length of nanosensors

For live cell experiments, it is important that the coverslip surface is densely and homogenously coated with nanosensors, since an insufficient coating density could lead to the failure to detect small DA secretion events and the true spatial distribution of DA due to gaps in the nanosensor layer. Although nanosensors immobilized on a PLL-coated surface appear evenly distributed (Figure 6a), I conducted AFM in collaboration with Florian Mann and Gabriele Selvaggio[11] on these surfaces in order to investigate the surface coverage at a high resolution (Figure 8a). Nanosensor surfaces were prepared to reflect the situation in live-cell experiments, with modifications required for AFM imaging. The conventional coverslips surfaces were too rough, and treatment with PBS or Imaging Buffer led to salt crystal formation during the drying procedure that obscured the shape of single nanosensors. Therefore, nanosensors were adsorbed on flat MICA surfaces optimal for AFM imaging, and non-adsorbed sensors were removed by washing for several minutes under a stream of ddH_2O. Figure 8a demonstrates that nanosensors are present at a high density on the surface, with no uncoated regions observed. The length of individual nanosensors is another important factor, as it is required to estimate the concentration of nanosensors in suspension applied on the surface. The (6,5)-SWCNT species are ~0.7 nm in diameter as determined by the arrangement of carbon atoms (Schöppler et al., 2011), but vary with respect to their lengths as a result of rupture during ultrasonication. Previous protocols have obtained functional nanosensors of 500 nm length on average using a 3-mm tip for 10 min and 30% output during sonication (Nißler et al., 2019). The sonication period for the dispersion of nanosensors used

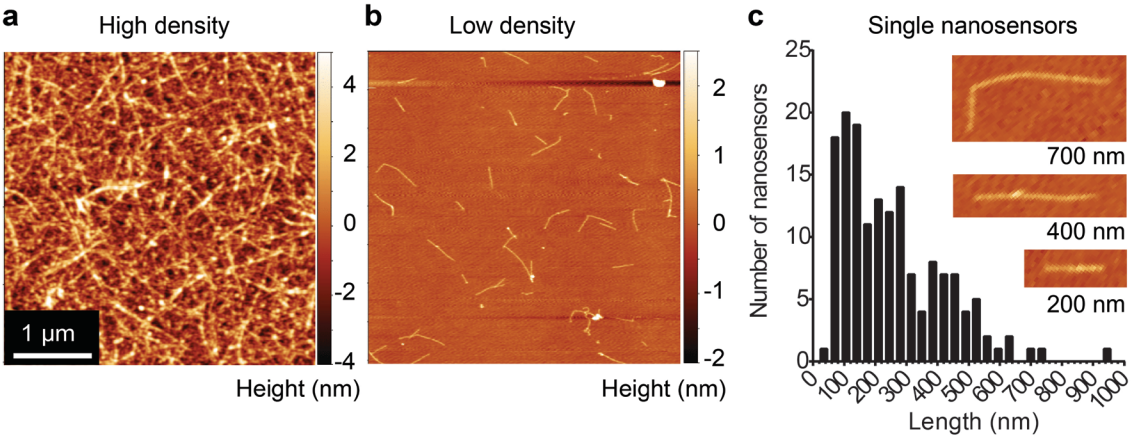

Figure 8: Surface coverage and length of single nanosensors.
a, AFM image of a PLL-coated MICA surface coated with nanosensors, illustrating the high density at which nanosensors are immobilized for live cell experiments. **b**, Nanosensor stock solution was diluted 1:10^4 prior to surface adsorption for visualization of single nanosensors. **c**, Frequency distribution of measured single nanosensor lengths from low-density preparations as shown in b. Exemplary AFM images of 700 nm, 400 nm and 200 nm long nanosensors are shown as inset. *n* = 1 nanosensor batch.

[11] Kruss laboratory, Institute for Physical Chemistry, University of Göttingen, Göttingen

in this study was prolonged to 1 h, and using a smaller sonication tip, compared to standard protocols of the Kruss laboratory. This sonication method yielded less nanosensor aggregates on the glass surface, but was likely to alter the average length of nanosensors as well compared to the standard procedure. To analyze the average nanosensor size obtained with the adapted sonication procedure, the physical lengths of single nanosensors were quantified by AFM imaging from a low-density surface preparation (Figure 8b). Nanosensors prepared with my adapted protocol were shorter (~200 nm, Figure 8c) than previously described due to the prolonged sonication.

With average dimensions of ~0.7 nm x 200 nm, the nanosensors used in this study are much smaller than individual DAergic varicosities, which are up to 2 µM in diameter (Cardozo, 1993; Ducrot et al., 2020; Pickel et al., 1996). From low density AFM images, which contained ~50 nanosensors (Figure 8b), it can be estimated that a single imaging field during live cell experiments (12800 μm^2) contains as many as ~400 million individual nanosensors, each which represent a point of measurement for DA detection. By positioning a large number of nanosensors around putative release sites, AndromeDA therefore allows imaging of DA release with high spatial resolution.

3.1.2 Optimization of neuronal culture conditions

SWCNT-ssDNA complexes have previously been used to detect DA secretion from a non-differentiated cell line (Kruss et al., 2017). In this approach, the nanosensors were immobilized on APTES-functionalized glass and PC12 cells were then cultured on top of the coated glass surface for maximum of 4 h. PC12 cells were depolarized by KCl addition after cells had adhered to the substrate. This study showed, that SWCNT-ssDNA conjugates can be used to investigate DA release with high spatial resolution *in vitro*. This approach, however, cannot be directly translated to standard methods for culturing of VM neurons, because these neurons require several weeks for differentiation, as well as trophic support from a confluent astrocyte feeder layer on top of which the neurons grow (Cardozo, 1993; Lautenschläger et al., 2018; Rayport et al., 1992). If nanosensor-coated glass were used in such a system, the glia would grow on top of the nanosensors, and the neurons then on top of the glia. Thus, the neurons would be spatially separated from the nanosensors, preventing their response to secreted DA. I therefore investigated the possibility of substituting the astrocytes with non-confluent neuron cultures. I chose hippocampal neurons as growth support, as hippocampal P0 neurons are routinely prepared in my host laboratory, show stability for weeks in the absence of glial monolayers and represent another (although less prevalent) target of VM projections (Gasbarri et al., 1997).

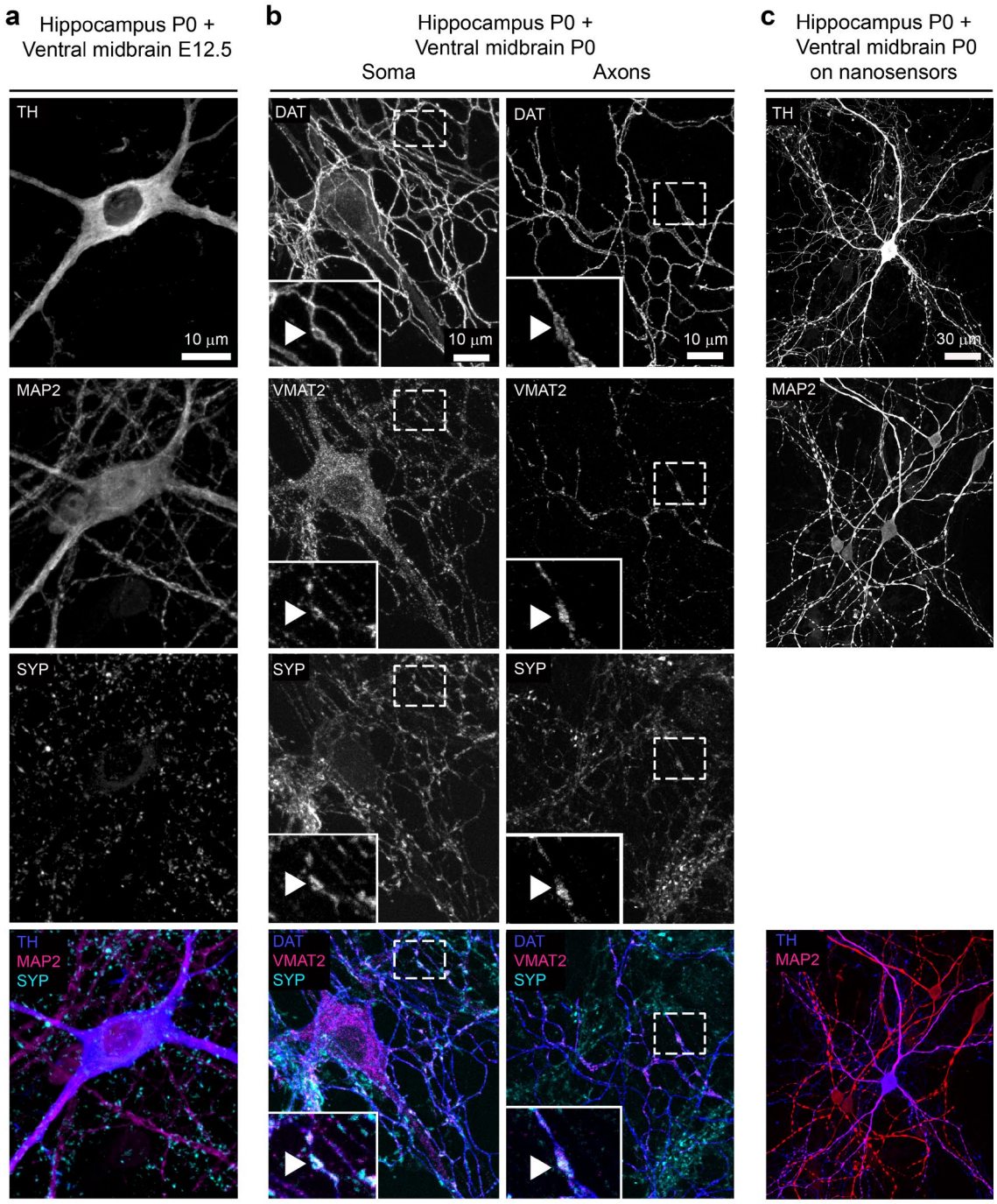

Figure 9: DAergic neurons grow with hippocampal neurons in the absence of glia.

To grow DAergic neurons directly on glass, VM neurons were seeded on established hippocampal P0 neurons DIV7 in the absence of glia. Confocal microscopy images show DAergic neurons after two weeks of maturation time in culture. **a**, VM neurons were prepared from E12.5 embryos and immunolabeled against TH (blue), MAP2 (magenta) and SYP (cyan). While neurons survive, complex arborization and DAergic synapse formation is not observed. **b**, VM neurons were prepared from neonatal P0 mice and immunolabeled against the DAT (blue), VMAT2 (magenta) and SYP (cyan). The region indicated by a white dashed box in each panel is shown in higher detail inset. P0 DAergic neurons form extensive axons with varicose structures what overlap with the synaptic markers VMAT2 and SYP (white arrowheads). **c**, VM neurons were prepared from neonatal P0 mice and immunolabeled against TH (blue) and MAP2 (magenta). In c, P0 neuron cultures were grown on coverslips coated with nanosensors.

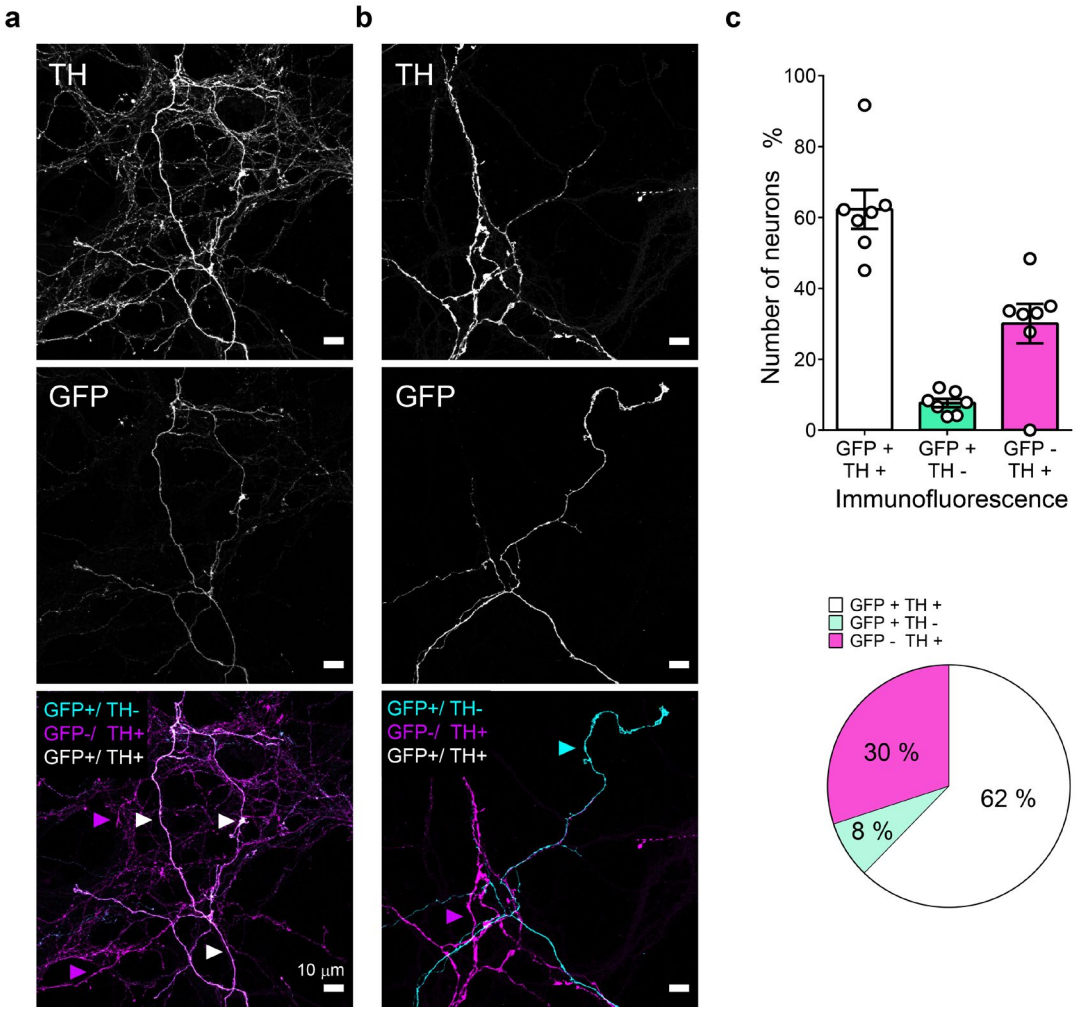

Figure 10: Expression of EGFP in DArgic neurons used in this study.
a and **b**, Immunolabeling of TH-EGFP VM neurons against GFP and TH. Lower panels show the overlay of both channels (TH in magenta, GFP in cyan), neurons expressing both markers appear in white. Fluorescence images show axonal regions. **a**, Neurons that are positive for anti-TH and anti-GFP labeling are indicated with white arrows, neurons that are positive for anti-TH and negative for anti-GFP labeling are indicated with magenta arrows. **b**, Neurons that are positive for anti-GFP and negative for anti-TH labeling are indicated with cyan arrows, neurons that are positive for anti-TH and negative for anti-GFP labeling are indicated with magenta arrows. **c**, Percentage of neurons expressing both or only one marker, respectively. Neuronal somata were counted. In column charts, white circles represent experiments across 3 independent neuron cultures, bars show mean ± SEM. The pie chart shows the mean contribution as a percentage made by each neuronal population to the total of all neurons. Scale bar = 10 µm. *n* = 7 coverslips from 3 independent neuron cultures.

A stable low-density co-culture was achieved by culturing E12.5 or P0 VM neurons on top of established, 7-days old hippocampal neurons (Figure 9a and b). The use of glia-conditioned medium (Engele et al., 1991) and additional washing steps further improved survival of VM neurons (for details, see section 2.3.2.8) for up to 2 months in culture, even on nanosensor coated coverslips (Figure 9c). Attempts to grow VM neurons on younger hippocampal cultures (DIV0 – 4), remained unsuccessful. A direct comparison of E12.5 and P0 derived neurons cultured in this manner showed that P0 (Figure 9b), but not E12.5 (Figure 9a) DAergic neurons contained varicosities with the presynaptic marker SYP at DIV14, indicating that E12.5 VM neurons did not form varicosities in this co-culture. P0 neurons showed a higher level of axonal branching, larger cell bodies with

more dendrites, consistent with an overall more differentiated appearance in culture (Figure 9b). Furthermore, P0 VM neurons, grown on established hippocampal neurons DIV7, yielded similar proportions of mature neurons expressing TH as well as EGFP (62 ± 5%, Figure 10a and b) compared to previous assessments of the TH-EGFP line used in this study (69 ± 4%) (Lammel et al., 2015). For these reasons, I opted to continue my work with hippocampal- VM P0 co-cultures.

3.1.3 Determination of nanosensor application strategy

To investigate in more detail how the nanosensor surface and the neuron cultures affected each other on the long-term, hippocampal-VM neuron co-cultures were grown on nanosensor/PLL-coated coverslips and imaged using live-cell fluorescence imaging after 3 weeks (Figure 11a). Unfortunately, it was apparent that these neuronal cultures underwent dramatic cell loss compared to neurons that were not exposed to nanosensors. Few living EGFP positive DAergic neurons were found growing on the nanosensor layer after three weeks in culture. In some cases, it appeared that nanosensor aggregates may have accumulated inside cells (Figure 11a, white arrowheads), as has been observed previously (Bianco et al., 2005). Neurons also displayed abnormal morphology such as axon fragmentation and excessive filopodia formation (Figure 11a, black arrowheads).

To examine nanosensor functionality in these cultures, coverslips from the same neuron preparation were subject to 100 µM applied DA after 14, 21 and 28 days in culture to determine if the nanosensors were still responsive to DA (Figure 11b). While the nanosensor surface was still responsive to 100 µM DA even after four weeks in culture (Figure 11b), as calculated by average relative fluorescence change ($\Delta F/F_0$), this fluorescence change (~2 - 3%) was much lower than I had observed in dose-response experiments (~40%, Figure 7b). To determine if the loss of sensitivity to DA was the result of the contact to cells or the time spent exposed to culture medium, a separate trial was performed by incubating nanosensor surfaces in medium without neurons. These experiments revealed, that the sensitivity of the nanosensor layers was reduced by ~76% already after 3 days incubation in media, and by ~91% after 22 days, compared to nanosensor surfaces that were incubated in PBS instead of medium (PBS control) (Figure 11c). A possible explanation is the phenomenon of biofouling, which describes the passivation of a sensor through accumulating biomolecules, resulting in an impermeable layer that hinders the direct interaction of the sensor with its analyte (Hanssen et al., 2016). Given that the nanosensors lost sensitivity and negatively impacted DAergic neurons in culture, I decided that neurons should be first

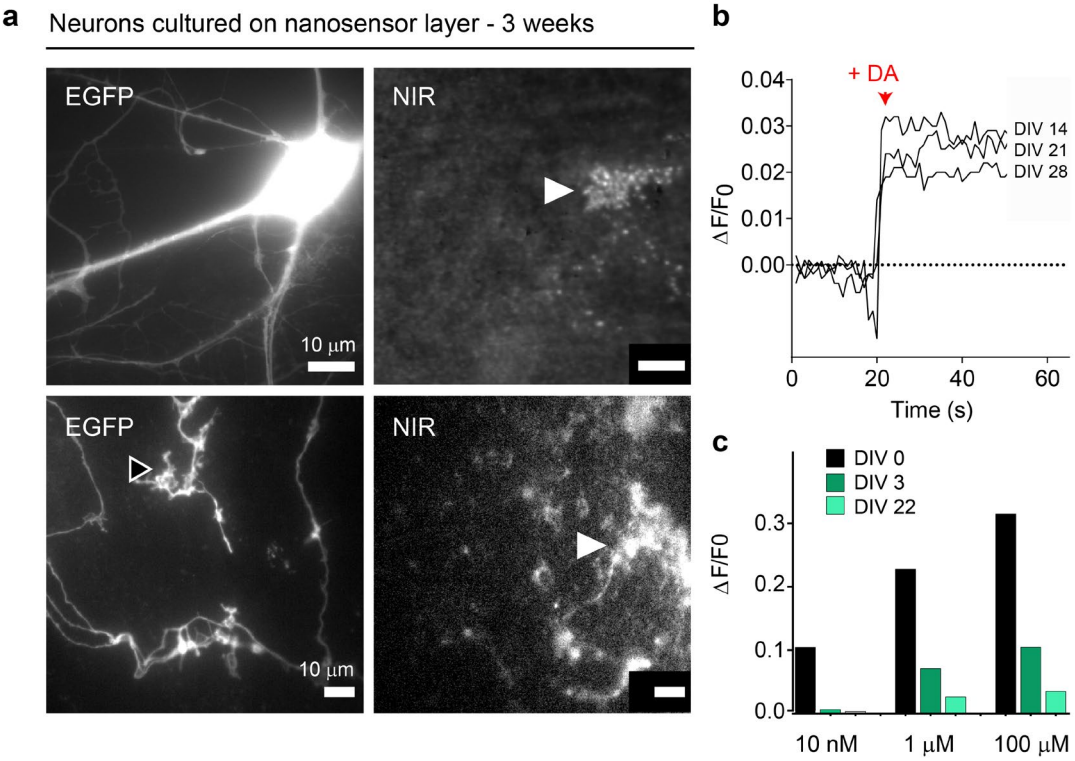

Figure 11: Prolonged exposure to culture conditions impairs nanosensor functionality.
a, Images show EGFP expressing live DAergic neurons grown on nanosensor-coated coverslips for 3 weeks (left panels) and the corresponding NIR images of the same imaging field (right panels). A DAergic axon with abnormal morphology is highlighted (black arrowhead). Nanosensor aggregates are observed on the surface (white arrowheads). Scale bar = 10 µm. **b**, Normalized DA responses of AndromeDA surfaces, on which neurons have been grown for 14, 21 and 28 days. 100 µM DA was applied at 20 s of imaging. **c**, Normalized peak responses of AndromeDA surfaces to 10 nM, 1 µM and 100 µM DA after incubation in neuron culture medium for 0 days (PBS control), 3 days and 22 days in the absence of cells. The activation of AndromeDA is dramatically reduced with prolonged exposure to culture medium. *n* = 1.

differentiated under established conditions for 3 - 6 weeks without nanosensors, and nanosensors added on mature neurons just prior to live cell imaging. The rationale behind this approach was, that the nanosensors would adsorb to the exposed glass surrounding the neurons.

What remained to be determined was the incubation period for which the nanosensor suspension should be applied on the mature neuron cultures. I initially tested 1 h as a suitable time period of nanosensor adsorption. On the day of imaging, mature cultures were thoroughly washed in buffer to remove residual cell culture medium. After removing as much buffer as possible, the nanosensor suspension (30 nM) was applied to the coverslip, incubated and then the excess nanosensors washed off. While morphologically intact EGFP-positive neurons were present in the culture (Figure 12a), the nanosensor surface was highly distorted (Figure 12a, NIR) and nanosensor clusters appeared to have been taken up into cells (Bianco et al., 2005), which could potentially interfere with normal cell function. Indeed, a cell viability assay conducted on DIV14 hippocampal neurons revealed, that sensors applied in solution to the neurons

significantly impaired cell metabolism (~11% reduction after 1 h, ~24% reduction after 2 h) and thus, compromised neuronal health after 1 h of exposure (Figure 12b).

Given the problems associated with 1 h application of nanosensors to neurons, I tested a range of adsorption times to determine the shortest period that would allow uniformity of the nanosensor surface around the cells, using hippocampal cultures at DIV14 as an approximation. Various time periods for nanosensor adsorption were tested: 1 h, 30 min, 10 min, 5 min, and immediate removal of the nanosensor suspension after application, which resulted in an adsorption time of ~3 s (Figure 13a). The frequency distribution of pixel intensities of the resulting NIR images served as a measure for the homogeneity of the nanosensor layer (Figure 13b). ~3 s of incubation resulted in a uniform layer of nanosensors and the smallest variation of pixel intensities (~4000 a. u.), with no adhesion observed in regions of the image that were covered by cells, creating a “negative image” of the cell in the NIR. This result indicated, that nanosensors adsorbed uniformly and specifically to the glass and were not taken up by neurons. Exemplary cell structures are marked with red dashed lines for comparison (Figure 13a).

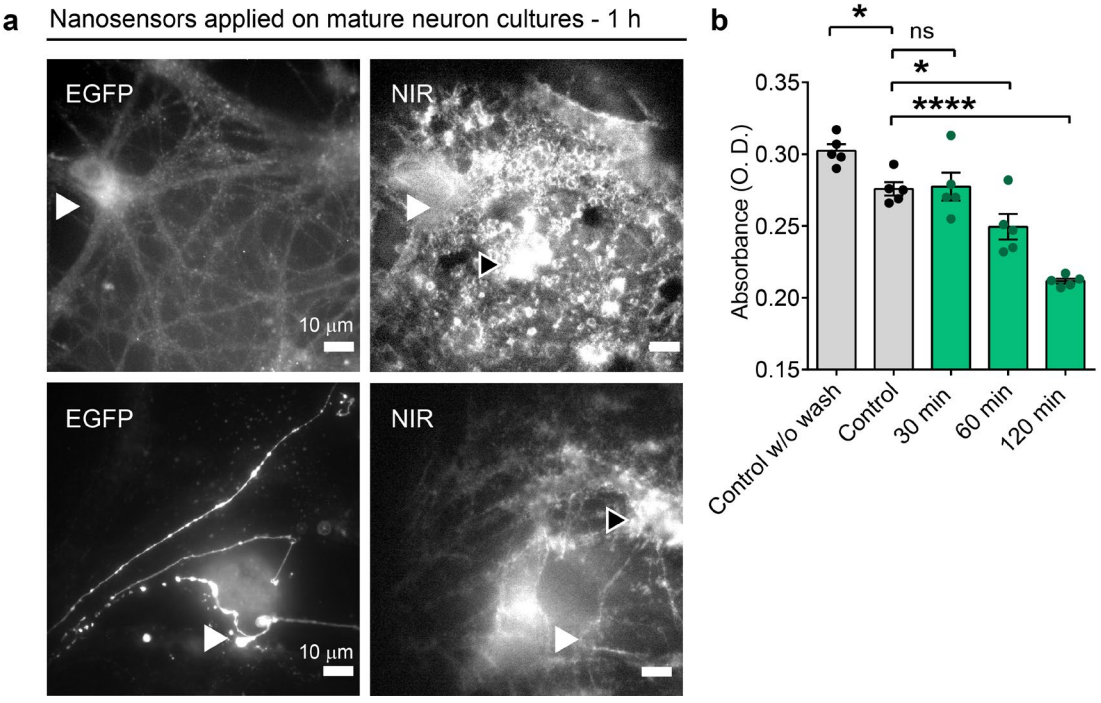

Figure 12: 1 h exposure of solubilized nanosensors compromises cell viability and uniformity of coating.
a, Diluted nanosensor stock (30 nM) was applied to mature neuron cultures and the solution was removed after a 1 h incubation. Left panels show fluorescence microscope images of EGFP-positive axons, while right panels show corresponding NIR images of the resulting nanosensor surface. If applied in this fashion, nanosensors appear to be present at cellular structures (white arrowheads), coat the coverslip surface non-homogeneously and form large aggregates (black arrows). Scale bar = 10 µm. **b**, The colorimetric MTS cell viability assay was performed on hippocampal neuron cultures incubated with solubilized nanosensors for 0 min (control), 30 min, 60 min or 120 min to determine if nanosensors are toxic to neurons. Prolonged exposure of solubilized nanosensors reduced metabolic activity after 60 min incubation. In b, dots represent technical replicates of n = 1 neuron culture and bars, means ± SEM. Data were compared using a one-way-ANOVA with multiple comparisons. * indicates $p < 0.05$, **** indicates $p < 0.0001$.

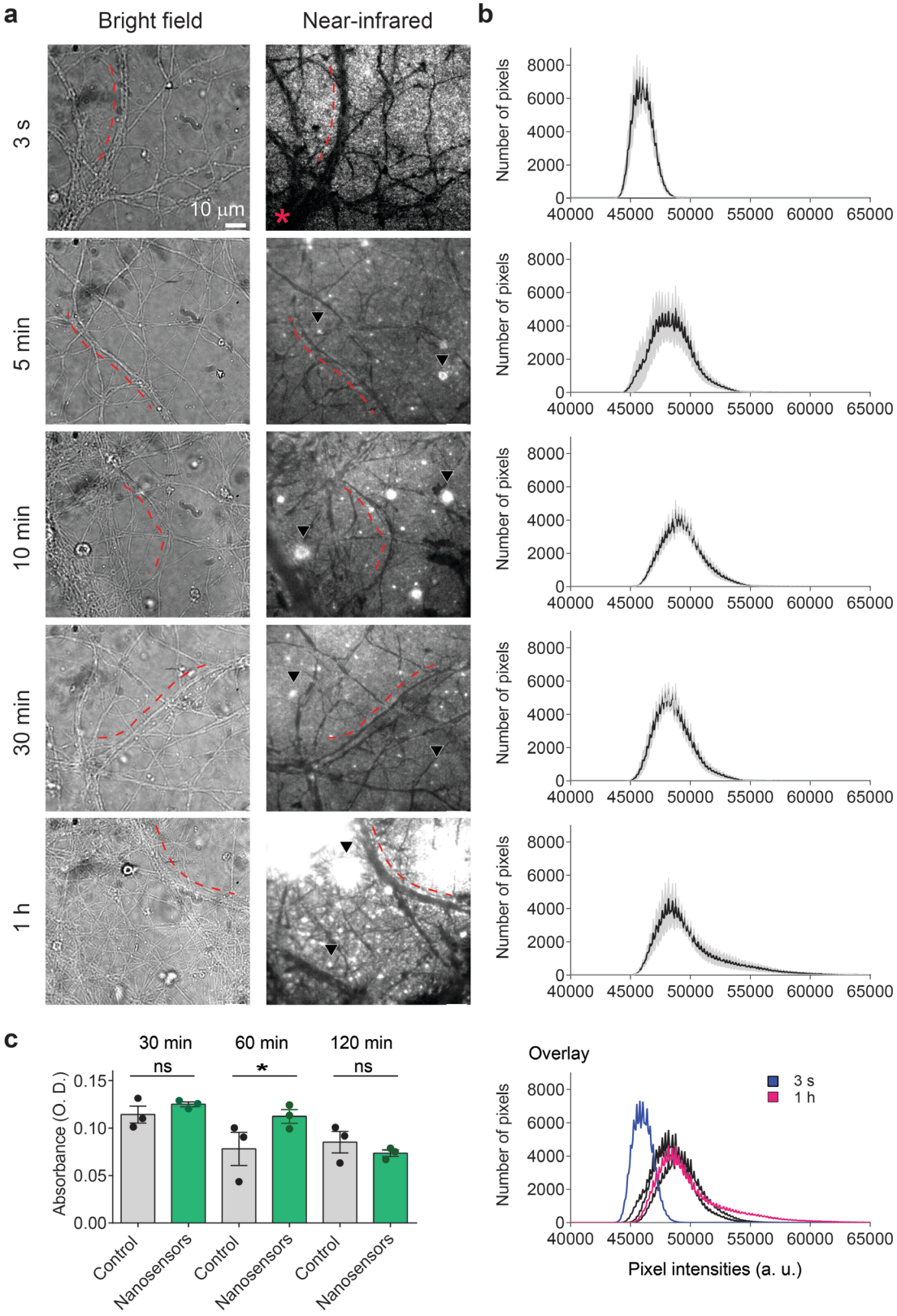
a
Bright field
Near-infrared
3 s
5 min
10 min
30 min
1 h
10 µm
b
Number of pixels
8000
6000
4000
2000
0
40000
45000
50000
55000
60000
65000
Overlay
3 s
1 h
Pixel intensities (a. u.)
c
30 min
60 min
120 min
ns
*
ns
Absorbance (O. D.)
0.15
0.10
0.05
0.00
Control
Nanosensors
Control
Nanosensors
Control
Nanosensors

Figure 13: Prolonged incubation leads to non-homogenous surface adsorption of nanosensors.
Nanosensor stock (300 nM) was applied to mature hippocampal neuron cultures at DIV 14 and the solution was removed after 3 s, 5 min, 10 min, 30 min or 1 h by repeated washes in Imaging Buffer. **a**, Images showing neurons using BF (left panels) and the corresponding nanosensor surface in the NIR (right panels). Dark regions in the NIR, indicating an absence of nanosensors, correspond to coverslip regions covered by cells (examples marked by red lines). Dark regions, which were covered by cells, were excluded from analysis. For better visibility, the image with the red asterisk has different contrast settings than the other NIR images. Scale bar = 10 µm. **b**, Frequency distribution of pixel intensities quantified from NIR images of resulting nanosensor surfaces. Graphs represent 6 images from *n* = 2 nanosensor batches (mean ± SEM). An overlay of mean intensity traces from b, with the shortest (3 s, blue) and longest incubation time (1 h, magenta) are highlighted. With prolonged incubation, nanosensor aggregates (black arrowheads) were more frequently observed. **c**, MTS cell viability assay indicating, that brief exposure (~3 s) of solubilized nanosensors is not toxic to neurons for up to 120 min after exposure and removal of non-adsorbed nanosensors. Dots represent a single mouse and bars represent means of *n* = 3 mice. Four technical replicates were measured for each mouse. Data were compared using a two-tailed Welch's t-test. * denotes $p < 0.05$, ns = not significant.

The nanosensor-free "negative" areas of the images were practical for aligning EGFP and NIR images, as well as detection and correction of *x*-*y* drifts during imaging, and were very useful in subsequent analysis. Compared to the brief ~3 s adsorption samples, the appearance and size of nanosensor aggregates (Figure 13a, black arrows) increased with longer adsorption times, which was reflected by increasing ranges of NIR pixel intensities (~4000 a. u. for 3 s, ~7000 a. u. for 5 min, ~9000 a. u. for 10 min and 30 min, ~16000 a. u. for 1 h (Figure 13b). These experiments were complemented by a colorimetric MTS cell viability assay using hippocampal neurons, examining the toxicity of the ~3 s adsorption condition. With ~3 s adsorption time, the viability of the neurons was not affected for up to 2 h after adsorption and washing (Figure 13c). Therefore, the ~3 s adsorption time yielded the best results with respect to neuronal health and surface uniformity, and was used for subsequent live cell experiments.

3.1.4 Overview of the experimental strategy

To summarize the observations that were made during the adaptation of nanosensor surfaces for DA release experiments: (i) nanosensors adsorbed to PLL-functionalized glass remain highly responsive (EC_{50} = 299 nM) to DA (ii); hippocampal neurons DIV7 can serve as substitute for astrocyte monolayers and promote DAergic neuron survival for up to two months on PLL-coated glass, providing an ideal substrate for nanosensor adsorption around the neurons; (iii) growing neurons on a nanosensor layer is toxic for the neurons and impairs nanosensor functionality, (iv) brief application of a concentrated nanosensor dispersion directly onto the cells creates a uniform nanosensor layer around the neurons with no detectable negative impact on cell viability. A schematic overview of this newly established methodology is provided in Figure 14. We call this two-dimensional nanosensor layer surrounding the cells *AndromeDA* – "Adsorbed Nanosensors Detecting Release of Dopamine".

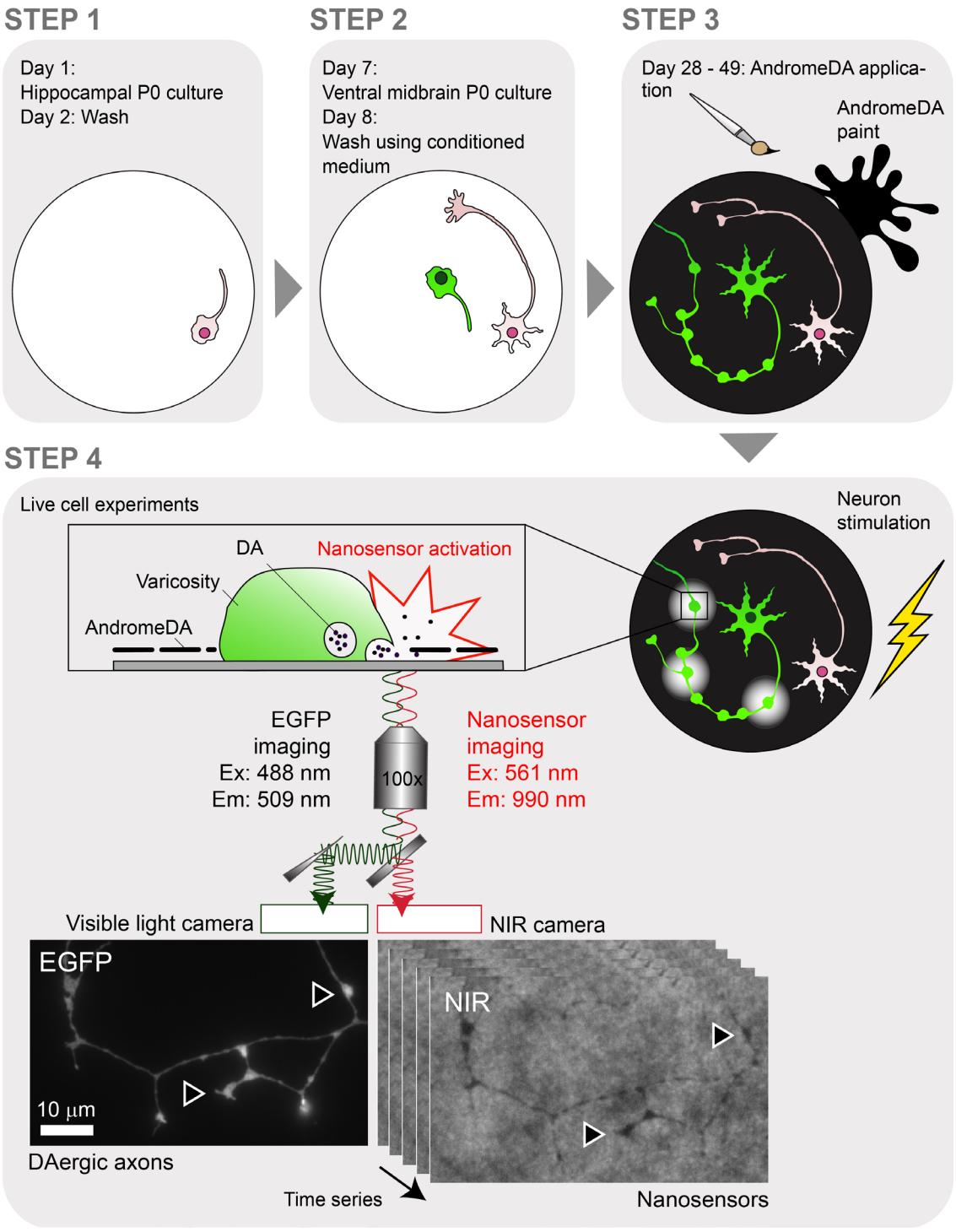

Figure 14: Overview of the cell culture strategy for AndromeDA imaging.
STEP 1, WT hippocampal neurons are prepared from P0 neonatal mice on PLL-coated coverslips. The next day, debris is removed by medium change, applied in drops directly on the cells. **STEP 2**, 7 days later, VM neurons from P0 neonatal mice that express EGFP under the TH promoter (TH-EGFP) are seeded on top of the hippocampal cells. On the next day, neurons are washed and cultured in conditioned medium. Cultures are grown for another 3 weeks at minimum. **STEP 3**, Mature neuron cultures are repeatedly washed in Imaging Buffer, nanosensors (300 nM) applied directly on the cells and unbound nanosensors are immediately removed by repeated washes. **STEP 4**, Neurons are subjected to live cell imaging experiments for a maximum of 90 min using a custom dual camera set up. DAergic axons are identified through their EGFP fluorescence by the visible light camera and nanosensors surrounding these axons are imaged through the NIR camera during neuronal depolarization. DA release sites are identified through activation of nanosensors in close proximity. DAergic varicosities are marked with black arrowheads. Ex = Excitation, Em = Emission.

3.2 Imaging DA release with AndromeDA

Resolving DA secretion at single varicosities has not been possible in the past due to methodological limitations, but can be achieved with the experimental strategy illustrated in Figure 14. The two-dimensional nanosensor surface established in the last section, called AndromeDA, surrounds DAergic varicosities during imaging. Thus, each release site is surrounded by hundreds of individual nanosensors, each of which is capable of reporting changes in local DA concentrations in a dose-dependent manner, providing an unprecedented spatial readout of DA transients in the culture. After having established a suitable protocol for its use in VM cultures, the next objectives of my doctoral work were to validate and apply AndromeDA for studies of evoked DA release.

Hippocampal-VM co-cultures were prepared as described in section 2.3.2.8. To identify DAergic neurons in this mixed culture system during live cell imaging, VM neurons were prepared from a mouse line that expresses EGFP under the control of the TH promoter (Matsushita et al., 2002; Sawamoto et al., 2001), resulting in EGFP-positive DAergic neurons. To study evoked DA release in this system, 3 consecutive treatments were used for each coverslip once during experimentation. In the brain, the greatest increases in extracellular DA release arise from burst firing at 15 – 30 Hz frequency (Floresco et al., 2003; Grace and Bunney, 1984b). To induce the secretion of large amounts of DA through burst activity, electrical field stimulation, which induces action potentials (Ryan et al., 1997) was applied first at 20 Hz for 200 pulses. Then, neurons were then treated with 90 mM extracellular KCl to cause strong neuronal depolarization and even greater release of DA. This treatment also served as a control for DAergic neuronal viability. If KCl failed to induce a nanosensor response, then it was decided that the culture being imaged was not viable since it did not exhibit evoked DA release, and that experiment was then excluded from data analysis. Finally, 100 µM DA was applied to confirm the functionality of nanosensors in the imaging field and to allow compensation of nanosensor batch-to-batch variations through normalization (for details, see section 2.4.2.6.2).

During neuronal depolarization, two phenomena were observed: (i) stimulation caused brief (generally ~400 ms long), localized increases in AndromeDA fluorescence, mostly adjacent to EGFP positive varicosities (Figure 15a, “hotspot”) and (ii) widespread, sustained activation of AndromeDA throughout the ECS (Figure 15a, “diffusion"). DA is stored at very high concentrations in SVs in varicosities formed along the axons and is secreted into the ECS through volume transmission (Sulzer et al., 2016). I therefore

hypothesized that phenomenon (i) describes the detection of DA release from a single varicosity that causes a localized, high DA concentration gradient that rapidly disappears as the secreted DA diffuses from the release site into the surrounding ECS. DA accumulation in the ECS results in the gradual activation of sensors within the entire imaging field, observed as phenomenon (ii). For methodological validation of the AndromeDA technique using negative controls without neurons (Figure 15b and c), as well as pharmacological treatments (Figure 16, Figure 17), I therefore choose to measure mean fluorescence intensities within 2 µm diameter around EGFP positive varicosities (section 2.4.2.6.3). This ROI analysis reflects the summed DA release from local varicosities, providing a measure of stimulation-evoked DA release and diffusion. Local, brief activation of AndromeDA at varicosities, representing discrete release sites and further termed “hotspots” were analyzed separately (section 3.2.2) using an alternative, artificial intelligence (AI)-based detection strategy (2.4.2.6.3).

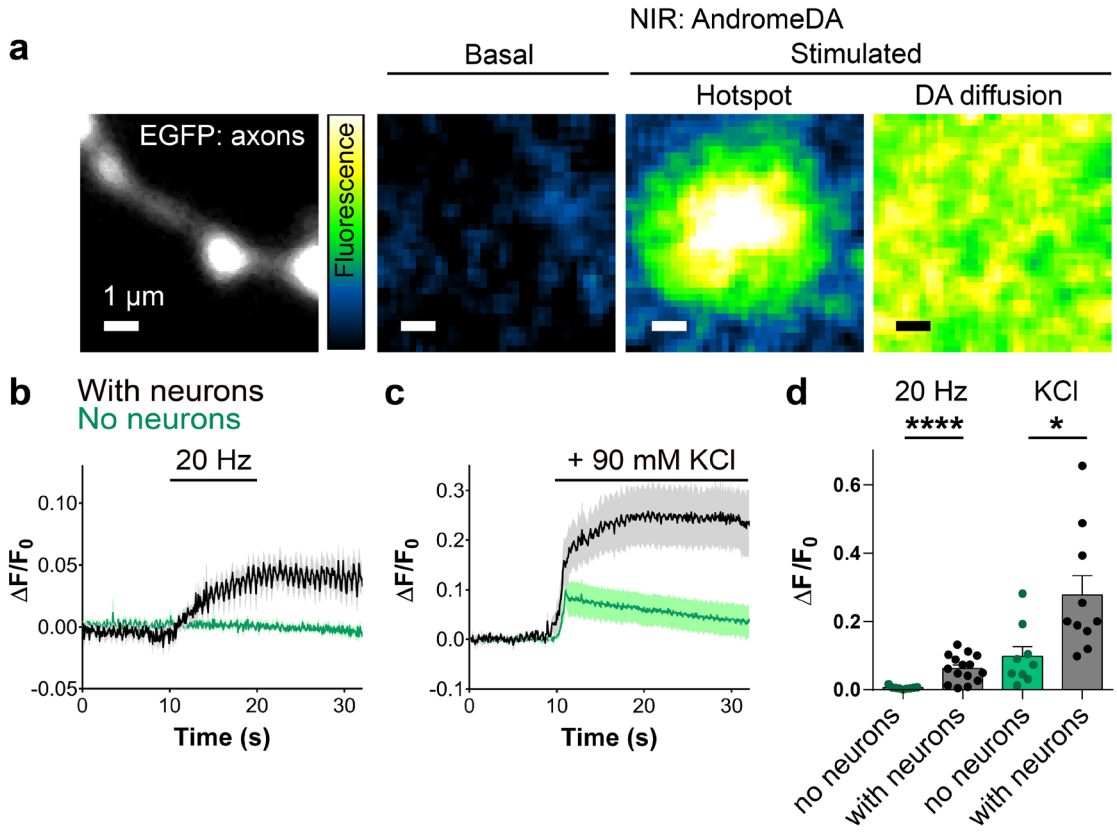

Figure 15: AndromeDA imaging of DA secreted from neurons.
a, Images showing an EGFP expressing varicosity (left panel) and 3 consecutive, normalized NIR images (right panels), illustrating AndromeDA fluorescence levels before (basal) and after neuron stimulation (stimulated). Upon neurons stimulation, AndromeDA activation is either localized (hotspot) or widespread (diffusion). Scale bar = 1 µm. **b,** Average AndromeDA activation from electrically stimulated samples at 20 Hz, either with neurons (black) or without neurons (green). **c**, Average normalized AndromeDA fluorescence over time of experiments treated with 90 mM KCl, either with neurons (black) or without neurons (green). **d**, Quantification of the peak fluorescence for each condition. * indicates $p < 0.05$, **** indicates $p < 0.0001$. 20 Hz data were compared using the Mann-Whitney test and KCl data were compared using a two-tailed Welch’s t-test. *n* = 15 for 20 Hz with neurons, *n* = 9 for 20 Hz without neurons, *n* = 10 for KCl with neurons, *n* = 9 for KCl without neurons. Data is presented as mean ± SEM

To determine whether the depolarizing stimuli themselves had an impact on AndromeDA fluorescence, independently of DA release, AndromeDA fluorescence was imaged over time during electrical or KCl stimulation in the absence of neurons, and then compared to AndromeDA fluorescence responses when DAergic neurons were present. In the absence of neurons, electrical stimulation did not evoke a nanosensor fluorescence change (Figure 15a). In contrast, the application of KCl caused a modest (~10%) increase in AndromeDA fluorescence (Figure 15b), presumably by altering the ionic environment around the nanosensors (Cognet et al., 2007). The activation of AndromeDA by KCl was significantly higher in the presence of DAergic neurons (~28%), corresponding to the activation of AndromeDA by evoked DA release (Figure 15c).

3.2.1 Pharmacological validation of AndromeDA specificity for secreted DA

I first examined whether the increased AndromeDA signal detected in cultures in response to neuronal depolarization was specifically due to secreted DA, using drugs that modulate the storage of DA in SVs, and thus alter the amount of evoked DA released. I therefore examined AndromeDA activation after first treating neuronal cultures with reserpine or L-DOPA. Reserpine inhibits the sequestration of DA into SVs by the transporter protein VMAT2, preventing SVs from storing DA and decreasing the amount of DA released (Kozminski et al., 1998). L-DOPA, on the contrary, is a DA precursor which increases the vesicular content of DA in DAergic boutons (Pothos et al., 1996). Normally, DA synthesis depends on the conversion of tyrosine to L-DOPA by TH, which is the rate limiting step in DA synthesis. By increasing the amount of free L-DOPA in the neuronal cytosol, the rate-limiting step in DA synthesis is circumvented. The L-DOPA is converted by Aromatic L-amino acid decarboxylase into DA, thus increasing the amount of DA stored in SVs and released upon neuronal stimulation. In summary, reserpine reduces the amount of secreted DA while L-DOPA increases the amount of secreted DA. After treatment of neurons, reserpine significantly decreased peak AndromeDA activation (~88% reduction) and KCl stimulation (~68% reduction) (Figure 16) consistent with a decrease in evoked DA release. Complementing this finding, L-DOPA significantly increased peak AndromeDA activation when neurons were depolarized (~225% increase after 20 Hz stimulation and ~101% increase after KCl addition) (Figure 17). Thus, altering the vesicular DA content correspondingly altered the AndromeDA signal. These data confirmed the specificity of AndromeDA for DA. Representative traces of single experiments can be viewed in Figure 16e and f and Figure 17e and f.

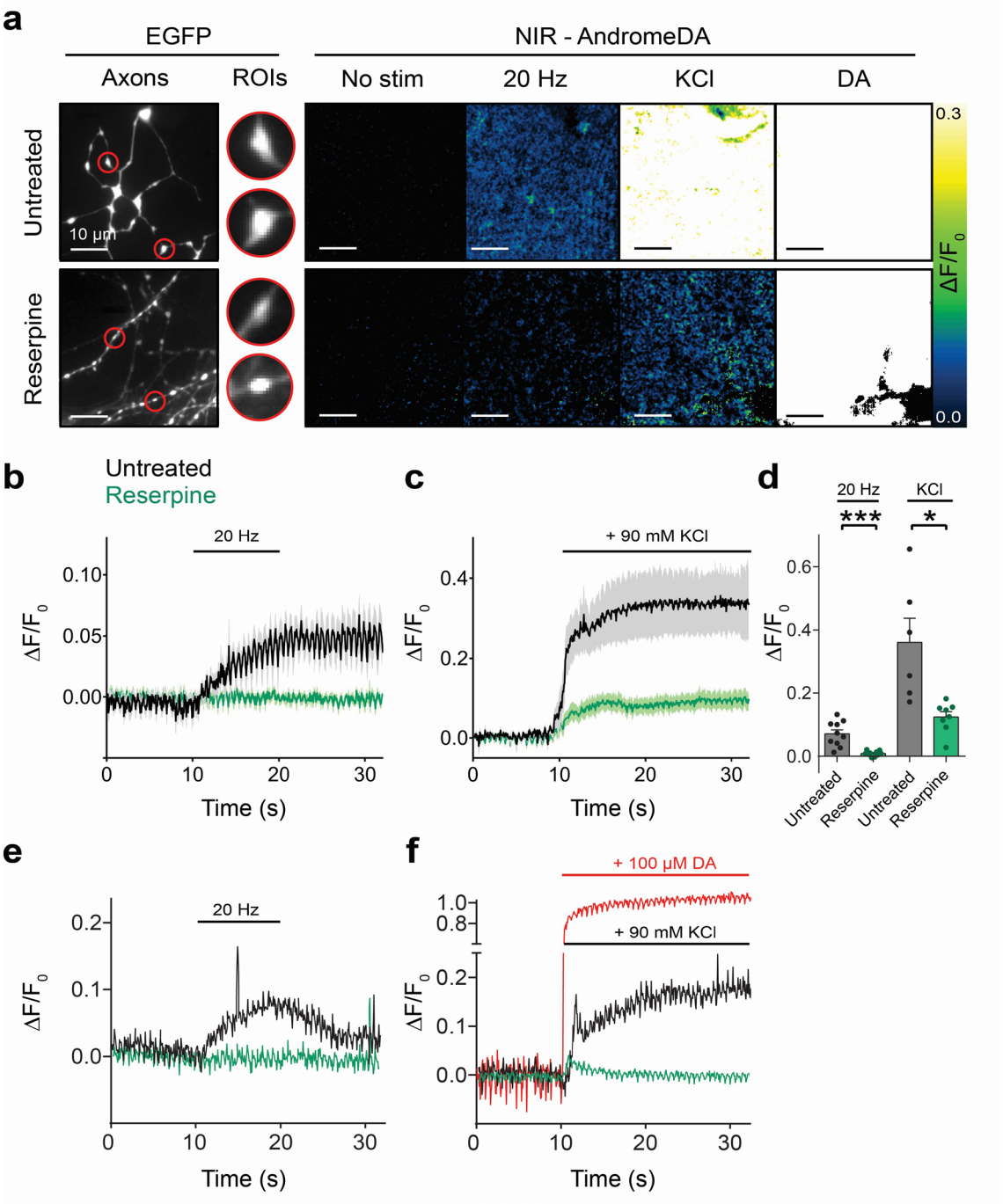

Figure 16: Pharmacological inhibition of vesicular DA uptake reduces DA release detected by AndromeDA. **a**, Normalized AndromeDA images (from left to right) prior to stimulation, during 20 Hz electrical stimulation, during 90 mM KCl stimulation, and during application of 100 µM DA reveal DA release in untreated neurons (upper panels) and neurons treated with 1 µM reserpine (lower panels). AndromeDA fluorescence was quantified at ROIs centered on EGFP-positive varicosities. **b** and **c,** Average AndromeDA fluorescence (mean ± SEM) over time from untreated neurons (black traces) and neurons treated with reserpine (green traces) during 20 Hz (b) or KCl stimulation (c). **d**, Peak fluorescence (mean ± SEM) for each stimulus method. For 20 Hz stimulation *n* = 10 experiments per condition. For KCl, *n* = 6 experiments (untreated) and 8 (reserpine). Scale bars = 10 µm. All statistical comparisons used a two-tailed Welch's t-test. * denotes $p < 0.05$ *** denotes $p < 0.001$. **e** and **f**, AndromeDA responses from a single imaging experiment in untreated neurons (black) and a single experiment in neurons treated with reserpine (green) during 20 Hz electrical field stimulation (e) 90 mM KCl stimulation (f). All data sets were normalized to the corresponding AndromeDA response to 100 µM DA (red traces in f).

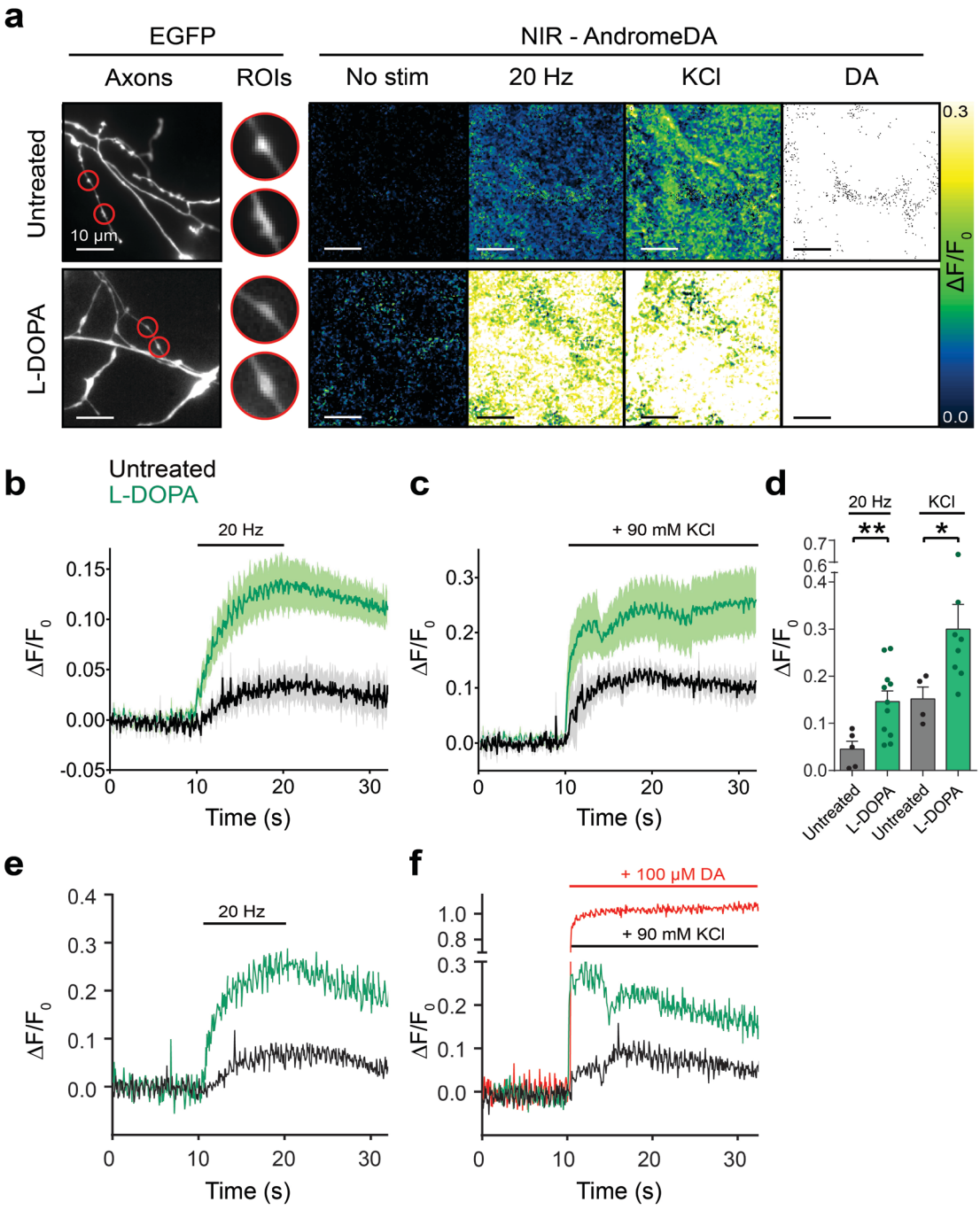

Figure 17: Pharmacological increase of vesicular DA content increases DA release detected by AndromeDA. **a**, Normalized AndromeDA images (from left to right) prior to stimulation, during 20 Hz electrical stimulation, during 90 mM KCl stimulation, and during application of 100 µM DA from untreated neurons (upper panels) and neurons treated with 100 µM L-DOPA (lower panels). AndromeDA fluorescence was quantified at ROIs centered on EGFP-positive varicosities. **b** and **c,** Average AndromeDA fluorescence (mean ± SEM) over time from untreated neurons (black traces) and neurons treated with L-DOPA (green traces) during 20 Hz (b) or KCl stimulation (c). **d**, Peak fluorescence (mean ± SEM) for each stimulus method. For 20 Hz stimulation n = 5 (untreated), 11 (L-DOPA) experiments. For KCl stimulation, n = 4 (untreated), 8 (L-DOPA) experiments. Scale bars = 10 µm. All statistical comparisons used a two-tailed Welch's t-test. * denotes $p < 0.05$, ** denotes $p < 0.01$.**e** and **f**, AndromeDA responses from a single imaging experiment in untreated neurons (black) and a single experiment in neurons treated with L-DOPA (green) during 20 Hz electrical field stimulation (e) 90 mM KCl stimulation (f). All data sets were normalized to the corresponding AndromeDA response to 100 µM DA (red traces in f).

3.2.2 Detection and validation of DA secretion “hotspots”

While AndromeDA “hotspots”, which are localized, brief increases in AndromeDA fluorescence, could be identified manually, this process was laborious, lacked sensitivity, and was potentially biased by human errors. I therefore collaborated with Dr. Ali Shaib[12] and Abed Chouaib[13] on the development of a Fiji plug-in that uses machine learning to identify AndromeDA hotspots from NIR videos, which we called the “Dopamine Recognition Tool” (DART). DART compares pixel intensities of consecutive images, detects regions of fluorescence changes above the background (hotspots), and automatically creates Fiji-compatible ROIs from the outline of these hotspots. For comparing hotspot characteristics, such as when each hotspot occurs and its fluorescence amplitude, it was crucial to quantify the fluorescence change corresponding specifically to each hotspot. In most cases, this was difficult because the activation of nanosensors in the entire imaging field (e.g. the area in Figure 18a and b), occurring due to DA release and accumulation in the ECS, obscured the brief, transient fluorescence changes of single hotspots. To isolate the fluorescence change of specific hotspots, the mean AndromeDA response of the ECS (seen in Figure 18c),was therefore subtracted from the mean fluorescence within an identified hotspot (e.g. regions outlined in red in Figure 18b) to create time traces of individual hotspots (e. g. shown in the right panels of Figure 18b). This corrected for the activation of AndromeDA by diffusing DA from other nearby release sites.

Figure 18a shows an exemplary imaging field containing ~90 EGFP positive varicosities. 49 hotspots were observed in the corresponding NIR image sequence from this experiment. Five representative varicosities with electrically evoked hotspots (numbered 1-5) and one region without a hotspot are highlighted with white boxes, shown magnified along with the corresponding NIR image of the hotspot in Figure 18b. The red boundaries drawn in the bottom right panels in Figure 18b show the DART-defined ROIs that outline the hotspots. Quantification of the AndromeDA signals within these regions resulted in fluorescent hotspots traces over time shown in Figure 18c. If specific regions around varicosities (such as region 6) did not show fluorescence peaks, it meant that the fluorescence within these regions was identical to the steady fluorescence increase of the ECS, with no contribution from detectable DA release events.

[12] Max Planck Institute of Experimental Medicine, Göttingen
[13] Center for Integrative Physiology and Molecular Medicine, Homburg

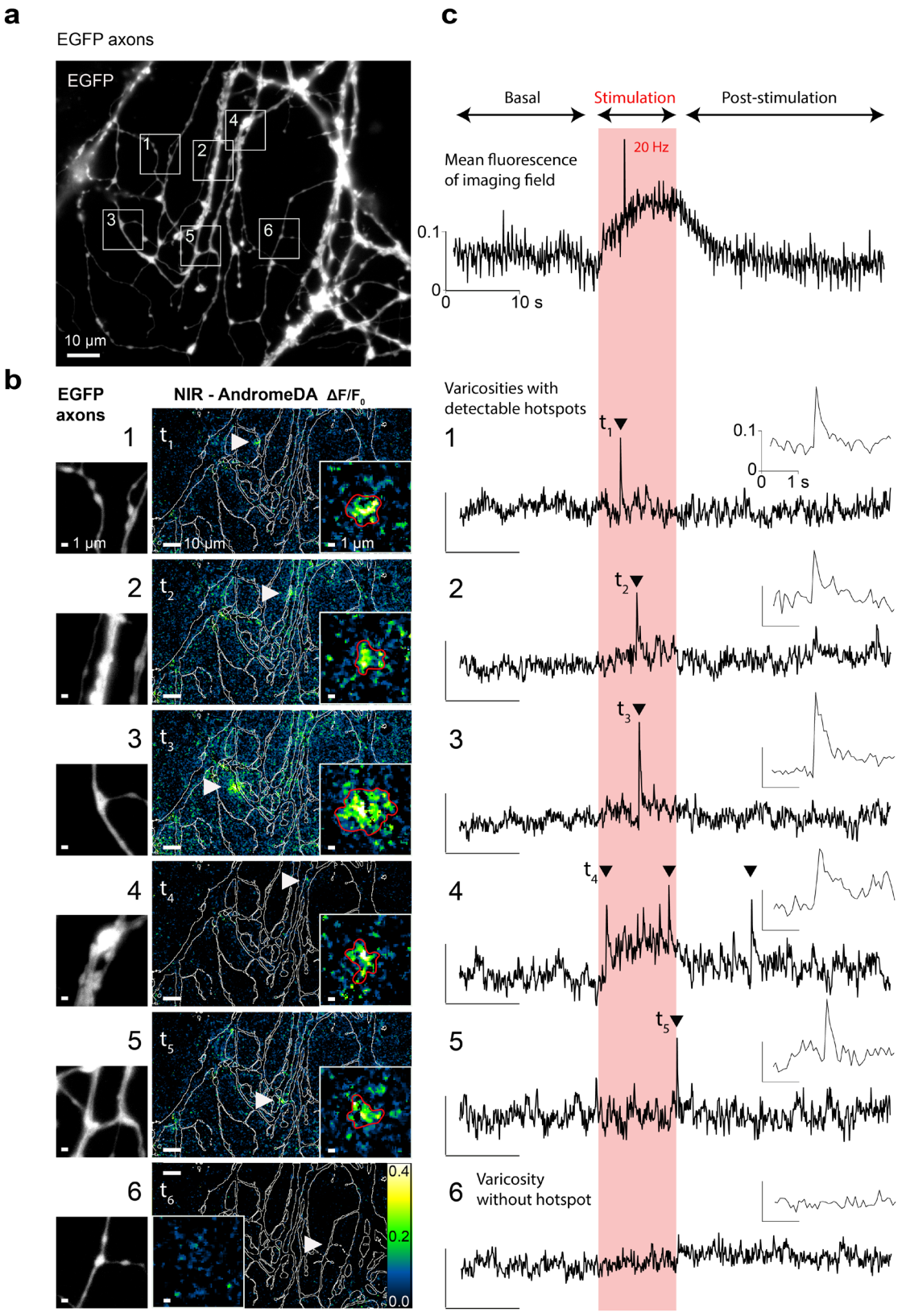
a
EGFP axons
EGFP
1
2
3
4
5
6
10 µm
b
EGFP axons
NIR - AndromeDA ΔF/F0
1
2
3
4
5
6
t1
t2
t3
t4
t5
t6
1 µm
10 µm
1 µm
0.4
0.2
0.0
c
Basal
Stimulation
Post-stimulation
20 Hz
Mean fluorescence of imaging field
0.1
0
0
10 s
Varicosities with detectable hotspots
0.1
0
0 1 s
Varicosity without hotspot

Figure 18: Electrically evoked hotspots of DA release at distinct varicosities.
a, Field of view showing EGFP-positive DAergic axons. Five exemplary regions that show adjacent hotspots of AndromeDA fluorescence during 20 Hz electrical field stimulation (white boxes, regions 1-5) and one varicosity without hotspot (region 6) are highlighted. **b**, Magnified images of EGFP-positive axonal varicosities (left panels, scale bar = 1 µm). Middle panels show the normalized AndromeDA NIR response ($\Delta F/F_0$) at the time point of the onset (t1 to t5) of the indicated hotspot (white arrowheads, scale bar = 10 µm). The outline of the EGFP-positive axon is overlaid in white, illustrating the position of the hotspot in relation to the axon. A magnified view of the hotspot is shown in the right corner of the middle panel, (scale bar = 1 µm). Region 6 shows a representative region without detectable hotspot. **c**, The uppermost trace shows the mean pixel intensity over time for the whole ECS. Subsequent panels show mean pixel intensities within single hotspot ROIs. Regions 1-5 contain hotspots and region 6 shows a varicosity without a hotspot. The 20 Hz electrical stimulation window is highlighted in pink. Arrowheads indicate fluorescence intensity peaks of hotspots. In c, the *y*-axis represents hotspot fluorescence and *x*-axis represents time. Hotspot fluorescence traces were generated by subtracting the signal of ECS ($\Delta F/F_0$) from the mean signal within the hotspots ROI ($\Delta F/F_0$) to highlight AndromeDA activation due to local DA release above overall DA diffusion.

Hotspot peaks (marked by black arrowheads) were generally brief in duration and appeared mostly within the stimulation window (Figure 18c, highlighted in pink). While most varicosities exhibited a single hotspot during imaging, some exhibited multiple hotspots (Figure 18c, region 4).

DA release is evoked by neuronal depolarization and occurs from SVs, which cluster at varicosities. Therefore, I hypothesized that if AndromeDA hotspots are truly representative of discrete DA release events, they should be observed primarily close to varicosities and occur primarily during the period of neuronal depolarization. To investigate this hypothesis, I analyzed the timepoint at which the maximum amplitude of each hotspot peak was observed, as well as the proximity of each hotspot to the nearest EGFP-positive varicosity. In this analysis I used image sequences from untreated and L-DOPA treated cultures acquired during the experiments described in section 3.2.1.

Regarding when the hotspots occurred during imaging, ~89% detected hotspots occurred during the period of electrical stimulation in L-DOPA treated samples (Figure 19 a-b, green dots) and ~78% in samples without L-DOPA pre-treatment (black dots). In both L-DOPA treated and untreated samples, the number of hotspots observed during electrical stimulation was significantly greater than the number of hotspots observed outside of the period of electrical field stimulation (Figure 19c), indicating a temporal association between exogenous electrical stimulation and hotspot occurrence. In experiments using KCl depolarization, 90 mM KCl was added to the samples and remained in the imaging chamber until the end of the experiment. Of all 173 hotspots observed in KCl experiments, only one hotspot occurred before KCl application (Figure 19d and e), further indicating that hotspots were associated with exogenous neuronal stimulation.

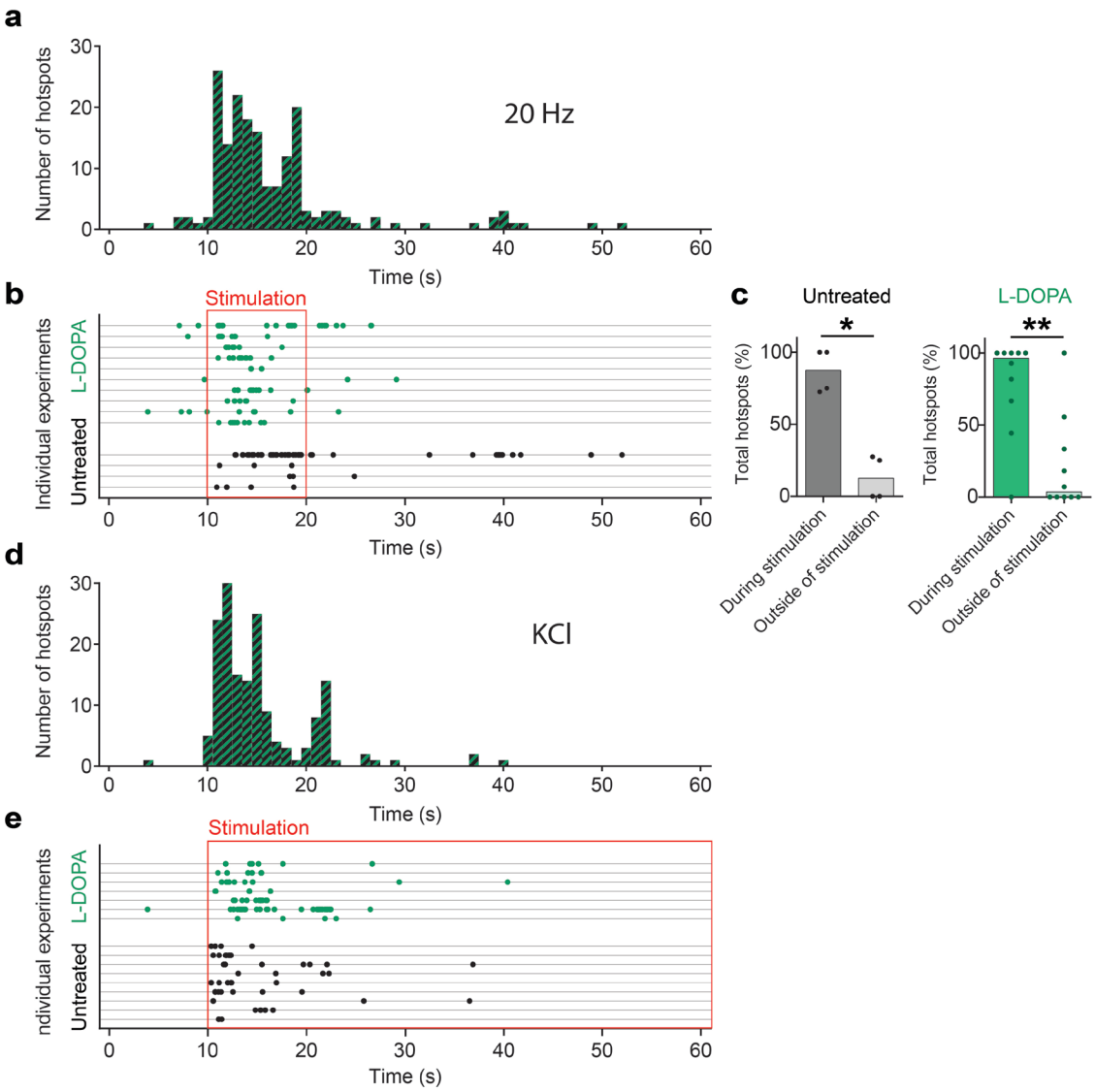

Figure 19: Hotspots are evoked by neuronal depolarization.
The time points at which hotspots occur in untreated (black dots) and L-DOPA treated (green dots) neurons are shown. **a**, Frequency distribution of all hotspots observed during 20 Hz electrical field stimulation. **b**, Onset of single electrically evoked hotspots, grouped by the experiments in which they were observed (arranged in lines along the *y*-axis). 20 Hz electrical field stimulation from 10 s to 20 s is highlighted (red). **c**, Hotspots occur preferentially during electrical stimulation. **d**, Frequency distribution of all hotspots observed during KCl stimulation. **e**, Onset of single KCl evoked hotspots, grouped by the experiments in which they were observed (arranged in lines along the *y*-axis). 90 mM KCl is applied at 10 s and remains in the samples until the end of the experiment. In b and e, dots represent individual hotspots. In c, dots represent percentage of total hotspots per experiment and bars represent median of all experiments. Data represents 68 hotspots from n = 4 (untreated) and 110 hotspots from n = 10 (L-DOPA) 20 Hz experiments, as well as 73 hotspots from n = 9 (untreated) and 100 hotspots from n = 7 experiments (L-DOPA) in KCl experiments. Data were tested for normality with the Shapiro-Wilk test and compared using the two-tailed Mann-Whitney test. * denotes $p < 0.05$, ** denotes $p < 0.01$, *** denotes $p < 0.001$.

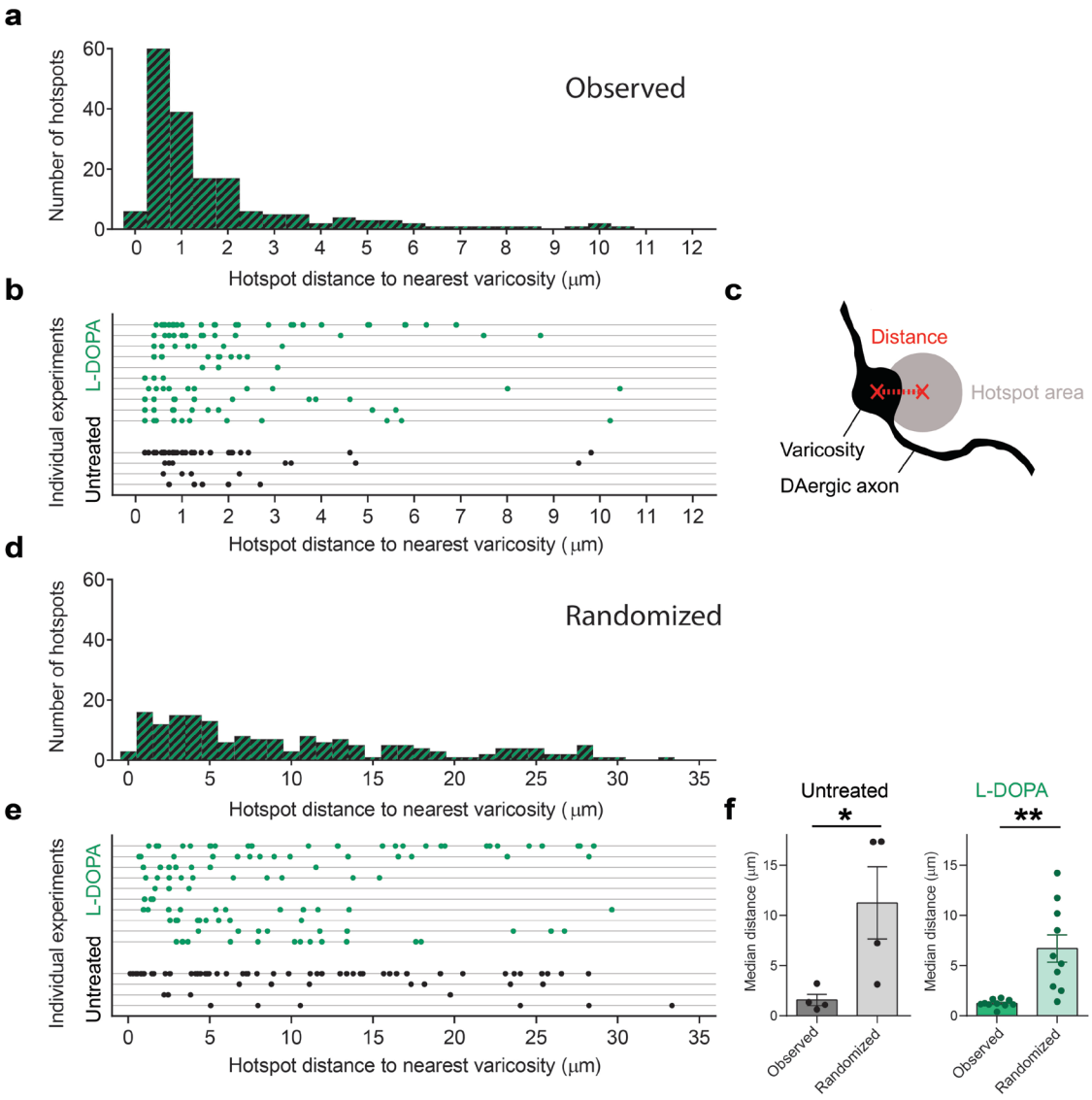

Figure 20: Electrically evoked hotspots are spatially associated with DAergic varicosities.
The spatial association of observed hotspots with potential DA release sites was quantified from 20 Hz stimulated neurons by measuring the distance of the hotspot centers to the center of the nearest varicosity. Hotspot-varicosity distances are shown for untreated (black dots) and L-DOPA treated neurons (green dots). **a**, Frequency distribution of all hotspots observed in experiments with 20 Hz electrical field stimulation. **b**, Measured distances of single electrically evoked hotspots, grouped by the experiments in which they were observed (arranged in lines along the *y*-axis). **c**, Schematic illustrating how "distance" was defined. **d**, Randomized controls were generated by measuring distances from hotspots with non-corresponding images of DAergic axons. The graph shows the frequency distribution of randomized controls. **e**, Hotspot-varicosity distances of single hotspots from randomized control measurements, grouped by the experiments in which they were observed (arranged in lines along the *y*-axis). **f**, Varicosity-hotspot distance was larger when non-corresponding EGFP images were used (randomized). In b and e, dots represent individual hotspots. In f, dots represent single experiments and bars represent means ± SEM of all experiments. In d and e, one data point was not displayed for better visibility (L-DOPA hotspot, distance = 54.3 µm). Data represents 68 hotspots from n = 4 (untreated) and 110 hotspots from n = 10 (L-DOPA) experiments. Data were tested for normality with the Shapiro-Wilk test and compared using the two-tailed Welch's t-test. * denotes $p < 0.05$, ** denotes $p < 0.01$, *** denotes $p < 0.001$.

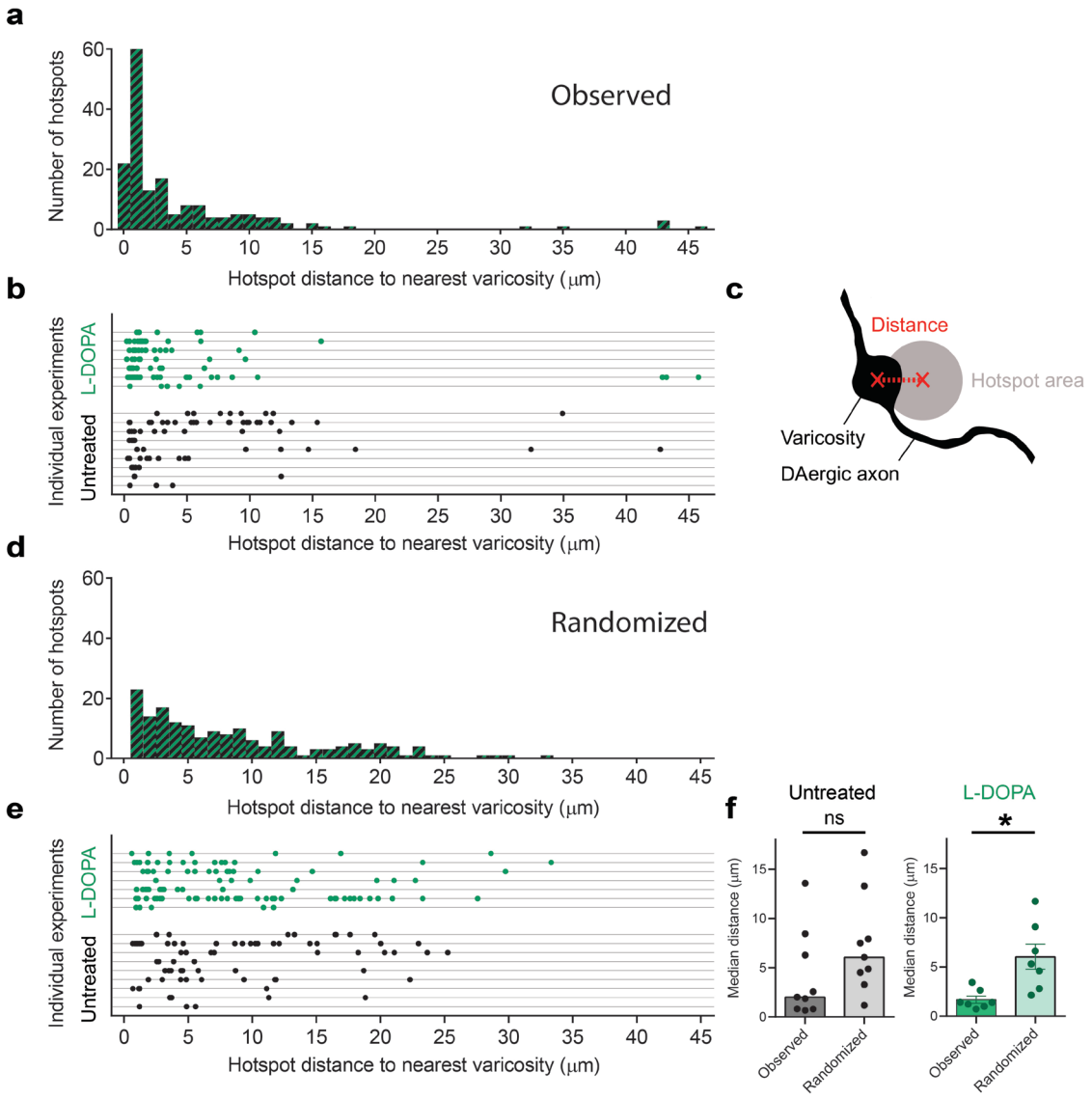

Figure 21: KCl evoked hotspots are spatially associated with DAergic varicosities.
The spatial association of observed hotspots with potential DA release sites was quantified from KCl stimulated neurons by measuring the distance of the hotspots centers to the center of the nearest varicosity. Hotspots-varicosity distances are shown for untreated (black dots) and L-DOPA treated neurons (green dots). **a**, Frequency distribution of all hotspots observed during in experiments with KCl application. **b**, Measured distances of single KCl evoked hotspots, grouped by the experiments in which they were observed (arranged in lines along the *y*-axis). **c**, Schematic illustrating how "distance" was defined. **d**, Randomized controls were generated by measuring distances from hotspots with non-corresponding images of DAergic axons. The graph shows the frequency distribution of randomized controls. **e**, Hotspot-varicosity distances of single hotspots from randomized control measurements, grouped by the experiments in which they were observed (arranged in lines along the *y*-axis). **f**, Varicosity-hotspot distance was larger in L-DOPA treated cultures when non-corresponding EGFP images were used (randomized). In b and e, dots represent individual hotspots. In f, dots represent single experiments and bars represent medians (left panel) or means ± SEM (right panel) of all experiments. Data represents 73 hotspots from $n = 9$ (untreated) and 100 hotspots from $n = 7$ (L-DOPA) experiments. Data were tested for normality with the Shapiro-Wilk test and compared using the Mann-Whitney test (left panel) or two-tailed Welch's t-test (right panel). * denotes $p < 0.05$, ns = not significant.

To investigate if hotspots were spatially associated with EGFP positive varicosities, I measured the distance from the hotspot centers to the center of the nearest varicosity identified in the corresponding EGFP image (Figure 20 and Figure 21). In experiments using electrical stimulation, the median hotspot-varicosity distance was ~1.2 µm for neurons that were pre-treated with L-DOPA (Figure 20a and b, green dots) and ~0.8 µm for neurons without L-DOPA pretreatment (Figure 20a and b, black dots). Experiments using KCl depolarization showed a median hotspot-varicosity distance of ~1.2 µm for neurons that were pre-treated with L-DOPA (Figure 21a and b, green dots) and ~3.8 µm for neurons without L-DOPA pretreatment (Figure 21a and b, black dots) Figure 21). For both stimulation paradigms, hotspot-varicosity distance measurements of hotspots ROIs using non-corresponding NIR and EGFP images served as randomized negative control (Figure 20d and e, Figure 21d and e). For untreated and L-DOPA-treated electrically stimulated neurons, the hotspot-varicosity distances were significantly larger in randomized control measurements than with corresponding NIR and EGFP images (Figure 20f). Thus, hotspots evoked by electrical field stimulation exhibited a significant spatial association with EGFP positive varicosities. In neurons stimulated with KCl, the hotspot-varicosity distances were only significantly larger in randomized control measurements than with corresponding NIR and EGFP images for L-DOPA-treated neurons, and not for untreated neurons (Figure 21f, $p = 0.135$). Thus, there was no significant spatial association between KCl evoked hotspots and varicosities for untreated neurons, but with L-DOPA treatment the spatial association was significant.

3.2.3 Non-evoked hotspots are dependent on neuronal firing

Although the majority of hotspots were associated with neuronal depolarization (evoked hotspots), some hotspots were also observed without exogenous stimulation (non-evoked hotspots) (Figure 19, outside of the red box). Electrical field stimulation has been shown to cause action potential firing in cultured neurons (Ryan et al., 1997) and all experiments were performed in the presence of glutamate receptor antagonists, therefore these hotspots could not be the result of activation of DAergic neurons due to glutamatergic neuron activity in the culture. DAergic neurons exhibit intrinsic pacemaker firing of action potentials, which could result in DA release independently of exogenous stimulation. I hypothesized, that hotspots occurring in the absence of exogenous neuronal stimulation could be due either to spontaneous action potential firing of DAergic neurons, or the spontaneous, action potential-independent fusion of SVs. While such spontaneous fusion has been shown for other neurotransmitter systems, it has never previously been observed in DAergic neurons.

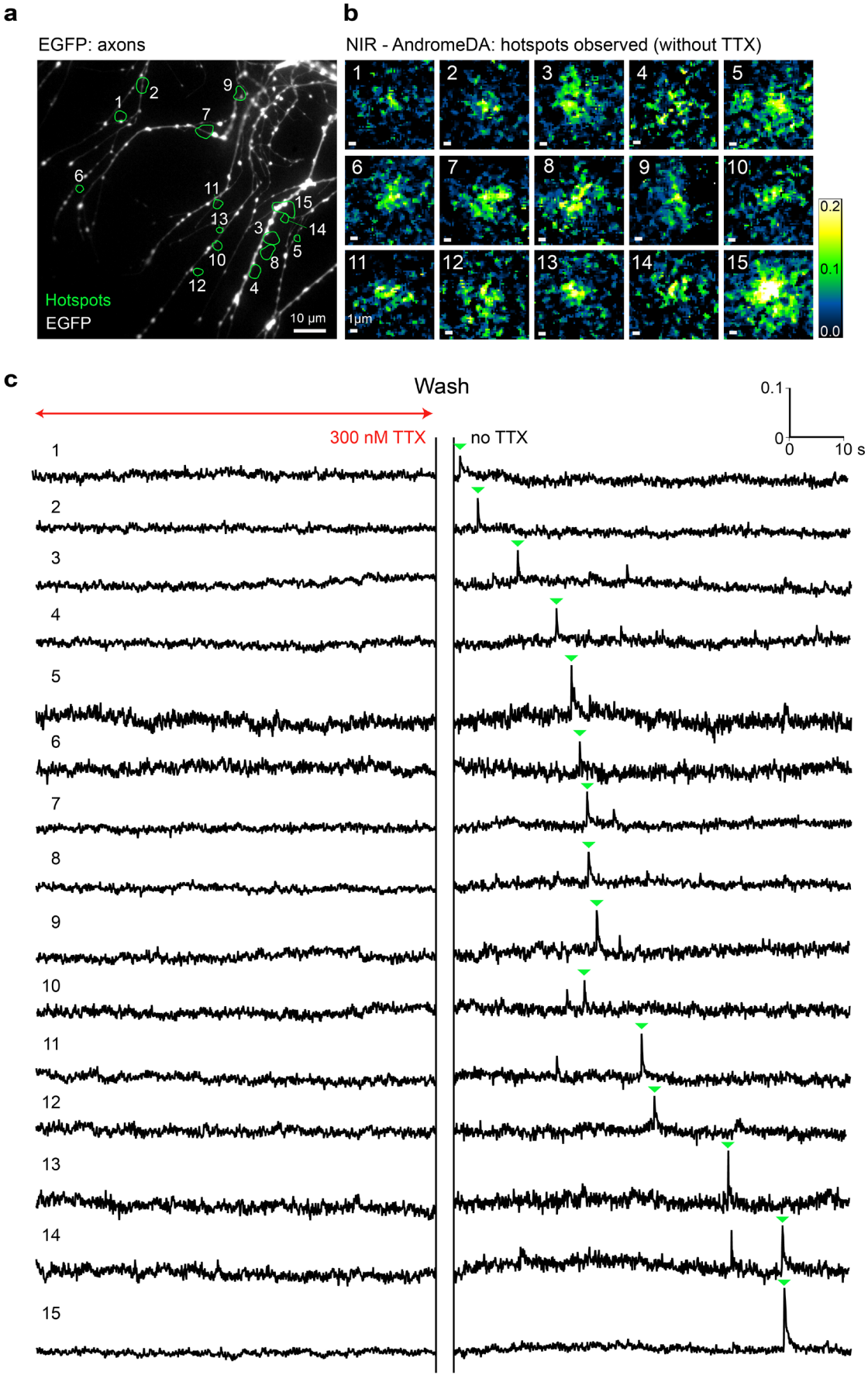
a
EGFP: axons
Hotspots
EGFP
10 µm
b
NIR - AndromeDA: hotspots observed (without TTX)
1µm
0.2
0.1
0.0
c
Wash
300 nM TTX
no TTX
0.1
0
0
10 s

Figure 22: TTX abolishes hotspots of DA release.
a, Primary neurons from the VM of TH-EGFP mice were pre-treated with L-DOPA prior to AndromeDA imaging. Neurons were imaged for 80 s in the presence of 300 nM TTX. An overview of the imaging field captured in the visible light spectrum shows EGFP-positive varicose axons of living DAergic neurons. During TTX application, no AndromeDA hotspots were observed. After TTX removal, neurons were imaged for another 80 s. After the removal of TTX, 15 hotspots were detected during imaging (green ROIs, 1-15). **b**, Magnified false-color NIR images of AndromeDA hotspots at the time point of peak hotspot fluorescence intensity. **c**, Traces show the mean pixel intensity within each hotspot ROIs over time, in the presence (left) and absence (right) of TTX. Hotspot peaks are marked with green arrowheads and correspond to the images in a and b. Scale bar in a = 10 µm, scale bar in b = 1 µm. In c, the *y*-axis represents hotspot fluorescence and *x*-axis represents time. Hotspot fluorescence traces were generated by subtracting the signal of ECS ($\Delta F/F_0$) from the mean signal within the hotspot ROIs ($\Delta F/F_0$) to highlight local DA release versus DA diffusion in the ECS.

To investigate if non-evoked hotspots were dependent on neuronal action potential firing, neurons were treated with 300 nM of the voltage-gated Na^+ channel blocker TTX and imaged without exogenous stimulation. 300 nM TTX inhibits action potential firing but does not inhibit spontaneous SV fusion (Nair et al., 2013; Rhee et al., 2019; Ripamonti et al., 2017). Neurons were treated with L-DOPA prior to these experiments to maximize the chances of detecting hotspots during TTX treatment, since hotspots are observed relatively infrequently in untreated cultures. In the presence of TTX, no hotspots were detected, as represented in (Figure 22 a-c, left traces in c). When TTX was removed by thorough washing of the coverslip, hotspots appeared during imaging of the same imaging field in the absence of stimulation (Figure 22c, right traces). Given that these hotspots were only observed in the absence of TTX, I conclude that the hotspots were the result of spontaneous action potential firing of the DAergic neurons. Further, while spontaneous SV fusion may still occur in DAergic neurons, I find no evidence that this phenomenon contributes to hotspots in my experiments.

Having imaged the neurons in the presence and absence of TTX, the neurons were then stimulated electrically and chemically as in previous experiments. The average AndromeDA signal around varicosities in these experiments (Figure 23a) was similar to previous experiments in which neurons were never been exposed to TTX. These data indicate that TTX did not have any toxic or lasting effect on the neurons after it was

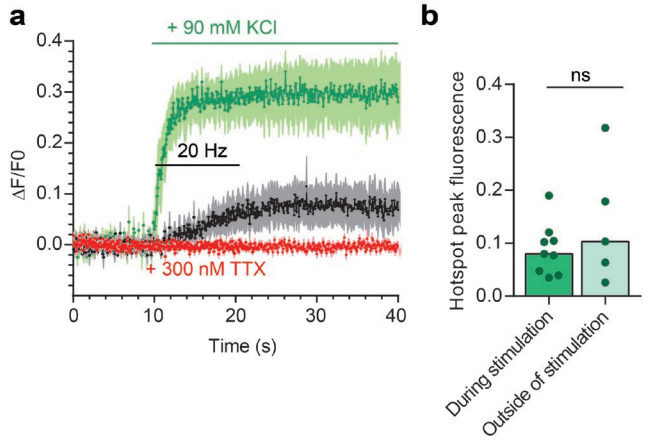

Figure 23: Assessment of TTX toxicity and comparison of evoked and non-evoked hotspots.
a, L-DOPA treated neurons were subjected to AndromeDA imaging for 80 s in the presence of 300 nM TTX (red trace). After washout of TTX, neurons were depolarized first by 20 Hz electrical field stimulation (black trace), and then 90 mM KCl (green trace). Graphs show average NIR fluorescence over time (mean ± SEM), quantified within ROIs of 2 µm radius drawn around all varicosities in the imaging field. *n* = 7 experiments. **b**, Non-evoked and evoked hotspots were quantitatively similar in experiments using L-DOPA and electrical stimulation.

washed out. Finally, I compared the peak intensities of hotspots observed during (evoked) and outside (non-evoked) the electrical stimulation period. No difference in the peak intensities of evoked and non-evoked hotspots were observed (Figure 23b), indicating that the hotspots, and thus the DA release events, we similar for evoked and non-evoked hotspots.

In summary, the occurrence of hotspots was temporally associated with exogenous neuronal stimulation and spatially associated with EGFP positive varicosities in general. These data are, along with the abolition of hotspots by 300 nM TTX, consistent with hotspots being caused by DA secretion from DAergic varicosities triggered by action potential firing.

3.2.4 Properties of individual AndromeDA hotspots

Previous studies using exocytosis assays to examine DA release at single boutons found considerable functional heterogeneity across individual varicosities, including variations in the relative probability of release (Daniel et al., 2009; Pan and Ryan, 2012) and the observation of silent varicosities that do not undergo secretion despite containing DAergic vesicle clusters (Daniel et al., 2009; Pereira et al., 2016). While these assays provide an indirect assessment of DA secretion, AndromeDA, in contrast, allows for the direct detection of DA secretion events which are not confounded by possible co-release of other neurotransmitters from the same neurons. To investigate, if AndromeDA hotspots were heterogenous, consistent with previous assessments of DA secretion, and to compare the relative amounts of DA released from individual varicosities, I analyzed the size of the surface area that was covered during the occurrence of individual hotspots, as well as their maximum peak intensity. Additionally, I analyzed the percentage of varicosities that exhibited adjacent AndromeDA hotspots and also compared the hotspots evoked by different type of stimuli. The hotspot peak fluorescence was derived from normalized and corrected fluorescence traces as shown in Figure 18. For regions that showed multiple peaks (Figure 18 region 4), the highest hotspot peak was taken as the maximum. The hotspot area was defined as the area enclosed by the ROI that was generated by DART during hotspot detection.

For both untreated and L-DOPA-treated neurons, the peak intensities and areas of hotspots were highly heterogeneous, varying both between separate experiments and within a single experiment, indicating that individual release events varied considerably across populations of varicosities (Figure 24). Maximum peak intensities of single

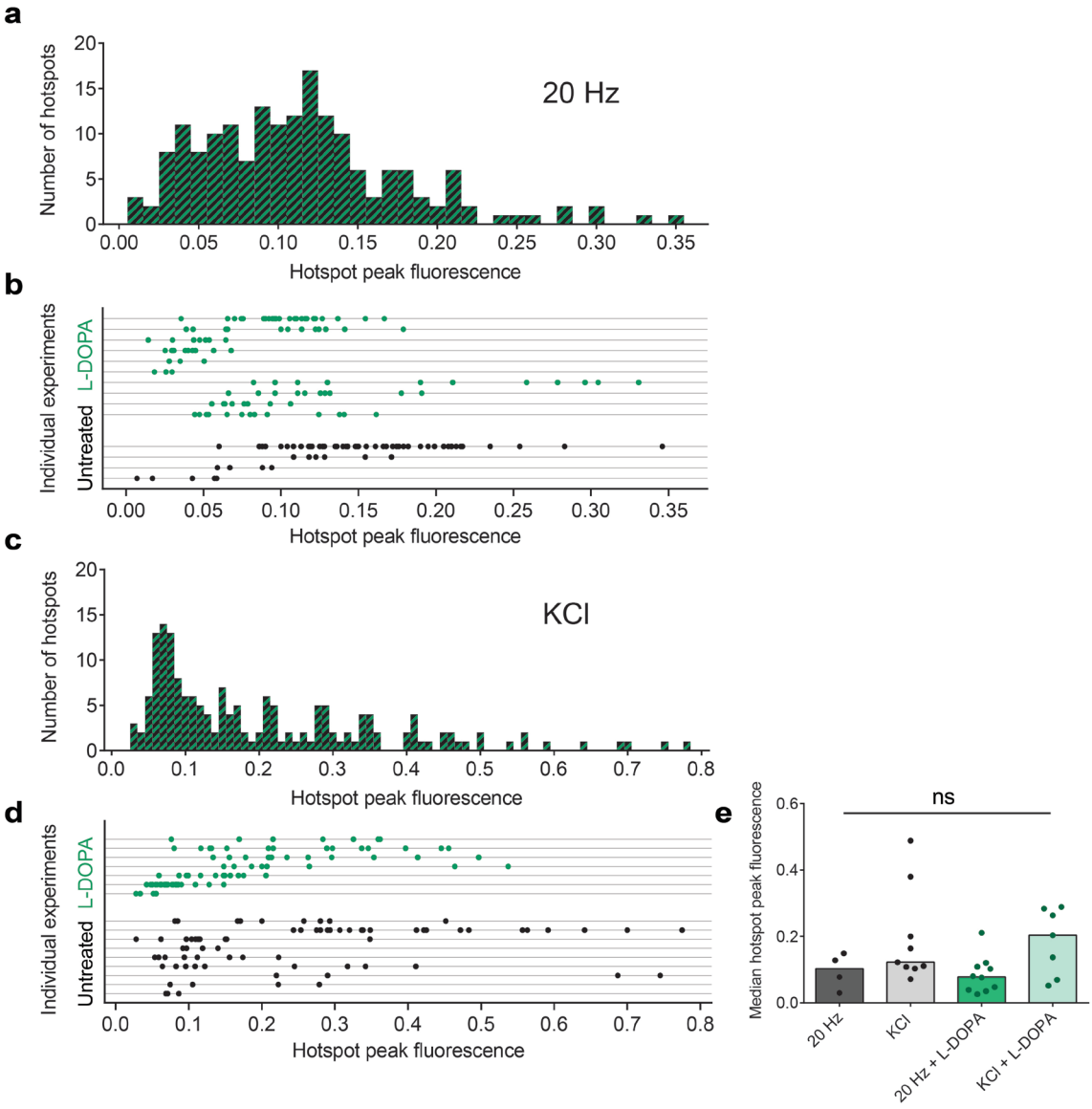

Figure 24: Heterogeneity of hotspot peak fluorescence.
Maximum fluorescence amplitudes of hotspots in untreated (black dots) and L-DOPA treated (green dots) neurons are shown. **a,** Frequency distribution of measured amplitudes from all hotspots observed during 20 Hz electrical field stimulation. **b**, Amplitudes of single electrically evoked hotspots, grouped by the experiments in which they were observed (arranged in lines along the *y*-axis). **c**, Frequency distribution of measured amplitudes from all hotspots observed during KCl stimulation. **d**, Amplitudes of single KCl evoked hotspots, grouped by the experiments in which they were observed (arranged in lines along the *y*-axis). **e**, Type of stimulus and L-DOPA pre-treatment does not affect the peak fluorescence of hotspots. In b and d, dots represent individual hotspots. In e, dots represent single experiments and bars represent median of all experiments. In d, one data point was not displayed for better visibility (L-DOPA hotspot, peak fluorescence = 1.26). Data represents 68 hotspots from *n* = 4 (untreated) and 110 hotspots from *n* = 10 (L-DOPA) 20 Hz experiments, as well as 73 hotspots from *n* = 9 (untreated) and 100 hotspots from *n* = 7 experiments (L-DOPA) in KCl experiments. Data were tested for normality with the Shapiro-Wilk test and compared using the two-tailed Mann-Whitney test. ns = not significant.

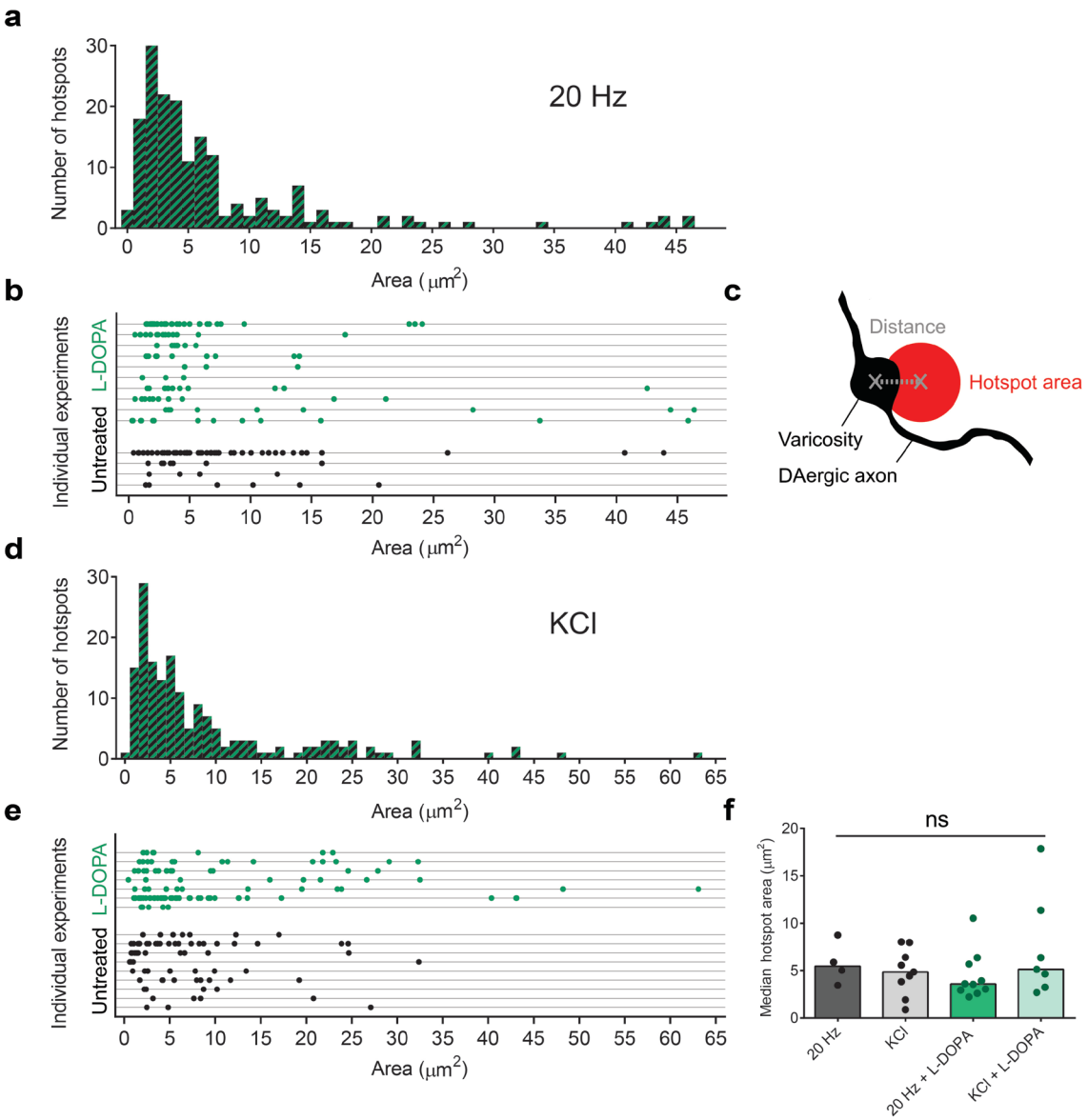

Figure 25: Heterogeneity of hotspot areas.
The area of activated AndromeDA on the coverslip at single hotspots in untreated (black dots) and L-DOPA treated (green dots) neurons are shown. **a**, Frequency distribution of measured areas from all hotspots observed in experiments using 20 Hz electrical field stimulation. **b**, Hotspot areas of single electrically evoked hotspots, grouped by the experiments in which they were observed (arranged in lines along the *y*-axis). **c**, Scheme illustrating how "hotspot area" is defined. **d**, Frequency distribution of measured areas from all hotspots observed in KCl experiments. **e**, Hotspot areas of single KCl evoked hotspots, grouped by the experiments in which they were observed (arranged in lines along the *y*-axis). **f**, Type of stimulus and L-DOPA pre-treatment does not affect the area of AndromeDA that is activated by one hotspot. In b and e, dots represent individual hotspots. In f, dots represent single experiments and bars represent median of all experiments. Data represents 68 hotspots from $n = 4$ (untreated) and 110 hotspots from $n = 10$ (L-DOPA) 20 Hz experiments, as well as 73 hotspots from $n = 9$ (untreated) and 100 hotspots from $n = 7$ experiments (L-DOPA) in KCl experiments. Data were tested for normality with the Shapiro-Wilk test and compared using the two-tailed Mann-Whitney test. ns = not significant.

hotspots were scattered between 0.007 – 0.35 (Figure 24a and b) in experiments using electrical stimulation, and between 0.03 – 0.78 when KCl was used for depolarization (Figure 24c and d).

The area of the hotspots was also heterogeneous, ranging from ~0.28 - ~46 µm^2 from electrically stimulated neurons (Figure 25a and b), and ~0.45 - ~65 µm^2 in KCl depolarized samples. Electrically stimulated samples showed median hotspot areas of ~5.8 µm^2, and ~3.6 µm^2 when pre-treated with L-DOPA. KCl stimulated samples showed median hotspot areas of ~5.4 µm^2 (KCl), and ~5.3 µm^2 when pre-treated with L-DOPA, respectively. Additionally, no significant difference with respect to the area or peak intensity was detected between hotspots observed under the distinct experimental conditions used in this study (Figure 24e and Figure 25f), although KCl evoked some hotspots with very large areas that were not observed in electrically stimulated neurons. These data indicate substantial heterogeneity of discrete DA release events.

Next, I examined the proportion of varicosities that exhibited closely associated hotspots upon neuron depolarization. An AndromeDA hotspot was considered to be closely associated with a DAergic varicosity, if the hotspot-varicosity distance was not larger than 3 µm, which was the case for ~86% of all hotspots. While this data indicated that most hotspots were close to varicosities, it raised the question of the origin of the remaining hotspots, which were relatively distant from any visible varicosities. I propose that the remaining hotspots are the result of DA release from EGFP-negative DAergic neurons, which comprised ~30% of all TH-positive neurons (Figure 10) (Lammel et al., 2015).

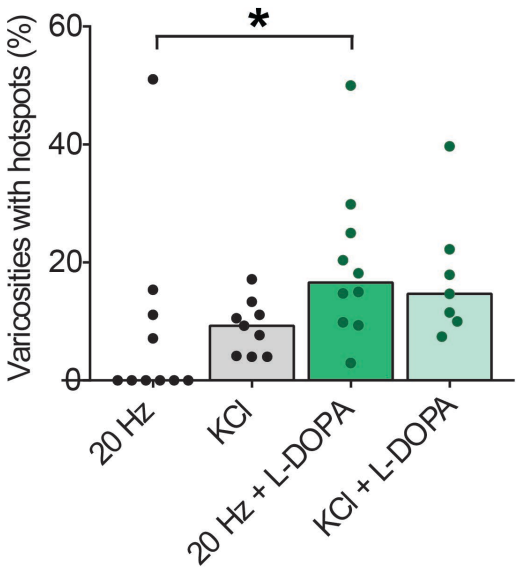

Figure 26: Percentage of varicosities exhibiting hotspots. Neurons (untreated = black dots, L-DOPA treated = green dots) were subjected to AndromeDA imaging during 20 Hz or KCl depolarization. Hotspots were detected with DART and assigned to varicosities if observed within 3 µm of the varicosity. All varicosities within the imaging field were counted and the percentage of varicosities with an assigned hotspot was calculated ("active" varicosities). L-DOPA increases the incidence of hotspots in electrically stimulated neurons. Dots represent individual coverslips and bars represent medians of all experiments. Data were tested for normality with the Shapiro-Wilk test and compared using the two-tailed Mann-Whitney test. * denotes $p < 0.05$

In untreated neurons, hotspots were relatively infrequent, observed in only 25% of all experiments, and only 13% of all varicosities had a closely associated (< 3 µm) hotspot on average. L-DOPA treatment significantly increased the incidence of hotspots, with hotspots observed in all experiments and adjacent to 17% of all varicosities (Figure 26, 20 Hz). In experiments using KCl stimulation, closely associated hotspots were observed at 9% of varicosities in untreated neurons and 15% of varicosities in L-DOPA treated neurons.

Overall, the majority of DAergic varicosities did not exhibit detectable hotspots. These data are highly consistent with the previously proposed phenomenon of “silent” DAergic varicosities. However, it cannot be ruled out that DA release from silent varicosities was simply below the detection limit of AndromeDA or was obscured by DA diffusion from nearby release sites.

Since neurons were subjected first to electrical and then to KCl stimulation, I next examined whether the hotspots observed during the two stimulation paradigms corresponded in space. This would provide important data on the activity of DA release sites under different conditions. Hotspots evoked by electrical stimulation and KCl were spatially compared by overlapping the hotspot ROIs as defined by DART from each stimulation condition on top of the outline of the corresponding EGFP-positive axons (Figure 27a). Given that whether a varicosity is capable of secreting DA (“active varicosity”) or not (“silent” varicosity) is likely to be determined by the underlying molecular composition (Banerjee et al., 2020a; Daniel et al., 2009), I hypothesized that varicosities that exhibit hotspots under electrical stimulation would also exhibit hotspots when subjected to KCl treatment. Surprisingly, these hotspots rarely corresponded in space. Only 4.2% of all hotspots evoked during the two separate experimental paradigms originated at the same location (Figure 27b), and the overlapping hotspot area of KCl induced and electrically induced hotspots was only 2% across all hotspots (Figure 27c). These findings indicate, that electrical stimulation and KCl induced stimulation cause the secretion of DA from distinct release sites.

In summary, AndromeDA hotspots were diverse with respect to their area, timing and peak fluorescence, and occurred only at a small fraction of DAergic varicosities.

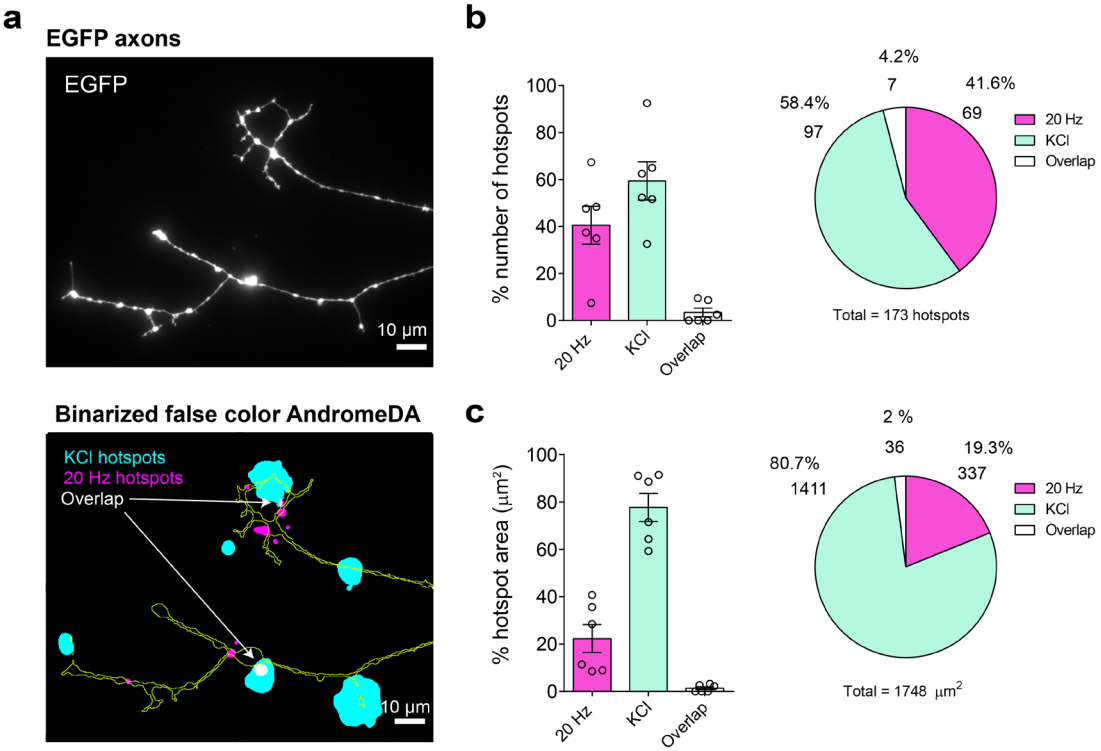

Figure 27: Electrical and KCl stimulation evoke DA release from distinct axonal locations.
a, A representative image showing EGFP-positive DAergic axons (top) which is then outlined and overlaid with color images showing the spatial location of AndromeDA hotspots (bottom) evoked either by 20 Hz electrical stimulation (magenta) or KCl stimulation (cyan). Hotspots that appeared at the same location on the coverslip during both 20 Hz and KCl stimulation appear in white (overlapping). **b**, Each hotspot was categorized as being observed either during 20 Hz stimulation only (magenta column), during KCl stimulation only (cyan column), or being observed in both 20 Hz and KCl simulation paradigms (spatial overlap as shown in a). Column charts showing the average proportions of hotspots grouped into these categories, as percentages of the total number of hotspots within one experiment (left panel). The pie chart illustrates the average proportions across all experiments (right panel). **c**, The area of activated AndromeDA by hotspots observed during 20 Hz stimulation only (magenta column), during KCl stimulation only (cyan column), or both 20 Hz and KCl simulation paradigms was calculated for each experiment (left panel). The pie chart illustrates the average proportions across all experiments (right panel). Neurons were pre-treated with L-DOPA (100 µM) prior to imaging. In column charts, circles represent single experiments, columns represent mean of all experiments, values and error bars represent ± SEM. *n* = 6 experiments. Scale bar = 10 µm.

3.3 DA release requires Munc13 priming proteins

Molecular priming of SVs by Munc13 proteins is regarded as an absolute requirement in glutamatergic and GABAergic neurotransmission. Munc13-1 and Munc13-2 deletion results in the complete loss of neurotransmitter release and SV docking (Augustin et al., 1999b; Imig et al., 2014; Varoqueaux et al., 2002). The requirement for individual Munc13 isoforms thereby varies across distinct types of synapses. In the mammalian brain, three isoforms of Munc13 are expressed, of which Munc13-1 is the most abundant isoform expressed throughout the central nervous system. Munc13-2 is abundant in the cortex, hippocampus and cerebellum, and Munc13-3 is primarily expressed in the cerebellum (Augustin et al., 2001, 1999a). In glutamatergic, hippocampal neurons Munc13-1 facilitates SV fusion competency at ~90% of synapses, while the remaining ~10% require the Munc13-2 isoform as priming factor (Rosenmund et al., 2002). Deletion of Munc13-2 alone has no effect, being fully compensated for by Munc13-1 (Augustin et al., 1999b; Varoqueaux et al., 2002). GABAergic synapses have distinct requirements for Munc13. Only the combined deletion of Munc13-1 and -2 leads to an arrest of neurotransmitter release, and the deletion of one of these isoforms alone has no effect in GABAergic synapses, due to complete redundancy of Munc13-1 and Munc13-2 in these synapses (Varoqueaux et al., 2002). Additionally, recent studies have discovered that some functionally and structurally specialized secretory structures function in the complete absence of Munc13 proteins, such as the retinal photoreceptor ribbon and cochlear hair cell ribbon synapse (Cooper et al., 2012; Vogl et al., 2015), highlighting how functional diversity is controlled by differences in molecular composition at secretory structures.

While DAergic release sites are functionally diverse, the role of Munc13 proteins, and thus the role of molecular priming, in DA secretion has not been investigated. Given the differences between DAergic and glutamatergic/GABAergic neurotransmission, it is possible that the requirement for SV priming by Munc13 proteins is reduced or absent in DAergic neurons. To examine this, I first analyzed the expression of Munc13-1, Munc13-2 and Munc13-3 by their co-immunolabeling at bassoon clusters in cultured DAergic axons, as vesicular DA release and hence SV priming are thought to occur at active zones (Daniel et al., 2009; Liu et al., 2018). I then used AndromeDA to examine if the simultaneous deletion of Munc13-1 and Munc13-2 abolishes DA release, as it does in fast neurotransmitter systems.

3.3.1 Expression analysis of Munc13 isoforms in DAergic neurons

Munc13-1 was abundant at active zones of WT DAergic axons, as defined by anti-bassoon co-immunolabeling (Figure 28 a, left panels). Neurons that lack the expression of Munc13-1 and Munc13-2 (DKO) (Figure 28 a, right panels) served as negative control for comparison and showed significantly reduced Munc13-1 immunolabeling (Figure 28 b). Because of the lack of effective antibodies for immunolabeling against Munc13-2 and Munc13-3, I used knock-in (KI) mouse lines that express Munc13-2-EYFP and Munc13-3-EGFP fusion proteins (Cooper et al., 2012). Immunolabeling showed no Munc13-2-EYFP-positive puncta in TH-positive DAergic axons (Figure 29a, left panels) and a significant reduction in quantitative immunolabeling compared to cultured hippocampal neurons (Figure 29b), that were immunolabeled and analyzed in parallel and served as a Munc13-2 positive control (Breustedt et al., 2010; Kawabe et al., 2017). Likewise, immunolabeling against Munc13-3-EGFP showed no puncta in DAergic neurons (Figure 30a, left panels) and quantitative immunolabeling was significantly lower compared to cultured cerebellar granule neurons (Figure 30b), which express Munc13-3 (Augustin et al., 2001; Ishiyama et al., 2014). These results indicate that Munc13-1 is expressed in DAergic axons at bassoon-positive active zones, and that Munc13-2 and Munc13-3, in contrast, are either absent or expressed at levels below the detection limits of my imaging.

3.3.2 Imaging of DA release from Munc13-1/2 DKO neurons using AndromeDA

To investigate the functional role of Munc13 priming proteins in DAergic neurons using AndromeDA, hippocampal-VM neurons were prepared as described in section 2.3.2.8, with the difference that VM neurons were thereby derived from E18 embryos that express EGFP under the TH promoter and lack the expression of Munc13-1 and Munc13-2 (TH-EGFP+/- Munc13-1-/- Munc13-2-/-, DKO) (section 2.3.2.7). To provide the greatest chance of reducing DA release by Munc13 KOs, both Munc13-1 and Munc13-2 were deleted. DA release from all EGFP-positive littermates prepared in parallel was examined using AndromeDA as well, regardless of their genotype. WT littermates (homozygous for expression of both Munc13-1 and -2) could not be not obtained from the parents used to generate Munc13 DKO offspring. Given that Munc13-2 was not detected in DAergic active zones (Figure 29) mice were accepted as unburdened controls, against which to compare Munc13 DKO mice, if both Munc13-1 alleles were present (Munc13-1+/+), regardless of Munc13-2 expression. Munc13-3 was not genetically deleted as part of these experiments,

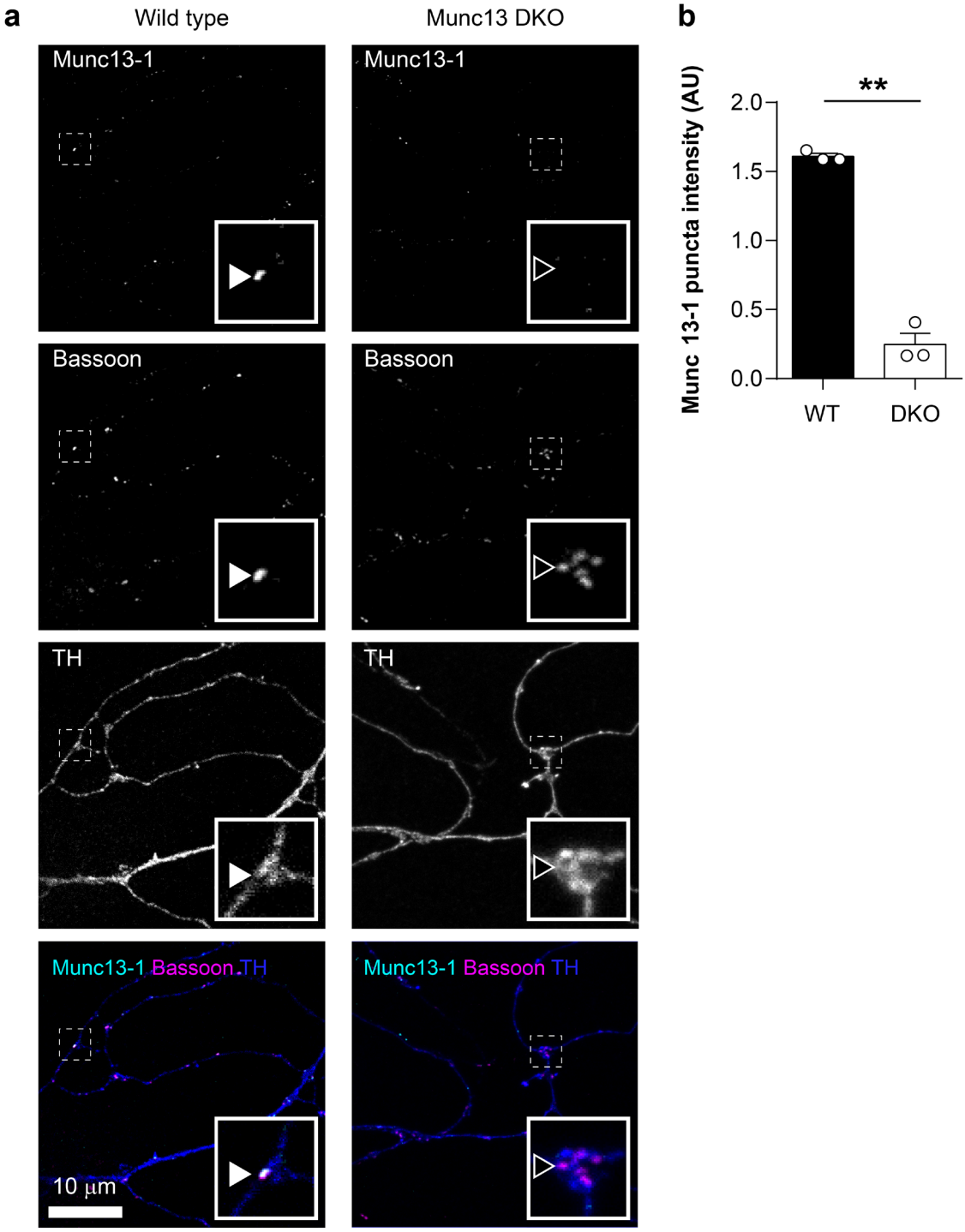

Figure 28: Active zones of DAergic neurons are positive for Munc13-1 in WT mice.
a, VM neuron cultures from WT (left) or Munc13-DKO (right) mice are shown with immunolabeling against Munc13-1, bassoon, and TH, as indicated. The lower panels show the three channels overlaid (Munc13-1 in cyan, bassoon in magenta, TH in blue). The region indicated by a white dashed box in each panel is shown in higher detail inset. An example of a bassoon-positive punctum that was also positive for Munc13-1 is indicated by a white arrowhead (left panels), while an example of a bassoon-positive punctum showing no Munc13-1 immunolabeling is indicated with a black arrowhead (right panels). **b**, Quantification of the average anti-Munc13-1 immunolabeling within bassoon-positive puncta in WT (black) and Munc13-DKO (white) mice is represented as a column chart (mean ± SEM). ** indicates $p < 0.01$, data is from images acquired across $n = 3$ independent neuron cultures (litters). Samples were compared using a two-tailed Welch's t-test.

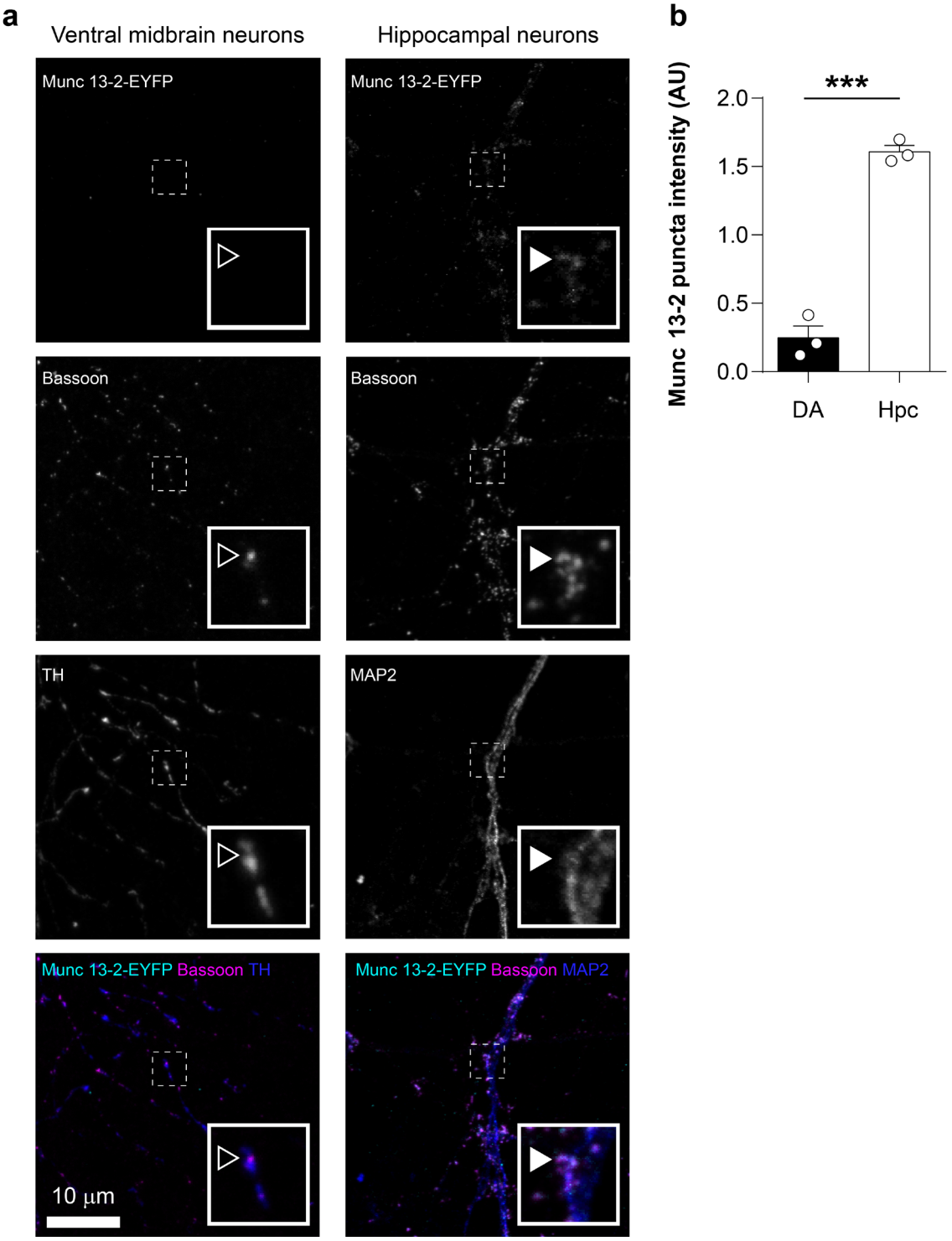

Figure 29: Active zones of DAergic neurons are negative for Munc13-2 in Munc13-2-EYFP KI mice.
a, Neurons from the VM (left) or hippocampus (right) of Munc13-2-EYFP KI mice are shown with immunolabeling against GFP, bassoon, and either TH to detect DAergic axons (left) or MAP2 to detect post-synaptic dendrites (right), as indicated. The lower panels show the three channels overlaid (GFP in cyan, bassoon in magenta, TH in blue). The region indicated by a white dashed box in each panel is shown in higher detail inset. An example of a bassoon-positive punctum that was also positive for anti-GFP labeling is indicated by a white arrowhead (right panels), while an example of a bassoon-positive punctum showing no GFP immunolabeling is indicated with a black arrowhead (left panels). **b**, Quantification of the average anti-GFP immunolabeling within bassoon-positive puncta in DAergic (black) and hippocampal (white) neurons is represented as a column chart (mean ± SEM). *** indicates $p < 0.001$, data is from images acquired from $n = 3$ Munc13-2-EYFP KI mice, with the VM and hippocampus harvested from each mouse and then cultured separately. Samples were compared using a two-tailed Welch's t-test.

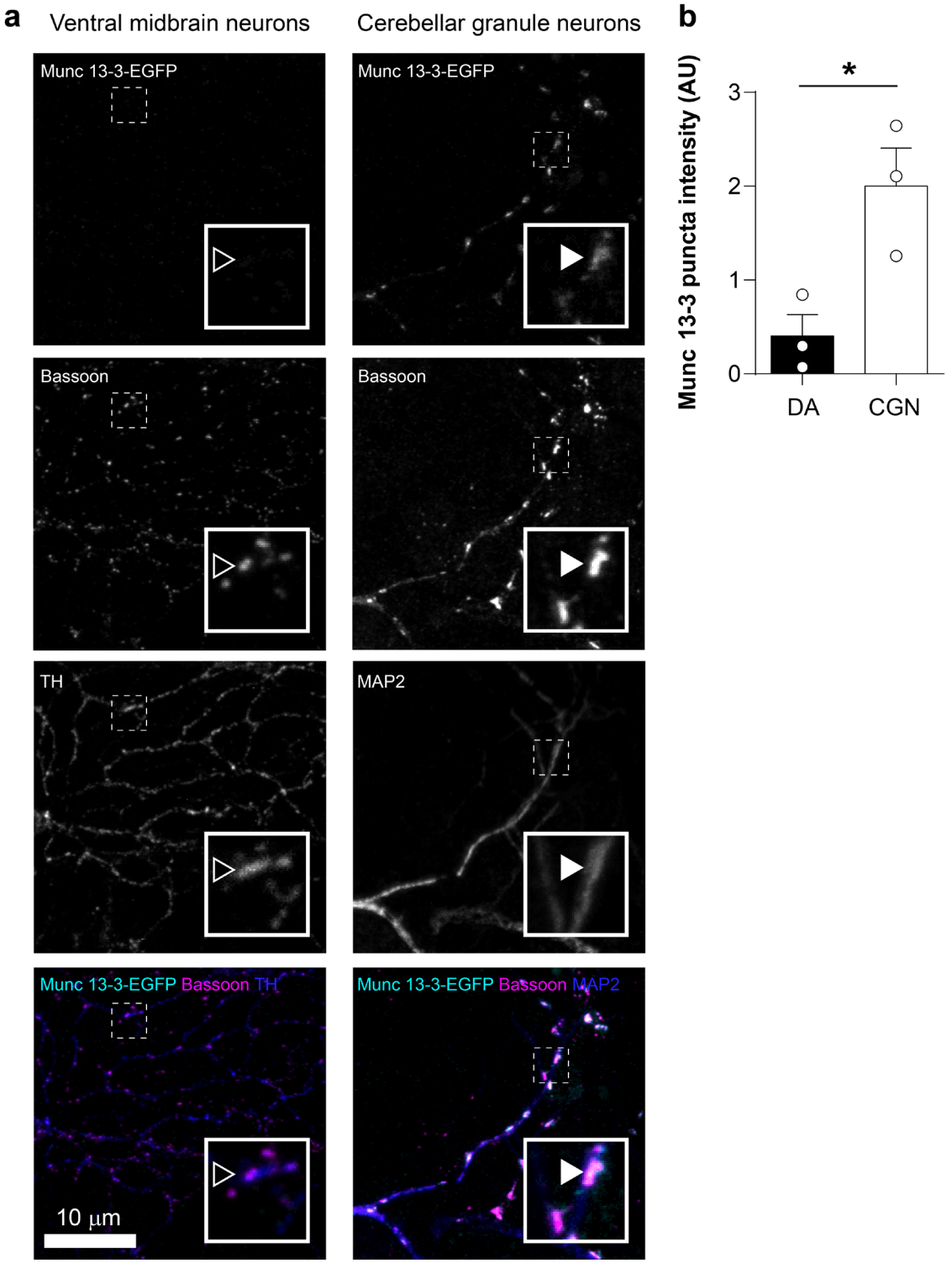

Figure 30: Active zones of DAergic neurons are negative for Munc13-3 in Munc13-3-EGFP KI mice.
a, VM neurons (DA, left) or cerebellar granule neurons (CGN, right) of Munc13-3-EGFP KI mice are shown with immunolabeling against GFP, bassoon, and either TH to detect DAergic axons (left) or MAP2 to detect post-synaptic dendrites (right), as indicated. The lower panels show the three channels overlaid (GFP in cyan, bassoon in magenta, TH in blue). The region indicated by a white dashed box in each panel is shown in higher detail inset. An example of a bassoon-positive punctum that was also positive for anti-GFP labeling is indicated by a white arrowhead (right panels), while an example of a bassoon-positive punctum showing no GFP immunolabeling is indicated with a black arrowhead (left panels). **b**, Quantification of the average anti-GFP immunolabeling within bassoon-positive puncta in DAergic (black) and CGNs (white) is represented as a column chart (mean ± SEM). * indicates $p < 0.05$, data is from images acquired across $n = 3$ independent cultures (litters). DAergic and CGN neurons were harvested from the same mouse brains. Samples were compared using a two-tailed Welch's t-test.

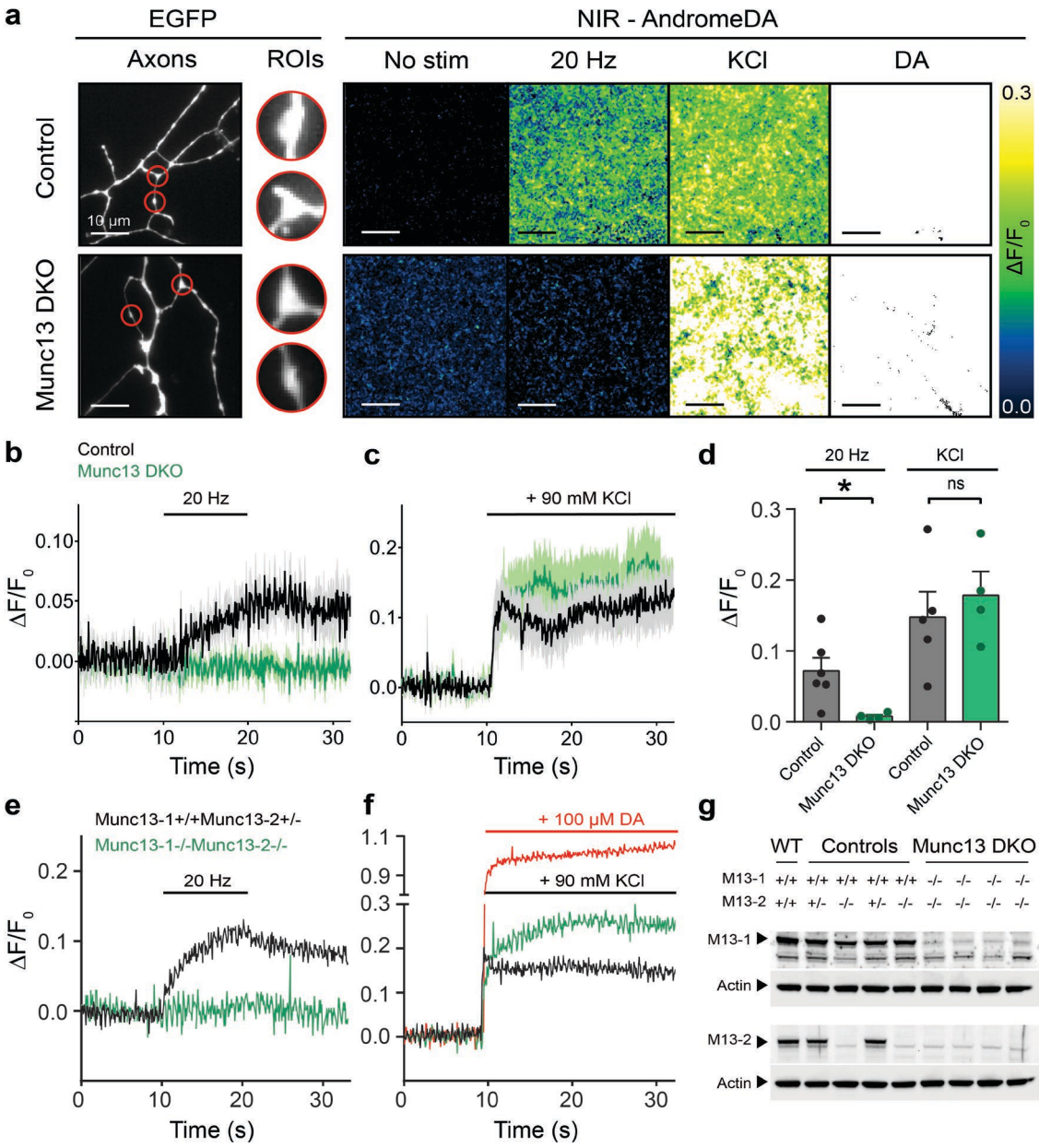

Figure 31: The SV priming protein Munc13 is required for electrically evoked DA release.
a, Representative images VM TH-EGFP neurons lacking expression of Munc13-1 and -2 (Munc13 DKO) compared to neurons from littermate control mice (EGFP) and the corresponding nanosensor surface (NIR). NIR images show normalized AndromeDA fluorescence prior to stimulation, during 20 Hz electrical field stimulation, during KCl stimulation and during application of 100 µM DA. NIR fluorescence was quantified at ROIs centered on EGFP-positive varicosities. Scale bars = 10 µm. **b**, NIR signal within ROIs over time for control (black traces) and Munc13 DKO (green traces) neurons with electrical stimulation. Munc13 DKO neurons abolished AndromeDA activation in response to electrical stimulation. **c**, NIR signal within ROIs over time for control and Munc13 DKO neurons with KCl stimulation. KCl evoked release is not affected in Munc13 DKO neurons. **d**, Peak fluorescence (mean ± SEM) for each stimulus method. For 20 Hz stimulation *n* = 4 Munc13 DKO mice and *n* = 6 control litter mates. For KCl stimulation, *n* = 4 Munc13 DKO mice and *n* = 5 for control littermates. Data were compared using a two-tailed Welch's t-test. * denotes $p < 0.05$. ns = not significant. **e**, Representative traces showing NIR fluorescence during 20 Hz stimulation from a single experiment from control mice (black) and Munc13 DKO mice (green). **f**, Representative traces showing NIR fluorescence during 90 mM KCl stimulation from a single experiment in control mice (black) and Munc13 DKO mice (green). All data sets were normalized to the corresponding AndromeDA response to 100 µM DA (red traces in f). **g**, WB analysis of Munc13-1 (upper panels) and Munc13-2 (lower panels) (~180 kDa) expression in mice used for AndromeDA imaging with labeling against Actin (~42 kDa) as loading control. Munc13 genotypes obtained by PCR amplifications of tail biopsies are displayed on the top. The first lane shows a non-littermate WT brain homogenate that served as positive control for immunolabeling.

as it is primarily expressed in hindbrain region and was not detected in the immunocytochemical experiments. The chances of Munc13-3 playing a role in DAergic transmission were therefore determined to be minimal and the deletion of Munc13-3 not included, as it would have added substantial time and complexity to the already complex mouse breeding scheme required for these experiments. Both, control and DKO neurons formed EGFP-positive, varicose axons in culture and showed no apparent morphological abnormalities (Figure 31a, left panels). When electrically stimulated, Munc13 DKO cultures displayed no AndromeDA activation above the noise level of fluorescence imaging (Figure 31b, d and e) and no hotspots, as opposed to neurons from littermate control mice analyzed in parallel (Figure 32a and b). Consistent with an unburdened phenotype, the average AndromeDA responses of these control mice were indistinguishable from non-littermate WT neurons collected in previous experiments (Figure 33a). Analysis of the average AndromeDA response around varicosities from all obtained Munc13 genotypes showed, that activation of AndromeDA upon electrical stimulation generally decreased with removal of Munc13 alleles with deletion of Munc13-1 alone eliminating the AndromeDA response in most but not all experiments. However, only Munc13 DKO samples exhibited a statistically significant reduction compared to the littermate controls (Figure 33b). Taken together, these results indicate that both Munc13-1 and -2 are required for electrically evoked DA release and that Munc13-2 plays a subordinate role in priming of DAergic SVs. The genotypes used for AndromeDA imaging were determined by genotyping and confirmed by WB (Figure 31g).

Unexpectedly, the simultaneous deletion of Munc13-1 and Munc13-2 had no effect of DA secretion evoked by KCl. The average AndromeDA response from these neurons to KCl was indistinguishable from control mice (Figure 31c, d and f), and 98 hotspots in total were observed during KCl depolarization in Munc13 DKO neurons (Figure 34 and Figure 35, white circles). To validate, that hotspots observed from Munc13-1/2 mutants were *bona fide* DA release events, I performed spatio-temporal analysis on these hotspots as described in Section 1.2.2.

Electrically evoked hotspots were observed in ~26% of all experiments performed with Munc13-1/2 mutants (excluding the Munc13-1/2 double KO, which showed no AndromeDA activation upon stimulation), which is similar to earlier experiments using untreated WT neurons (~25%) (Figure 21, 20 Hz). Since an altered genotype should have no effect on the proximity at which hotpot occur to nearby varicosities, I analyzed the varicosity-hotspots distance of all 20 Hz stimulated Munc13-1/2 mutants pooled. The median distance of hotspots from Munc13-1/2 mutant neurons to nearby varicosities was

2.4 µm (Figure 32a), which is larger than the hotspot-varicosity distance obtained in previous experiments from untreated neurons (~0.8 µm, Figure 15a). 29 hotspots were observed in total during 20 Hz experiments, of which 21 occurred during the stimulation period, and only 8 occurred in the absence of electrical stimulation (Figure 32b).

KCl evoked hotspots were observed in all Munc13 genotypes obtained. In total, 297 hotspots were observed in KCl experiments, of which only one hotspot occurred before KCl was applied (Figure 34). The numbers of observed hotspots for the distinct genotypes were as follows: 98 hotspots for M13-1-/- M13-2-/- from *n* = 3 experiments, 49 hotspots for M13-1-/- M13-2+/- from *n* = 3 experiments, 66 hotspots for M13-1+/- M13-2-/- from *n* = 5 experiments, 18 hotspots for M13-1+/- M13-2+/- from *n* = 1 experiment, 32 hotspots for M13-1+/+ M13-2-/- from *n* = 4 experiments and 34 hotspots for M13-1-/- M13-2+/- from *n* = 1 experiment (Figure 35 and Figure 34). Data from all genotypes was pooled for subsequent analyses, since all genotypes appeared to exhibit similar KCl evoked DA release. The median distance to nearby varicosities of these hotspots across all genotypes was 2.24 µm, which was smaller than hotspot varicosity distances obtained from KCl evoked hotspots in previous experiments using TH-EGFP mice (~3.8 µm, Figure 21). Moreover, the hotspot-varicosity distances became significantly larger when non-corresponding EGFP and NIR images were used for randomized control measurements (Figure 35d), verifying that the KCl evoked hotspots observed in experiments using Munc13 mutants were spatially associated with varicosities.

These data indicate that both electrically evoked and KCl evoked hotspots observed from Munc13-1/2 mutants are temporally dependent on neuronal depolarization and spatially associated with varicosities, similarity to previous validation analysis of hotspots from TH-EGFP neurons, and are therefore, too, indicative of DA release events. Therefore, the data presented here indicates that Munc13-1 and -2 are required for electrically evoked, but not KCl evoked DA release from primary VM neuron cultures.

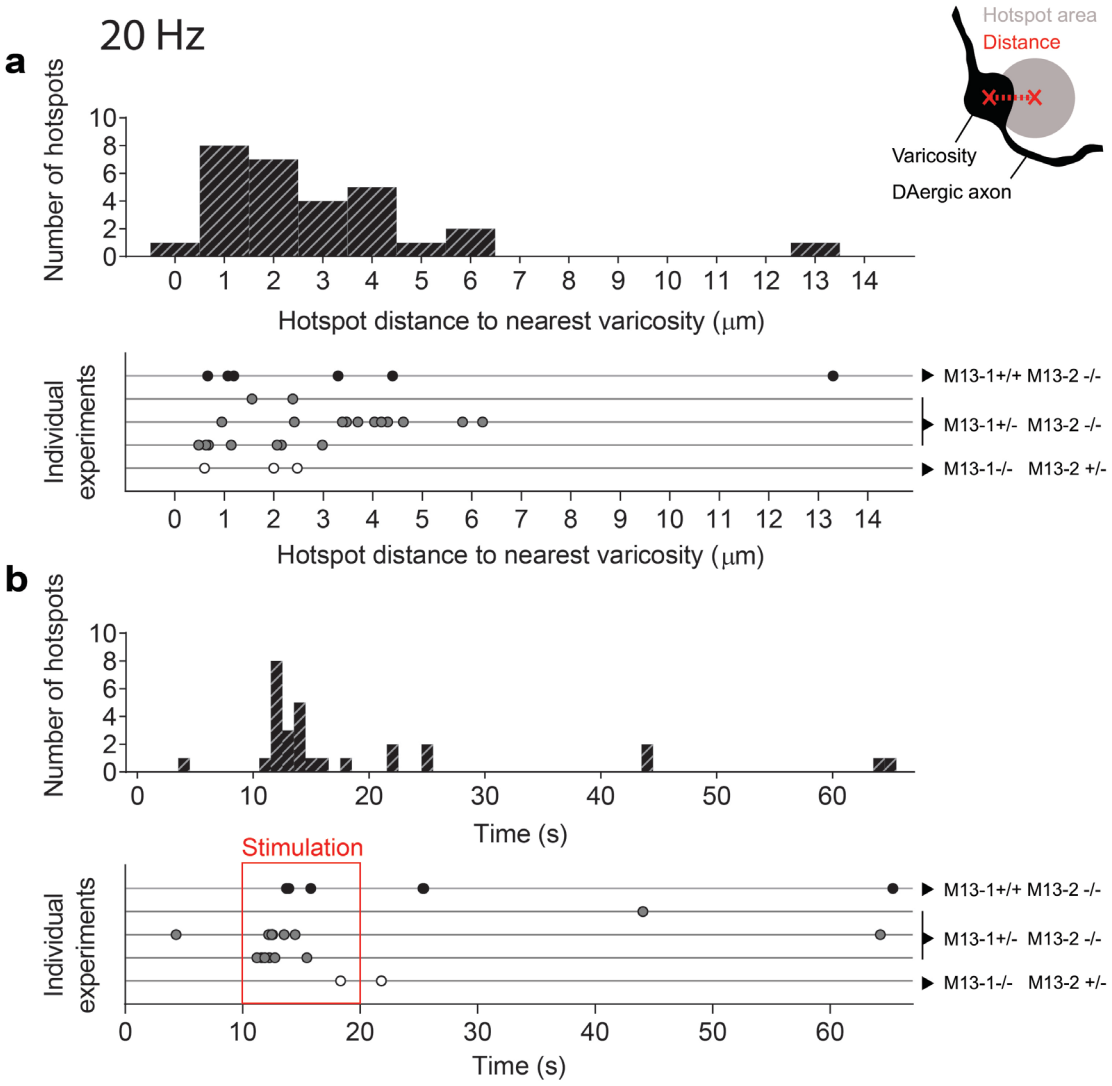

Figure 32: Electrically evoked hotspots in neurons from Munc13-1/2 mutant mice.
Electrically evoked hotspots were only observed in the three genotypes indicated (M13-1+/+ M13-2-/-, M13-1+/- M13-2-/-, M13-1-/- M13-2+/-). No hotspots were observed in experiments using Munc13 DKO neurons. **a**, The spatial association of observed hotspots with potential DA release sites was quantified by measuring the distance of the hotspots centers to the center of the nearest varicosity, as illustrated in the schematic. The upper panel shows the frequency distribution of all distances measured in experiments using in 20 Hz stimulation and the lower panel shows measured distances of single hotspots, grouped by the experiments in which they were observed (arranged in lines along the *y*-axis). **b,** Timepoint of the peak NIR fluorescence of observed hotspots. The upper panel shows the frequency distribution of all hotspot timepoints observed during in 20 Hz stimulation and the lower panel shows timepoints of single hotspots, grouped by the experiments in which they were observed (arranged in lines along the *y*-axis). The corresponding genotypes are indicated on the right (M13-1 = Munc13-1, M13-2 = Munc13-2). Electrical stimulation period from 10 s to 20 s is highlighted in red.

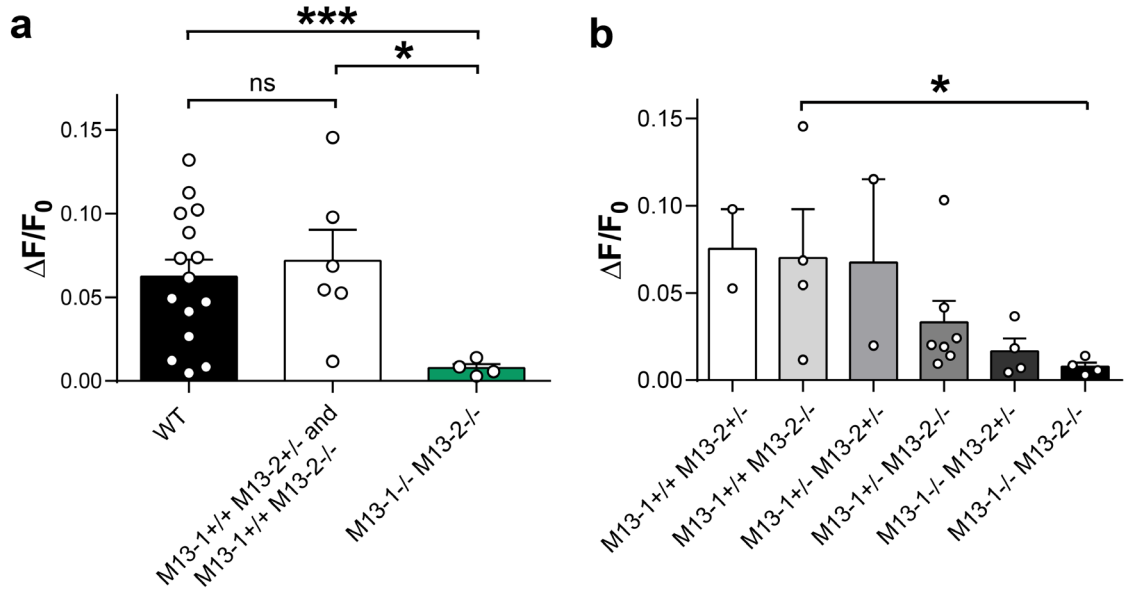

Figure 33: Electrically evoked DA release in neurons from Munc13-1/2 mutant mice.
a, AndromeDA fluorescence data from untreated WT neurons stimulated at 20 Hz alongside data from M13-1+/+ M13-2+/- and M13-1+/+ M13-2-/- mice (pooled), and from M13-1-/- M13-2-/- (Munc13 DKO) mice.* indicates $p < 0.05$, *** indicates $p < 0.001$. *n* values for each genotype were as follows: WT = 15, M13-1+/+ M13-2+/- and M13-1+/+ M13-2-/- = 6, M13-1-/- M13-2-/- = 4. **b**, Column chart showing the average peak AndromeDA fluorescence observed during 20 Hz electrical stimulation from each of the Munc13 mutants examined. M13-1-/- M13-2-/- (Munc13 DKO) exhibits a significant reduction in peak fluorescence compared to M13-1+/+ M13-2-/- mice. *n* values for each genotype were as follows: M13-1+/+ M13-2+/- = 2, M13-1+/+ M13-2-/- = 4, M13-1+/- M13-2+/- = 2, M13-1+/- M13-2-/- = 7, M13-1-/- M13-2+/- = 4, M13-1-/- M13-2-/- = 4. M13-1 = Munc13-1, M13-2 = Munc13-2. For all experiments, *n* represents the number of mice analyzed. Samples were compared using a Kruskal-Wallis multiple comparisons test. Error bars represent ± SEM in all charts.

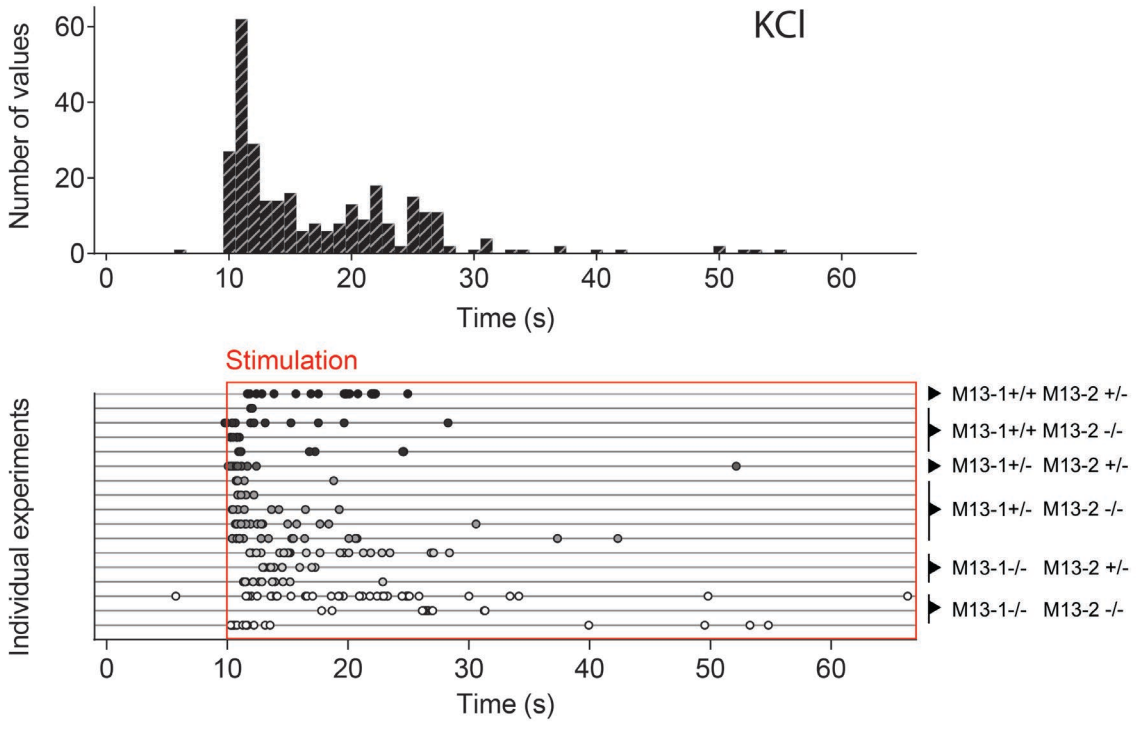

Figure 34: KCl evoked hotspots in neurons from Munc13-1/2 mutants.
The timepoints at which hotspots occur during KCl evoked depolarization in Munc13-1/2 mutants used in this study are shown. The upper panel shows the frequency distribution of all hotspots and the lower panel shows single KCl evoked hotspots, grouped by the experiments in which they were observed (arranged in lines along the *y*-axis), with dots representing individual hotspots. Corresponding genotypes are indicated on the right (M13-1 = Munc13-1, M13-2 = Munc13-2). 90 mM KCl is applied at 10 s and remains in the samples until the end of the experiment, indicated by a red box. Data represents 297 hotspots from 17 experiments.

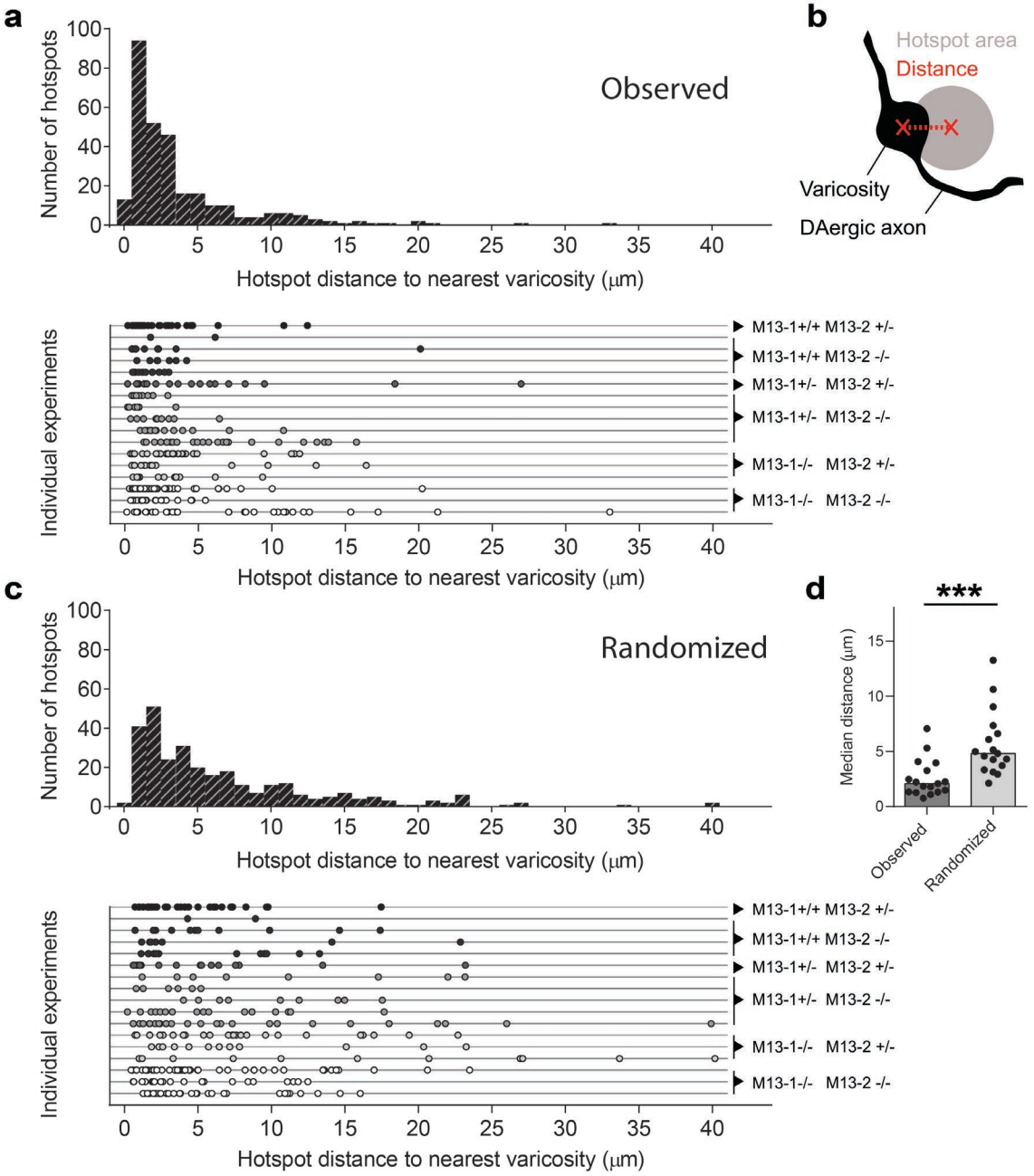

Figure 35: KCl evoked hotspots are spatially associated with DAergic varicosities in neurons from Munc13-1/2 mutant mice.

The spatial association of observed hotspots with potential DA release sites was quantified from KCl stimulated neurons lacking Munc13-alleles by measuring the distance of the hotspots centers to the center of the nearest varicosity. Hotspots-varicosity distances are shown for the different genotypes used in this study. **a**, Frequency distribution of all hotspots observed during in experiments with KCl application (upper panel) and measured distances of single KCl evoked hotspots, grouped by the experiments in which they were observed (arranged in lines along the *y*-axis, lower panel). **b**, Schematic illustrating how "distance" was defined. **c**, Randomized controls were generated by measuring distances from hotspots with non-corresponding images of DAergic axons. The graph shows the frequency distribution of randomized controls (upper panel) and hotspot-varicosity distances of single hotspots from randomized control measurements, grouped by the experiments in which they were observed (arranged in lines along the *y*-axis, lower panel). **d**, Varicosity-hotspot distance was larger when non-corresponding EGFP images were used (randomized). In a and c, dots represent individual hotspots, with corresponding genotypes indicated on the right (M13-1 = Munc13-1, M13-2 = Munc13-2). In d, dots represent single experiments and bars represent medians of all experiments, irrespective of the genotype. Data represents 297 hotspots from $n = 17$ experiments. Data were tested for normality with the Shapiro-Wilk test and compared using the Mann-Whitney test. *** denotes $p < 0.001$.

4 Discussion

4.1 AndromeDA for high resolution imaging of DA release

The invention of amperometry facilitated the understanding of fundamental mechanisms of catecholamine release in the brain, SV fusion in cultured adrenal chromaffin cells (releasing epinephrine and norepinephrine) and PC12 cells (releasing primarily DA), which was possible due to the superior sub-millisecond time resolution and sensitivity of this method (Ewing et al., 1983; Omiatek et al., 2010; Trouillon and Ewing, 2014; Wittenberg et al., 2007). FSCV further improved the selectivity of the electrochemical detection of DA at the expense of temporal resolution (~100 ms between data points) (Bucher and Wightman, 2015; Robinson et al., 2003). Yet, these electrochemical methods are not suited to investigate DA release on the level of single release sites from DAergic neurons and are primarily used to measure DA release from large areas of the brain. Electrochemical recordings from single neurons have been performed but are technically challenging, labor-intensive and time consuming (Mosharov and Sulzer, 2005). Single-varicosity amperometry is even more difficult to achieve due to the high density of DAergic release sites and relatively large size of the carbon electrode (Pothos et al., 1998; Staal et al., 2007, 2004). Even then, data is collected from only one varicosity at a time, and considerable time is required to obtain statistically significant data. Electrochemical methods are not suited to gather data on individual release sites across populations of varicosities, and do not inform us about the heterogeneity across individual varicosities formed by one neuron or axon. Microchips with electrode arrays (White and Kim, 2021) and electrode channels (Yakushenko et al., 2013) substantially increase the information that can be obtained from many PC12 cells in parallel. However, these chips are costly and still yield only one measurement per cell, and only if the cell settles directly on the electrode, which is as large as the cell itself. Microchips are therefore not suited to investigate subcellular DA release, especially from cells that require long-term differentiation, such as primary DAergic neurons.

In recent years, a variety of alternative DA sensing strategies have been developed for studying DA secretion *in vivo* and *in vitro* (Dinarvand et al., 2020; Labouesse et al., 2020). The development of optical DA sensors was a landmark development for the field as they provide increased spatial resolution. The ability to resolve DA release at the level of discrete secretory structures is a crucial requirement for the understanding of how

differences in the molecular composition at varicosities give rise to the functional and structural heterogeneity that has been observed across varicosity populations (Daniel et al., 2009; Descarries et al., 1996; Liu et al., 2018).

While optical exocytosis assays have been valuable in visualizing SV dynamics at DAergic varicosities (Daniel et al., 2009; Pan and Ryan, 2012; Pereira et al., 2016), these assays do not provide data on the secretion of DA specifically, in part due to the capacity of DAergic neurons to release multiple transmitters (Trudeau et al., 2014).

Optical methods utilizing microscopic imaging can achieve greater spatial resolution as many sensors are present and distributed over the area under analysis. All optical DA detection methods discussed here are capable of selectively detecting DA over other catecholamines and have dynamic ranges spanning between 1 nM to 10 µM, which is sensitive enough to detect the DA concentration expected at the release site, as quantal studies estimated an intra-vesicular DA concentration of > 0.1 M (Omiatek et al., 2013). These optical methods differ, however, in their ability to monitor DA secretion and diffusion through space. This ability is crucial for resolving single secretion events at discrete sites, and depend on the number of sensors that can be monitored simultaneously, their spatial distribution and the frequency at which data points are collected.

The most recent breakthrough for optical DA detection is provided by dLight and $GRAB_{DA}$ DA sensors, which are genetically modified DA receptors coupled to circularly permuted GFP (Patriarchi et al., 2018; Sun et al., 2018). DA binding by these receptors causes a conformational change of the GFP, increasing its fluorescence emission and providing an optical readout for DA abundance in the ECS. Using imaging or photometry, researchers have achieved a similar temporal resolution to FSCV. Thus, these sensors have gained popularity as an alternative to FSCV for detection of local DA transients in the brain. However, their popularity is based on other advantages, such as the circumvention of electrode biofouling (Harreither et al., 2016), and not the potential gain in spatial resolution of DA secretion. In fact, they have been developed primarily for fiber photometry, which utilizes an implanted optical fiber in target brain regions, measuring DA transients during behavior in awake animals by detecting fluorescence emitted by the sensors (Patriarchi et al., 2019). The potential of these genetically encoded sensors to be used for subcellular measurements of DA secretion and diffusion within small areas has not been explored.

Genetically-encoded sensors include the CNiFERs, $GRAB_{DA}$ and dLight. CNiFERs are not suited for addressing single varicosity release, since CNiFERs are whole cells and thus have a large size (~15 µm in diameter) (Muller et al., 2014). CNiFERs also have low time resolution, with a second-scale delay between binding of DA to the surface receptors and optical FRET readout (Muller et al., 2014). $GRAB_{DA}$ and dLight, in contrast, are small proteins expressed on plasma membrane. It is presently unclear whether $GRAB_{DA}$ and dLight could resolve DA secretion at individual varicosities, as no attempts have been made to use them for this purpose. It seems possible that their restricted localization at cell membranes and high expression levels in cells would hinder the discrimination of DA release events or correlating these with single subcellular secretory structures, especially since varicosities are usually close to each other. Varicosities that are potentially capable of secreting DA occur on average every 4 µm along a DAergic axon, as estimated by the presence of active zone proteins (Liu et al., 2018). The microscopic investigation of dLight sensors in acute brain slices has demonstrated the detection of local “hotspots” of ~20 µm diameter that were responsive to electrical stimulation, and line scans through these hotspots achieved data point collection at up to 500 Hz (Patriarchi et al., 2018). However, this line scanning approach trades high temporal resolution for reduced spatial resolution. These experiments were performed to characterize the sensor with no emphasis on correlating the observed hotspots with subcellular DAergic structures. A more typical temporal resolution is demonstrated when dLight is used in fiber photometry in the brain during behavior, with ~100 ms temporal resolution (Patriarchi et al., 2019, 2018). Overall, $GRAB_{DA}$ and dLight have simply not been used to examine subcellular DA release, and thus it remains an open question whether these sensors may prove useful in examining DA release from discrete varicosities in the future.

SWCNT-based DA sensors are promising candidates for resolving DA secretion at discrete DAergic varicosities, as they do not require genetic expression (which could potentially interfere with normal cell function), are not limited to cell structures (which could be located far from the release site), and can monitor not only DA release but also diffusion through space. However, SWCNT-based DA sensors have not been used for this purpose until now. In the following, I present AndromeDA as the ideal method to examine single-varicosity DA secretion in cultured primary neurons.

4.1.1 AndromeDA is a substantial advance in DA detection

When using a sensor, the properties of the sensing technique have to match the requirements for addressing the biological question. Sensor characteristics include the spatial and temporal resolution of analyte detection, as well as sensitivity and selectivity of the sensor for the analyte. A sensor that is suitable for all biological questions does not exist – and the sensor used therefore has to be carefully chosen for each study. In this work, I focus on resolving brief, local DA secretion events from individual varicosities, which are ~2 µm in diameter and often located only micrometers apart along one axon.

I used SWCNT-based DA sensors to achieve the required spatial resolution for resolving DA secretion at discrete release sites. SWCNT-based DA sensors are small (~0.7 nm x > 200 nm), compared to CNiFERs and electrochemical probes (~7 µm) (Pike et al., 2009), and can be applied to tissue and cells at a high density. SWCNTs are not limited to membrane structures, permitting the detection of local DA release events directly at the release site as well as DA diffusion from release sites in the ECS. Since every individual sensor reports the presence of DA locally in a dose-dependent manner, every sensor represents a point of measurement during imaging. This gives the potential of concurrently measuring millions of nanosensors during imaging. Since more sensors are present in the imaging field than the number of pixels of the resulting images, every pixel of the image effectively serves as a point of local DA measurement. Importantly, AndromeDA imaging provides a spatiotemporal readout not only of DA secretion but also DA diffusion through the ECS, which has direct relevance to the spatiotemporal patterns of DAergic volume transmission (Cragg and Rice, 2004).

Importantly, SWCNT-based sensors are the only optical DA detection method to have detected KCl evoked subcellular “hotspots” of DA release. This was done using immobilized SWCNT-based nanosensors on coverslips, on top of which PC12 cells were then seeded (Kruss et al., 2017). The observed hotspots spanned a time frame of ~100 ms to s and correlated with protrusions on the plasma membrane. While this study highlights how immobilized SWCNT-based DA sensors can be used in cell culture to optically monitor DA release dynamics from subcellular structures with temporal resolution comparable to FSCV, this experimental design did not exploit the full potential of SWCNT, as the fluorescence response of the nanosensors was analyzed only at the cell membrane, neglecting the possibility of monitoring DA diffusion through space. The SWCNT-based sensor employed in this study also could not discriminate between DA and other catecholamines. PC12 cells primarily secrete DA but have been reported to

also secrete epinephrine (Byrd et al., 1986). The selectivity of SWCNT-based sensors for DA, however, has been improved since these experiments (Mann et al., 2017), which I took advantage of in developing AndromeDA. My study built upon previous studies in PC12 cells using sensors with greater sensitivity and selectivity for DA, higher temporal resolution and, importantly, a more biologically relevant system in terms of understanding DAergic transmission in the brain.

SWCNT-based DA detection has also been applied to examining DA secretion in brain tissue (Beyene et al., 2019). Acute brain slices containing the striatum were bathed in a solution containing SWCNT-based monoamine sensors for 15 min, washed to remove nanosensors that did not attach to the tissue, and nanosensors were then imaged during slice stimulation. The specific stimulation of DAergic boutons through optogenetic methods caused an increase in nanosensor fluorescence, which scaled up with increasing stimulation frequency and strength (Beyene et al., 2019). However, the observed peaks in nanosensor fluorescence lasted up to 10 s and likely reflected mostly DA bulk release rather than single events, which are much shorter (Jaffe et al., 1998; Staal et al., 2004). This application strategy therefore did not demonstrably improve the temporal resolution of DA detection in comparison with other optical methods, such as dLight or FSCV. Although Beyene and colleagues (2019) report local DA secretion “hotspots” with a median size of 2 µm, which indicated an improved spatial detection of DA abundance, these hotspots were not correlated to DAergic subcellular structures. Moreover, it is not possible to determine whether these hotspots reflect discrete DA release events from single varicosities and the authors do not characterize them further. The penetration of single sensors into the tissue and adsorption on the complex cellular landscape of the brain slice were not controlled in these experiments. The sensor distribution appeared to be uneven across the tissue, which may reflect nanosensor aggregates or simply heterogenous adsorption across the tissue, which could influence the fluorescence readout of the sensors. Nanosensor clusters introduce several technical challenges to DA imaging, since their fluorescence to DA can be altered by proximity quenching (Powell et al., 2018) or contamination with unresponsive non-functionalized SWCNTs. In contrast, I used SWCNT-based sensors immobilized on coverslips, which allowed the optical validation of nanosensor coating homogeneity and the responsiveness to DA of sensors on a single pixel level through the application of a known DA concentration as calibration control.

In the current work, I present a new application strategy for using SWCNT nanosensors, that takes advantage of the potential of this newly emerged class of DA sensors for high spatiotemporal resolution of DA detection. AndromeDA combines a novel low-density VM neuron co-culture, with the advantages of nanosensor surface immobilization and multiplexing with EGFP fluorophores for the reliable identification of DAergic varicosities. The low cell density of this new, glia-free culture system facilitates the clear distinction of individual varicosities, as well as homogenous, aggregate-free nanosensors adsorption on the glass surface surrounding the varicosities. Adsorbing SWCNT sensors on the glass surrounding the neurons, rather than culturing the neurons on top of the nanosensor layer, circumvents critical issues such as nanosensor biofouling and nanosensor-induced cell toxicity. It also allows the application of this technique to long-term differentiated neuron cultures of any kind. Adsorbing nanosensors at high density (~400 million sensors per imaging field), and monitoring the fluorescence of all sensors in parallel during neuronal stimulation, furthermore allows the detection of local DA secretion hotspots and correlation of these hotspots with individual varicosities. My data shows that AndromeDA is capable of monitoring DA secretion from up to hundred varicosities in parallel, thereby identifying varicosities with clear DA secretion events of ~5 μm^2 median size in space, and varicosities that either do not secrete DA or secrete DA at undetectable levels. AndromeDA therefore allows the comparison of single release events across large varicosity populations.

The ability of AndromeDA to distinguish discrete DA release events from many sites simultaneously and correlate them with subcellular structures is unique and has not been achieved by any other DA detection method. Importantly, the technique detects both DA release at subcellular structures and diffusion through the ECS, and is capable of separating these two phenomena through image analysis. The specific kinetics of the sensors used in AndromeDA with regards to DA binding and unbinding are unknown at present (but are estimated at K_d = 9.2 nmol/L, Mann et al. 2017) and therefore it is unclear how fast data point collection can potentially be. However, the custom NIR microscope used in the present work allowed monitoring of an entire imaging field of 12800 μm^2 with 200 nm pixel size with ~67 ms in-between frames (15 images/s), which results in a temporal resolution comparable to FSCV. Using these settings, the response of imaged nanosensors to external DA application was immediate (Figure 16f and Figure 17f). The temporal resolution of AndromeDA imaging could be further improved by acquiring line-scans through pre-identified varicosities as opposed to the entire imaging field, or improved camera technology. The properties of nanosensors used in AndromeDA can also be further adapted to the biological question examined. For example, a less

sensitive sensor could ease the detection of hotspots by reducing the detection of diffusing DA in the ECS. AndromeDA detection is specific for secreted DA, as demonstrated by altering the vesicular DA content of the DAergic neuron cultures examined in the present study. Moreover, the SWCNT-$(GT)_{10}$ nanosensors used in AndromeDA detect DA selectively over other catecholamines (Mann et al., 2017). AndromeDAs' dynamic range (10 nM – 10 µM) and sensitivity (EC_{50} 299 nM) competes with the sensing properties of other optical DA detection methods and, importantly, these properties can be easily adjusted, by changing the oligonucleotide sequence used for SWCNT functionalization, to sensing requirements ideal for other type of cells (Mann et al., 2017). The application of AndromeDA is fast and simple and is not restricted by the time required for sufficient gene expression, which can take up to three weeks (Patriarchi et al., 2019). In contrast to other optical DA sensors, AndromeDA imaging is not limited by fluorophore bleaching and does not potentially interference with endogenous signaling pathways, e. g. by altering the number of DA receptors on the plasma membrane in examined neurons. Moreover, AndromeDA response can be calibrated on the level of single pixels, by terminal application of known DA concentrations. In conclusion, the advancements described in my work for preparing and using an immobilized nanosensor layer, "AndromeDA", constitutes a substantial and validated development in the nanosensor field. Moreover, AndromeDA presents the most suitable tool currently available to interrogate the molecular regulation of DA secretion on the level of single release sites.

4.1.2 Detection of DA diffusion in the extracellular space

Using AndromeDA in neuronal VM cultures, I observed two phenomena upon neuronal depolarization: local AndromeDA hotspots indicative of discrete DA release events, and gradual, more subtle increase of AndromeDA fluorescence in the entire imaging field, indicative of DA diffusion through the ECS. Importantly, both phenomena were dependent on neuronal stimulation, and susceptible to manipulations of the vesicular DA content through L-DOPA and reserpine, validating the specificity of this signal for secreted DA. This highlights that AndromeDA can be used for both, measuring the summed DA release from a large area (similar to other optical DA detection methods) and, at the same time, the detection of discrete DA release events.

AndromeDA activation in the ECS during electrically induced neuron depolarization was increased only in the stimulation window, consistent with the detection of stimulated DA secretion. Interestingly, when the stimulus stopped, the AndromeDA signal in the ECS often remained at the fluorescence intensity reached during the stimulation train and only

slowly returned to baseline. This observation raises the question, if the AndromeDA fluorescence in the ECS reflects a change in the concentration of DA in the entire bath, or whether DA is accumulating at the nanosensor layer due to its interaction with the many sensors located on the nanosensor surface, which could considerably slow down the diffusion of a DA molecule. As all relative fluorescence changes of AndromeDA in this study are expressed as fraction of the response to 100 µM DA of the corresponding imaging field (activation by 100 µM DA = 1), a 0.05 fluorescence increase in the ECS therefore corresponds to 5% of the maximum possible fluorescence response of that region. Given that AndromeDA saturates at ~10 µM, a 5% increase in AndromeDA indicates a DA concentration in the ECS of ~500 nM. Whether this concentration could have been reached during live-cell experiments can be estimated with the following calculation: Taking into consideration the bath dimensions and the DAergic cells count determined per coverslip, it can be estimated that ~50 DAergic neurons are located in the imaging bath. If every cell forms 300000 presynaptic boutons (Matsuda et al., 2009), from which at least one SV is released during one action potential, and one SV contains 33000 DA molecules (Omiatek et al., 2013; Sulzer et al., 2016), then 33000 x 300000 x 50 x 200 = 10^{14} DA molecules are released into the 500 µL bath volume after a train of 200 action potentials. This would result in a DA concentration of ~330 nM DA concentration in the imaging bath. This calculation does not take into consideration somatodendritic release, nor the release of DA by spontaneous firing, and it is thus theoretically possible that the fluorescence response of AndromeDA in the ECS is representative of the DA concentration across the entire imaging bath. This could be further confirmed by measurements of the DA concentrations in the bath volume before and after application of electrical stimulation trains, for example by high-performance liquid chromatography. Such a pilot experiment was conducted but was not successful and should be repeated in the future.

Moreover, it is important to consider that these live cell experiments were performed without a perfusion flow. Additionally, the observed AndromeDA fluorescence is a convolution of the kinetics of individual sensors, together with the diffusion of DA from many release sites in close proximity. Hence, AndromeDA measurements do not reflect real-time DA secretion, but a delayed and convoluted image of complex DA secretion events. Fortunately, this leads to the advantage that image acquisition frame rates, which are much slower than the duration of single DA secretion events as previously measured with amperometry (200 µs) (Pothos et al., 1998), have enough time to capture the delayed fluorescence response. A perfusion flow could be installed during live cell experiments to prevent the accumulation of DA in the imaging bath, thus further enable

the detection of AndromeDA hotspots. In summary, in addition to DA secretion hotspots located at varicosities, AndromeDA detects DA that has diffused from the release sites into the ECS.

4.1.3 Detection of distinct DA release events

In contrast to extracellular DA diffusion, local AndromeDA hotspots were generally brief (~400 ms), associated with DAergic varicosities, and reached local fluorescence amplitudes close to the saturation limit of the sensors. AndromeDA nanosensors saturate at 10 µM DA, and the fluorescence intensity of single AndromeDA hotspots is therefore consistent with the previous estimation of high intra-vesicular DA concentrations (Omiatek et al., 2013).

Addressing synaptic physiology of individual DAergic presynaptic boutons was previously only possible with exocytosis assays, such as styryl dyes (Daniel et al., 2009), FFNs (Pereira et al., 2016; Zhang et al., 2009) and pHluorin-based probes (Pan and Ryan, 2012). Although these dyes do not reflect the secretion of DA itself, these studies demonstrated that neurotransmitter release from DAergic varicosities exhibits a high degree of functional diversity, with respect to the relative number of SVs available for exocytic release at each varicosity and the relative likelihood that an action potential will trigger SV fusion, which are important functional parameters in neurotransmitter secretion. Consistent with these previous studies and the proposition that DA release events are heterogeneous, I found that AndromeDA hotspots varied considerably with respect to their timing, amplitude and area. Furthermore, my data demonstrates, that AndromeDA can detect spontaneous pacemaker activity of DAergic neurons (Grace and Bunney, 1984a), as I observed AndromeDA hotspots in the absence of external stimulation, but not when TTX is present in the Imaging Buffer. This indicates that spontaneous AndromeDA hotspots are a result of spontaneous action potential firing and not spontaneous SV fusion. Moreover, the electrical stimulation used in this study (20 Hz) evokes action potential frequencies that are similar to DAergic action potential firing during phasic DA release (20 – 30 Hz) (Grace and Bunney, 1984b). Therefore, AndromeDA can in principle detect both defined modes of DAergic firing.

Importantly, AndromeDA detects secreted DA directly, thus is not obscured by potential release of other neurotransmitters (Kruss et al., 2017, 2014, 2013; Mann et al., 2017). Therefore, AndromeDA not only directly confirms the functional heterogeneity of single DAergic boutons observed in previous studies, but will allow the interrogation of how this

diversity gives rise to spatiotemporal patterns of DA release and diffusion, which is highly important in DA signaling (Cragg and Rice, 2004; Liu et al., 2021; Sulzer et al., 2016).

4.1.4 Identification of silent varicosities

While many hotspots were detected at varicosities upon neuronal stimulation through AndromeDA imaging, a large proportion (~83%) of examined DAergic varicosities did not exhibit detectable AndromeDA hotspots. Although it cannot be excluded that these varicosities secreted DA at low levels that did not allow the clear distinction of local hotspots from DA diffusing from adjacent release sites, this observation is consistent with previous studies that have proposed the existence of so-called “silent” DAergic varicosities. Analyses in cultured neurons using FM1-43 (Daniel et al., 2009) and in striatal slices using FFN200 (Pereira et al., 2016) both showed that within a population of simultaneously imaged varicosities, only a subpopulation exhibits exocytosis during stimulation. However, exocytosis assays in DAergic neurons are only an approximation for the analysis of DA release. Given the potential for DAergic neurons to release other classical neurotransmitters (Hnasko et al., 2010; Sulzer et al., 1998; Tritsch et al., 2012) this approximation likely misrepresents the release of DA itself. The parallel analysis of DA release from large varicosity populations with AndromeDA provides the first evidence that DA is released from a subpopulation of varicosities, using a direct DA detection method. My data indicates, that even after using L-DOPA to increase DA release, the proportion of varicosities exhibiting electrically evoked DA release hotspots treatment is ~17% which is strikingly similar to the proportion of varicosities that exhibited release of FFN200 in the striatum (~17%) (Pereira et al., 2016). These data indicate that functionally silent varicosities are an inherent property of DAergic neurons both *in vitro* and *in vivo.* Silent varicosities may be a consequence of the sparse distribution of active zone-like structures in DAergic axons (Daniel et al., 2009; Liu et al., 2018). Future studies using *post-hoc* ICC in combination with AndromeDA to link AndromeDA hotspots with varicosities that contain active zone proteins will be informative about the molecular basis of silent varicosities.

4.2 The role of Munc13 in vesicular DA release

In fast synaptic transmission, such as is mediated by glutamate, the spatial and temporal precision of the signal is partly ensured by the structure of the synapse and the specialized molecular machinery present at the active zone of the presynaptic bouton. Scaffolding proteins, priming proteins, Ca^{2+} sensors and proteins that mediate SV fusion all coordinate neurotransmitter release into the synaptic cleft on a millisecond timescale after arrival of the action potential (Südhof, 2013, 2012). Glial cells surrounding the synapse prevent glutamate diffusion outside of the synaptic cleft and rapidly terminate the signal by glutamate uptake (Zoli et al., 1998). The persistence of glutamate is therefore restricted to the narrow synaptic cleft (~30 nm wide) (Imig et al., 2014; Zuber et al., 2005) and very brief (~0.8 ms half-life) (Clements et al., 1992). In addition, glutamate acts on the post-synapse through fast ionotropic receptors, which rapidly propagate the signal to the target cell. Neurotransmitters such as glutamate therefore act with a high degree of temporal and spatial precision.

DAergic volume transmission, which requires DA diffusion from the release site in order to reach extra-synaptic DA receptors, is substantially different from fast neurotransmission (Descarries et al., 1996; Pickel et al., 1996; Rice and Cragg, 2008; Taber and Hurley, 2014). It was estimated, that DA travels up to 7 µm away from its secretion site and persists in the ECS with a half-life of 30 ms (Sulzer et al., 2016). DA clearance from the ECS is mostly performed by DAergic neurons themselves through uptake activity of DAT (Cragg and Rice, 2004; Sulzer et al., 2016). In addition, metabotropic signaling through DA receptors is more than two orders of magnitude slower than ionotropic signaling (Ford 2014, Gonon 1997, Missale et al. 1998). Thus, DAergic transmission is spatially and temporally less precise than neurotransmission by fast-acting neurotransmitters.

While the molecular mechanisms underlying fast neurotransmission, especially neurotransmission mediated by glutamate, are well characterized, little is known about the molecular machinery that governs the secretion of DA. Given the differences between glutamatergic and DAergic transmission modes, it cannot be assumed that the molecular components that mediate glutamate release are also required for the secretion of DA. Previous studies have shown that at least some molecular components are common to both, DAergic release and the release of fast neurotransmitters. DAergic varicosities, for instance, also rely on extracellular Ca^{2+}, and utilize the Ca^{2+} sensor SYT1 for excitation-secretion coupling (Banerjee et al., 2020b; Brimblecombe et al., 2015;

Fortin et al., 2006). In addition, DA release requires active zones, as DA release is abolished by deletion of the active zone scaffold RIM (Liu et al., 2018), and exocytosis in DAergic varicosities was observed almost exclusively at varicosities that contain bassoon (Daniel et al., 2009). Other molecules, however, that are involved in fast neurotransmission appear to be less important for DAergic signaling. Deletion of the active zone scaffold ELKS, for example, leads to a reduction of neurotransmitter release by ~50% in excitatory glutamatergic synapses (Held et al., 2016), but has no effect on DA release as measured my amperometry in striatal slices (Liu et al., 2018). In contrast, the presynaptic protein α-synuclein appears to play a prominent role in the regulation of DA release but not in glutamate release. Deletion of α-synuclein and members of the same protein family result in increased DA release in the dorsal striatum (Abeliovich et al., 2000; Anwar et al., 2011; Senior et al., 2008), but has relatively mild effects on glutamatergic transmission (Chandra et al., 2004; Greten-Harrison et al., 2010; Vargas et al., 2017, 2014). The molecular machinery that mediates neurotransmitter release at DAergic varicosities is therefore distinct, at least partially, from the molecular machinery that controls neurotransmitter release at fast synapses. When viewed in combination with the fundamental differences in the spatiotemporal aspects of DAergic and glutamatergic neurotransmission, it is clear that DAergic varicosities must be more thoroughly characterized to understand the molecular basis for DA release.

4.2.1 Munc13-mediated SV priming is required for DA release

In fast synapses, the process of SV priming is essential for SV exocytosis. The importance of priming proteins such as Ca^{2+} dependent activator protein for secretion (CAPS) and Munc13 is highlighted by the high degree of evolutionary conservation in their protein interaction domains (Koch et al., 2000) and the lethal phenotype of their deletion (Jockusch et al., 2007; Speidel et al., 2003). While the deletion of CAPS causes a dramatic reduction in neurotransmitter release and a rather complex phenotype in cultured glutamatergic neurons, the deletion of Munc13-1 and -2 leads to the total arrest of neurotransmitter release at all fast synapses (Augustin et al., 1999b; Varoqueaux et al., 2002). Munc13 proteins are therefore regarded as absolutely required for fast neurotransmission. While is it likely that SV priming is as important for vesicular DAergic secretion as it is for the secretion of fast neurotransmitters, the significance of known priming proteins for DA release has not been investigated to date. Some structurally specialized synapses, such as the retinal photoreceptor ribbon synapse and the cochlear hair cell ribbon synapse (Cooper et al., 2012; Vogl et al., 2015) function in the complete absence of Munc13, and thus it cannot be concluded that Munc13 mediated priming

plays a role in DA release without directly investigating the impact of Munc13 deletion on DA secretion.

My data shows that simultaneous genetic deletion of Munc13-1 and -2 results in the loss of electrically evoked AndromeDA activation, and therefore, action potential evoked DA release in VM neurons. Thus, my data demonstrates, for the first time, that Munc13 mediated SV priming is required for DA secretion. This further emphasizes the fundamental role of Munc13 in neurotransmitter secretion and adds new molecular information to the growing model of DA secretion mechanisms.

4.2.2 Munc13-1 is the only isoform detected at DAergic varicosities

Although Munc13 is essential for neurotransmission in all fast synapses, the requirement for individual Munc13 isoforms varies across distinct types of synapses. Three Munc13 isoforms are expressed throughout the central nervous system. Munc13-1 is the most abundant isoform expressed the in central nervous system, whereas Munc13-2 expression is mainly restricted to the cortex, hippocampus and cerebellum. Munc13-3 is almost exclusively expressed in the cerebellum (Augustin et al., 1999b, 2001). In glutamatergic hippocampal neurons, ~90% of synapses utilize the Munc13-1 isoform for SV priming, while the remaining ~10% require the Munc13-2 isoform as priming factor (Rosenmund et al., 2002). These data demonstrate that Munc13-1 is the dominant isoform in glutamate secretion. In GABAergic neurons, Munc13-1 and Munc13-2 are completely redundant, and both must be deleted to abolish GABA release (Varoqueaux et al., 2002). The deletion of Munc13-2 alone has no effect on both types of synapses and can be completely compensated for by Munc13-1, which is reflected by the fact that Munc13-2 and Munc13-3 KO mice are viable and fertile, while Munc13-1 KO mice are paralyzed and die immediately after birth (Augustin et al., 1999b; Varoqueaux et al., 2002).

The first assessment of the abundance of Munc13 isoforms in the adult rat brain did not detect clear Munc13 mRNA abundance in the VM (Augustin et al., 1999a). More recent studies, however, found evidence of unc13b and unc13c mRNA expression, which encode Munc13-2 and -3, respectively, in some DAergic neuron populations, but did not find unc13a (Munc13-1) (Tiklová et al., 2019).These findings, however, do not prove whether Munc13 isoforms are expressed or absent in DAergic neurons, as Munc13 proteins could be expressed at relatively low levels or at unexamined developmental stages, and various intermediate regulations mechanisms (such as siRNA inhibition) affect protein synthesis downstream to DNA transcription (Chernikov et al., 2019).

Protein detection using validated antibodies, in contrast, more directly demonstrates the expression and localization of proteins. WB analysis of Munc13 isoform abundance revelated that Munc13-1 and Munc13-2, but not Munc13-3 are present in the striatum, the major target region of VM projections (Augustin et al., 1999a), indicating that Munc13-3 is not present at DAergic presynaptic boutons. However, DAergic varicosities represent only a small fraction of all synapses in the striatum (Arluison et al., 1984) and it is thus possible, that Munc13-1 and Munc13-2 are present in other types of synapses and not DAergic boutons. Further evidence for the abundance of Munc13 at DAergic axons was provided by Liu and colleagues (2018) by immunolabeling striatal synaptosomes for Munc13-1, but these data did not include a Munc13-1 KO negative control nor addressed the presence and role of individual Munc13 isoforms. As a part of my work, it was clear that a thorough examination of Munc13 expression in DAergic varicosities was necessary to fill a gap in the existing literature.

In this study, I used an immunocytochemical approach to quantify Munc13 abundance specifically at DAergic varicosities. The use of neuronal culture allowed thereby the clear distinction of presynaptic boutons, as well as the reliable affirmation that the analyzed axonal structures were DAergic. Munc13-1 puncta, but not Munc13-2 or -3 puncta, were detected at DAergic active zones by ICC in my cultures. This was further supported by data showing that immunostaining against the fluorescent tags expressed in the Munc13-2-EYFP and Munc13-3-EGFP mice was significantly reduced at DAergic active zones compared to active zones in other neurons expressing these Munc13 isoforms. These data indicate that Munc13-1 is the only Munc13 protein present in DAergic varicosities.

4.2.3 Munc13-1 and -2 are required for electrically evoked DA release

My analysis of DA secretion from mutant mice showed that the deletion of Munc13-2 alone had no impact of electrically evoked DA release as measured by AndromeDA, compared littermate neurons that carried one Munc13-2 allele. Mice that expressed a single allele of the gene encoding Munc13-1, or lacked Munc13-1 expression entirely, exhibited trends towards a reduction in DA release, although these trends were not statistically significant. Only three hotspots were observed in all experiments using mice that lacked Munc13-1 expression. Only when Munc13-2 was deleted in addition to Munc13-1, AndromeDA hotspots were abolished and DA release remained at background levels in these cultures during neuronal stimulation. Therefore, I conclude that Munc13-2 is also involved, to some extent, in DA release.

In interpreting these data, it is important to consider that the breeding scheme used in this study could not yield WT littermate neurons, expressing two copies of the genes encoding Munc13-1 and -2 for comparison with Munc13 KO mutants. Instead, mice that were either heterozygous or homozygous for Munc13-2 deletion were pooled and used as a control group. This was done due to the observation that Munc13-2 KOs showed DA release indistinguishable from non-littermate WT neurons. In terms of electrically evoked DA release, I conclude that Munc13-2 deletion is fully compensated for by Munc13-1 expression in DAergic neurons. However, a comparison with all these Munc13 mutants against WT littermates would be informative. One limitation of these experiments was the relatively low number of neurons analyzed of each genotype, which was a direct result of the variety of different genotypes possible from the breeding scheme used. Increasing the number of mice analyzed from each genotype would potentially help to clarify some of the trends towards reduced DA release. This was not done as a part of my study, as the primary purpose was to determine whether Munc13-dependent priming was required for DA release, which is clearly established by the abolition of DA release in Munc13 DKO mice. Moreover, while my ICC data indicates, that Munc13-2 is not present at DAergic active zones, it is possible that it is expressed at low levels below the detection limit of my immunolabeling, and thus contributes to evoked DA release.

In summary, my data indicates that while Munc13-1 is the only detectable isoform at DAergic active zones, deletion of both Munc13-1 and -2 is necessary to abolish DA release as measured using AndromeDA, indicating that Munc13-2 might play a role in regulating DA release. This result is further supported by a recent preprint from Banerjee and colleagues, that implicates Munc13 proteins in DA release (Banerjee et al., 2020a).

4.2.4 KCl treatment evokes DA release that is mechanistically distinct from action potential-evoked DA release

Unexpectedly, all examined Munc13 DKO neurons exhibited KCl induced DA release indistinguishable from the control cells, including AndromeDA hotspots that indicate DA release events at varicosities. This is a puzzling result, given that the genetic deletion of Munc13-1 and Munc13-2 abolished electrically evoked DA secretion in the same axons. These findings indicate that, while SV priming by Munc13 proteins is required for DA release evoked by action potentials, Munc13 is not required for KCl evoked axonal DA release. The possibility, that AndromeDA hotspots from Munc13 DKO neurons were not representative of DA secretion events can be excluded, since the specificity of AndromeDA for DA has been thoroughly validated. While KCl itself does mediate a small

activation (~10%) of AndromeDA in the absence of DAergic neurons, the activation mediated by KCl stimulation of DAergic neurons is significantly greater and is sensitive to alterations in the SV content of DA. Further, the spatial association of KCl evoked hotspots in Munc13 DKO cultures indicates that KCl evokes *bona fide* DA release from discrete release sites. It is therefore necessary to consider why DA release by electrical stimulation is abolished by Munc13 deletion but KCl evoked DA release is apparently unaffected.

The first possibility to consider is that Munc13-3, which was not deleted in my mutant mice, facilitates KCl evoked DA release but not action potential-stimulated release. However, it is unlikely that Munc13-3 alone maintained the observed high KCl induced DA secretion levels, given that my cytochemical data indicates the absence of Munc13-3 at DAergic active zones, and previous WB analysis did not detect Munc13-3 in the striatum (Augustin et al., 1999a). The ICC data, however, was obtained from DAergic neurons derived from a mouse line in which Munc13-3 was fluorescently labeled with EGFP (Cooper et al., 2012). The Munc13-1/2 DKO, in contrast, was derived by breeding two mouse lines in which Munc13-1 or Munc13-2 alleles were constitutively removed (Augustin et al., 1999b; Varoqueaux et al., 2002). Therefore, it cannot be ruled out that Munc13-3 was upregulated in the Munc13-1/2 DKO cells during neuronal development and compensated for Munc13 loss in live cell experiments. *Post-hoc* immunolabeling of the DAergic varicosities that were subject to AndromeDA imaging could reveal, if Munc13-3 was upregulated in these axons. However, it would be expected that this compensatory effect would also be evident during electrical stimulation. Munc13-1/2 DKO neurons showed no evidence of electrically evoked-DA secretion nor hotspots. Overall, I conclude that Munc13-3 mediated priming of SVs in KCl evoked DA release is an unlikely explanation for my data.

A more likely explanation for the high degree of DA secretion evoked by KCl in Munc13-1/2 DKO neurons is that the mechanisms of DA release driven by electrical stimulation, which induces action potentials, and KCl evoked depolarization are distinct.

The ability of a neuron to initiate action potentials and to maintain the negative membrane potential at rest is determined mainly by K^+ and Na^{2+} gradients across the plasma membrane. Under physiological conditions, the K^+ concentration within the cell is higher than in the ECS, resulting in a strong electrochemical driving force for K^+ to move outside of the cell. Because the neuronal plasma membrane at rest is highly permeable to K^+, the membrane potential is determined by the electrochemical equilibrium of K^+ currents

across the plasma membrane. Na^{2+} concentrations are higher in the ECS than inside the cell, but the Na^{2+} conductance is low, because the neuronal plasma membrane is not permeable to Na^{2+} ions at rest. K^+ cations, on the other hand, are constantly leaking into the ECS and are transported back by ATP-dependent ion pumps which maintain the K^+ and Na^{2+} gradients, and therefore the resting potential of the membrane. An action potential is initiated, when voltage-gated sodium and potassium channels located on the axon hillock open sequentially, resulting in a brief, local membrane depolarization (due to Na^{2+} influx), followed by a brief local hyperpolarization (due to K^+ efflux) – which are the two phases of the action potential. The resting potential is rapidly restored afterwards by ATP-driven ion pumps. The induced action potential propagates along the axonal membrane, until it reaches a synaptic terminal and causes neurotransmitter release through the local molecular SV fusion machinery. Electrical field stimulation causes action potential firing in cultured neurons (Ryan et al., 1997) by briefly altering the resting membrane potential, leading to the initiation of an action potential in the axon (Ye and Steiger, 2015). Electrical field stimulation therefore evokes release by inducing a physiological mechanism by which DA release occurs in neurons of the brain.

KCl induced depolarization occurs via a distinct mechanism. Instead of briefly triggering the activation of voltage-gated ion channels to drive action potentials, elevation of the extracellular K^+ concentration collapses the physiological K^+ gradient across the neuronal plasma membrane. The driving force for K^+ ions to exit the neuron reduces and may even reverse, leading to K^+ influx into the cell cytosol. The neuronal membrane depolarizes globally, until the threshold for opening voltage-gated Ca^{2+} is reached, leading to Ca^{2+} influx and Ca^{2+} triggered neurotransmitter secretion. KCl induced depolarization is therefore a very strong stimulus that leads to neurotransmitter secretion, but also renders the neuron incapable of initiating new action potentials as long as the physiological ion gradients are disturbed. KCl mediated depolarization is experimentally simple compared to field stimulation, and is widely used in spite of its limitations in terms of physiological relevance. I used KCl treatment primarily as a strong stimulus to examine the viability of the neuronal cultures, and to validate that the examined cultures were capable of secreting DA.

Given the differences in the way that the two stimuli depolarize neurons, it is possible that the molecular mechanisms that drive action potential-evoked DA release and DA release evoked by KCl depolarization are distinct. This interpretation is supported by my observation that hotspots, indicating DA release events, are induced at distinct axonal sites by 20 Hz stimulation compared to KCl. My findings are also consistent with a

previous study addressing DA release from striatal varicosities with FFNs (Pereira et al., 2016). This study reported that varicosities that did not exhibit exocytosis during 15 Hz electrical stimulation exhibited exocytosis when subsequently stimulated with 40 mM KCl. Furthermore, varicosities that responded initially to electrical stimulation showed a significant decrease in their response when then stimulated with KCl. These data support the notion that the two stimuli mediate different responses in cells. Another later study (Banerjee et al., 2020b) found that the genetic deletion of SYT1 abolished electrically evoked DA release measured in striatal slices by amperometry, but DA release evoked by local K^+ application was not altered in SYT1 KO mice, consistent with my proposition that these two stimulation methods act on DAergic neurons through distinct mechanisms. I therefore propose that the distinct results obtained using action potential and KCl evoked DA release in Munc13 DKO neurons are the result of the two depolarization methods inducing distinct mechanisms of DA release. Since action potential-induced release is representative of a physiological DA release mechanism, I conclude that Munc13s are required for physiologically relevant DA release. As KCl induced depolarization is a widespread method for studying neurotransmitter release (Rienecker et al., 2020), including DA secretion, my findings indicate that data from chemically stimulated cells should be interpreted with caution.

The KCl solution used in the study was not adjusted for osmolarity, and cells were therefore subject to osmotic shock, in addition to neuronal depolarization, when KCl was added to the extracellular solution. Hypertonic sucrose, which induces an osmotic shock to neurons, triggers secretion by inducing the fusion of docked SVs (Rosenmund and Stevens, 1996; Stevens and Tsujimoto, 1995). However, it is unlikely that the change in osmolarity caused by KCl addition explains my data, since the fusion of SVs requires Munc13-mediated priming in other neurotransmitter systems. In glutamatergic synapses, the deletion of Munc13-1 and Munc13-2 renders SV incapable of “docking” to the plasma membrane (Imig et al., 2014), leading to a complete absence of an RRP. This lack of physical docking completely abolishes neurotransmitter release, even when neurons are treated with a pulse of hypertonic sucrose solution (Augustin et al., 1999b). The discrepancy between the electrically evoked and chemically evoked DA release in Munc13-DKO mutants is therefore unlikely due to osmotic shock of the neurons by elevated KCl.

Moreover, the mechanism of DA release evoked by KCl application remains unclear. SVs in DAergic neurons lacking Munc13s may be presumed to lack docked/primed SVs, given the lack of electrically evoked DA release. Thus, there should be no SVs physically

docked to undergo evoked release when depolarized with KCl. However, DA uptake by DAT is coupled to an inward-directed Na^+ gradient and requires a negative membrane potential. It was observed that reversing the Na^+ gradient in combination with membrane depolarization induced DA efflux through DAT (Chen and Reith, 2004). It is therefore possible that application of KCl in my experiments may have mediated release via non-vesicular mechanisms, such as reversal of DAT activity. This would result in transport of DA out of the neuron into the ECS, though it is unclear whether this would result in localized hotspots of AndromeDA activation. Immunolabeling of DAT in murine DAergic neurons indicates that the protein is present at varicosities and axonal segments in-between varicosities (Daniel 2009). Thus, while I conclude that the KCl evoked release of DA is mechanistically distinct from electrically evoked DA, further research is required to dissect this phenomenon. Given the limited physiological relevance of KCl evoked DA release, and the clear result regarding the dependence of electrically evoked release on Munc13-1 and -2, the further examination of Munc13-independent, KCl evoked DA release lays outside of the scope of this project.

4.3 Future directions

AndromeDA is an ideal tool to interrogate the molecular regulation of DA release at subcellular structures, such as DAergic varicosities, and complements the growing toolkit of optical methods available for the direct detection of DA release. Future studies will utilize AndromeDA to characterize proteins at individual synapses, for example, by *post-hoc* immunolabeling of neuron cultures after AndromeDA imaging, using a coordinate grid system on the coverslip that allows the return to the imaged region and overlay fluorescent labeling of synaptic structures with regions that secreted DA (Daniel et al., 2009). Another possibility is the use of fluorescently-labeled synaptic proteins, delivered either by viral transduction in genetically engineered mice, those presence can be directly observed during live cell imaging. AndromeDA allows multiplexing with all commonly used fluorophores and therefore facilitates, for the first time, the direct linkage of DA-secreting structures with molecules present at the secretion site.

It would be interesting to combine AndromeDA with previously employed exocytosis assays to investigate the proportion of varicosities that secrete neurotransmitters but not DA. These studies could also utilize optical glutamate or GABA sensors (Helassa et al., 2018; Masharina et al., 2012; Namiki et al., 2007; Okubo et al., 2010) and resolve questions such as whether DA secretion and the co-release of glutamate or GABA is segregated from distinct varicosity populations (Descarries et al., 2008; Fortin et al., 2019; Sulzer and Rayport, 2000; Trudeau et al., 2014; Zhang et al., 2015). Furthermore, AndromeDA should be used to investigate distinct modes of axonal firing in VM neurons, as it is possible, for example, that tonic and phasic DA release occur from distinct axonal structures, which could not be examined using previous methods. The capacity of AndromeDA to investigate DA release from DAergic somata and dendrites should also be explored, as this would allow a deeper characterization of the distinct secretion pathways employed by DAergic neurons.

DAergic neurons are classically defined by virtue of the fact that they secrete DA. It has become increasingly clear, however, that VM neurons comprise diverse neuronal populations. At a minimum, VTA DAergic neurons should be investigated separately from SNc neurons, those independent cultivation is relatively simple to achieve due to their anatomical separation (Björklund and Dunnett, 2007; Lautenschläger et al., 2018). VTA DAergic neurons differ substantially from SNc DAergic neurons, as shown by their distinct susceptibility in Parkinson’s disease, as well as their distinct gene expression and physiology (Fu et al., 2012; Pan and Ryan, 2012; Reyes et al., 2012). However,

recent literature proposes even up to seven neuronal subtypes in the VM, that vary with respect to their gene expression profiles, target projections and physiological properties such as firing rate (Bodea and Blaess, 2015; Morales and Margolis, 2017; Poulin et al., 2020; Tiklová et al., 2019). This highlights the heterogeneity of the DA system not only across varicosities but also across neuronal populations. Characterization of each of these subtypes is relevant for the understanding of how DAergic transmission controls brain function and behavior, and can be addressed by independent cultivation of DAergic neuronal sub-populations, for example, by fluorophore expression under promoters of known genetic markers with subsequent fluorescence-activated cell sorting (FACS).

In this context, the dependency of Munc13-mediated SV priming should be further investigated with an emphasis on the role of individual Munc13 isoforms at discrete release sites. For example, future studies could utilize AndromeDA to link the presence of Munc13 isoforms at individual DAergic varicosities to AndromeDA hotspots observed at these varicosities, which could be compared across FACS-sorted DAergic neuron populations. In addition, my observation of a Munc13-independent mechanism of DA secretion should be further dissected. Application of hypertonic sucrose solutions in combination with a DAT inhibitor such as nomifensine to DAergic Munc13-1/2 DKO cultures could help understand if the observed KCl evoked DA secretion is a result of reversed DAT activity. The fluorescent labeling of DAT during AndromeDA imaging would furthermore reveal, if KCl evoked AndromeDA hotspots occur at sites with locally high DAT concentrations, which could provide an explanation for the observation of hotspots in the absence of SV clusters.

AndromeDA is inexpensive and readily applicable to any *in vitro* system, and will be of particular use in systems where an *in vitro* approach is required, such as examining human-derived neurons or high-throughput drug screening. Cellular models of human disease with aberrant DA function, such as neurons derived from human Parkinson's disease patients, can be studied with AndromeDA, which would contribute not only to a better understanding of the pathophysiological mechanisms involved but also to the development of a more effective treatment for these conditions.

In summary, Imaging DA release using AndromeDA is versatile, with an unprecedented ability to image DA release sites across large varicosity populations, and will enable a better understanding the synaptic diversity of DA transmission and the underlying molecular machinery involved.

5 Supplementary Figures

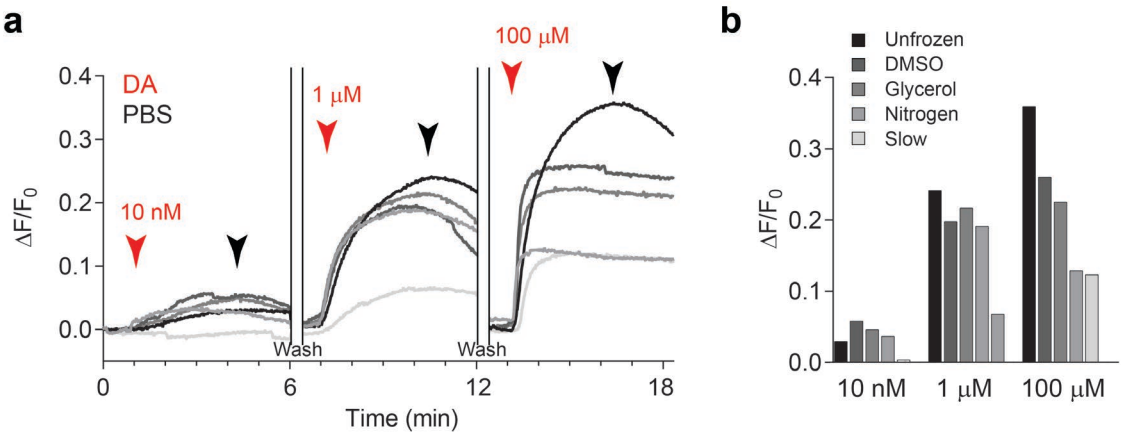

Figure 36: Freezing nanosensors impairs their responsiveness to DA.
The Nanosensor stock was kept for a maximum of three weeks and discarded afterwards to ensure good quality sensors. Sensors can reaggregate over time and lose responsiveness to DA. The possibility of freezing the Nanosensor stock for storage was explored, which would prolong the time a single Nanosensor stock could be used, and would also allow the use of freshly thawed aliquots that are derived from an identical nanosensor batch. This could potentially reduce nanosensor batch-to-batch variations in between experiments, as different batches vary in their responsiveness to DA, and shorten the time required for the preparation of live cell experiments. **a**, Plots showing average nanosensor NIR fluorescence during the perfusion of nanosensor surfaces with increasing DA concentrations (10 nM, 1μM, or 100 μM). DA was applied freshly dissolved in PBS at the time point shown (red arrowheads), followed by a PBS wash to remove the DA (black arrowheads). Imaging was temporarily stopped after 6 min (indicated by breaks in the *x*-axis) and washing continued for 10 min in-between DA treatments. The black trace represents nanosensors that were kept at 4°C after preparation (unfrozen, black trace) for three weeks. Gray traces represent nanosensor aliquots from the same batch that were frozen at –20°C (at 30 μL) using different methods. Nanosensors were either frozen by simply placing an aliquot into a –20°C freezer, thereby causing slow freezing of the sample (Slow); by snap-freezing in liquid nitrogen, causing a rapid freezing (Nitrogen); or by snap-freezing in 10% glycerol (Glycerol) or 10% DMSO (DMSO). **b,** Maximum peak responses of traces shown in a**.** *n* = 1 nanosensor batch.

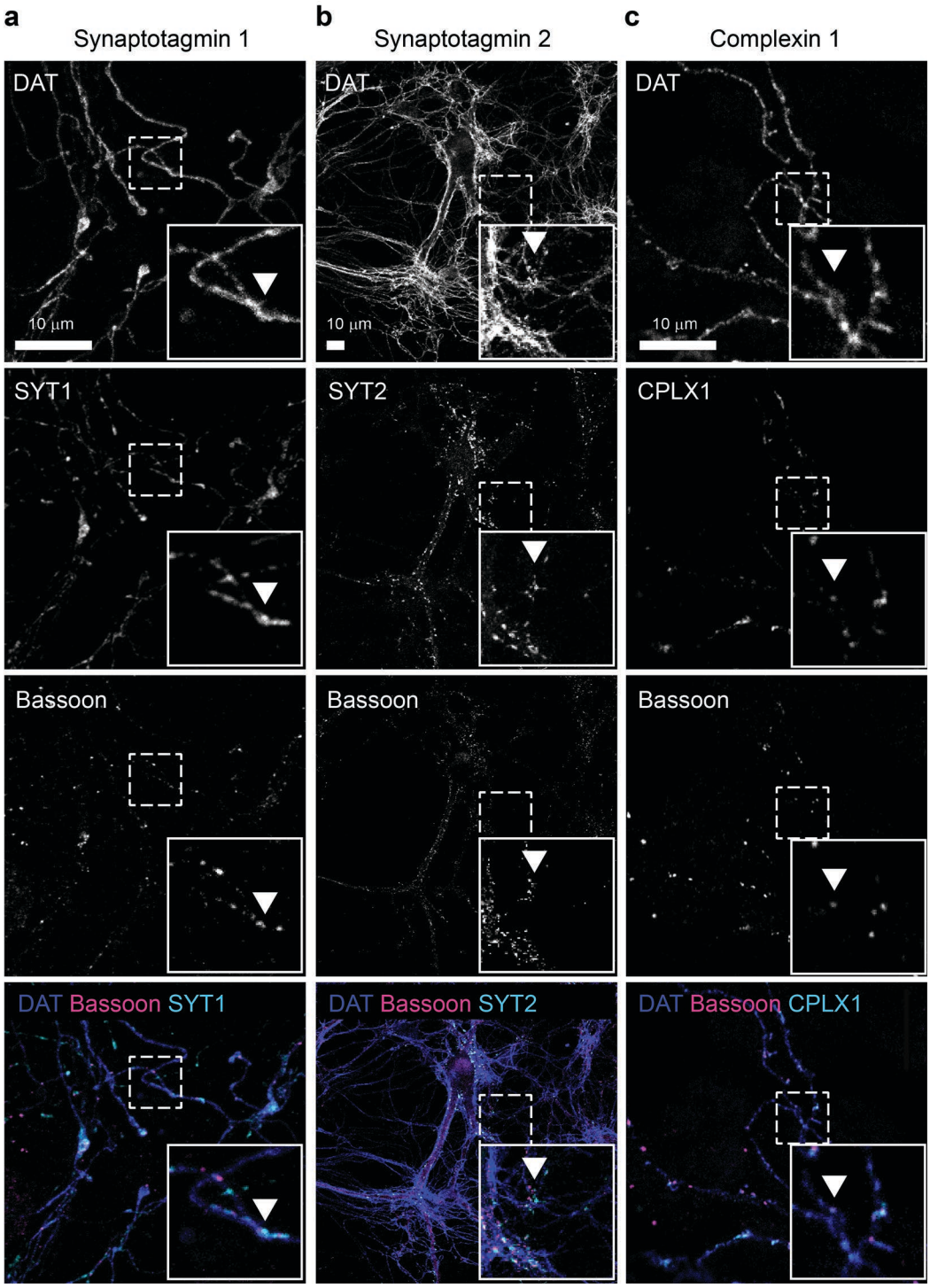

Figure 37: Presynaptic proteins at DAergic active zones – SYT1, SYT2 and CPLX1.
VM neurons are shown with immunolabeling against DAT, bassoon and either SYT1 (**a**) SYT2 (**b**) or CPLX1 (**c**) as indicated. The lower panels show the three channels overlaid, with DAT in blue, bassoon in magenta and the presynaptic protein of interest in cyan. The region indicated by a white dashed box in each panel is shown in higher detail inset. Examples of bassoon-positive puncta within DAergic, DAT positive axons that were also positive for the protein of interest are highlighted by white arrowheads. Scale bar = 10 µm.

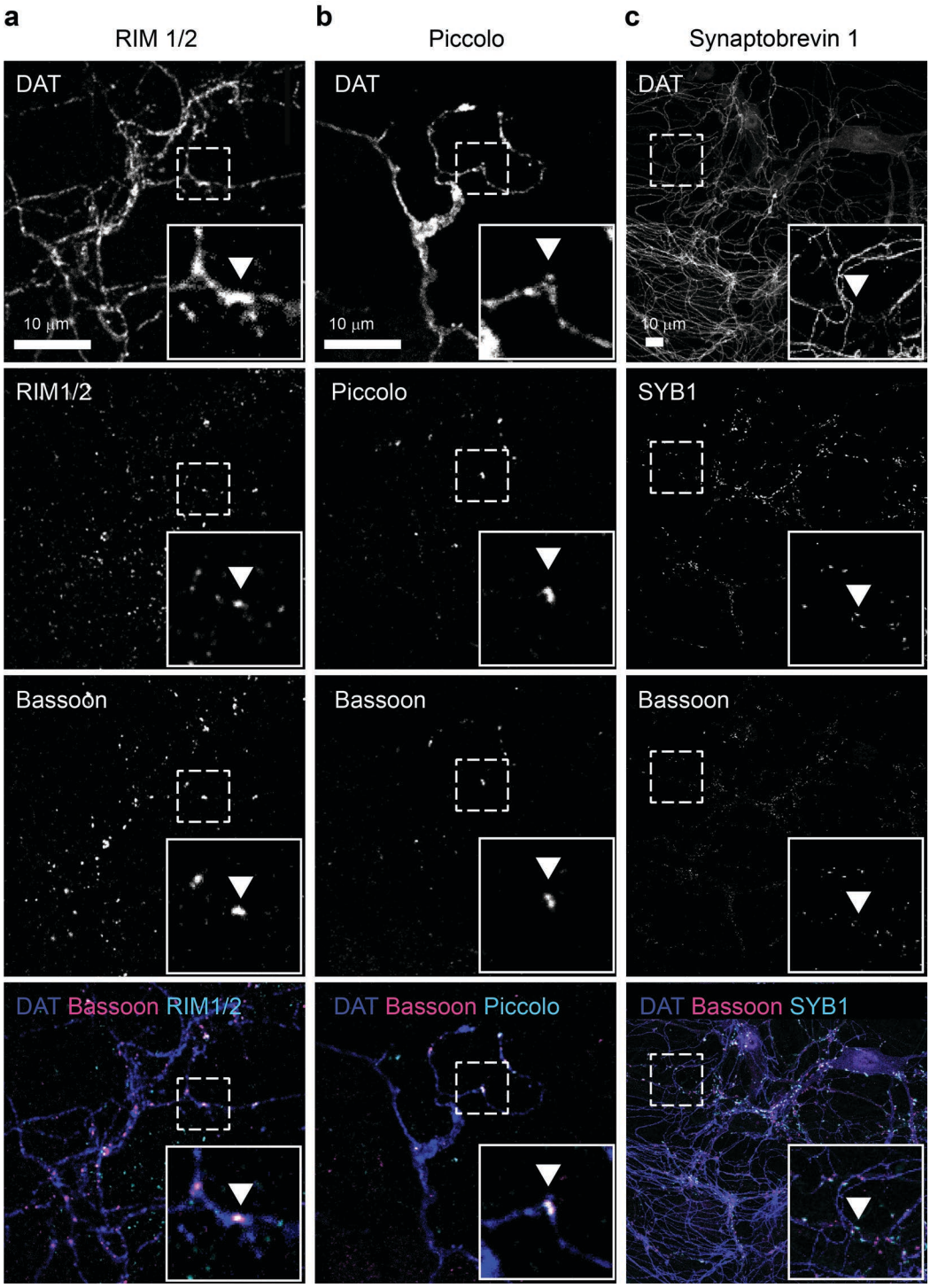

Figure 38: Presynaptic proteins at DAergic active zones – RIM1/2, piccolo and SYB1.
VM neurons are shown with immunolabeling against DAT, bassoon and either RIM1/2(**a**), piccolo (**b**) or SYB1 **(c)**, as indictaed. The lower panels show the three channels overlaid, with DAT in blue, bassoon in magenta and the presynaptic protein of interest in cyan. The region indicated by a white dashed box in each panel is shown in higher detail inset. Examples of bassoon-positive puncta within DAergic, DAT positive axons that were also positive for the protein of interest are highlighted by white arrowheads. Scale bar = 10 µm.

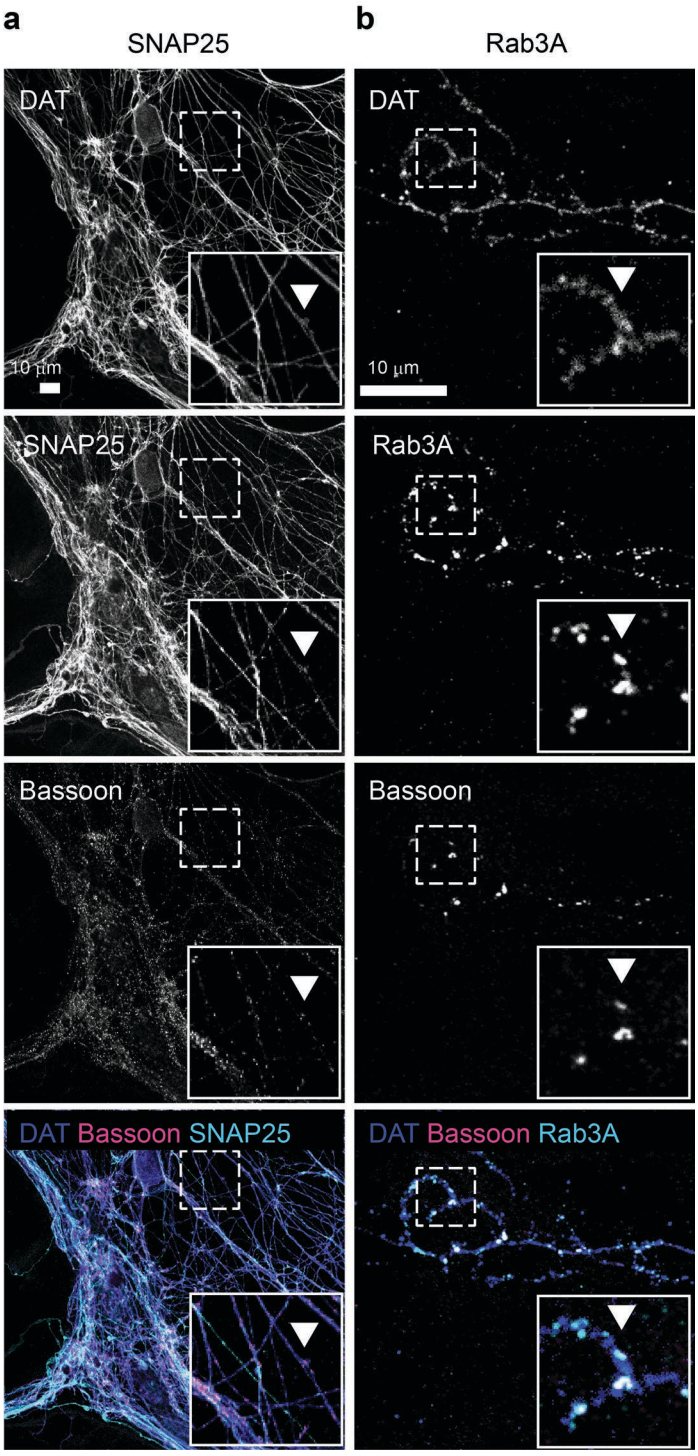

Figure 39: Presynaptic proteins at DAergic active zones – SNAP25 and Rab3A.
VM neurons are shown with immunolabeling against DAT, bassoon and either SNAP25 (**a**) or rab3A (**b**), as indicated. The lower panels show the three channels overlaid, with DAT in blue, bassoon in magenta and the presynaptic protein of interest in cyan. The region indicated by a white dashed box in each panel is shown in higher detail inset. Examples of bassoon-positive puncta within DAergic, DAT positive axons that were also positive for the protein of interest are highlighted by white arrowheads. Scale bar = 10 µm.

6 Bibliography

Abeliovich, A., Schmitz, Y., Fariñas, I., Choi-Lundberg, D., Ho, W.H., Castillo, P.E., Shinsky, N., Verdugo, J.M., Armanini, M., Ryan, A., Hynes, M., Phillips, H., Sulzer, D., Rosenthal, A., 2000. Mice lacking alpha-synuclein display functional deficits in the nigrostriatal dopamine system. Neuron 25, 239–252. doi:10.1016/s0896-6273(00)80886-7

Anwar, S., Peters, O., Millership, S., Ninkina, N., Doig, N., Connor-Robson, N., Threlfell, S., Kooner, G., Deacon, R.M., Bannerman, D.M., Bolam, J.P., Chandra, S.S., Cragg, S.J., Wade-Martins, R., Buchman, V.L., 2011. Functional alterations to the nigrostriatal system in mice lacking all three members of the synuclein family. J. Neurosci. 31, 7264–7274. doi:10.1523/JNEUROSCI.6194-10.2011

Arluison, M., Dietl, M., Thibault, J., 1984. Ultrastructural morphology of dopaminergic nerve terminals and synapses in the striatum of the rat using tyrosine hydroxylase immunocytochemistry: A topographical study. Brain Res. Bull. 13, 269–285. doi:10.1016/0361-9230(84)90128-X

Augustin, I., Betz, A., Herrmann, C., Jo, T., Brose, N., 1999a. Differential expression of two novel Munc13 proteins in rat brain. Biochem. J. 337 (Pt 3), 363–371. doi:10.1042/0264-6021:3370363

Augustin, I., Korte, S., Rickmann, M., Kretzschmar, H.A., Südhof, T.C., Herms, J.W., Brose, N., 2001. The cerebellum-specific Munc13 isoform Munc13-3 regulates cerebellar synaptic transmission and motor learning in mice. J. Neurosci. 21, 10–17.

Augustin, I., Rosenmund, C., Südhof, T.C., Brose, N., 1999b. Munc13-1 is essential for fusion competence of glutamatergic synaptic vesicles. Nature 400, 457–461. doi:10.1038/22768

Bachilo, S.M., Strano, M.S., Kittrell, C., Hauge, R.H., Smalley, R.E., Weisman, R.B., 2002. Structure-assigned optical spectra of single-walled carbon nanotubes. Science 298, 2361–2366. doi:10.1126/science.1078727

Banerjee, A., Imig, C., Balakrishnan, K., Kershberg, L., Lipstein, N., Uronen, R.-L., Wang, J., Cai, X., Benseler, F., Rhee, J.S., Cooper, B.H., Liu, C., Wojcik, S.M., Brose, N., Kaeser, P.S., 2020a. Molecular and functional architecture of striatal dopamine release sites. BioRxiv. doi:10.1101/2020.11.25.398255

Banerjee, A., Lee, J., Nemcova, P., Liu, C., Kaeser, P.S., 2020b. Synaptotagmin-1 is the Ca2+ sensor for fast striatal dopamine release. Elife 9. doi:10.7554/eLife.58359

Beaulieu, J.M., Espinoza, S., Gainetdinov, R.R., 2015. Dopamine receptors - IUPHAR Review 13. Br. J. Pharmacol. 172, 1–23. doi:10.1111/bph.12906

Bergquist, F., Ludwig, M., 2008. Dendritic transmitter release: a comparison of two model systems. J. Neuroendocrinol. 20, 677–686. doi:10.1111/j.1365-2826.2008.01714.x

Bergquist, F., Niazi, H.S., Nissbrandt, H., 2002. Evidence for different exocytosis pathways in dendritic and terminal dopamine release in vivo. Brain Res. 950, 245–253. doi:10.1016/s0006-8993(02)03047-0

Berke, J.D., 2018. What does dopamine mean? Nat. Neurosci. 21, 787–793. doi:10.1038/s41593-018-0152-y

Beyene, A.G., Delevich, K., Del Bonis-O'Donnell, J.T., Piekarski, D.J., Lin, W.C., Thomas, A.W., Yang, S.J., Kosillo, P., Yang, D., Prounis, G.S., Wilbrecht, L., Landry, M.P., 2019. Imaging striatal dopamine release using a nongenetically encoded near infrared fluorescent catecholamine nanosensor. Sci. Adv. 5, eaaw3108. doi:10.1126/sciadv.aaw3108

Bianco, A., Kostarelos, K., Prato, M., 2005. Applications of carbon nanotubes in drug delivery. Curr. Opin. Chem. Biol. 9, 674–679. doi:10.1016/j.cbpa.2005.10.005

Bisker, G., Dong, J., Park, H.D., Iverson, N.M., Ahn, J., Nelson, J.T., Landry, M.P., Kruss, S., Strano, M.S., 2016. Protein-targeted corona phase molecular recognition. Nat. Commun. 7, 10241. doi:10.1038/ncomms10241

Björklund, A., Dunnett, S.B., 2007. Dopamine neuron systems in the brain: an update. Trends Neurosci. 30, 194–202. doi:10.1016/j.tins.2007.03.006

Borland, L.M., Shi, G., Yang, H., Michael, A.C., 2005. Voltammetric study of extracellular dopamine near microdialysis probes acutely implanted in the striatum of the anesthetized rat. J. Neurosci. Methods 146, 149–158. doi:10.1016/j.jneumeth.2005.02.002

Breustedt, J., Gundlfinger, A., Varoqueaux, F., Reim, K., Brose, N., Schmitz, D., 2010. Munc13-2 differentially affects hippocampal synaptic transmission and plasticity. Cereb. Cortex 20, 1109–1120. doi:10.1093/cercor/bhp170

Brimblecombe, K.R., Gracie, C.J., Platt, N.J., Cragg, S.J., 2015. Gating of dopamine transmission by calcium and axonal N-, Q-, T- and L-type voltage-gated calcium channels differs between striatal domains. J. Physiol. (Lond.) 593, 929–946. doi:10.1113/jphysiol.2014.285890

Bucher, E.S., Wightman, R.M., 2015. Electrochemical analysis of neurotransmitters. Annu. Rev. Anal. Chem. (Palo Alto, Calif.) 8, 239–261. doi:10.1146/annurev-anchem-071114-040426

Burgalossi, A., Jung, S., Man, K.M., Nair, R., Jockusch, W.J., Wojcik, S.M., Brose, N., Rhee, J.-S., 2012. Analysis of neurotransmitter release mechanisms by photolysis of caged Ca^{2+} in an autaptic neuron culture system. Nat. Protoc. 7, 1351–1365. doi:10.1038/nprot.2012.074

Byrd, J.C., Hadjiconstantinou, M., Cavalla, D., 1986. Epinephrine synthesis in the PC12 pheochromocytoma cell line. Eur. J. Pharmacol. 127, 139–142. doi:10.1016/0014-2999(86)90216-5

Carboni, E., Imperato, A., Perezzani, L., Di Chiara, G., 1989. Amphetamine, cocaine, phencyclidine and nomifensine increase extracellular dopamine concentrations preferentially in the nucleus accumbens of freely moving rats. Neuroscience 28, 653–661. doi:10.1016/0306-4522(89)90012-2

Cardozo, D.L., 1993. Midbrain dopaminergic neurons from postnatal rat in long-term primary culture. Neuroscience 56, 409–421. doi:10.1016/0306-4522(93)90342-d

Carlsson, A., 1959. The occurrence, distribution and physiological role of catecholamines in the nervous system. Pharmacol. Rev. 11, 490–493.

Cha, C., Shin, S.R., Annabi, N., Dokmeci, M.R., Khademhosseini, A., 2013. Carbon-based nanomaterials: multifunctional materials for biomedical engineering. ACS Nano 7, 2891–2897. doi:10.1021/nn401196a

Chanaday, N.L., Cousin, M.A., Milosevic, I., Watanabe, S., Morgan, J.R., 2019. The Synaptic Vesicle Cycle Revisited: New Insights into the Modes and Mechanisms. J. Neurosci. 39, 8209–8216. doi:10.1523/JNEUROSCI.1158-19.2019

Chandra, S., Fornai, F., Kwon, H.-B., Yazdani, U., Atasoy, D., Liu, X., Hammer, R.E., Battaglia, G., German, D.C., Castillo, P.E., Südhof, T.C., 2004. Double-knockout mice for alpha- and beta-synucleins: effect on synaptic functions. Proc. Natl. Acad. Sci. USA 101, 14966–14971. doi:10.1073/pnas.0406283101

Charlson, F.J., Ferrari, A.J., Santomauro, D.F., Diminic, S., Stockings, E., Scott, J.G., McGrath, J.J., Whiteford, H.A., 2018. Global epidemiology and burden of schizophrenia: findings from the global burden of disease study 2016. Schizophr. Bull. 44, 1195–1203. doi:10.1093/schbul/sby058

Chen, N., Reith, M.E.A., 2004. Interaction between dopamine and its transporter: role of intracellular sodium ions and membrane potential. J. Neurochem. 89, 750–765. doi:10.1111/j.1471-4159.2004.02409.x

Chernikov, I.V., Vlassov, V.V., Chernolovskaya, E.L., 2019. Current Development of siRNA Bioconjugates: From Research to the Clinic. Front. Pharmacol. 10, 444. doi:10.3389/fphar.2019.00444

Clements, J.D., Lester, R.A., Tong, G., Jahr, C.E., Westbrook, G.L., 1992. The time course of glutamate in the synaptic cleft. Science 258, 1498–1501. doi:10.1126/science.1359647

Cognet, L., Tsyboulski, D.A., Rocha, J.-D.R., Doyle, C.D., Tour, J.M., Weisman, R.B., 2007. Stepwise quenching of exciton fluorescence in carbon nanotubes by single-molecule reactions. Science 316, 1465–1468. doi:10.1126/science.1141316

Cools, R., 2006. Dopaminergic modulation of cognitive function-implications for L-DOPA treatment in Parkinson's disease. Neurosci. Biobehav. Rev. 30, 1–23. doi:10.1016/j.neubiorev.2005.03.024

Cooper, B., Hemmerlein, M., Ammermüller, J., Imig, C., Reim, K., Lipstein, N., Kalla, S., Kawabe, H., Brose, N., Brandstätter, J.H., Varoqueaux, F., 2012. Munc13-independent vesicle priming at mouse photoreceptor ribbon synapses. J. Neurosci. 32, 8040–8052. doi:10.1523/JNEUROSCI.4240-11.2012

Cousin, M.A., Pocock, J.M., Nicholls, D.G., 1995. Intracellular free Ca2+ responses in electrically stimulated cerebellar granule cells. Biochem. Soc. Trans. 23, 648–652. doi:10.1042/bst0230648

Cragg, S.J., Nicholson, C., Kume-Kick, J., Tao, L., Rice, M.E., 2001. Dopamine-mediated volume transmission in midbrain is regulated by distinct extracellular geometry and uptake. J. Neurophysiol. 85, 1761–1771. doi:10.1152/jn.2001.85.4.1761

Cragg, S.J., Rice, M.E., 2004. DAncing past the DAT at a DA synapse. Trends Neurosci. 27, 270–277. doi:10.1016/j.tins.2004.03.011

Dal Bo, G., St-Gelais, F., Danik, M., Williams, S., Cotton, M., Trudeau, L.-E., 2004. Dopamine neurons in culture express VGLUT2 explaining their capacity to release glutamate at synapses in addition to dopamine. J. Neurochem. 88, 1398–1405. doi:10.1046/j.1471-4159.2003.02277.x

Daniel, J.A., Galbraith, S., Iacovitti, L., Abdipranoto, A., Vissel, B., 2009. Functional heterogeneity at dopamine release sites. J. Neurosci. 29, 14670–14680. doi:10.1523/JNEUROSCI.1349-09.2009

Descarries, L., Bérubé-Carrière, N., Riad, M., Bo, G.D., Mendez, J.A., Trudeau, L.-E., 2008. Glutamate in dopamine neurons: synaptic versus diffuse transmission. Brain Res. Rev. 58, 290–302. doi:10.1016/j.brainresrev.2007.10.005

Descarries, L., Watkins, K.C., Garcia, S., Bosler, O., Doucet, G., 1996. Dual character, asynaptic and synaptic, of the dopamine innervation in adult rat neostriatum: a quantitative autoradiographic and immunocytochemical analysis. J. Comp. Neurol. 375, 167–186. doi:10.1002/(SICI)1096-9861(19961111)375:2<167::AID-CNE1>3.0.CO;2-0

Dinarvand, M., Elizarova, S., Daniel, J., Kruss, S., 2020. Imaging of Monoamine Neurotransmitters with Fluorescent Nanoscale Sensors. Chempluschem 85, 1465–1480. doi:10.1002/cplu.202000248

Ducrot, C., Bourque, M.-J., Delmas, C.V.L., Racine, A.-S., Bello, D.G., Delignat-Lavaud, B., Lycas, M.D., Fallon, A., Michaud-Tardif, C., Burke Nanni, S., Herborg, F., Gether, U., Nanci, A., Takahashi, H., Parent, M., Trudeau, L.-E., 2020. Dopaminergic neurons establish a distinctive axonal arbor with a majority of non-synaptic terminals. BioRxiv. doi:10.1101/2020.05.11.088351

Elizarova, S., Chouaib, A., Shaib, A., Mann, F., Brose, N., Kruss, S., Daniel, J.A., 2021. A fluorescent nanosensor paint reveals the heterogeneity of dopamine release from neurons at individual release sites. BioRxiv. doi:10.1101/2021.03.28.437019

Engele, J., Schubert, D., Bohn, M.C., 1991. Conditioned media derived from glial cell lines promote survival and differentiation of dopaminergic neurons in vitro: role of mesencephalic glia. J. Neurosci. Res. 30, 359–371. doi:10.1002/jnr.490300212

Ewing, A.G., Bigelow, J.C., Wightman, R.M., 1983. Direct in vivo monitoring of dopamine released from two striatal compartments in the rat. Science 221, 169–171. doi:10.1126/science.6857277

Floresco, S.B., West, A.R., Ash, B., Moore, H., Grace, A.A., 2003. Afferent modulation of dopamine neuron firing differentially regulates tonic and phasic dopamine transmission. Nat. Neurosci. 6, 968–973. doi:10.1038/nn1103

Fon, E.A., Pothos, E.N., Sun, B.C., Killeen, N., Sulzer, D., Edwards, R.H., 1997. Vesicular transport regulates monoamine storage and release but is not essential for amphetamine action. Neuron 19, 1271–1283. doi:10.1016/s0896-6273(00)80418-3

Ford, C.P., 2014. The role of D2-autoreceptors in regulating dopamine neuron activity and transmission. Neuroscience 282, 13–22. doi:10.1016/j.neuroscience.2014.01.025

Fortin, G.D., Desrosiers, C.C., Yamaguchi, N., Trudeau, L.-E., 2006. Basal somatodendritic dopamine release requires snare proteins. J. Neurochem. 96, 1740–1749. doi:10.1111/j.1471-4159.2006.03699.x

Fortin, G.M., Ducrot, C., Giguère, N., Kouwenhoven, W.M., Bourque, M.-J., Pacelli, C., Varaschin, R.K., Brill, M., Singh, S., Wiseman, P.W., Trudeau, L.-É., 2019. Segregation of dopamine and glutamate release sites in dopamine neuron axons: regulation by striatal target cells. FASEB J. 33, 400–417. doi:10.1096/fj.201800713RR

Fu, Y., Yuan, Y., Halliday, G., Rusznák, Z., Watson, C., Paxinos, G., 2012. A cytoarchitectonic and chemoarchitectonic analysis of the dopamine cell groups in the substantia nigra, ventral tegmental area, and retrorubral field in the mouse. Brain Struct. Funct. 217, 591–612. doi:10.1007/s00429-011-0349-2

Gasbarri, A., Sulli, A., Packard, M.G., 1997. The dopaminergic mesencephalic projections to the hippocampal formation in the rat. Prog. Neuropsychopharmacol. Biol. Psychiatry 21, 1–22. doi:10.1016/S0278-5846(96)00157-1

German, D.C., Schlusselberg, D.S., Woodward, D.J., 1983. Three-dimensional computer reconstruction of midbrain dopaminergic neuronal populations: from mouse to man. J. Neural Transm. 57, 243–254.

Gershman, S.J., Uchida, N., 2019. Believing in dopamine. Nat. Rev. Neurosci. 20, 703–714. doi:10.1038/s41583-019-0220-7

Giraldo, J.P., Wu, H., Newkirk, G.M., Kruss, S., 2019. Nanobiotechnology approaches for engineering smart plant sensors. Nat. Nanotechnol. 14, 541–553. doi:10.1038/s41565-019-0470-6

Gonon, F., 1997. Prolonged and extrasynaptic excitatory action of dopamine mediated by D1 receptors in the rat striatum in vivo. J. Neurosci. 17, 5972–5978.

Gonon, F., Cespuglio, R., Ponchon, J.L., Buda, M., Jouvet, M., Adams, R.N., Pujol, J.F., 1978. [In vivo continuous electrochemical determination of dopamine release in rat neostriatum]. C. R. Acad. Sci. Hebd. Seances Acad. Sci. D 286, 1203–1206.

Grace, A.A., 2016. Dysregulation of the dopamine system in the pathophysiology of schizophrenia and depression. Nat. Rev. Neurosci. 17, 524–532. doi:10.1038/nrn.2016.57

Grace, A.A., Bunney, B.S., 1984a. The control of firing pattern in nigral dopamine neurons: single spike firing. J. Neurosci. 4, 2866–2876.

Grace, A.A., Bunney, B.S., 1984b. The control of firing pattern in nigral dopamine neurons: burst firing. J. Neurosci. 4, 2877–2890. doi:10.1523/JNEUROSCI.04-11-02877.1984

Greten-Harrison, B., Polydoro, M., Morimoto-Tomita, M., Diao, L., Williams, A.M., Nie, E.H., Makani, S., Tian, N., Castillo, P.E., Buchman, V.L., Chandra, S.S., 2010. αβγ-Synuclein triple knockout mice reveal age-dependent neuronal dysfunction. Proc. Natl. Acad. Sci. USA 107, 19573–19578. doi:10.1073/pnas.1005005107

Gubernator, N.G., Zhang, H., Staal, R.G.W., Mosharov, E.V., Pereira, D.B., Yue, M., Balsanek, V., Vadola, P.A., Mukherjee, B., Edwards, R.H., Sulzer, D., Sames, D., 2009. Fluorescent false neurotransmitters visualize dopamine release from individual presynaptic terminals. Science 324, 1441–1444. doi:10.1126/science.1172278

Hanssen, B.L., Siraj, S., Wong, D.K.Y., 2016. Recent strategies to minimise fouling in electrochemical detection systems. Rev. Anal. Chem. 35, 1–28. doi:10.1515/revac-2015-0008

Harreither, W., Trouillon, R., Poulin, P., Neri, W., Ewing, A.G., Safina, G., 2016. Cysteine residues reduce the severity of dopamine electrochemical fouling. Electrochim. Acta 210, 622–629. doi:10.1016/j.electacta.2016.05.124

Harvey, J.D., Baker, H.A., Ortiz, M.V., Kentsis, A., Heller, D.A., 2019. HIV detection via a carbon nanotube RNA sensor. ACS Sens. 4, 1236–1244. doi:10.1021/acssensors.9b00025

Helassa, N., Dürst, C.D., Coates, C., Kerruth, S., Arif, U., Schulze, C., Wiegert, J.S., Geeves, M., Oertner, T.G., Török, K., 2018. Ultrafast glutamate sensors resolve high-frequency release at Schaffer collateral synapses. Proc. Natl. Acad. Sci. USA 115, 5594–5599. doi:10.1073/pnas.1720648115

Held, R.G., Liu, C., Kaeser, P.S., 2016. ELKS controls the pool of readily releasable vesicles at excitatory synapses through its N-terminal coiled-coil domains. Elife 5. doi:10.7554/eLife.14862

Heller, D.A., Baik, S., Eurell, T.E., Strano, M.S., 2005. Single-Walled Carbon Nanotube Spectroscopy in Live Cells: Towards Long-Term Labels and Optical Sensors. Adv. Mater. Weinheim 17, 2793–2799. doi:10.1002/adma.200500477

Hendler-Neumark, A., Bisker, G., 2019. Fluorescent Single-Walled Carbon Nanotubes for Protein Detection. Sensors (Basel) 19. doi:10.3390/s19245403

Hnasko, T.S., Chuhma, N., Zhang, H., Goh, G.Y., Sulzer, D., Palmiter, R.D., Rayport, S., Edwards, R.H., 2010. Vesicular glutamate transport promotes dopamine storage and glutamate corelease in vivo. Neuron 65, 643–656. doi:10.1016/j.neuron.2010.02.012

Hoopmann, P., Rizzoli, S.O., Betz, W.J., 2012. Imaging synaptic vesicle recycling by staining and destaining vesicles with FM dyes. Cold Spring Harb. Protoc. 2012, 77–83. doi:10.1101/pdb.prot067603

Hsieh, J.H., Stein, D.J., Howells, F.M., 2014. The neurobiology of methamphetamine induced psychosis. Front. Hum. Neurosci. 8, 537. doi:10.3389/fnhum.2014.00537

Hyland, B.I., Reynolds, J.N.J., Hay, J., Perk, C.G., Miller, R., 2002. Firing modes of midbrain dopamine cells in the freely moving rat. Neuroscience 114, 475–492. doi:10.1016/s0306-4522(02)00267-1

Iijima, S., Ichihashi, T., 1993. Single-shell carbon nanotubes of 1-nm diameter. Nature 363, 603–605. doi:10.1038/363603a0

Imig, C., Min, S.-W., Krinner, S., Arancillo, M., Rosenmund, C., Südhof, T.C., Rhee, J., Brose, N., Cooper, B.H., 2014. The morphological and molecular nature of synaptic vesicle priming at presynaptic active zones. Neuron 84, 416–431. doi:10.1016/j.neuron.2014.10.009

Ishiyama, S., Schmidt, H., Cooper, B.H., Brose, N., Eilers, J., 2014. Munc13-3 superprimes synaptic vesicles at granule cell-to-basket cell synapses in the mouse cerebellum. J. Neurosci. 34, 14687–14696. doi:10.1523/JNEUROSCI.2060-14.2014

Jaffe, E.H., Marty, A., Schulte, A., Chow, R.H., 1998. Extrasynaptic vesicular transmitter release from the somata of substantia nigra neurons in rat midbrain slices. J. Neurosci. 18, 3548–3553.

Jiang, Y., Pei, L., Li, S., Wang, M., Liu, F., 2008. Extracellular dopamine induces the oxidative toxicity of SH-SY5Y cells. Synapse 62, 797–803. doi:10.1002/syn.20554

Jockusch, W.J., Speidel, D., Sigler, A., Sørensen, J.B., Varoqueaux, F., Rhee, J.-S., Brose, N., 2007. CAPS-1 and CAPS-2 are essential synaptic vesicle priming proteins. Cell 131, 796–808. doi:10.1016/j.cell.2007.11.002

Kawabe, H., Mitkovski, M., Kaeser, P.S., Hirrlinger, J., Opazo, F., Nestvogel, D., Kalla, S., Fejtova, A., Verrier, S.E., Bungers, S.R., Cooper, B.H., Varoqueaux, F., Wang, Y., Nehring, R.B., Gundelfinger, E.D., Rosenmund, C., Rizzoli, S.O., Südhof, T.C., Rhee, J.-S., Brose, N., 2017. ELKS1 localizes the synaptic vesicle priming protein bMunc13-2 to a specific subset of active zones. J. Cell Biol. 216, 1143–1161. doi:10.1083/jcb.201606086

Kesby, J.P., Eyles, D.W., McGrath, J.J., Scott, J.G., 2018. Dopamine, psychosis and schizophrenia: the widening gap between basic and clinical neuroscience. Transl. Psychiatry 8, 30. doi:10.1038/s41398-017-0071-9

Kile, B.M., Walsh, P.L., McElligott, Z.A., Bucher, E.S., Guillot, T.S., Salahpour, A., Caron, M.G., Wightman, R.M., 2012. Optimizing the Temporal Resolution of Fast-Scan Cyclic Voltammetry. ACS Chem. Neurosci. 3, 285–292. doi:10.1021/cn200119u

Kissinger, P.T., Hart, J.B., Adams, R.N., 1973. Voltammetry in brain tissue--a new neurophysiological measurement. Brain Res. 55, 209–213. doi:10.1016/0006-8993(73)90503-9

Klein, M.O., Battagello, D.S., Cardoso, A.R., Hauser, D.N., Bittencourt, J.C., Correa, R.G., 2019. Dopamine: Functions, Signaling, and Association with Neurological Diseases. Cell Mol. Neurobiol. 39, 31–59. doi:10.1007/s10571-018-0632-3

Koch, H., Hofmann, K., Brose, N., 2000. Definition of Munc13-homology-domains and characterization of a novel ubiquitously expressed Munc13 isoform. Biochem. J. 349, 247–253. doi:10.1042/0264-6021:3490247

Kozminski, K.D., Gutman, D.A., Davila, V., Sulzer, D., Ewing, A.G., 1998. Voltammetric and pharmacological characterization of dopamine release from single exocytotic events at rat pheochromocytoma (PC12) cells. Anal. Chem. 70, 3123–3130. doi:10.1021/ac980129f

Kruss, S., Hilmer, A.J., Zhang, J., Reuel, N.F., Mu, B., Strano, M.S., 2013. Carbon nanotubes as optical biomedical sensors. Adv. Drug Deliv. Rev. 65, 1933–1950. doi:10.1016/j.addr.2013.07.015

Kruss, S., Landry, M.P., Vander Ende, E., Lima, B.M.A., Reuel, N.F., Zhang, J., Nelson, J., Mu, B., Hilmer, A., Strano, M., 2014. Neurotransmitter detection using corona phase molecular recognition on fluorescent single-walled carbon nanotube sensors. J. Am. Chem. Soc. 136, 713–724. doi:10.1021/ja410433b

Kruss, S., Salem, D.P., Vuković, L., Lima, B., Vander Ende, E., Boyden, E.S., Strano, M.S., 2017. High-resolution imaging of cellular dopamine efflux using a fluorescent nanosensor array. Proc. Natl. Acad. Sci. USA 114, 1789–1794. doi:10.1073/pnas.1613541114

Labouesse, M.A., Cola, R.B., Patriarchi, T., 2020. GPCR-Based Dopamine Sensors-A Detailed Guide to Inform Sensor Choice for In vivo Imaging. Int. J. Mol. Sci. 21. doi:10.3390/ijms21218048

Lammel, S., Steinberg, E.E., Földy, C., Wall, N.R., Beier, K., Luo, L., Malenka, R.C., 2015. Diversity of transgenic mouse models for selective targeting of midbrain dopamine neurons. Neuron 85, 429–438. doi:10.1016/j.neuron.2014.12.036

Lautenschläger, J., Mosharov, E.V., Kanter, E., Sulzer, D., Kaminski Schierle, G.S., 2018. An Easy-to-Implement Protocol for Preparing Postnatal Ventral Mesencephalic Cultures. Front. Cell Neurosci. 12, 44. doi:10.3389/fncel.2018.00044

Liu, C., Goel, P., Kaeser, P.S., 2021. Spatial and temporal scales of dopamine transmission. Nat. Rev. Neurosci. doi:10.1038/s41583-021-00455-7

Liu, C., Kershberg, L., Wang, J., Schneeberger, S., Kaeser, P.S., 2018. Dopamine Secretion Is Mediated by Sparse Active Zone-like Release Sites. Cell 172, 706–718.e15. doi:10.1016/j.cell.2018.01.008

Ludwig, M., Apps, D., Menzies, J., Patel, J.C., Rice, M.E., 2016. Dendritic release of neurotransmitters. Compr. Physiol. 7, 235–252. doi:10.1002/cphy.c160007

Lyon, G.J., Abi-Dargham, A., Moore, H., Lieberman, J.A., Javitch, J.A., Sulzer, D., 2011. Presynaptic regulation of dopamine transmission in schizophrenia. Schizophr. Bull. 37, 108–117. doi:10.1093/schbul/sbp010

Ma, C., Li, W., Xu, Y., Rizo, J., 2011. Munc13 mediates the transition from the closed syntaxin-Munc18 complex to the SNARE complex. Nat. Struct. Mol. Biol. 18, 542–549. doi:10.1038/nsmb.2047

Madadi Asl, M., Vahabie, A.-H., Valizadeh, A., 2019. Dopaminergic modulation of synaptic plasticity, its role in neuropsychiatric disorders, and its computational modeling. Basic Clin. Neurosci. 10, 1–12. doi:10.32598/bcn.9.10.125

Mann, F.A., Herrmann, N., Meyer, D., Kruss, S., 2017. Tuning Selectivity of Fluorescent Carbon Nanotube-Based Neurotransmitter Sensors. Sensors (Basel) 17. doi:10.3390/s17071521

Masharina, A., Reymond, L., Maurel, D., Umezawa, K., Johnsson, K., 2012. A fluorescent sensor for GABA and synthetic GABA(B) receptor ligands. J. Am. Chem. Soc. 134, 19026–19034. doi:10.1021/ja306320s

Matsuda, W., Furuta, T., Nakamura, K.C., Hioki, H., Fujiyama, F., Arai, R., Kaneko, T., 2009. Single nigrostriatal dopaminergic neurons form widely spread and highly dense axonal arborizations in the neostriatum. J. Neurosci. 29, 444–453. doi:10.1523/JNEUROSCI.4029-08.2009

Matsushita, N., Okada, H., Yasoshima, Y., Takahashi, K., Kiuchi, K., Kobayashi, K., 2002. Dynamics of tyrosine hydroxylase promoter activity during midbrain dopaminergic neuron development. J. Neurochem. 82, 295-304. doi: 10.1046/j.1471-4159.2002.00972

Mendez, J.A., Bourque, M.-J., Fasano, C., Kortleven, C., Trudeau, L.-E., 2011. Somatodendritic dopamine release requires synaptotagmin 4 and 7 and the participation of voltage-gated calcium channels. J. Biol. Chem. 286, 23928–23937. doi:10.1074/jbc.M111.218032

Meyer, D., Hagemann, A., Kruss, S., 2017. Kinetic Requirements for Spatiotemporal Chemical Imaging with Fluorescent Nanosensors. ACS Nano 11, 4017–4027. doi:10.1021/acsnano.7b00569

Missale, C., Nash, S.R., Robinson, S.W., Jaber, M., Caron, M.G., 1998. Dopamine receptors: from structure to function. Physiol. Rev. 78, 189–225. doi:10.1152/physrev.1998.78.1.189

Mohebi, A., Pettibone, J.R., Hamid, A.A., Wong, J.-M.T., Vinson, L.T., Patriarchi, T., Tian, L., Kennedy, R.T., Berke, J.D., 2019. Dissociable dopamine dynamics for learning and motivation. Nature 570, 65–70. doi:10.1038/s41586-019-1235-y

Mosharov, E.V., Borgkvist, A., Sulzer, D., 2015. Presynaptic effects of levodopa and their possible role in dyskinesia. Mov. Disord. 30, 45–53. doi:10.1002/mds.26103

Mosharov, E.V., Sulzer, D., 2005. Analysis of exocytotic events recorded by amperometry. Nat. Methods 2, 651–658. doi:10.1038/nmeth782

Muller, A., Joseph, V., Slesinger, P.A., Kleinfeld, D., 2014. Cell-based reporters reveal in vivo dynamics of dopamine and norepinephrine release in murine cortex. Nat. Methods 11, 1245–1252. doi:10.1038/nmeth.3151

Murthy, V.N., Sejnowski, T.J., Stevens, C.F., 1997. Heterogeneous release properties of visualized individual hippocampal synapses. Neuron 18, 599–612. doi:10.1016/s0896-6273(00)80301-3

Nair, R., Lauks, J., Jung, S., Cooke, N.E., de Wit, H., Brose, N., Kilimann, M.W., Verhage, M., Rhee, J., 2013. Neurobeachin regulates neurotransmitter receptor trafficking to synapses. J. Cell Biol. 200, 61–80. doi:10.1083/jcb.201207113

Namiki, S., Sakamoto, H., Iinuma, S., Iino, M., Hirose, K., 2007. Optical glutamate sensor for spatiotemporal analysis of synaptic transmission. Eur. J. Neurosci. 25, 2249–2259. doi:10.1111/j.1460-9568.2007.05511.x

Nirenberg, M.J., Chan, J., Liu, Y., Edwards, R.H., Pickel, V.M., 1996a. Ultrastructural localization of the vesicular monoamine transporter-2 in midbrain dopaminergic neurons: potential sites for somatodendritic storage and release of dopamine. J. Neurosci. 16, 4135–4145. doi:10.1523/JNEUROSCI.16-13-04135.1996

Nirenberg, M.J., Vaughan, R.A., Uhl, G.R., Kuhar, M.J., Pickel, V.M., 1996b. The dopamine transporter is localized to dendritic and axonal plasma membranes of nigrostriatal dopaminergic neurons. J. Neurosci. 16, 436–447.

Nißler, R., Mann, F.A., Chaturvedi, P., Horlebein, J., Meyer, D., Vukovic, L., Kruss, S., 2019. Quantification of the Number of Adsorbed DNA Molecules on Single-Walled Carbon Nanotubes. J. Phys. Chem. C. doi:10.1021/acs.jpcc.8b11058

Niu, Y., Chan, W.-I., Yu, N., Gan, J., Dong, L., Wang, C., 2015. APTES-modified nanosilica--but neither APTES nor nanosilica--inhibits endothelial cell growth via arrest of cell cycle at G1 phase. J Biomater Appl 30, 608–617. doi:10.1177/0885328215598497

O'Connell, M.J., Bachilo, S.M., Huffman, C.B., Moore, V.C., Strano, M.S., Haroz, E.H., Rialon, K.L., Boul, P.J., Noon, W.H., Kittrell, C., Ma, J., Hauge, R.H., Weisman, R.B., Smalley, R.E., 2002. Band gap fluorescence from individual single-walled carbon nanotubes. Science 297, 593–596. doi:10.1126/science.1072631

Okubo, Y., Sekiya, H., Namiki, S., Sakamoto, H., Iinuma, S., Yamasaki, M., Watanabe, M., Hirose, K., Iino, M., 2010. Imaging extrasynaptic glutamate dynamics in the brain. Proc. Natl. Acad. Sci. USA 107, 6526–6531. doi:10.1073/pnas.0913154107

Omiatek, D.M., Bressler, A.J., Cans, A.-S., Andrews, A.M., Heien, M.L., Ewing, A.G., 2013. The real catecholamine content of secretory vesicles in the CNS revealed by electrochemical cytometry. Sci. Rep. 3, 1447. doi:10.1038/srep01447

Omiatek, D.M., Dong, Y., Heien, M.L., Ewing, A.G., 2010. Only a fraction of quantal content is released during exocytosis as revealed by electrochemical cytometry of secretory vesicles. ACS Chem. Neurosci. 1, 234–245. doi:10.1021/cn900040e

Oorschot, D.E., 1996. Total number of neurons in the neostriatal, pallidal, subthalamic, and substantia nigral nuclei of the rat basal ganglia: a stereological study using the cavalieri and optical disector methods. J. Comp. Neurol. 366, 580–599. doi:10.1002/(SICI)1096-9861(19960318)366:4<580::AID-CNE3>3.0.CO;2-0

Pan, P.-Y., Ryan, T.A., 2012. Calbindin controls release probability in ventral tegmental area dopamine neurons. Nat. Neurosci. 15, 813–815. doi:10.1038/nn.3099

Patriarchi, T., Cho, J.R., Merten, K., Howe, M.W., Marley, A., Xiong, W.-H., Folk, R.W., Broussard, G.J., Liang, R., Jang, M.J., Zhong, H., Dombeck, D., von Zastrow, M., Nimmerjahn, A., Gradinaru, V., Williams, J.T., Tian, L., 2018. Ultrafast neuronal imaging of dopamine dynamics with designed genetically encoded sensors. Science 360. doi:10.1126/science.aat4422

Patriarchi, T., Cho, J.R., Merten, K., Marley, A., Broussard, G.J., Liang, R., Williams, J., Nimmerjahn, A., von Zastrow, M., Gradinaru, V., Tian, L., 2019. Imaging neuromodulators with high spatiotemporal

resolution using genetically encoded indicators. Nat. Protoc. 14, 3471–3505. doi:10.1038/s41596-019-0239-2

Pereira, D.B., Schmitz, Y., Mészáros, J., Merchant, P., Hu, G., Li, S., Henke, A., Lizardi-Ortiz, J.E., Karpowicz, R.J., Morgenstern, T.J., Sonders, M.S., Kanter, E., Rodriguez, P.C., Mosharov, E.V., Sames, D., Sulzer, D., 2016. Fluorescent false neurotransmitter reveals functionally silent dopamine vesicle clusters in the striatum. Nat. Neurosci. 19, 578–586. doi:10.1038/nn.4252

Pickel, V.M., Nirenberg, M.J., Milner, T.A., 1996. Ultrastructural view of central catecholaminergic transmission: immunocytochemical localization of synthesizing enzymes, transporters and receptors. J Neurocytol 25, 843–856. doi:10.1007/BF02284846

Pike, C.M., Grabner, C.P., Harkins, A.B., 2009. Fabrication of amperometric electrodes. J. Vis. Exp. doi:10.3791/1040

Polo, E, Kruss, S., 2016. Nanosensors for neurotransmitters. Anal. Bioanal. Chem. 408, 2727–2741. doi:10.1007/s00216-015-9160-x

Polo, Elena, Kruss, S., 2016. Impact of Redox-Active Molecules on the Fluorescence of Polymer-Wrapped Carbon Nanotubes. J. Phys. Chem. C 120, 3061–3070. doi:10.1021/acs.jpcc.5b12183

Pothos, E., Desmond, M., Sulzer, D., 1996. L-3,4-dihydroxyphenylalanine increases the quantal size of exocytotic dopamine release in vitro. J. Neurochem. 66, 629–636. doi:10.1046/j.1471-4159.1996.66020629.x

Pothos, E.N., Davila, V., Sulzer, D., 1998. Presynaptic recording of quanta from midbrain dopamine neurons and modulation of the quantal size. J. Neurosci. 18, 4106–4118.

Powell, L.R., Piao, Y., Ng, A.L., Wang, Y., 2018. Channeling Excitons to Emissive Defect Sites in Carbon Nanotube Semiconductors beyond the Dilute Regime. J. Phys. Chem. Lett. 9, 2803–2807. doi:10.1021/acs.jpclett.8b00930

Rayport, S., Sulzer, D., Shi, W.X., Sawasdikosol, S., Monaco, J., Batson, D., Rajendran, G., 1992. Identified postnatal mesolimbic dopamine neurons in culture: morphology and electrophysiology. J. Neurosci. 12, 4264–4280.

Reyes, S., Fu, Y., Double, K., Thompson, L., Kirik, D., Paxinos, G., Halliday, G.M., 2012. GIRK2 expression in dopamine neurons of the substantia nigra and ventral tegmental area. J. Comp. Neurol. 520, 2591–2607. doi:10.1002/cne.23051

Rhee, H.J., Shaib, A.H., Rehbach, K., Lee, C., Seif, P., Thomas, C., Gideons, E., Guenther, A., Krutenko, T., Hebisch, M., Peitz, M., Brose, N., Brüstle, O., Rhee, J.S., 2019. An Autaptic Culture System for Standardized Analyses of iPSC-Derived Human Neurons. Cell Rep. 27, 2212–2228.e7. doi:10.1016/j.celrep.2019.04.059

Rice, M.E., Cragg, S.J., 2008. Dopamine spillover after quantal release: rethinking dopamine transmission in the nigrostriatal pathway. Brain Res. Rev. 58, 303–313. doi:10.1016/j.brainresrev.2008.02.004

Rienecker, K.D.A., Poston, R.G., Saha, R.N., 2020. Merits and Limitations of Studying Neuronal Depolarization-Dependent Processes Using Elevated External Potassium. ASN Neuro 12, 1759091420974807. doi:10.1177/1759091420974807

Ripamonti, S., Ambrozkiewicz, M.C., Guzzi, F., Gravati, M., Biella, G., Bormuth, I., Hammer, M., Tuffy, L.P., Sigler, A., Kawabe, H., Nishimori, K., Toselli, M., Brose, N., Parenti, M., Rhee, J., 2017. Transient oxytocin signaling primes the development and function of excitatory hippocampal neurons. Elife 6. doi:10.7554/eLife.22466

Robinson, D.L., Venton, B.J., Heien, M.L.A.V., Wightman, R.M., 2003. Detecting subsecond dopamine release with fast-scan cyclic voltammetry in vivo. Clin. Chem. 49, 1763–1773. doi:10.1373/49.10.1763

Rosenmund, C., Sigler, A., Augustin, I., Reim, K., Brose, N., Rhee, J.S., 2002. Differential control of vesicle priming and short-term plasticity by Munc13 isoforms. Neuron 33, 411–424. doi:10.1016/s0896-6273(02)00568-8

Rosenmund, C., Stevens, C.F., 1996. Definition of the readily releasable pool of vesicles at hippocampal synapses. Neuron 16, 1197–1207. doi:10.1016/s0896-6273(00)80146-4

Ryan, T.A., Reuter, H., Smith, S.J., 1997. Optical detection of a quantal presynaptic membrane turnover. Nature 388, 478–482. doi:10.1038/41335

Sawamoto, K., Nakao, N., Kobayashi, K., Matsushita, N., Takahashi, H., Kakishita, K., Yamamoto, A., Yoshizaki, T., Terashima, T., Murakami, F., Itakura, T., Okano, H., 2001. Visualization, direct isolation, and transplantation of midbrain dopaminergic neurons. Proc. Natl. Acad. Sci. USA 98, 6423–6428. doi:10.1073/pnas.111152398

Schöppler, F., Mann, C., Hain, T.C., Neubauer, F.M., Privitera, G., Bonaccorso, F., Chu, D., Ferrari, A.C., Hertel, T., 2011. Molar Extinction Coefficient of Single-Wall Carbon Nanotubes. J. Phys. Chem. C 115, 14682–14686. doi:10.1021/jp205289h

Schultz, W., 2019. Recent advances in understanding the role of phasic dopamine activity. [version 1; peer review: 3 approved]. F1000Res. 8. doi:10.12688/f1000research.19793.1

Senior, S.L., Ninkina, N., Deacon, R., Bannerman, D., Buchman, V.L., Cragg, S.J., Wade-Martins, R., 2008. Increased striatal dopamine release and hyperdopaminergic-like behaviour in mice lacking both alpha-synuclein and gamma-synuclein. Eur. J. Neurosci. 27, 947–957. doi:10.1111/j.1460-9568.2008.06055.x

Sesack, S.R., Aoki, C., Pickel, V.M., 1994. Ultrastructural localization of D2 receptor-like immunoreactivity in midbrain dopamine neurons and their striatal targets. J. Neurosci. 14, 88–106. doi:10.1523/JNEUROSCI.14-01-00088.1994

Söllner, T., Whiteheart, S.W., Brunner, M., Erdjument-Bromage, H., Geromanos, S., Tempst, P., Rothman, J.E., 1993. SNAP receptors implicated in vesicle targeting and fusion. Nature 362, 318–324. doi:10.1038/362318a0

Speidel, D., Varoqueaux, F., Enk, C., Nojiri, M., Grishanin, R.N., Martin, T.F.J., Hofmann, K., Brose, N., Reim, K., 2003. A family of Ca2+-dependent activator proteins for secretion: comparative analysis of structure, expression, localization, and function. J. Biol. Chem. 278, 52802–52809. doi:10.1074/jbc.M304727200

Staal, R.G.W., Mosharov, E.V., Sulzer, D., 2004. Dopamine neurons release transmitter via a flickering fusion pore. Nat. Neurosci. 7, 341–346. doi:10.1038/nn1205

Staal, R.G.W., Rayport, S., Sulzer, D., 2007. Amperometric Detection of Dopamine Exocytosis from Synaptic Terminals, in: Michael, A.C., Borland, L.M. (Eds.), Electrochemical methods for neuroscience. CRC Press/Taylor & Francis, Boca Raton (FL). doi:10.1201/9781420005868.ch16

Stevens, C.F., Tsujimoto, T., 1995. Estimates for the pool size of releasable quanta at a single central synapse and for the time required to refill the pool. Proc. Natl. Acad. Sci. USA 92, 846–849. doi:10.1073/pnas.92.3.846

Sudhof, T.C., 2004. The synaptic vesicle cycle. Annu. Rev. Neurosci. 27, 509–547. doi:10.1146/annurev.neuro.26.041002.131412

Südhof, T.C., 2012. The presynaptic active zone. Neuron 75, 11–25. doi:10.1016/j.neuron.2012.06.012

Südhof, T.C., 2013. Neurotransmitter release: the last millisecond in the life of a synaptic vesicle. Neuron 80, 675–690. doi:10.1016/j.neuron.2013.10.022

Sulzer, D., 2011. How addictive drugs disrupt presynaptic dopamine neurotransmission. Neuron 69, 628–649. doi:10.1016/j.neuron.2011.02.010

Sulzer, D., Cragg, S.J., Rice, M.E., 2016. Striatal dopamine neurotransmission: regulation of release and uptake. Basal Ganglia 6, 123–148. doi:10.1016/j.baga.2016.02.001

Sulzer, D., Joyce, M.P., Lin, L., Geldwert, D., Haber, S.N., Hattori, T., Rayport, S., 1998. Dopamine neurons make glutamatergic synapses in vitro. J. Neurosci. 18, 4588–4602.

Sulzer, D., Rayport, S., 2000. Dale's principle and glutamate corelease from ventral midbrain dopamine neurons. Amino Acids 19, 45–52.

Sulzer, D., Sonders, M.S., Poulsen, N.W., Galli, A., 2005. Mechanisms of neurotransmitter release by amphetamines: a review. Prog. Neurobiol. 75, 406–433. doi:10.1016/j.pneurobio.2005.04.003

Sulzer, D., St Remy, C., Rayport, S., 1996. Reserpine inhibits amphetamine action in ventral midbrain culture. Mol. Pharmacol. 49, 338–342.

Sun, F., Zeng, J., Jing, M., Zhou, J., Feng, J., Owen, S.F., Luo, Y., Li, F., Wang, H., Yamaguchi, T., Yong, Z., Gao, Y., Peng, W., Wang, L., Zhang, S., Du, J., Lin, D., Xu, M., Kreitzer, A.C., Cui, G., Li, Y., 2018. A genetically encoded fluorescent sensor enables rapid and specific detection of dopamine in flies, fish, and mice. Cell 174, 481–496.e19. doi:10.1016/j.cell.2018.06.042

Taber, K.H., Hurley, R.A., 2014. Volume transmission in the brain: beyond the synapse. J. Neuropsychiatry Clin. Neurosci. 26, iv, 1–4. doi:10.1176/appi.neuropsych.13110351

Thuret, S., Bhatt, L., O'Leary, D.D.M., Simon, H.H., 2004. Identification and developmental analysis of genes expressed by dopaminergic neurons of the substantia nigra pars compacta. Mol. Cell. Neurosci. 25, 394–405. doi:10.1016/j.mcn.2003.11.004

Tiklová, K., Björklund, Å.K., Lahti, L., Fiorenzano, A., Nolbrant, S., Gillberg, L., Volakakis, N., Yokota, C., Hilscher, M.M., Hauling, T., Holmström, F., Joodmardi, E., Nilsson, M., Parmar, M., Perlmann, T., 2019. Single-cell RNA sequencing reveals midbrain dopamine neuron diversity emerging during mouse brain development. Nat. Commun. 10, 581. doi:10.1038/s41467-019-08453-1

Tritsch, N.X., Ding, J.B., Sabatini, B.L., 2012. Dopaminergic neurons inhibit striatal output through non-canonical release of GABA. Nature 490, 262–266. doi:10.1038/nature11466

Tritsch, N.X., Granger, A.J., Sabatini, B.L., 2016. Mechanisms and functions of GABA co-release. Nat. Rev. Neurosci. 17, 139–145. doi:10.1038/nrn.2015.21

Tritsch, N.X., Sabatini, B.L., 2012. Dopaminergic modulation of synaptic transmission in cortex and striatum. Neuron 76, 33–50. doi:10.1016/j.neuron.2012.09.023

Trouillon, R., Ewing, A.G., 2014. Actin controls the vesicular fraction of dopamine released during extended kiss and run exocytosis. ACS Chem. Biol. 9, 812–820. doi:10.1021/cb400665f

Trudeau, L.-E., Hnasko, T.S., Wallén-Mackenzie, A., Morales, M., Rayport, S., Sulzer, D., 2014. The multilingual nature of dopamine neurons. Prog. Brain Res. 211, 141–164. doi:10.1016/B978-0-444-63425-2.00006-4

Tysnes, O.-B., Storstein, A., 2017. Epidemiology of Parkinson's disease. J. Neural Transm. 124, 901–905. doi:10.1007/s00702-017-1686-y

Vargas, K.J., Makani, S., Davis, T., Westphal, C.H., Castillo, P.E., Chandra, S.S., 2014. Synucleins regulate the kinetics of synaptic vesicle endocytosis. J. Neurosci. 34, 9364–9376. doi:10.1523/JNEUROSCI.4787-13.2014

Vargas, K.J., Schrod, N., Davis, T., Fernandez-Busnadiego, R., Taguchi, Y.V., Laugks, U., Lucic, V., Chandra, S.S., 2017. Synucleins have multiple effects on presynaptic architecture. Cell Rep. 18, 161–173. doi:10.1016/j.celrep.2016.12.023

Varoqueaux, F., Sigler, A., Rhee, J.-S., Brose, N., Enk, C., Reim, K., Rosenmund, C., 2002. Total arrest of spontaneous and evoked synaptic transmission but normal synaptogenesis in the absence of

Munc13-mediated vesicle priming. Proc. Natl. Acad. Sci. USA 99, 9037–9042. doi:10.1073/pnas.122623799

Venton, B.J., Zhang, H., Garris, P.A., Phillips, P.E.M., Sulzer, D., Wightman, R.M., 2003. Real-time decoding of dopamine concentration changes in the caudate-putamen during tonic and phasic firing. J. Neurochem. 87, 1284–1295. doi:10.1046/j.1471-4159.2003.02109.x

Verhage, M., Maia, A.S., Plomp, J.J., Brussaard, A.B., Heeroma, J.H., Vermeer, H., Toonen, R.F., Hammer, R.E., van den Berg, T.K., Missler, M., Geuze, H.J., Südhof, T.C., 2000. Synaptic assembly of the brain in the absence of neurotransmitter secretion. Science 287, 864–869. doi:10.1126/science.287.5454.864

Vogl, C., Cooper, B.H., Neef, J., Wojcik, S.M., Reim, K., Reisinger, E., Brose, N., Rhee, J.-S., Moser, T., Wichmann, C., 2015. Unconventional molecular regulation of synaptic vesicle replenishment in cochlear inner hair cells. J. Cell Sci. 128, 638–644. doi:10.1242/jcs.162099

Weinert, M., Selvakumar, T., Tierney, T.S., Alavian, K.N., 2015. Isolation, culture and long-term maintenance of primary mesencephalic dopaminergic neurons from embryonic rodent brains. J. Vis. Exp. doi:10.3791/52475

Welsher, K., Sherlock, S.P., Dai, H., 2011. Deep-tissue anatomical imaging of mice using carbon nanotube fluorophores in the second near-infrared window. Proc. Natl. Acad. Sci. USA 108, 8943–8948. doi:10.1073/pnas.1014501108

White, K.A., Kim, B.N., 2021. Quantifying neurotransmitter secretion at single-vesicle resolution using high-density complementary metal-oxide-semiconductor electrode array. Nat. Commun. 12, 431. doi:10.1038/s41467-020-20267-0

Witkovsky, P., Patel, J.C., Lee, C.R., Rice, M.E., 2009. Immunocytochemical identification of proteins involved in dopamine release from the somatodendritic compartment of nigral dopaminergic neurons. Neuroscience 164, 488–496. doi:10.1016/j.neuroscience.2009.08.017

Wittenberg, N., Maxson, M., Eves, D., Cans, A.-S., Ewing, A.G., 2007. Electrochemistry at the cell membrane/solution interface, in: Michael, A.C., Borland, L.M. (Eds.), Electrochemical methods for neuroscience, Frontiers

in Neuroengineering. CRC Press/Taylor & Francis, Boca Raton (FL).

Wojcik, S.M., Brose, N., 2007. Regulation of membrane fusion in synaptic excitation-secretion coupling: speed and accuracy matter. Neuron 55, 11–24. doi:10.1016/j.neuron.2007.06.013

Yakushenko, A., Kätelhön, E., Wolfrum, B., 2013. Parallel on-chip analysis of single vesicle neurotransmitter release. Anal. Chem. 85, 5483–5490. doi:10.1021/ac4006183

Ye, H., Steiger, A., 2015. Neuron matters: electric activation of neuronal tissue is dependent on the interaction between the neuron and the electric field. J Neuroeng Rehabil 12, 65. doi:10.1186/s12984-015-0061-1

Zhang, H., Gubernator, N.G., Yue, M., Staal, R.G.W., Mosharov, E.V., Pereira, D., Balsanek, V., Vadola, P.A., Mukherjee, B., Edwards, R.H., Sulzer, D., Sames, D., 2009. Dopamine release at individual presynaptic terminals visualized with FFNs. J. Vis. Exp. doi:10.3791/1562

Zhang, J., Landry, M.P., Barone, P.W., Kim, J.-H., Lin, S., Ulissi, Z.W., Lin, D., Mu, B., Boghossian, A.A., Hilmer, A.J., Rwei, A., Hinckley, A.C., Kruss, S., Shandell, M.A., Nair, N., Blake, S., Şen, F., Şen, S., Croy, R.G., Li, D., Yum, K., Ahn, J.-H., Jin, H., Heller, D.A., Essigmann, J.M., Blankschtein, D., Strano, M.S., 2013. Molecular recognition using corona phase complexes made of synthetic polymers adsorbed on carbon nanotubes. Nat. Nanotechnol. 8, 959–968. doi:10.1038/nnano.2013.236

Zhang, S., Qi, J., Li, X., Wang, H.-L., Britt, J.P., Hoffman, A.F., Bonci, A., Lupica, C.R., Morales, M., 2015. Dopaminergic and glutamatergic microdomains in a subset of rodent mesoaccumbens axons. Nat. Neurosci. 18, 386–392. doi:10.1038/nn.3945

Zoli, M., Torri, C., Ferrari, R., Jansson, A., Zini, I., Fuxe, K., Agnati, L.F., 1998. The emergence of the volume transmission concept. Brain Res Brain Res Rev 26, 136–147. doi:10.1016/s0165-0173(97)00048-9

Zuber, B., Nikonenko, I., Klauser, P., Muller, D., Dubochet, J., 2005. The mammalian central nervous synaptic cleft contains a high density of periodically organized complexes. Proc. Natl. Acad. Sci. USA 102, 19192–19197. doi:10.1073/pnas.0509527102

7 Acknowledgements

First of all, I would like thank Dr. James Daniel, who took me on as his rotation student, master student, and finally, doctoral student. All my lab and writing skills I learned from him. I am sincerely grateful for his patience, teaching, support, guidance, encouragement, constructive feedback and most importantly friendship over the last six years. I know how lucky I was to have him as my supervisor, who made this journey inspiring and enjoyable.

I am thankful also especially to Prof. Dr. Nils Brose for inviting me to work and pursue my doctoral degree in his laboratory, for all the opportunities he gave me along the way, for kindly agreeing on being my first examiner and for helping and encouraging me during my work. His positive attitude and trust is what gave me room for personal and professional growth.

I would like to thank my Thesis Committee members: Prof. Dr. Nils Brose, Prof. Dr. Tiago Fleming Outeiro and Dr. Sebastian Kruss for taking the time to evaluate my dissertation and for their valuable feedback during committee meetings. I would also like to thank members of my extended examination board Prof. Dr. Thomas Dresbach, Prof. Dr. Silvio O. Rizzoli and Prof. Dr. Dr. Oliver Schlüter for taking the time to act as examiners in my thesis defense.

Furthermore I would like to thank the members of the molecular neurobiology laboratory who created an amazing community, for their fun company, never tired of intense scientific and non-scientific discussions over coffee or lunch and even mid-night snacks: Heba Ali, Jutta Meyer, Aisha Ahmad, Bekir Altas, Olga Babaev, Carolina Thomas, Lydia Bickford Maus, Benjamin Cooper, Hugo Cruces-Solis, Silvia Ripamonti, Ali Shaib, Ines Hojas Garcia-Plaza, Marilyn Tirard, Liam Tuffy, Albrecht Sigler, Erinn Gideons, Lena Sünke Mortensen, Francisco Lopez Murcia, Öyküm Kaplan, Manuela Schwark, Dragana Ilic, Valentina Cirkovic, Sven Wagner, Dominik Sakry, Hong Jun Rhee, Chungku Lee, Noa Lipstein, Kerstin Reim, Prof. Dr.Rhee Jeong Seop, Dilja Krüger-Burg, Jennifer Day, Aline Breitenbach, Holger Taschenberger Anja Günther, Thea und Klaus Hellmann, Frederike Maaß, Valentin Schwarze, Sally Wenger, Sonja Wojcik, Astrid Zeuch and Birgit Gläser.

I would like to appreciate the great work of the AGCT lab, who provided me with DNA for nanosensors synthesis, performed the genotyping and finally, established in no time after start of the pandemic a routine Covid-19 test station, which allowed me to continue my lab work in a safe environment: Fritz Benseler, Christiane Harenberg, Dayana Schwerdtfeger and Ivonne Thanhäuser.

Especially I would like to thank Cordelia Imig, Noa Lipstein, Anke Schraepler, Ursula Fünfschilling and Sarah Kimmina who advised me on the management and breeding of mouse-lines and

helped me through the jungle of animal-related paperwork, and Bianca Nickel for her amazing technical support of colony maintenance. I would like to thank Prof. Dr. Paul Lingor, K. Kobayashi and the RIKEN Institute, Japan, for providing us with the TH-EGFP mice.

I would like to thank our collaborators, the Kruss' and Jahnshoffs' laboratory, who introduced me to the adventures of nanotube and AFM imaging, offered me to work in their facilities and use their equipment, as well as technical and scientific support during my experiments, without which this work would not have been possible: Prof. Dr. Andreas Janshoff, Angela Rübeling, Dr. Tabea Oswald, Robert Nissler, Gabriele Selvaggio, Meshkat Dinarvand, Maria Dohmen, Florian Alexander Mann, Larissa Kurth, Elsa Neubert, Niklas Herrmann, Daniel Meyer, Alexander Spreinat and Elena Alexandra Polo.

I would like to give special thanks to the colleagues who became dear friends to me: Valérie Clavet-Fournier, Heba Ali and Anouk Meeuwissen. You made the PhD madness bearable and I sincerely hope that our friendship will last beyond borders, wherever we will be scattered by destiny!

I would like to thank the people who took the time to proofread and edit my thesis, (especially on a very short notice!): Most of all James Daniel, and also Sebastian Kruss, Erinn Gideons, Anouk Meeuwissen and Heba Ali.

… and of course I am grateful to everyone else whom I had the honor to meet during the course of my PhD and who made my stay the wonderful experience that is was!

I am grateful to my old friends and family from the hanover community, especially Jonny, Mo and Ana and my sister Anna, who always have an ear and door open in difficult and fun times. Returning to you always feels like coming home. I had the best times of my life with you will never forget our adventures! Hopefully, after the pandemic there will be many more to come.

Finally, to Sheetansh Kaushik, my partner in life: You know me for as long as I pursued my scientific studies. You made the whole journey with me, despite hundreds of kilometers that were between us most of the time. I am really happy that we met 😊 and I could not imagine having survived these stressful times without your support. To the future!